Title
Design and Synthesis of Dynamically Controllable DNA Nanostructures

Author
Agarwal, Siddharth

Publication Date
2021

Peer reviewed|Thesis/dissertation

UNIVERSITY OF CALIFORNIA

Los Angeles

Design and Synthesis of Dynamically Controllable DNA Nanostructures

A dissertation submitted in partial satisfaction of the requirements for the degree of

Doctor of Philosophy in Bioengineering

by

Siddharth Agarwal

2021

ABSTRACT OF THE DISSERTATION

Design and Synthesis of Dynamically Controllable Nanostructures

by

Siddharth Agarwal

Doctor of Philosophy in Bioengineering

University of California, Los Angeles, 2021

Professor Elisa Franco, Chair

Deoxyribonucleic acid (DNA) and Ribonucleic acid (RNA) are molecules that store and transmit genetic information and are present nearly all living organisms. The field of nucleic acid nanotechnology uses these molecules out of its biological context and employs it to build structures and then to connect their operation. Although DNA nanotechnology was originally developed to elucidate protein crystallization, recent developments in the field are testing the limits of its application towards a multitude of fields ranging from nanofabrication to computation. One of the important frontiers that remain to be addressed is the production of ‘active’ material that can interact with its environment and adapt to it intelligently, rivalling organelles present inside cells. This dissertation reports on the construction of responsive nucleic acid structures that can demonstrate autonomous function and capability to respond to physical and chemical inputs.

As the first example, we show how the self-assembly process of monomers made out of DNA strands can be triggered into activation by specific chemical inputs, in our case RNA molecules to build tubular structures. These ‘nanotubes’ can be temporally controlled by simple

molecular programs, mimicking the architecture used by biological cells to direct their internal scaffolds. Our molecular programs use enzymes to produce or degrade RNA molecules embedded in the DNA nanotubes. Our results indicate that RNA can be used as a fuel for assembly, and that genetic circuits and enzymes can be an integral part in the operation of active nanostructures. This activatable self-assembly technique could be used to create a programmable synthetic version of filaments whose operation may mimic the cytoskeleton.

The second theme of this dissertation is the autonomous control of assembly and disassembly of nucleic acid nanotubes inside cell-sized environments. We used different designs to observe and control nucleation, polymerization and depolymerization steps in the self-assembly dynamics of encapsulated structures. The kinetics of growth and degradation of these encapsulated tubular structures were quantified using epi-fluorescence microscopy. We were also able to demonstrate the production of nucleotide assemblies with external stimuli, such as heat and light. These demonstrations can pave the way for designing and observing the functionality of responsive materials across the nanometer to micron size scales.

The dissertation of Siddharth Agarwal is approved.

Samanvaya Srivastava

Yvonne Chen

Chang-Jin Kim

Elisa Franco, Committee Chair

University of California Los Angeles

2021

Dedication

This work is dedicated to people around me, who supported me along the way. First and foremost, I would like to express my deepest gratitude to my advisor, Dr. Elisa Franco. I can't imagine what would have happened without her tutelage and constant encouragement. She took the risk of accepting a disorganized but enthusiastic young novice in her lab and transform him into a scientist and a better human being. Her door and zoom room were always open for me at all times and her patience and positive attitude gave me a high motivation to keep moving forward. I have no doubt that I owe more to her for my scientific and personal growth than I presently realize. I aspire to mentor others in the same way she has mentored me.

I am thankful to my doctoral committee members, Dr. Chang-Jin Kim, Dr. Yvonne Chen and Dr. Samanvaya Srivastava for their critical feedback on my research progress and helpful suggestions throughout my Ph.D. journey.

My journey as a graduate student might have ended before it began, had it not been for the brilliant and kind members of the Franco Lab. I am grateful to Hari Subramanian and Leopold Green for your patience in training me, answering my stupid questions on everything from dilutions and unit conversions to DNA helicity. I am extremely thankful for Jaimie Stewart for her friendship and sharing her expertise in designing RNA assemblies. Special thanks to Christian Cuba for making my Ph.D. journey fun with all the travel, being a bouncing board for my ideas and a constant motivating push to complete my studies. Thanks Jenny Le, Dino Osmanovic, and Xun Tang for their constant encouragement, constructive feedback and stimulating discussions. Lastly, thank you Melissa Klocke for tolerating my poor attempt at humor, entertaining my craziness and still being my closest friend.

I would like to thank my friends, who shared my happiness, sadness and gave me a strong sense of belonging to society. Thank you Tommaso and Lasata for being my travelling

companions and lending a patient ear to my frustrated rants. Thank you Gianluca and Lorenzo for being at my constant beck and call to find free food across the campus. I will also forever be grateful to my bioengineering cohort for helping me adjust to grad school. Thank you Nikhil for picking up my call whenever I needed a break. I want to specifically mention Aakash, Tushar, Rajashekhar and Rameswar for the late night hangouts and all the love and enjoyable times.

My highest dedication goes to my family for their unwavering support. My mother, Kavita Agarwal who is the most supportive, encouraging, and understanding soul in this world. She was a Ph.D. student in India at a time when there was slight support for women in academia. Mom, this one is for you. My father, Kamal Agarwal, who is the most loving and caring person in this world. I may not admit it later but you are the funniest person I know. My brother and my best friend Adhip Agarwal, spending my childhood with you was the best warm up for the game that is adulthood.

Lastly, but very importantly, I would like to express my love and gratitude to my wife, Maïko Le Lay for the unconditional love, joy and encouragement she has offered me over the years and making me realize what is truly valuable in life.

TABLE OF CONTENTS

LIST OF FIGURES

LIST OF SUPPLEMENTARY FIGURES

Acknowledgements

A version of Chapter 1 was published:

Reproduced with permission from S. Agarwal and E. Franco, "Enzyme-Driven Assembly and Disassembly of Hybrid DNA–RNA Nanotubes." Journal of the American Chemical Society 141, no. 19 (2019): 7831-7841. Copyright 2019 American Chemical Society.

Agarwal and Franco designed the research; Agarwal performed the research; Agarwal and Franco analyzed the data; Agarwal and Franco wrote the paper.

A version of Chapter 2 was published:

Reproduced with permission from Pacella, Michael S., Vahid Mardanlou, Siddharth Agarwal, Anusha Patel, Elizabeth Jelezniakov, Abdul M. Mohammed, Elisa Franco, and Rebecca Schulman. "Characterizing the length-dependence of DNA nanotube end-to-end joining rates." Molecular Systems Design & Engineering 5, no. 2 (2020): 544-558. Copyright 2020 Royal Society of Chemistry

Mohammed, Agarwal, Pacella, Franco and Shulman designed the research; Simulations in this chapter were done by Agarwal based on experiments conducted by Mohammed and were not included in the manuscript above; Above manuscript has simulations conducted by Mardanlou on experimental data collected by Pacella, Patel and Jelezniakov; Agarwal and Franco wrote the text in this chapter; Pacella, Franco and Schulman wrote the manuscript with feedback from the other authors.

A version of Chapter 3 was published:

Reproduced with permission from S. Agarwal, M. Klocke, P. Pungchai and E. Franco, "Dynamic self-assembly of compartmentalized DNA nanotubes." Nature communications 12, no. 1 (2021): 1-13. Copyright 2021 Springer Nature.

Agarwal , Klocke, and Franco designed the research; Agarwal and Klocke performed the research; Klocke conducted the data processing; Pungchai and Franco performed the simulations. Agarwal, Klocke, and Franco wrote the manuscript with feedback from the other authors.

I acknowledge the use of the Advance Light Microscopy/Spectroscopy Laboratory and the Leica Microsystems Center of Excellence at the California NanoSystems Institute at UCLA with funding support from the NIH Shared Instrumentation Grant S10OD025017 and NSF Major Research Instrumentation grant CHE-0722519 for confocal microscopy images in chapter 3.

I also acknowledge financial support provided by Dr. Franco via the U.S. Department of Energy under Award Number DE- SC0010595.

VITA

EDUCATION

B.Tech. in Pharmaceutical Sciences and Technology, Institute of Chemical Technology, Mumbai — 2015

RESEARCH EXPERIENCE

Graduate Researcher, UCR Bioengineering — 2015-2016
Advisor: Elisa Franco, Ph.D.

Graduate Researcher, UCR Mechanical Engineering — 2016-2019
Advisor: Elisa Franco, Ph.D.

Graduate Student Researcher, UCLA Bioengineering — 2019-2021
Advisor: Elisa Franco, Ph.D.

PUBLICATIONS (selected)

Siddharth Agarwal, Melissa A. Klocke, Passa E. Pungchai, and Elisa Franco. "Dynamic self-assembly of compartmentalized DNA nanotubes." Nature communications 12, no. 1 (2021): 1-13.

Pacella, Michael S., Vahid Mardanlou, **Siddharth Agarwal**, Anusha Patel, Elizabeth Jelezniakov, Abdul M. Mohammed, Elisa Franco, and Rebecca Schulman. "Characterizing the length-dependence of DNA nanotube end-to-end joining rates." Molecular Systems Design & Engineering 5, no. 2 (2020): 544-558.

Siddharth Agarwal and Elisa Franco. "Enzyme-Driven Assembly and Disassembly of Hybrid DNA–RNA Nanotubes." Journal of the American Chemical Society 141, no. 19 (2019): 7831-7841.

Jeong, Dohyun, Melissa Klocke, **Siddharth Agarwal**, Jeongwon Kim, Seungdo Choi, Elisa Franco, and Jongmin Kim. "Cell-Free Synthetic Biology Platform for Engineering Synthetic Biological Circuits and Systems." Methods and Protocols no. 2 (2019): 39.

1. Chapter 1: Enzyme-driven assembly and disassembly of hybrid tubes containing DNA and RNA

Adapted, with permission from Siddharth Agarwal and Elisa Franco. "Enzyme-Driven Assembly and Disassembly of Hybrid DNA–RNA Nanotubes." Journal of the American Chemical Society 141, no. 19 (2019): 7831-7841.

1.1 Abstract

Living cells have the ability to control the dynamics of responsive assemblies such as the cytoskeleton by temporally activating and deactivating inert precursors. While DNA nanotechnology has demonstrated many synthetic supramolecular assemblies that rival biological ones in size and complexity, dynamic control of their formation is still challenging. Taking inspiration from nature, we developed a DNA-RNA nanotube system whose assembly and disassembly can be temporally controlled at physiological temperature using transcriptional programs. Nanotubes assemble when inert DNA monomers are directly and selectively activated by RNA molecules that become embedded in the structure, producing hybrid DNA-RNA assemblies. The reactions and molecular programs controlling nanotube formation are fueled by enzymes that produce or degrade RNA. We show that the speed of assembly and disassembly of the nanotubes can be controlled by tuning various reaction parameters in the transcriptional programs. We anticipate that these hybrid structures are a starting point to build integrated biological circuits and functional scaffolds inside natural and artificial cells, where RNA produced by gene networks could fuel the assembly of nucleic acid components on demand.

1.2 Introduction

Nucleic acid nanotechnology is a promising approach to understand and replicate the ability of living organisms to build complex machinery at the nanoscale[1-4]. The cytoskeleton, for example, is an impressive dynamic self-assembling system that spatially organizes the contents of the cell, connects it physically and biochemically to the environment and generates coordinated forces that enable the cell to move and change shape[5-7]. Rationally designed nucleic acid systems have been used to build tubular scaffolds with mechanical properties comparable to cytoskeletal filaments[8-13]. In some cases, it has been possible to decorate these nucleic acid nanotubes with various molecules[9,10,12], to use them as gliding paths for motor proteins[14], and to dynamically control their assembly and disassembly using molecular inputs[15,16].

Beyond tubular scaffolds, nucleic acids have been programmed to build a variety of complex structures[17]. Due to its stability and well-understood thermodynamics, DNA has been primarily used for this purpose[17-20]. Self-assembly of RNA structures is challenging due to non-canonical base pairing and to the higher stability of RNA double helices relative to DNA, which increase the likelihood of spurious folding pathways[21]. As a consequence, methods to build RNA nanostructures are still lagging in terms of yield, precision, and scalability when compared to methods targeting DNA. Yet, RNA presents several advantages: it can be transcribed by cells, it can fold into many functional motifs, and it presents better immune compatibility relative to DNA, which may prove crucial for delivery and transport of molecular cargo[22-28]. Building nanostructures that include both DNA and RNA molecules could make it possible to take advantage of the features of both DNA and RNA for manufacturing functional assemblies[26,29,30].

In addition to complex nanostructures, nucleic acids can also be used to build nanodevices capable of dynamic operation. Combining the principles of self-assembly and strand displacement reactions, it was possible to design devices such as motors, autonomous circuits, and walkers[31-34]. Yet, so far few approaches to build responsive, dynamic nanostructures have been demonstrated[15,16,35,36]. It is even more challenging to achieve these behaviors in physiological conditions, highlighting the need for broad design principles that would make it possible to interface complex DNA structures with the cellular machinery in time and space[37]. Since RNA is naturally a carrier of information in living cells, DNA structures that respond to RNA signals could be used to build dynamic nanodevices that can compete with cellular machinery.

Here we demonstrate a strategy to obtain dynamic control of nanostructure self-assembly using DNA and RNA components. Our building blocks are double crossover (DX) DNA tiles, which yield micron-long nanotubes[38]; we engineered DX DNA tiles so that their assembly can be activated only in the presence of an RNA molecular trigger, which is incorporated in the nanostructure. We demonstrate that assembly of these hybrid DNA-RNA structures proceeds at 37 ºC, and can be controlled by simple transcriptional programs producing the RNA trigger with a viral RNA polymerase. We further show that disassembly of filaments can be induced by an RNA-degrading enzyme. By tuning the RNA production and degradation rates we are able to demonstrate temporal control of assembly directed by enzymatic reactions.

Hybrid DNA-RNA assemblies have the potential to combine the natural functionalities of RNA molecules with the stability and predictability of DNA self-assembled systems. We envision that our results are relevant for synthetic biology and artificial life, and will promote the development of rationally designed, responsive assemblies that could

perform complex tasks such as supporting motility, transport of molecular cargo, maintenance of structural integrity, and signal transduction, similarly to natural cytoskeletal filaments.

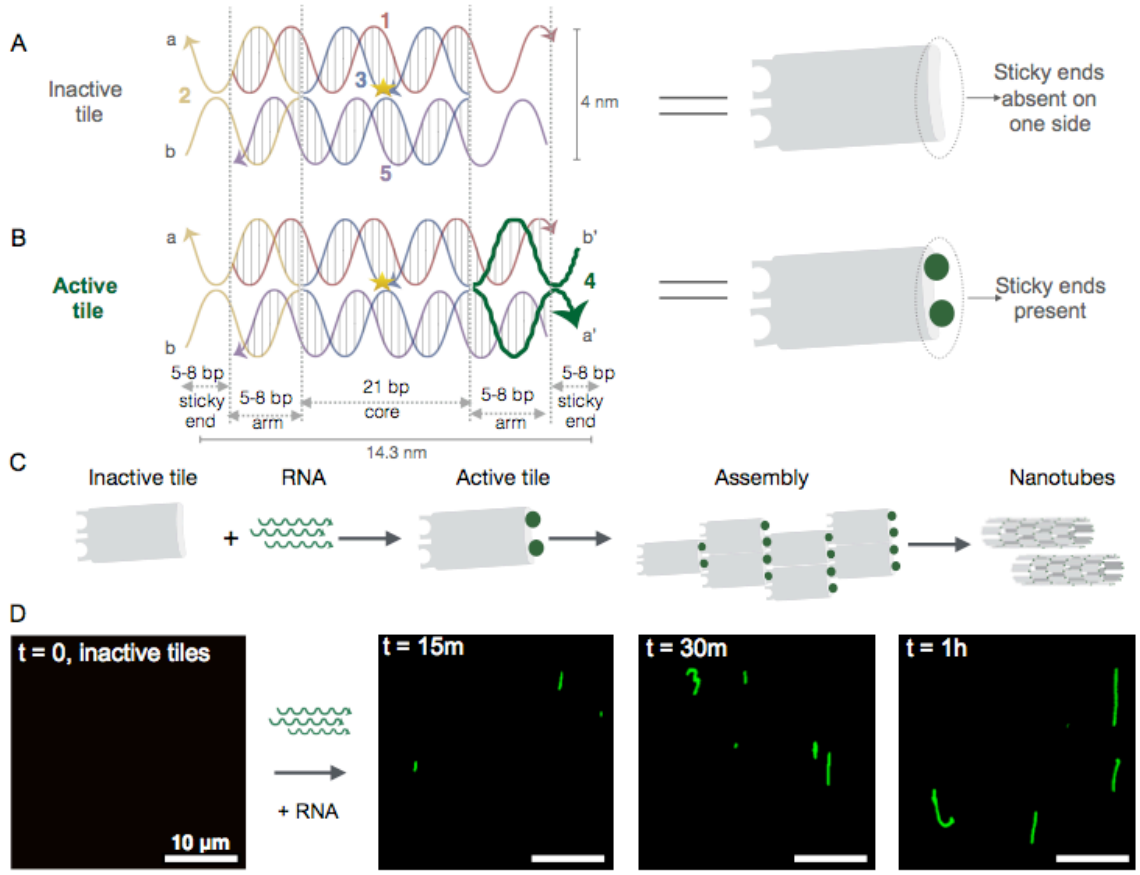

Figure 1-1: A hybrid DNA-RNA tile motif. We illustrate the features of our tiles and their proposed RNA-based activation mechanism. We designed several tile variants in which DNA strands are always denoted as number 1 (red), 2 (yellow), 3 (blue), 5 (purple) and the RNA strand is number 4 (green). Variants differ in the length of the sticky end and arm domains. Detailed diagrams of each variant are in SI Section 1. A) Inactive DAE-E tile. The yellow star indicates the presence of a fluorescent label. B) Activated hybrid DNA-RNA DAE-E tile. C) Addition of RNA activates the tiles and triggers self-assembly into nanotubes. D) Example fluorescence microscopy images for triggered assembly of nanotubes having 5 base sticky ends by addition of purified RNA strand. All scale bars are 10 µm.

1.3 Results

Design and characterization of hybrid DNA-RNA nanotubes Many variants of DNA double-crossover (DX) tiles have been used to demonstrate a variety of assemblies[2,8]. These tiles interact via single stranded domains, or sticky ends, that can be programmed to yield lattices, tubular structures, and algorithmic assemblies[8,15]. As DX tile variants differ by the orientation of DNA strands and by the crossover distances, the 'DAE-E' acronym describes precisely the tile structure, indicating the number of crossovers (Double), the orientation of the strands through the crossover (Antiparallel), the number of half-turns between intramolecular crossovers (Even), and the number of half-turns between intermolecular crossovers (Even)[2]. We engineered DX tiles designed to form nanotubes[2,8]. These tiles consist of five strands that form two parallel heteroduplexes coming together at two points where strands cross over, from one duplex to the other, via Holliday junctions, and are known as DAE-E tiles (Fig. 1-1A and B). Two strands (on opposite sides of tile) include sticky end domains that allow multiple copies of the tile to self-assemble into a nanotube (Fig. 1-1C). The rigidity of each tile inhibits any interaction between the sticky ends present on its opposite ends.

Tiles annealed without one of the sticky end strands (strands 2 or 4) are inactive, because self-assembly in the absence of one (or both) complementary sticky ends cannot proceed. The expected structure of an inactive tile is in Fig. 1-1 A. Pre-annealed inactive tiles can be activated by adding in solution the missing DNA strand, which triggers assembly of nanotubes within minutes at room temperature, as reported by Zhang at al.[15] for a particular DAE-E variant.

We hypothesized that an RNA sticky end strand could operate in a similar manner to activate assembly and that the speed of nanotube formation should be comparable to what was previously observed in all-DNA tiles[16,39]. To test these hypotheses, we designed three different tile variants in which strand 4 is an RNA molecule. Because the thermodynamics and kinetics of tile-tile interactions are determined by the sticky end bonds, these three tile variants differ in the length of the sticky end domains (5, 7, and 8 bases). To ensure formation of tubular structures, the distance between inter-tile crossovers (two helical turns) was maintained constant. We verified that these three tile variants yield nanotubes upon thermal annealing (Fig. 1-2A) when all strands are DNA. Then, we checked if nanotube assembly occurs when annealing tiles in which DNA strand 4 is replaced with an RNA strand (with the corresponding sequence). In these experiments, RNA strand 4 of each variant was gel-extracted. The DNA components of the tile and the RNA strand were then annealed using standard protocols. After annealing, all the tile variants formed nanotubes when including RNA strand 4. Fig. 1-2B shows example fluorescence microscopy images of these hybrid DNA-RNA nanotubes. Example atomic force microscopy (AFM) images are in the SI; analysis of AFM images of open nanotubes suggests that the diameter of hybrid nanotubes is comparable to the diameter of all-DNA nanotubes.

Next, we asked if RNA strand 4 can bind to inactive tiles after anneal, acting as a trigger for nanotube formation.

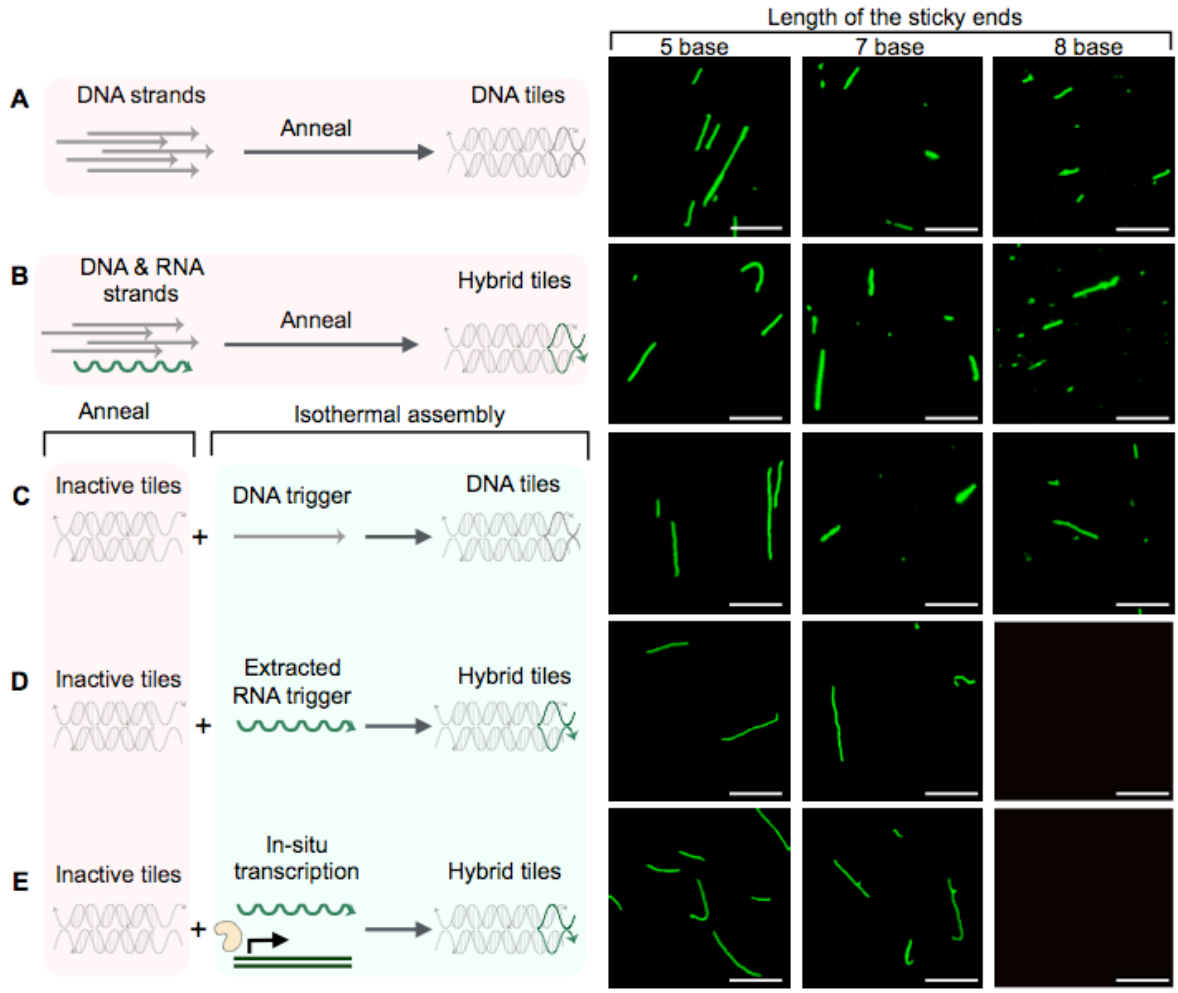

Figure 1-2: Activation of hybrid DNA-RNA nanotube assembly: Assembly of nanotubes is achieved with different approaches. In the schematics on the left, DNA strands are shown in gray and RNA strands in green. In all the example fluorescence microscopy images the inactive tile concentration in each case is 0.5 μM. A) Annealing all DNA strands components together. B) Triggering iso-thermal assembly of all DNA nanotubes by a sticky end DNA strand (ratio of inactive tiles to DNA trigger strand is 1:1). C) Triggering isothermal assembly of Hybrid DNA/RNA nanotubes by addition of purified RNA sticky end strand (ratio of inactive tiles to RNA trigger strand is 1:1). D) Triggering isothermal assembly via in-situ transcription of RNA strand (ratio of inactive tiles to RNA producing template is 5:1). Images were taken after 1 hour of trigger strand addition. All scale bars are 10 μm.

Isothermal and co-transcriptional activation of tiles with RNA trigger strands. First, we verified that each variant of pre-annealed inactive tiles can be activated by adding the corresponding DNA strand 4 at 37 ºC, thereby triggering assembly of nanotubes as shown in earlier experiments by Zhang et al. [15] (Fig. 1-2C). (Control samples including annealed inactive tiles to which no DNA trigger was added did not form any assembly at 37 ºC.) Then, we used gel purified RNA strand 4 as a trigger for assembly: as shown in the fluorescence microscopy images in Fig. 1-2D we observed RNA-triggered isothermal (at 37 ºC) assembly of 5 and 7 base sticky end tile variants into nanotubes. In contrast, the RNA trigger did not activate the 8 base sticky end tile variant, resulting in no nanotube formation.

Finally, we tested if inactive tiles can be activated co-transcriptionally, *i.e.* by RNA transcribed from a DNA template by a viral RNA polymerase (bacteriophage T7 RNAP), in a one pot reaction at 37°C (*in situ*). Using standard transcription conditions, and a 1:5 ratio of DNA template to inactive tile concentration, we observed triggered isothermal assembly of 5 and 7 base sticky end variants. (Fig. 1-2E). In contrast, we again did not observe assembly of the 8 base sticky end variant, confirming that it cannot be triggered by the RNA sticky end strand (extracted or transcribed *in situ*). This may be caused by unwanted secondary structure present in that particular variant of RNA strand 4; further, we conjecture that a longer RNA strand 4 may interact with DNA strand 2 first, rather than activating the tile, forming a “waste” RNA trigger-tile complex that cannot assemble into nanotubes.

We note that in principle RNA trigger molecules could be transcribed by other types of polymerases; for example, we achieved *in situ* activation of assembly by transcribing RNA with SP6 RNAP, another well-known type of bacteriophage RNA polymerase.

The successful assembly of several hybrid DNA-RNA tile variants prompted us to investigate whether multiple DNA nanotube populations, with distinct sequence content, can be simultaneously and selectively triggered with high specificity.

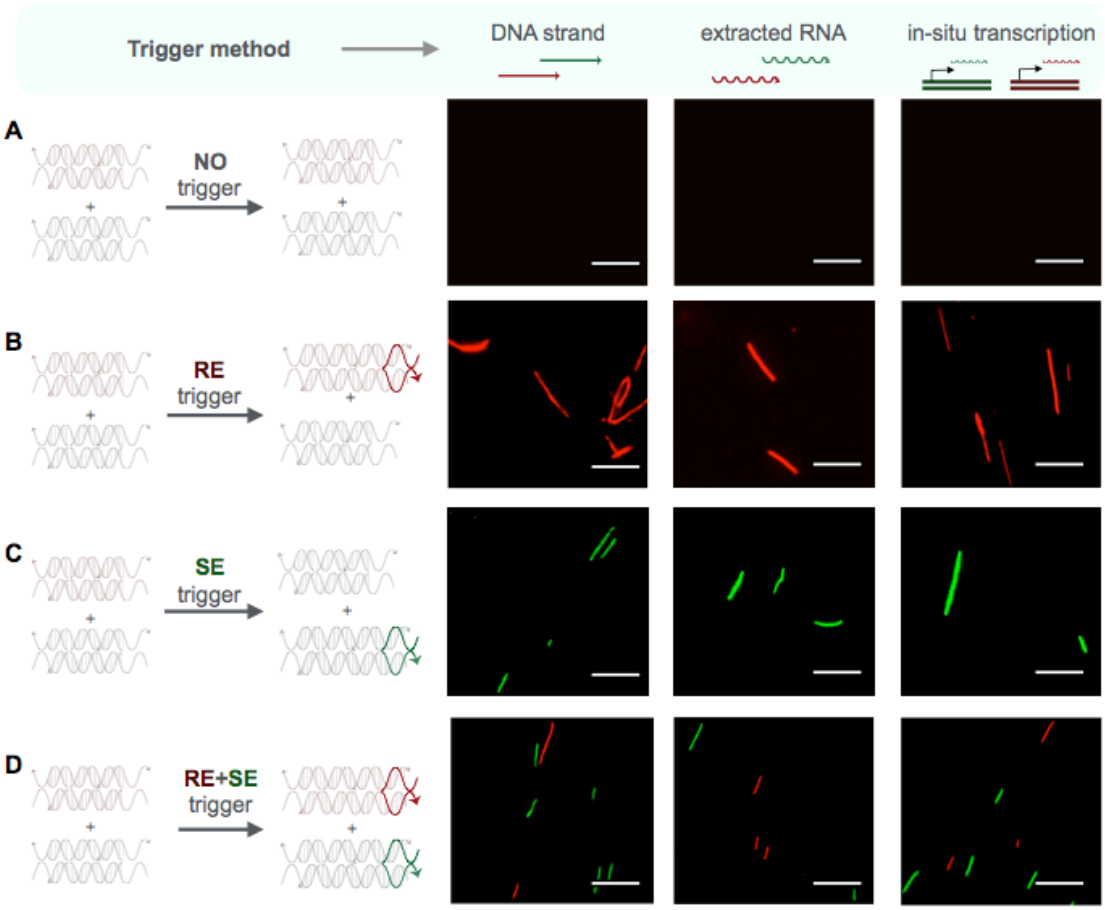

Figure 1-3: Specificity of tile activation: Fluorescence microscopy images show selective nanotube assembly isothermally when specific trig-ger strands are added to a solution containing both RE and SE inactive core tiles. A) If no RNA trigger is present, nanotubes do not form. B) In the presence of exclusively RE RNA trigger, we observe assembly of only RE nanotubes (red colored, Atto 647 N label). C) In the presence of exclusively SE RNA trigger, we observe assembly of only SE nanotubes (green colored, CY3 label). D) In the presence of both RE and SE RNA triggers, assembly of both RE (red) and SE (green) nanotubes occurs. Images were taken after 1 hour of trigger strand addition or initiation of trigger transcription. All scale bars are 10 μm.

The growth of distinct nanotube species can be selectively activated by transcription of specific RNA molecules. To assess the specificity of the trigger RNA strands, we used two types of DNA-RNA tiles that differ exclusively in the sequence of each strand. (These tiles present 5 base long sticky ends.) Our designs are adapted from the 'RE' and 'SE' tile variants developed by Rothemund, et.al.[8]; these tiles present the same geometric features and self-assembly patterns, but have different sequence content. Thus, inactive tiles in each design need distinct trigger sequences to activate them. If the RE and SE inactive tiles are mixed together, they are not expected to interact, nor assemble in the absence of triggers (Fig. 1-3A).

To test whether selective activation can be achieved, we labeled RE and SE tiles with distinct fluorophores, Atto 647N (RE tile) and Cy3 (SE tile). In Fig. 1-3, the RE nanotubes are in red color, and SE nanotubes are in green. First, in a control experiment, we verified that addition of RE or SE DNA trigger strand number 4 to a mix of both RE and SE inactive tiles, causes activation of exclusively RE or SE tiles, respectively.

Next, we tested activation of tiles using RNA RE and SE trigger strands. Addition of RNA RE trigger to a mix of RE and SE pre-annealed tiles yields only RE nanotubes (Fig. 1-3B); similarly, addition of RNA SE trigger produces only SE nanotubes (Fig. 1-3C). This was observed when extracted RNA trigger is added and also when the RNA trigger is transcribed *in situ* by artificial templates (Fig. 1-3B-D, middle and right columns). Only when both RE and SE trigger strands are added or transcribed simultaneously, assembly of both RE and SE nanotube populations occurs (Fig. 1-3D). Remarkably, we found that all the nanotube variants whose growth is successfully activated by RNA produced *in situ*, are also very stable in transcription conditions.

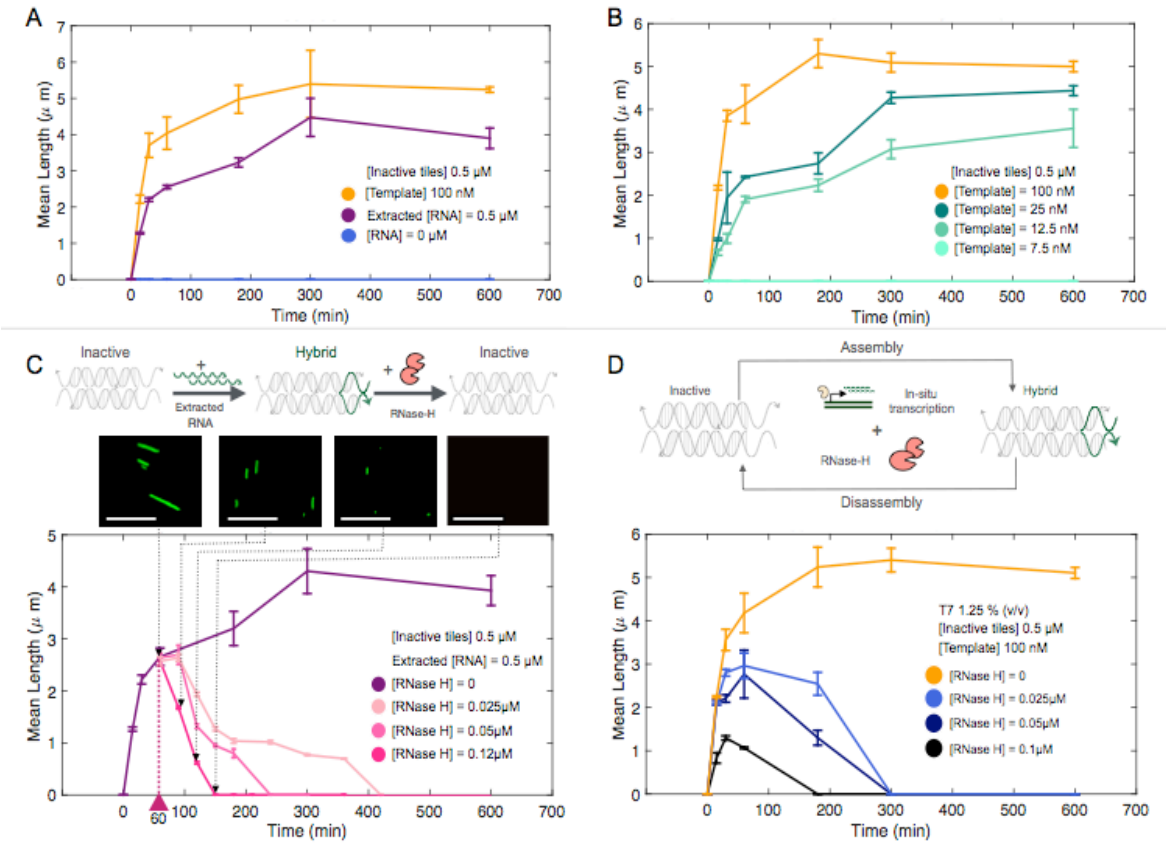

Figure 1-4: Enzyme-mediated control of assembly and disassembly of hybrid DNA/RNA tubes. We quantitatively tracked the mean length of nanotubes grown under different transcription and degradation conditions. Length histograms were obtained by processing fluorescence microscopy images; we report the nanotube mean length, with error bars obtained by bootstrapping. A) Comparison of assembly triggered via in situ transcription (orange), via addition of gel extracted RNA (purple), and with no RNA addition (blue). B) The speed of assembly depends on the concentration of DNA template producing the trigger RNA strand. C) Top: schematic of the reactions occurring in a sample that includes inactive tiles, extracted RNA trigger, and RNase H. Bottom: Experiments showing that the mean nanotube length increases when growth is triggered by addition of extracted trigger RNA (Time=0), and decreases when subsequently RNase H is added to the sample (pink marker, time= 60 min). D) Top: Schematic of the reactions occurring in a sample that includes inactive tiles, DNA template transcribing the RNA trigger, and RNase H. Bottom: Experimental results showing that, when RNA trigger transcription and degradation components are simultaneously present, the nanotube mean length increases transiently: eventually RNase H causes disassembly of the nanotubes at a speed that depends on the RNase H concentration, presumably due to a decrease of RNAP activity. All scale bars are 10 μm.

These nanotubes were stable in transcription mix for more than 2 weeks when stored at room temperature. These results suggest this system is amenable to being

controlled by more complex transcriptional programs. For this purpose, we quantitatively characterized whether the kinetics of nanotube assembly can be controlled by tuning the concentration of DNA template and RNA polymerase. We further examine if assembly can be reversed by introducing components for RNA degradation.

The kinetics of hybrid nanotube growth can be controlled with enzymes producing and degrading RNA. A striking property of biological materials such as the cytoskeleton is their capacity to assemble and disassemble in response to endogenous molecular signals generated by gene networks[7]. To achieve similar levels of kinetic control of assembly of our artificial nanotubes, we *quantitatively* characterized the growth of our hybrid nanotubes when tiles are activated by RNA molecules generated by synthetic genes. We tracked the nanotube growth by measuring their mean length as a function of time from fluorescence microscopy images[16], using an automated image processing protocol.

As shown in Fig. 1-4A, addition of a template transcribing the RNA trigger results in rapid nanotube growth; the nanotube mean length plateaus to roughly 5 μm after about 3 hours, consistent with previous work[40]. The nanotube mean length increases more slowly when growth is triggered with a finite concentration of gel purified RNA, as shown by purple trace in Fig. 1-4A, where ratio of inactive tiles to gel purified RNA is 1:1 (0.5 μM). This suggests that the yield of RNA in our transcription conditions, as defined by concentrations of RNAP and template, exceeds the concentration of inactive RNA tiles and promotes faster assembly of longer nanotubes.

We then checked how the temporal evolution of the nanotube mean length is affected by the concentration of template that produces the RNA sticky end. We found that at low concentration of template, the mean length of nanotubes is also reduced at all points in time (Fig. 1-4B). We also found that if the concentration of template producing the RNA sticky is less than 7.5 nM, no assemblies are observed in fluorescence microscopy images, suggesting that that the concentration of transcribed RNA never builds up to exceed the minimum threshold required for nucleation and assembly (we recall that the activity of RNA polymerase decreases rapidly after 4 hours of incubation in transcription conditions).

Next, we sought to control nanotube disassembly using an RNA-degrading enzyme. An ideal candidate for this purpose is RNase H, an enzyme that hydrolyzes RNA in DNA-RNA complexes. RNase H has been previously used to control degradation in a variety of artificial *in vitro* transcriptional circuits[41]. We expected that RNase H could deactivate free (unpolymerized) tiles by degrading the portion of RNA strand 4 bound to DNA; because nanotubes continuously polymerize and depolymerize, RNase H could promote disassembly by simply reducing the concentration of free active tiles, thereby reducing the polymerization rate (depolymerization, in contrast, does not depend on the concentration of free tiles); RNase H could also degrade RNA incorporated in nanotubes, thereby breaking the sticky end bonds holding together the nanostructure and resulting in nanotube disassembly[42].

To investigate RNase H promoted disassembly, we first added RNase H to a sample including hybrid nanotubes after 60 minutes of triggered growth with gel purified RNA strand, maintaining the reaction mixture at 37 ºC. As shown in Fig. 1-4C, nanotubes disassembled completely at a speed that is controllable by tuning the estimated RNase H concentration in solution.

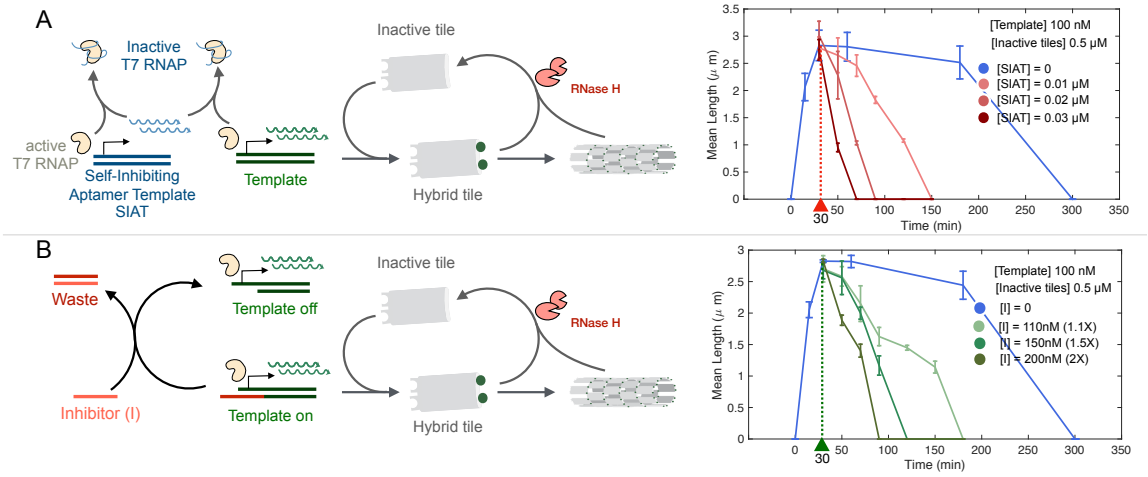

Figure 1-5: Nanotube assembly using simple molecular programs. A) Left: Reaction scheme of a timer circuit controlling the production of trigger RNA strand; a self-inhibiting aptamer template (SIAT) produces an aptamer that binds to and inactivates T7 RNAP. Right: Experimental results. By tuning the concentration of SIAT we can tune the time it takes to switch off production of the trigger; as soon as production of RNA strand 4 is reduced with introduction of SIAT (red marker, time= 30 min), RNase H-mediated degradation dominates, and nanotubes disassemble. B) Left: Reaction scheme showing how we can control trigger pro-duction with a synthetic transcriptional switch. Right: Experimental results. After the inhibitor strand is added (green marker, time= 30 min), the production rate of trigger decreases and nanotubes are degraded by RNase H. As noted earlier, T7 RNAP activity naturally decays after 4-5 hours in the absence of aptamer (blue line in Fig. 1-4D). Error bars are obtained by bootstrapping.

We then quantified the nanotube mean length in the presence of both RNA transcription and degradation processes, which respectively control assembly and disassembly. In this scenario, we expect to observe an increase or decrease of the mean length depending on whether the transcription or degradation reaction rate dominates. Thus, in samples containing 0.5 μM of inactive tiles we fixed the RNAP and template concentrations, and we varied the concentration of RNase H. In all samples, transcription is faster than degradation and promotes nanotube growth for the first 30-60 minutes of the reaction; this behavior could be due to the known phenomenon of transcription burst of T7 RNAP[43,44]. As the activity of T7 RNAP

decreases over time, the effects of RNA degradation become more prominent and nanotube disassembly occurs on a timescale that decreases at high concentration of RNase H. Overall, the interplay of RNA production and degradation results in a "pulse" of nanotube formation, in which the peak of the mean length and the time constant of the decrease of the mean length can be both controlled by tuning the relative concentration of enzymes and template for RNA production (Fig. 1-4D).

Temporal control of hybrid nanotube assembly using simple molecular programs. A primary attribute of biology is the precise control it exhibits in complex intra-cellular functions. To make a molecular-level machinery, we need a collection of molecular components which perform tasks (output) as a consequence of a specific stimuli (input). The molecular machine must be sensitive enough that any change in the input gives quantifiable difference in output[45]. A significant advantage of hybrid DNA-RNA tubes, seen as a molecular machine, is that we can control their formation or degradation (output) with specific RNA molecules (inputs) that can be generated as a result of molecular programs. We devised two molecular programs to test the functionality and applicability of our system, in which we exploit the simultaneous presence of RNA production and degradation to control nanotube assembly.

First, we built a 'genetic timer circuit' that uses an RNA aptamer to control the activity of bacteriophage T7 RNA polymerase (RNAP)[46]. We designed a synthetic template to produce an aptamer that binds to and inhibits the activity of T7 RNAP[47]; if the template includes a T7 RNAP promoter, then the aptamer operates as a self-inhibitor motif and we call this template a T7 Self-Inhibiting Aptamer Template (SIAT). We first characterized the T7 SIAT using a template transcribing an RNA fluorescent reporter. We found that transcription can be stopped within 15 minutes to 2 hours, using SIAT concentrations

between 0.03 μM to 0.01 μM, and amounts of T7 RNAP comparable to those used in our transcription experiments (Fig. S1.6).

We used the SIAT to control production of RNA trigger for our DNA-RNA nanotube system, in which nanotube growth is promoted by T7 RNA polymerase via RNA transcription, and nanotube degradation is directed by RNase H[47,48]. When the SIAT is added, the transcription rate decreases as the RNAP inhibitor concentration is being produced; then, RNase H degradation dominates causing nanotube disassembly (Fig. 1-5A). The concentration of SIAT determines how quickly the concentration of aptamer inhibitor builds up, and thus the timescale at which transcription is turned off (Fig. 1-5A, right), acting as a timer element that controls for how long nanotubes are present in solution.

Next, we designed an *in vitro* artificial transcriptional switch to produce the RNA trigger[49,50]. RNA transcription of a transcriptional switch is controlled via a partially single stranded promoter. As shown in Fig. 1-5B, transcription is activated in the presence of an activator strand complementary to the single stranded promoter region; transcription is inhibited when the activator is absent, or when it is displaced by a complementary inhibitor strand via toehold-mediated strand displacement[49,51]. Additional design details are in SI Fig. S1.7. We controlled activation of our hybrid DNA-RNA tiles with a transcriptional switch: first, the active switch produces the RNA trigger, promoting formation of nanotubes. When the DNA inhibitor for the switch is added at a concentration that is 1.1X the template concentration, transcription is turned off and after about 180 minutes, RNase H degradation dominates over transcription (Fig. 1-5B, right). As more DNA inhibitor is added (in relation to the concentration of DNA template), the rate of disassembly takes over the rate of assembly

more rapidly; when the inhibitor is present at 2X the concentration of template, no nanotubes are visible in the sample after about 90 minutes.

METHODS

Oligonucleotides and enzymes

DNA oligonucleotides were purchased from Integrated DNA Technologies (IDT). Sequences and modifications are listed in the SI file. RNA strands were individually transcribed *in vitro* from the corresponding DNA templates (the sequences and modifications are given in the SI Appendix), using the AmpliScribe™ T7-Flash™ Transcription kit (Lucigen™) and gel extracted as described in the SI file. RNase H was purchased from Cellscript™.

Inactive tile preparation

Each variant of inactive tiles was prepared by mixing DNA strands 1, 2, 3, and 5 in stoichiometric proportion with 1x TXN buffer (RNA Pol Reaction Buffer from New England Biolabs, Inc.) and nanopure water inside DNA Lo-bind tubes. The solution was annealed using an Eppendorf Mastercycler Gradient thermal cycler by heating to 90°C, and cooling to 25°C, over a 6 hour period.

Production of annealed hybrid nanotubes

Each variant of hybrid DNA-RNA tiles was prepared by mixing DNA strands 1, 2, 3, 5, and RNA strand 4 in stoichiometric proportion, with 1x TXN buffer (RNA Pol Reaction Buffer from New England Biolabs, Inc.) and nanopure water inside DNA Lo-bind tubes. The mix was annealed using an Eppendorf Mastercycler Gradient thermal cycler by heating to 70°C, and

cooling to 22°C, over a 24 hour period. The maximum annealing temperature was limited to 70°C to avoid degradation of the RNA strand[29,68].

Assembly activation by trigger strand addition

Inactive tiles were annealed and then incubated at 37°C prior to adding the trigger strand (4). DNA or RNA strand 4 was added in stoichiometric amount to the inactive tile concentration at 37°C; samples were imaged using a fluorescence microscope for several hours.

Assembly activation by co-transcription of the trigger strand (in situ activation)

Inactive tiles were annealed and incubated at 37°C prior to production of the trigger strand (4). The annealed synthetic template for transcribing missing RNA strand (4) was mixed with inactive tiles (100nM template for a 0.5 μM concentration of inactive tile, unless otherwise stated) and transcription mix (RNAP, transcription buffer, 2 mM each nucleoside triphosphates (NTPs) and total 8mM $MgCL_2$) at 37°C. Samples were imaged using a fluorescence microscope for several hours.

Fluorescence microscopy

Nanotube samples were imaged using an inverted microscope (Nikon Eclipse TI-E) with 60X/1.40 NA oil immersion objectives, using built-in filter cubes. For imaging, samples were diluted targeting a 50 nM tile concentration using experimental buffer conditions. Samples were placed on Fischerbrand microscope cover glass (#12-545E No. 1, thickness=0.13 to 0.17 mm, size: 50 x 22 mm); VWR Micro Slides (Plain, Selected, Pre-cleaned, 25 x 75 mm, 1.0 mm thick) were placed gently on the cover glass. Images were processed to correct for uneven illumination and superimposed to produce multicolor images. Exposure time was set to 90 ms.

1.5 Conclusion

Hybrid DNA-RNA nanotubes as molecular machines for nanotechnology One of the goals of nucleic acids nanotechnology is to generate programmable machines and scaffolds that can operate in biological environments like cells and tissues. For this purpose, it is desirable to develop systems that can assemble at constant, physiological temperatures. However, the vast majority of self-assembled nucleic acid structures (including some tile-based structures) require a thermal annealing process, in which a solution containing all the required strands is heated and slowly cooled to room temperature. Our hybrid DNA-RNA nanotubes assemble isothermally from pre-formed tiles at 37ºC, an essential requirement for designing any synthetic machinery intended to work in biological cells. We suggest that annealed tiles could be transfected in cells, and their assembly could be activated by RNA transcription like in this study. Chemical modifications such as phosphorothioation could be used to render tiles resilient to degradation in the cytoplasm[52].

Another desirable feature of synthetic molecular machines is that they should perform multiple rounds of operation reliably. Our DNA-RNA hybrid nanotubes have the potential to satisfy this requirement, since their assembly and disassembly can be precisely controlled by tuning a variety of parameters. However, preliminary experiments suggest it is challenging to achieve multiple rounds of assembly and disassembly; in particular, reassembly of our hybrid nanotubes after RNase H-induced disassembly is difficult to achieve. A possible explanation is that RNase H is not able to completely degrade the RNA trigger strand; specifically, in unpolymerized active tiles, RNase H cannot hydrolyze the non-DNA bound portion of RNA strand 4 (the sticky-ends); further, it is known that RNase H generates incomplete degradation products up to 7 bases long[53]. It is plausible that “incomplete” hydrolysis results in the accumulation of small RNA molecules that remain bound to inactive tiles and prevent binding of

new trigger strands to these tiles, contributing to the formation of “waste” tiles. Further experiments are needed to test this hypothesis.

Structural considerations Our hybrid tiles incorporate RNA molecules to create tile-tile connectors, or sticky-ends, while all other tile components are DNA molecules. While we activated our DAE-E tiles using one specific sticky end strand as trigger (strand 4), similarly it would be possible to trigger assembly with the other sticky end (strand 2) or both sticky ends, as indicated by control experiments on DNA-only tiles. This would expand options for building more complex tile activation systems.

Using an RNA molecule as a DNA tile connector poses some questions about the structural features of assemblies. While DNA-DNA duplexes predominately exist in B-form helical conformation in nature and also when prepared synthetically[54,55], DNA–RNA and RNA–RNA duplexes exists in A-form helical conformation[54]. Both A-form and B-form duplexes are helical structures, but they differ in their geometry and dimensions[21]. To increase the structural predictability of assemblies, other hybrid DNA-RNA tiles have included RNA strands that do not cross-over in the tile, so all helices are expected to be in A-form[29,56]. In our case, the crossover of a single RNA strand between duplexes poses a question whether different conformations of helicity occur and whether they affect the assembly dynamics. It is possible that the helicity switches between A-form and B-form: the DNA only duplexes may form a segment of B-form helix that stacks collinearly with the DNA-RNA duplex at the sticky end, that is expected to be an A-form helix.

Challenges to tile activation *in situ* Our hybrid tubes were obtained with a one-pot method in which the trigger strand is transcribed simultaneously in presence of inactive tiles to yield nanotubes. Previous studies have reported successful one-pot assembly of smaller multi-stranded RNA–DNA structures which are up to 100 nm long[56]. One-pot methods are less time

consuming than protocols requiring multiple steps of gel purification, thus they are convenient for scaling up nanostructure production. However, a notable challenge of unpurified transcription products is that they include abortive and elongated transcripts[57-60]. These undesired RNA species can result in side reactions and crosstalk, and in the sequestration of relevant species in inert complexes or waste. These abortive and elongated transcripts are expected to bind to inactive tiles, in some cases producing "waste" complexes that can no longer be activated by the correct RNA trigger. These waste products can accumulate in the system and decrease the maximum achievable concentration of active tiles. Abortive transcription can be mitigated by using G-rich transcription initiation sequences[60] and elongated transcription can be reduced by enforcing strong secondary structure at the 3' end of the transcript[50]. Unfortunately, these methods to control incorrect RNA products introduce restrictions in the sequence design space of tiles.

Inactive tiles robustly assemble into nanotubes in the presence of the RNA trigger strands. However, in case of *in situ* transcription, we observed that nanotube growth is affected by the concentration of trigger strand producing template. At template concentrations below 7.5 nM, we were unable to observe formation of structures large enough to be observed with fluorescence microscopy. This suggests that there is a critical concentration of template required to produce an amount of RNA trigger strand sufficient to initiate nanotube formation. It is noteworthy that since the activity of T7 bacteriophage enzyme is maximum in the first two hours[43,44], and drastically reduces after 4-6 hours, there is a limited time window in which the template can transcribe the trigger strand. If it is not possible to produce a sufficient quantity of the trigger strand within this time window, co-transcriptional assembly may not occur. Unfortunately, this problem cannot be mitigated by simply increasing the volume of T7 RNA polymerase, as this promotes nanotube disassembly (Fig. S1.4); recent experiments on similar nanotubes suggest that this may be due to undesired RNA strands transcribed from the

nanotubes, which then bind to and inactivate unpolymerized tiles and may strand invade the sticky ends of polymerized tiles[61].

Application opportunities in dissipative self-assembly Dynamic materials in living cells assemble and disassemble kinetically as energy is converted and dissipated. For example, guanosine triphosphate (GTP)–triggers assembly and disassembly of tubulin into microtubules. Collapse of microtubules occurs when GTP is hydrolyzed, a reaction that is accelerated when tubulin is in an aggregated state. Another example is nucleation of monomeric G-actin by the Arp2/3 complex for directed cell migration[62]. Also, assembly and disassembly of actin filaments themselves is controlled by binding and hydrolysis of ATP molecules[63]. Understanding and recreating similar chemically fueled synthetic reactions are long-standing challenges in the field of supramolecular chemistry[64], and are crucial to our ability to build dynamic, adaptive materials. In the nanotube system presented here, nucleoside triphosphates (NTPs) are the fuel needed by RNAP to produce RNA, which activates tiles and triggers assembly of nanotubes; thus, nanotube formation requires a source of energy. RNase H hydrolyzes RNA incorporated in the nanotubes and tiles, resulting in dissipation of energy[65]. While additional work is needed to precisely classify the dissipative nature of our system[66], we believe that it could serve as a tunable model to study dissipative self-assembly. Its advantages include the fact that nucleic acid interactions are typically more programmable than proteins and other small molecules, and their thermodynamic properties are well understood, which means assembly rates are controllable. Further, the fuel production and degradation rates can be easily tuned: the RNA production rate can be modified by, for instance, varying the promoter sequence as well as the NTP, template and enzyme concentration. The RNA degradation rate can be tuned by varying the concentration of RNase H as well as by including additional RNA-degrading enzymes, or by chemically modifying some nucleobases in the DNA tiles.

Conclusive remarks In conclusion, our experiments highlight that RNA molecules can be successfully incorporated in well characterized DNA structures, producing a hybrid DNA-RNA self-assembling system. In this system RNA serves as a fuel that enables the assembly of nanoscale tiles into micrometer sized nanotubes. More importantly, we demonstrated that the kinetics assembly and disassembly of our DNA-RNA nanotubes can be controlled isothermally by managing the enzymatic production and degradation of RNA activating the tiles; this can be done by using molecular circuits whose outputs are RNA molecules with programmable concentration kinetics. An important feature of this system is its ability to operate isothermally at 37ºC, which makes it potentially useful for biological applications. These nanotubes could also be functionalized with protein binding domains or small RNA molecules with therapeutic properties (siRNA, microRNA or antisense RNA)[9,67]. Hybrid DNA-RNA nanotubes are thus a good candidate to be used together with synthetic biochemical networks in natural and artificial cells, and have potential to serve as a model system in engineering nano-machines operating out of equilibrium.

1.4 Methods

Oligonucleotides and enzymes: DNA oligonucleotides were purchased from Integrated DNA Technologies (IDT). Sequences and modifications are listed in the SI file. RNA strands were individually transcribed *in vitro* from the corresponding DNA templates (the sequences and modifications are given in the SI Appendix), using the AmpliScribe™ T7-Flash™ Transcription kit (Lucigen™) and gel extracted as described in the SI file. RNase H was purchased from Cellscript™.

Inactive tile preparation: Each variant of inactive tiles was prepared by mixing DNA strands 1, 2, 3, and 5 in stoichiometric proportion with 1x TXN buffer (RNA Pol Reaction Buffer from New England Biolabs, Inc.) and nanopure water inside DNA Lo-bind tubes. The solution was annealed using an Eppendorf Mastercycler Gradient thermal cycler by heating to 90°C, and cooling to 25°C, over a 6 hour period.

Production of annealed hybrid nanotubes: Each variant of hybrid DNA-RNA tiles was prepared by mixing DNA strands 1, 2, 3, 5, and RNA strand 4 in stoichiometric proportion, with 1x TXN buffer (RNA Pol Reaction Buffer from New England Biolabs, Inc.) and nanopure water inside DNA Lo-bind tubes. The mix was annealed using an Eppendorf Mastercycler Gradient thermal cycler by heating to 70°C, and cooling to 22°C, over a 24 hour period. The maximum annealing temperature was limited to 70°C to avoid degradation of the RNA strand[29,68].

Assembly activation by trigger strand addition: Inactive tiles were annealed and then incubated at 37°C prior to adding the trigger strand (4). DNA or RNA strand 4 was added in stoichiometric amount to the inactive tile concentration at 37°C; samples were imaged using a fluorescence microscope for several hours.

Assembly activation by co-transcription of the trigger strand (in situ activation): Inactive tiles were annealed and incubated at 37°C prior to production of the trigger strand (4). The annealed synthetic template for transcribing missing RNA strand (4) was mixed with inactive tiles (100nM template for a 0.5 μM concentration of inactive tile, unless otherwise stated) and transcription mix (RNAP, transcription buffer, 2 mM each nucleoside triphosphates (NTPs) and total 8mM $MgCL_2$) at 37°C. Samples were imaged using a fluorescence microscope for several hours.

Fluorescence microscopy: Nanotube samples were imaged using an inverted microscope (Nikon Eclipse TI-E) with 60X/1.40 NA oil immersion objectives, using built-in filter

cubes. For imaging, samples were diluted targeting a 50 nM tile concentration using experimental buffer conditions. Samples were placed on Fischerbrand microscope cover glass (#12-545E No. 1, thickness=0.13 to 0.17 mm, size: 50 x 22 mm); VWR Micro Slides (Plain, Selected, Pre-cleaned, 25 x 75 mm, 1.0 mm thick) were placed gently on the cover glass. Images were processed to correct for uneven illumination and superimposed to produce multicolor images. Exposure time was set to 90 ms.

Acknowledgement

We thank J. Lloyd, H.K.K. Subramanian, S. Schaffter and J. M. Stewart for discussions and advise.

1.6 References

1 Chen, J. & Seeman, N. C. Synthesis from DNA of a molecule with the connectivity of a cube. *Nature* **350**, 631, doi:10.1038/350631a0 (1991).

2 Fu, T. J. & Seeman, N. C. DNA double-crossover molecules. *Biochemistry* **32**, 3211-3220 (1993).

3 Kallenbach, N. R., Ma, R.-I. & Seeman, N. C. An immobile nucleic acid junction constructed from oligonucleotides. *Nature* **305**, 829, doi:10.1038/305829a0 (1983).

4 Seeman, N. C. Biochemistry and Structural DNA Nanotechnology: An Evolving Symbiotic Relationship. *Biochemistry* **42**, 7259-7269, doi:10.1021/bi030079v (2003).

5 Hall, A. Rho GTPases and the actin cytoskeleton. *Science* **279**, 509-514 (1998).

6 Howard, J. Mechanics of motor proteins and the cytoskeleton. (2001).

7 Fletcher, D. A. & Mullins, R. D. Cell mechanics and the cytoskeleton. *Nature* **463**, 485, doi:10.1038/nature08908 (2010).

8 Rothemund, P. W. K. *et al.* Design and Characterization of Programmable DNA Nanotubes. *Journal of the American Chemical Society* **126**, 16344-16352, doi:10.1021/ja044319l (2004).

9 Stewart, J. M. *et al.* Programmable RNA microstructures for coordinated delivery of siRNAs. *Nanoscale* **8**, 17542-17550 (2016).

10 Sharma, J. *et al.* Control of self-assembly of DNA tubules through integration of gold nanoparticles. *Science* **323**, 112-116 (2009).

11 Mohammed, A. *et al.* Self-assembly of precisely defined DNA nanotube superstructures using DNA origami seeds. *Nanoscale* **9**, 522-526 (2017).

12 Mitchell, J. C., Harris, J. R., Malo, J., Bath, J. & Turberfield, A. J. Self-assembly of chiral DNA nanotubes. *Journal of the American Chemical Society* **126**, 16342-16343 (2004).

13 Douglas, S. M., Chou, J. J. & Shih, W. M. DNA-nanotube-induced alignment of membrane proteins for NMR structure determination. *Proceedings of the National Academy of Sciences* **104**, 6644-6648 (2007).

14 Hariadi, R. F., Appukutty, A. J. & Sivaramakrishnan, S. Engineering Circular Gliding of Actin Filaments Along Myosin-Patterned DNA Nanotube Rings To Study Long-Term Actin–Myosin Behaviors. *ACS nano* **10**, 8281-8288 (2016).

15 Zhang, D. Y., Hariadi, R. F., Choi, H. M. T. & Winfree, E. Integrating DNA strand-displacement circuitry with DNA tile self-assembly. *Nature Communications* **4**, 1965, doi:10.1038/ncomms2965 (2013).

16 Green, L. N., Amodio, A., Subramanian, H. K. K., Ricci, F. & Franco, E. pH-Driven Reversible Self-Assembly of Micron-Scale DNA Scaffolds. *Nano Letters* **17**, 7283-7288, doi:10.1021/acs.nanolett.7b02787 (2017).

17 Zhang, F., Nangreave, J., Liu, Y. & Yan, H. Structural DNA Nanotechnology: State of the Art and Future Perspective. *Journal of the American Chemical Society* **136**, 11198-11211, doi:10.1021/ja505101a (2014).

18 Seeman, N. C. *Structural DNA nanotechnology*. (Cambridge University Press, 2016).

19 Seeman, N. C. & Sleiman, H. F. DNA nanotechnology. *Nature Reviews Materials* **3**, 17068 (2017).

20 Wang, P. *et al.* Practical aspects of structural and dynamic DNA nanotechnology. *MRS Bulletin* **42**, 889-896 (2017).

21 Stewart, J. M. & Franco, E. Self-assembly of large RNA structures: learning from DNA nanotechnology. *DNA and RNA Nanotechnology* **2**, 23-35 (2015).

22 Geary, C., Rothemund, P. W. K. & Andersen, E. S. A single-stranded architecture for cotranscriptional folding of RNA nanostructures. *Science* **345**, 799-804, doi:10.1126/science.1253920 (2014).

23 Afonin, K. A. *et al.* Co-transcriptional Assembly of Chemically Modified RNA Nanoparticles Functionalized with siRNAs. *Nano Letters* **12**, 5192-5195, doi:10.1021/nl302302e (2012).

24 Surana, S., Shenoy, A. R. & Krishnan, Y. Designing DNA nanodevices for compatibility with the immune system of higher organisms. *Nature nanotechnology* **10**, 741 (2015).

25 Jepsen, M. D. *et al.* Development of a genetically encodable FRET system using fluorescent RNA aptamers. *Nature communications* **9**, 18 (2018).

26 Dao, B. N. *et al.* Triggering RNAi with multifunctional RNA nanoparticles and their delivery. *DNA and RNA nanotechnology* **2**, 1-12 (2015).

27 Afonin, K. A. *et al.* In vitro assembly of cubic RNA-based scaffolds designed in silico. *Nature nanotechnology* **5**, 676 (2010).

28 Jaeger, L. & Chworos, A. The architectonics of programmable RNA and DNA nanostructures. *Current opinion in structural biology* **16**, 531-543 (2006).

29 Ko, S. H. *et al.* Synergistic self-assembly of RNA and DNA molecules. *Nature chemistry* **2**, 1050 (2010).

30 Monferrer, A., Zhang, D., Lushnikov, A. J. & Hermann, T. Versatile kit of robust nanoshapes self-assembling from RNA and DNA modules. *Nature Communications* **10**, 608 (2019).

31 Yurke, B., Turberfield, A. J., Mills Jr, A. P., Simmel, F. C. & Neumann, J. L. A DNA-fuelled molecular machine made of DNA. *Nature* **406**, 605 (2000).

32 Seelig, G., Soloveichik, D., Zhang, D. Y. & Winfree, E. Enzyme-free nucleic acid logic circuits. *science* **314**, 1585-1588 (2006).

33 Yin, P., Yan, H., Daniell, X. G., Turberfield, A. J. & Reif, J. H. A unidirectional DNA walker that moves autonomously along a track. *Angewandte Chemie* **116**, 5014-5019 (2004).

34 Kim, J. & Winfree, E. Synthetic in vitro transcriptional oscillators. *Molecular systems biology* **7**, 465 (2011).

35 Gerling, T., Wagenbauer, K. F., Neuner, A. M. & Dietz, H. Dynamic DNA devices and assemblies formed by shape-complementary, non–base pairing 3D components. *Science* **347**, 1446-1452 (2015).

36 Aldaye, F. A. & Sleiman, H. F. Modular access to structurally switchable 3D discrete DNA assemblies. *Journal of the American Chemical Society* **129**, 13376-13377 (2007).

37 Chen, Y.-J., Groves, B., Muscat, R. A. & Seelig, G. DNA nanotechnology from the test tube to the cell. *Nature nanotechnology* **10**, 748 (2015).

38 Winfree, E., Liu, F., Wenzler, L. A. & Seeman, N. C. Design and self-assembly of two-dimensional DNA crystals. *Nature* **394**, 539 (1998).

39 Mardanlou, V. *et al.* A coarse-grained model captures the temporal evolution of DNA nanotube length distributions. *Natural Computing* **17**, 183-199 (2018).

40 Ekani-Nkodo, A., Kumar, A. & Fygenson, D. K. Joining and scission in the self-assembly of nanotubes from DNA tiles. *Physical review letters* **93**, 268301 (2004).

41 Cerritelli, S. M. & Crouch, R. J. Ribonuclease H: the enzymes in eukaryotes. *The FEBS journal* **276**, 1494-1505 (2009).

42 Lima, W. F. & Crooke, S. T. Cleavage of single strand RNA adjacent to RNA-DNA duplex regions by Escherichia coli RNase H1. *Journal of Biological Chemistry* **272**, 27513-27516 (1997).

43 Studier, F. W. & Moffatt, B. A. Use of bacteriophage T7 RNA polymerase to direct selective high-level expression of cloned genes. *Journal of molecular biology* **189**, 113-130 (1986).

44 Bustin, S. A. Absolute quantification of mRNA using real-time reverse transcription polymerase chain reaction assays. *Journal of molecular endocrinology* **25**, 169-193 (2000).

45 Ballardini, R., Balzani, V., Credi, A., Gandolfi, M. T. & Venturi, M. Artificial molecular-level machines: Which energy to make them work? *Accounts of Chemical Research* **34**, 445-455 (2001).

46 Lloyd, J. *et al.* Dynamic Control of Aptamer–Ligand Activity Using Strand Displacement Reactions. *ACS Synthetic Biology* **7**, 30-37, doi:10.1021/acssynbio.7b00277 (2018).

47 Ohuchi, S., Mori, Y. & Nakamura, Y. Evolution of an inhibitory RNA aptamer against T7 RNA polymerase. *FEBS open bio* **2**, 203-207 (2012).

48 Kim, J., Quijano, J. F., Yeung, E. & Murray, R. M. Synthetic logic circuits using RNA aptamer against T7 RNA polymerase. *bioRxiv*, 008771 (2014).

49 Franco, E. *et al.* Timing molecular motion and production with a synthetic transcriptional clock. *Proceedings of the National Academy of Sciences* (2011).

50 Kim, J., White, K. S. & Winfree, E. Construction of an in vitro bistable circuit from synthetic transcriptional switches. *Molecular systems biology* **2**, 68 (2006).

51 Zhang, D. Y. & Seelig, G. Dynamic DNA nanotechnology using strand-displacement reactions. *Nature chemistry* **3**, 103 (2011).

52 Klocke, M. A., Garamella, J., Subramanian, H. K., Noireaux, V. & Franco, E. Engineering DNA nanotubes for resilience in an E. coli TXTL system. *Synthetic Biology* **3**, ysy001 (2018).

53 Rizzo, J., Gifford, L., Zhang, X., Gewirtz, A. & Lu, P. Chimeric RNA–DNA molecular beacon assay for ribonuclease H activity. *Molecular and cellular probes* **16**, 277-283 (2002).

54 Richmond, T. J. & Davey, C. A. The structure of DNA in the nucleosome core. *Nature* **423**, 145, doi:10.1038/nature01595

55 Watson, J. D. & Crick, F. H. Molecular structure of nucleic acids. *Nature* **171**, 737-738 (1953).

56 Wang, P., Ko, S. H., Tian, C., Hao, C. & Mao, C. RNA–DNA hybrid origami: folding of a long RNA single strand into complex nanostructures using short DNA helper strands. *Chemical Communications* **49**, 5462-5464 (2013).

57 Stewart, J. M., Subramanian, H. K. & Franco, E. Self-assembly of multi-stranded RNA motifs into lattices and tubular structures. *Nucleic acids research* **45**, 5449-5457 (2017).

58 Goldman, S. R., Ebright, R. H. & Nickels, B. E. Direct detection of abortive RNA transcripts in vivo. *Science* **324**, 927-928 (2009).

59 Hsu, L. M., Vo, N. V., Kane, C. M. & Chamberlin, M. J. In vitro studies of transcript initiation by Escherichia coli RNA polymerase. 1. RNA chain initiation, abortive initiation, and promoter escape at three bacteriophage promoters. *Biochemistry* **42**, 3777-3786 (2003).

60 Triana-Alonso, F. J., Dabrowski, M., Wadzack, J. & Nierhaus, K. H. Self-coded 3′-extension of run-off transcripts produces aberrant products during in vitro transcription with T7 RNA polymerase. *Journal of Biological Chemistry* **270**, 6298-6307 (1995).

61 Schaffter, S. W. *et al.* T7 RNA polymerase non-specifically transcribes and induces disassembly of DNA nanostructures. *Nucleic Acids Research* **46**, 5332-5343, doi:10.1093/nar/gky283 (2018).

62 Suraneni, P. *et al.* A mechanism of leading-edge protrusion in the absence of Arp2/3 complex. *Molecular biology of the cell* **26**, 901-912 (2015).

63 Rohatgi, R. *et al.* The interaction between N-WASP and the Arp2/3 complex links Cdc42-dependent signals to actin assembly. *Cell* **97**, 221-231 (1999).

64 Aida, T., Meijer, E. & Stupp, S. Functional supramolecular polymers. *Science* **335**, 813-817 (2012).

65 Del Grosso, E., Amodio, A., Ragazzon, G., Prins, L. J. & Ricci, F. Dissipative Synthetic DNA-Based Receptors for the Transient Loading and Release of Molecular Cargo. *Angewandte Chemie International Edition* (2018).

66 Ragazzon, G. & Prins, L. J. Energy consumption in chemical fuel-driven self-assembly. *Nature nanotechnology*, 1 (2018).

67 Sharma, A. *et al.* Nanogel—an advanced drug delivery tool: Current and future. *Artificial cells, nanomedicine, and biotechnology* **44**, 165-177 (2016).

68 Li, Y. & Breaker, R. R. Kinetics of RNA degradation by specific base catalysis of transesterification involving the 2 ‘-hydroxyl group. *Journal of the American Chemical society* **121**, 5364-5372 (1999).

1.7 Supplementary Information

Sequences

PAGE purified DNA sequences were ordered from IDT DNA (Coralville, IA, USA).. This section contains a series of schematic figures, which represent the most relevant predicted interactions among the nucleic acids composing the genes and the tiles. Templates include 4 base “sealing” domains in genes (5’ end of non-template strand) to prevent breathing at the promoter site. Each RNA strand was designed to start with ‘G’ on the 3’ end, to ensure good transcription yield.

5b sticky end SE tile system

DNA strands

5bSE1: 5’- CTC AGT GGA CAG CCG TTC TGG AGC GTT GGA CGA AAC T

5bSE2: 5’- GTC TGG TAG AGC ACC ACT GAG AGG TA

5bSE3: 5’- cy3-CCA GAA CGG CTG TGG CTA AAC AGT AAC CGA AGC ACC AAC GCT

5bSE4: 5’- CAG ACA GTT TCG TGG TCA TCG TAC CT

5bSE5: 5’- CGA TGA CCT GCT TCG GTT ACT GTT TAG CCT GCT CTA C

RNA strand

5bSE4(RNA): 5’- CAG ACA GUU UCG UGG UCA UCG UAC CU

5b sticky end RE tile system

DNA strands

5bRE1: 5’- CGT ATT GGA CAT TTC CGT AGA CCG ACT GGA CAT CTT C

5bRE2: 5’- CTG GTC CTT CAC ACC AAT ACG GCA TT

5bRE3: 5’- atto647N-TCT ACG GAA ATG TGG CAG AAT CAA TCA TAA GAC ACC AGT CGG

5bRE4: 5’- ACC AGG AAG ATG TGG TAG TGG AAT GC

5bRE5: 5’- CCA CTA CCT GTC TTA TGA TTG ATT CTG CCT GTG AAG G

RNA strand

5bRE4(RNA): 5’- ACC AGG AAG AUG UGG UAG UGG AAU GC

7b sticky end SE tile system

DNA strands

7bSE1: 5’- TCA GTG GAC AGC CGT TCT GGA GCG TTG GAC GAA AC

7bSE2: 5’- TGT CTG GTA GAG CAC CAC TGA GAG GTA C

7bSE3: 5’- cy3-CCA GAA CGG CTG TGG CTA AAC AGT AAC CGA AGC ACC AAC GCT

7bSE4: 5’- CCA GAC AGT TTC GTG GTC ATC GTA CCT C

7bSE5: 5’- GAT GAC CTG CTT CGG TTA CTG TTT AGC CTG CTC TA

RNA strand

7bSE4(RNA): 5’- CCA GAC AGU UUC GUG GUC AUC GUA CCU C

8b sticky end SE tile system

DNA strands

8bSE1: 5’- AGT GGA CAG CCG TTC TGG AGC GTT GGA CGA AAC T

8bSE2: 5’- TCG TGC CCG AGC ACC ACT GAG AGG TA

8bSE3: 5’- cy3-CCA GAA CGG CTG TGG CTA AAC AGT AAC CGA AGC ACC AAC GCT

8bSE4: 5’- GGG CAC GAA GTT TCG TGG TCA TCG TAC CTC TC

8bSE5: 5’- CGA TGA CCT GCT TCG GTT ACT GTT TAG CCT GCT C

RNA strand

8bSE4(RNA): 5’- GGG CAC GAA GUU UCG UGG UCA UCG UAC CUC UC

Genes for production of RNA strands

5BSE4 RNA T7 gene
NonTemplate: 5’- GCG CTA ATA CGA CTC ACT ATA GCA GAC AGT TTC GTG GTC ATC GTA CCT
Template: 5’- AGG TAC GAT GAC CAC GAA ACT GTC TGC TAT AGT GAG TCG TAT TAG CGC

5BSE4 RNA SP6 gene
NonTemplate: 5’- GCG CAT TTA GGT GAC ACT ATA GCA GAC AGT TTC GTG GTC ATC GTA CCT
Template: 5’- AGG TAC GAT GAC CAC GAA ACT GTC TGC TAT AGT GTC ACC TAA ATG CGC

5BRE4 RNA T7 gene
NonTemplate: 5’- GCG CTA ATA CGA CTC ACT ATA GAC CAG GAA GAT GTG GTA GTG GAA TGC
Template: 5’- GCA TTC CAC TAC CAC ATC TTC CTG GTC TAT AGT GAG TCG TAT TAG CGC

7BSE4 RNA T7 gene

NonTemplate: 5’- GCG CTA ATA CGA CTC ACT ATA GCC AGA CAG TTT CGT GGT CAT CGT ACC TC

Template: 5’- GAG GTA CGA TGA CCA CGA AAC TGT CTG GCT ATA GTG AGT CGT ATT AGC GC

8BSE4 RNA T7 gene

NonTemplate: 5’- GCG CTA ATA CGA CTC ACT ATA GCC AGA CAG TTT CGT GGT CAT CGT ACC TC

Template: 5’- GAG GTA CGA TGA CCA CGA AAC TGT CTG GCT ATA GTG AGT CGT ATT AGC GC

T7 Self inhibitor gene

NonTemplate: 5’- TTC TAA TAC GAC TCA CTA TA G CGT AAG TCA ATT CCA CTA TCA TTG CTG CTT C

Template: 5’- AAG ATT ATG CTG AGT GAT AT C GCA TTC AGT TAA GGT GAT AGT AAC GAC GAA G

Switch gene system

NonTemplate: 5’- AAG CAA GGG TAA GAT GGA ATG ATA ATA CGA CTC ACT ATA GCA G AC AGT TTC GTG GTC ATC GTA CCT

A1Temp: 5’- TAT TAT CAT TCC ATC TTA CCC TTG CTT CAA TCC G

A2Temp: 5’- AGG TAC GAT GAC CAC GAA ACT GTC TGC TAT AGT GAG TCG

Inh_switch: 5’- ACG GAT TGA AGC AAG GGT AAG ATG GAA TGA TAA TA

Reagents

Oligonucleotides

Lyophilized, PAGE-purified DNA oligonucleotides were purchased from Integrated DNA Technologies (Coralville, IA). All strands were resuspended in nuclease free water (Thermo Fisher Cat. no. AM9932), quantitated by UV absorbance at 260 nm using a Thermo Scientific

Nanodrop 2000c Spectrophotometer, and stored at -20°C. RNA strands were transcribed and gel extracted in house according to the protocol in Section 4.5.

Enzymes

T7 RNA Polymerase was purchased from Lucigen® (AmpliScribe™ T7-Flash™ Transcription Kit, Cat. No. ASF3507). SP6 RNA Polymerase was purchased from CellScript™ (SP6-Scribe™ Standard RNA IVT Kit, Cat. No. C-AS3106). RNase H was purchased from Promega™(Ref. No. M4281). All enzymes were stored at -20°C.

Buffers, dyes, and other reagents

Transcription buffer was purchased by New England Biolabs (NEB, Cat. No. M0251S). 1X Transcription buffer contains: 40 mM Tris-HCl, 6 mM $MgCl_2$, 1 mM DTT, 2 mM spermidine (pH 7.9 @ 25°C). Nucleotide Triphosphates (NTPs) were purchased from New England Biolabs (NEB, Cat. No.N0450S).Tris-acetate-EDTA (TAE, Cat. no. 15558026) and Tris-borate-EDTA (TBE, Cat. no.LC6675) buffers were purchased from Thermo Scientific. Reporter molecule 3,5-difluoro-4-hydroxybenzylidene imidazolinone (DFHBI), was purchased from Lucerna technologies (Cat. No. 400-5). DFHBI was resuspended in DMSO (Thermo Scientific, Cat. no. D12345) and stored at -20°C. SYBR™ Gold Nucleic Acid Gel Stain was purchased from Invitrogen™, Thermo Fisher Scientific (Cat. no. S11494).

Additional methods

Atomic Force Microscopy

AFM images were obtained in tapping mode using 1X TAE/12.5 mM Magnesium Chloride as imaging buffer with a Digital Instruments Multimode AFM, equipped with a Nanoscope III controller. Sharp Nitride Lever (SNL) tips from Bruker with a nominal spring

constant of 0.24 N/m (resonant frequency of 56 kHz) or Micro Cantilever from Olympus® (BL-AC40TS-C2) with a nominal spring constant of 0.09 N/m were used for imaging (resonant frequency of 110 kHz). After annealing 5μL of sample was taken directly from the test tube and was added to a freshly cleaved mica surface, it was allowed to adsorb for 30 seconds, then 25μL of AFM buffer was added onto the sample on the mica surface and 25μL of AFM buffer was added to the AFM tip.

Polyacrylamide gel electrophoresis (PAGE)

Denaturing PAGE: Pre-mix was prepared (for a final volume of 100 mL) by adding 42 g of urea to 25 ml of nanopure water, the mixture was then heated until the urea completely dissolved. This mixture was allowed to cool to room temperature, then acrylamide/bis-acrylamide 19:1, 40% solution was added. The pre-mix was added in appropriate ratios with TBE and nanopure water, ammonium persulfate (APS), and Tetramethylethylenediamine (TEMED) to cast the desired polyacrylamide percentage. Gels were cast in 10X10 cm, 1 mm thick disposable mini gel cassettes (ThermoScientific, Cat. No. NC2010) and allowed to polymerize for at least 2 hours before electrophoresis. Gels were run at room temperature at 100 V in 1X TBE unless otherwise noted. Unless otherwise noted, after electrophoresis the gels were stained in SYBR Gold Nucleic Acid Gel Stain for 20-30 minutes and then imaged using the Biorad ChemiDocTM MP system. We purchased the 10bp DNA ladder used in denaturing gels from Invitrogen™ (Cat. No. 10821- 015).

Non-Denaturing PAGE: Acrylamide/bis-acrylamide 19:1, 40% solution, TAE, Magnesium Chloride 12.5 mM (final concentration), APS, and TEMED were added together at appropriate concentrations for the desired polyacrylamide percentage, then cast in 10X10 cm, 1 mm thick disposable mini gel cassettes (Thermo Scientific, Cat. No. NC2010) and allowed to polymerize

for at least 2 hours before electrophoresis. Gels were run at 4□C at 150 V in 1X TBE buffer. After electrophoresis gels were stained in SYBR Gold Nucleic Acid Gel Stain for 20 minutes then imaged using the Biorad ChemiDocTM MP system.

RNA extraction

RNA was transcribed in vitro using the AmpliScribe-T7-Flash Transcription Kit. The following components were mixed at room temperature: RNase-free water, 1-1.5μg template, AmpliScribe T7-Flash 1X Reaction Buffer (Epicentre, Cat. No. ASF3507)9 mM NTPs, 40 U/μL RiboGuard RNase Inhibitor (Epicentre, Cat. No. RG90925), and 2μL of AmpliScribe T7-Flash Enzyme Solution (Epicentre, Cat. No. ASF3507). This mix was then incubated at 37C for 4 hours. After incubation, 20μL of loading dye was added to the 20μL transcription solution, and 8μL of the transcription/dye mix was added to each of the middle 5 lanes of the gel. The gel was run at 100 V at room temperature in 1X TBE.

After electrophoresis the gel was stained in 80 mL 1X TBE and 1μL SYBR Gold Nucleic Acid Gel Stain (Thermo Scientific, Cat. No. S-11494) for 20-30 minutes. The gel was then placed on a TLC silica gel 60 W F254S aluminum sheet (EMD Millipore, Cat. No. 1055590001) covered in plastic wrap. The gel was then illuminated with UV light and the desired RNA band was excised and crushed, and eluted using 200μL of 0.3 M sodium acetate at pH 5.3. The elution reaction was done in 0.5 mL DNA Lobind tubes (Eppendorf, Cat. No. 022431005), incubated at 42μC for ~20 hours. After incubation, the sodium acetate was removed and placed into 1.7 mL RNase/DNase free tubes. The old Lobind tubes were further rinsed with 100μL of 0.3 M sodium acetate pH 5.3, which was added to the new tubes. Then 1 mL of freezer cold

100% ETOH and 1μL of glycogen was added into each tube and the sample was incubated at -20C for 20 hours.

Next, the samples were spun at 13500 rpm at 4C for 15 minutes. The white precipitate pellet (RNA) at the bottom of the tube was located and the supernatant was carefully pipetted out of the tubes to avoid removal of the pellet. Then, 500μL of 70% freezer cold ETOH was added to the tubes and spun at 13500 rpm at 4C for 5 minutes. The supernatant was carefully decanted again with a pipette. This washing procedure was repeated a third time. After the last wash, as much supernatant was removed as possible, then the tubes were opened and placed in the vacuum concentrator and allowed to spin at room temperature for 15 minutes. The samples were then re-suspended in 10-15μL of Ambion nuclease free water (Ambion, Cat. No. AM9932).

Fluorescence microscopy data and image processing

Fluorescence microscopy images were processed using ImageJ plugin Skeletonize to collect nanotube length distributions. Branching or looping nanotubes were eliminated from the length dataset using an in-house MATLAB script. Pixels were converted to micrometers using the 60X objective conversion factor 1 pixel = 0.11 μm. Due to camera limitations, tubes having length below 0.33 μm were also eliminated from the length distributions. Nanotube length distributions measured in fluorescence microscopy experiments are shown in the main paper, Fig. 1-4 and Fig. 1-5. These plots were prepared using an in-house MATLAB File script, error bars were produced using bootstrapping.

Reagents

Oligonucleotides

Lyophilized, PAGE-purified DNA oligonucleotides were purchased from Integrated DNA Technologies (Coralville, IA). All strands were resuspended in nuclease free water (Thermo Fisher Cat. no. AM9932), quantitated by UV absorbance at 260 nm using a Thermo Scientific Nanodrop 2000c Spectrophotometer, and stored at -20°C. RNA strands were transcribed and gel extracted in house according to the protocol in Section 4.5.

Enzymes

T7 RNA Polymerase was purchased from Lucigen® (AmpliScribe™ T7-Flash™ Transcription Kit, Cat. No. ASF3507). SP6 RNA Polymerase was purchased from CellScript™ (SP6-Scribe™ Standard RNA IVT Kit, Cat. No. C-AS3106). RNase H was purchased from Promega™(Ref. No. M4281). All enzymes were stored at -20°C.

Buffers, dyes, and other reagents

Transcription buffer was purchased by New England Biolabs (NEB, Cat. No. M0251S). 1X Transcription buffer contains: 40 mM Tris-HCl, 6 mM $MgCl_2$, 1 mM DTT, 2 mM spermidine (pH 7.9 @ 25°C). Nucleotide Triphosphates (NTPs) were purchased from New England Biolabs (NEB, Cat. No.N0450S).Tris-acetate-EDTA (TAE, Cat. no. 15558026) and Tris-borate-EDTA (TBE, Cat. no.LC6675) buffers were purchased from Thermo Scientific. Reporter molecule 3,5-difluoro-4-hydroxybenzylidene imidazolinone (DFHBI), was purchased from Lucerna technologies (Cat. No. 400-5). DFHBI was resuspended in DMSO (Thermo Scientific, Cat. no. D12345) and stored at -20°C. SYBR™ Gold Nucleic Acid Gel Stain was purchased from Invitrogen™, Thermo Fisher Scientific (Cat. no. S11494).

Analysis of tubular structures using AFM images

This section compares representative AFM images of DNA-RNA nanostructures produced from all our tile designs.

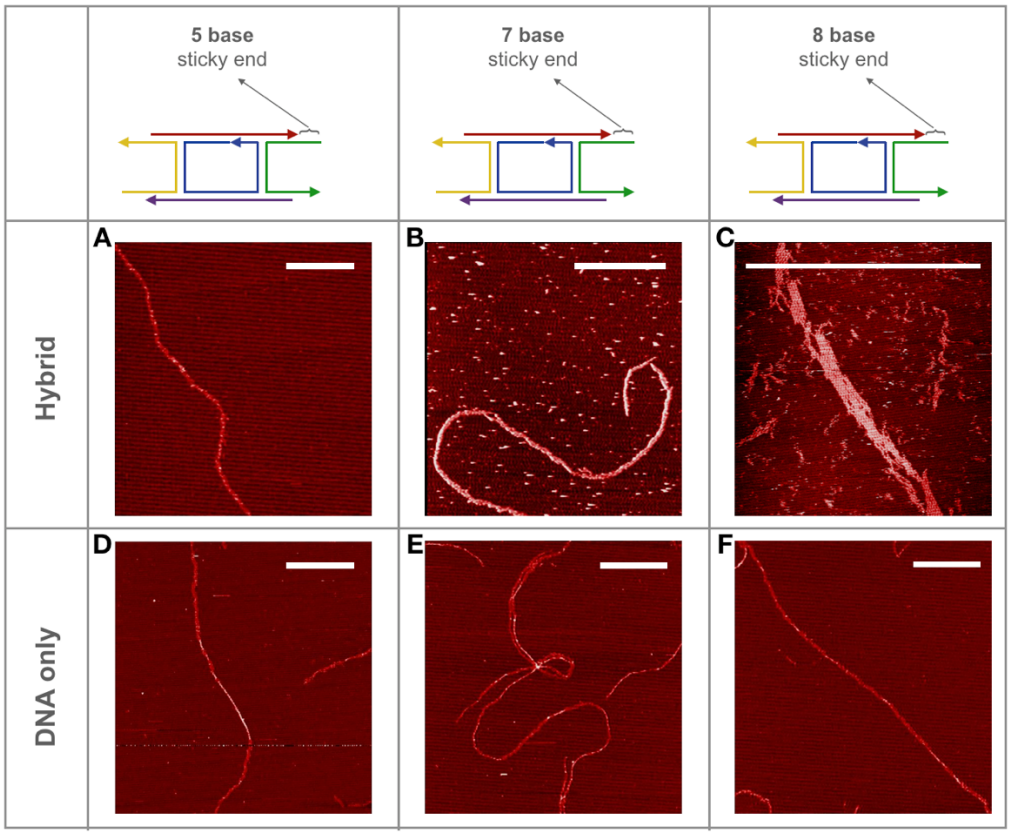

Figure S1.1: Overview of AFM images of assembled structures. A) DNA-RNA hybrid tubes with 5 base sticky end, assembled by extracted RNA addition, B) DNA-RNA hybrid tubes with 7 base sticky end, assembled by extracted RNA addition, C) DNA-RNA hybrid tubes with 8 base sticky end, assembled by extracted RNA addition, D) DNA tubes with 5 base sticky end, E) DNA tubes with 7 base sticky end, E) DNA tubes with 8 base sticky end. In each case, scale bar represents 1 μm.

We used AFM to quantify width of the DNA-RNA hybrid tubes with 5 base sticky end variant. We considered AFM images of tubes assembled by extracted RNA addition. We picked 6 isolated, tubular structures and measured their length and width. Width was measured at the extrema and at the center of the tube, and tube overall width was computed as the average of

these three measurements. We compared our results with those provided by Rothemund et. al. and observed that hybrid nanotube width lies within the width range of DNA nanotubes, as reported by Rothemund et. al.

A

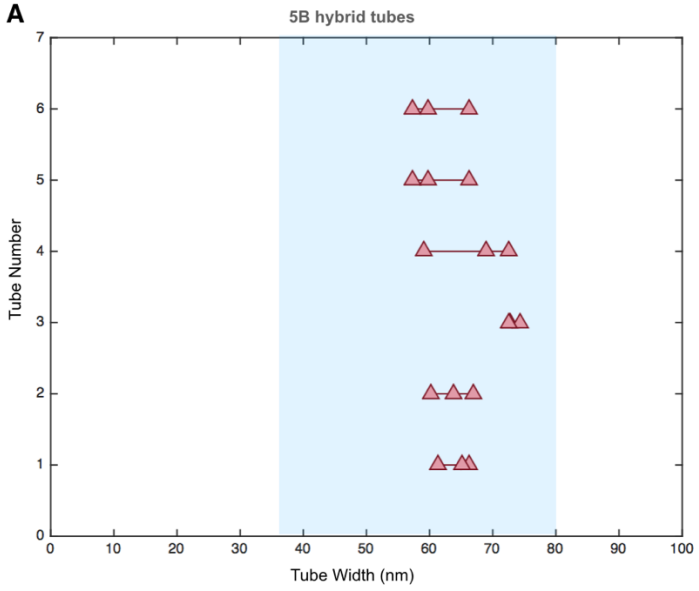

B

Tube number	Tube width (nm)	Mean width of individual tube (nm)	Mean width of 5b Hybrid tubes (nm)
1	66.205	64.231	65.289
	61.257		
	65.232		
2	63.899	63.718	
	66.994		
	60.262		
3	72.657	73.180	
	74.397		
	72.487		
4	68.904	66.865	
	72.617		
	59.075		
5	57.267	61.096	
	59.824		
	66.197		
6	63.557	62.642	
	64.812		
	59.557		

Figure S1.2: Analysis of 5b sticky end hybrid tube width. A) Graphical representation of width recorded for six individual tubes. Blue shaded area represents the limits of DNA nanotubes (minimum width = 36nm, maximum width = 80nm) as reported by Rothemund et.al.[1] B) Mean width calculated by taking mean of each individual mean tube length for 5b hybrid tubes = 65.289 nm.

Characterizing assembly of partially formed DNA tiles

We conducted 3 different set of experiments to validate that the partially formed DNA tiles form DNA nanotubes when the missing strand/s are added to it isothermally at 37°C. We used 8 base sticky end variant for this experiment. Target concentration of each strand is 1 μM. The images for incubation at 37°C were taken after 1 hour of addition of the missing strand..

As shown in the following figure, we were able to prove that it was possible to form nanotubes with annealing partially formed DNA tiles. The nanotubes were observed at room temperature (25°C) using fluorescence microscopy . Each assay was conducted in triplicates.

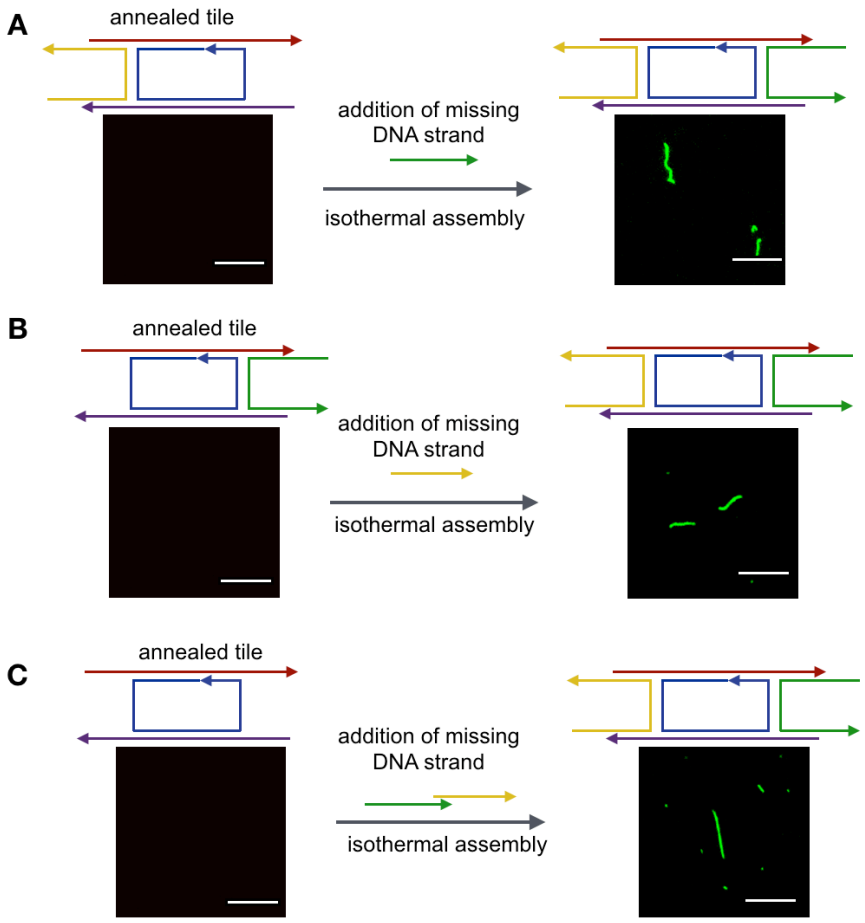

Figure S1.3: Fluorescence microscope images for DNA trigger experiments. Left images were taken after anneal and right after incubation at 37°C with remaining missing strands. A) Having DNA strand S1,S2,S3,S5 during anneal and addition of DNA S4 while incubation, 3)Having DNA strand S1,S3,S4,S5 during anneal and addition of DNA S2 while incubation, 4)Having DNA strand S1,S3,S5 during anneal and addition of DNA S2 and DNA S4 while incubation. All scale bars represent 10 μm..

Effect of increasing enzyme concentration on co-transcriptional assembly

Increasing the volume of T7 RNA polymerase has a detrimental effect on assembly, and recent experiments on similar nanotubes suggest that this may be due to undesired RNA strands transcribed from the nanotubes, which then bind to and inactivate unpolymerized tiles and may strand invade the sticky ends of polymerized tiles[5]. The T7 conc. used for all our experiments in the main paper is represented by the orange trace (1.25% v/v).

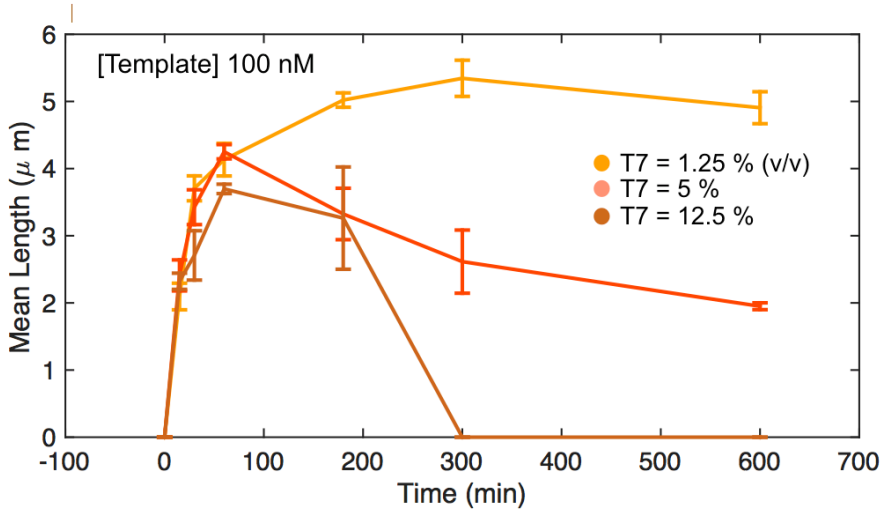

Figure S1.4: Effect of increasing enzyme concentration on co-transcriptional assembly. Increasing the volume of T7 RNA polymerase has a detrimental effect on assembly, and other ongoing experiments suggest this effect is due to non-specific binding of the polymerase to the nanotubes.

Trigger activation using Sp6 enzyme

Inactive tiles with 5 base sticky ends were activated using the in-situ transcription using Sp6 enzyme and a gene template with corresponding promoter region. Target concentration of each strand is the inactive tile is 0.5 μM. Gene template concentration for missing RNA strand production is 100nM. The images for activated tubes were taken after 1 hour of template addition. The protocol for annealing inactive tiles are provided in.

As shown in the following figure, we were able to achieve trigger activation using the Sp6 enzyme. The nanotubes were observed at room temperature (25°C) using fluorescence microscopy. The experiment was conducted in triplicates.

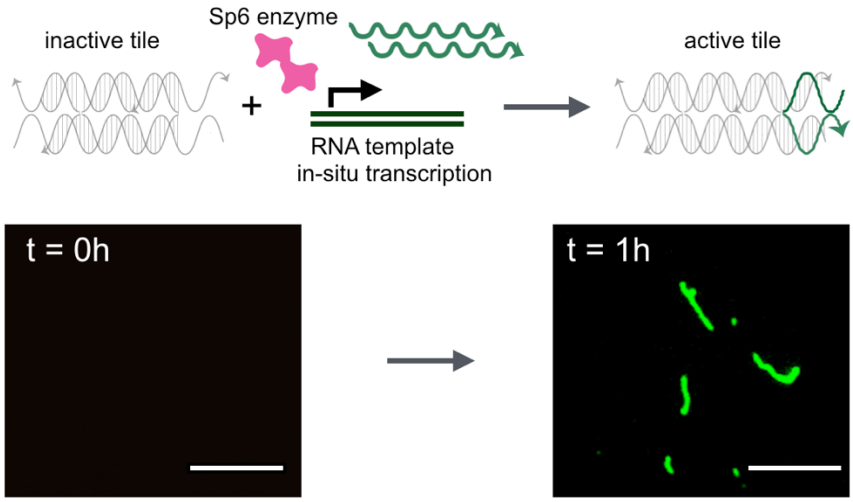

Figure S1.5: Activation using Sp6 enzyme. Triggering isothermal assembly via in-situ transcription of RNA strand. Images were taken after 1 hour of trigger strand addition. All scale bars = 10μm.

Self-inhibition of T7 RNA Polymerase

In order to slow down transcription rates, we designed a self-inhibiting aptamer template (SIAT) with a T7 promoter, coding for T7 RNAP inhibiting aptamer. When T7 RNAP transcribes this gene, the nascent RNA transcript will bind to the enzyme and inhibit it. This can be seen using fluorometry by measuring the transcription rate of Broccoli aptamer(DFHBI) from a gene also has a T7 promoter. The red trace represents negative control in which there is no SIAT. It is evident that the transcription turns off completely with [SIAT]>0.02μM.

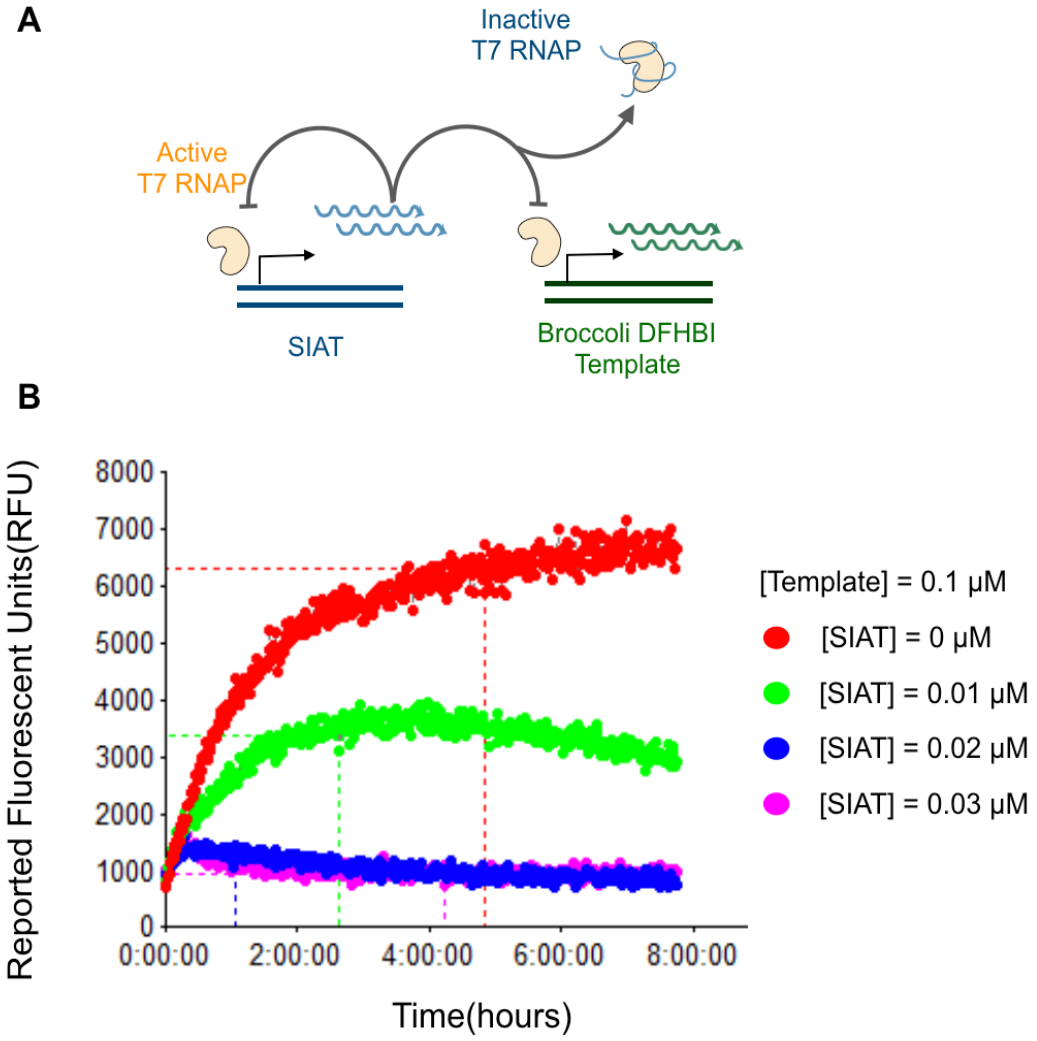

Figure S1.6: Self-inhibition of T7 RNA Polymerase. A) Reaction scheme. The SIAT gene codes for T7 RNAP inhibiting aptamer, resulting in self-inhibition by T7 RNAP. B) Fluorometry data verifying this mechanism. As a reporter we have Broccoli DFHBI aptamer gene with T7 promoter. T7 RNA Polymerase activity is suppressed upon the addition of SIAT.

Switch Gene system

This section contains a schematic for the series of strands used for the 'switch gene system' demonstrated in Fig. 1-5 of the main paper. These represent the most relevant predicted interactions among the nucleic acids. Transcription is activated by adding an activator strand complementary to the single stranded promoter region; transcription is inhibited when the activator is absent, or is displaced by a complementary inhibitor strand via toehold-mediated branch migration.

These schemes have an illustrative purpose and are not an exhaustive list of all secondary structures that can occur in the system. The main activation, Transcription and Inhibition reaction are:

Activation: NonTemp·A2Temp + A1Temp → NonTemplate·A2Temp·A1Temp

Transcription: NonTemplate·A2Temp·A1Temp + RNAP ⇌
NonTemplate·A2Temp·A1Temp·RNAP → RNA product +
NonTemplate·A1Temp·A2Temp·RNAP

Inhibition: Inh_switch + NonTemplate·A2Temp·A1Temp → Inh_switch·A1Temp +
NonTemp·A2Temp

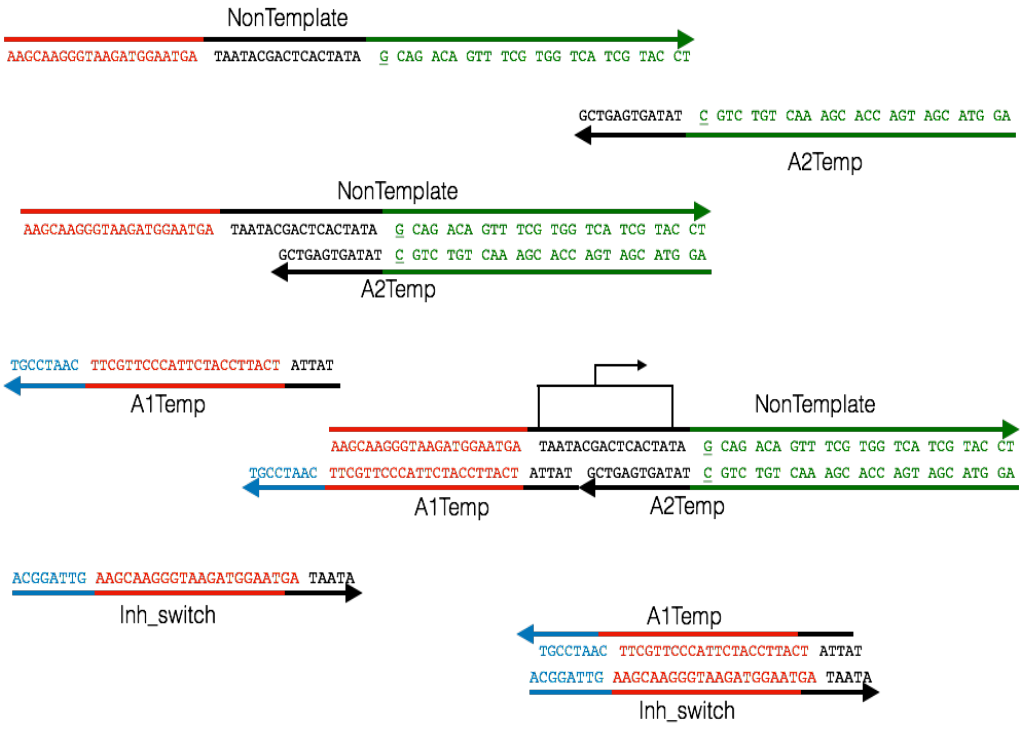

Figure S1.7: Relevant interactions in the Switch Gene system: From top to bottom: Non Template strand and A2Temp bind to form the incomplete gene (black domain represent T7 promoter region); A1Temp binds to this to complete the gene, enabling it to produce RNA production. The inhibitor strand (Inh_switch) can displace the A1Temp by competitive strand displacement reaction, by attaching to the overhanging toehold (blue) region.

2. Chapter 2: A coarse-grained model for estimation of joining rates in DNA nanotube systems

Adapted with permission from Pacella, Michael S., Vahid Mardanlou, Siddharth Agarwal, Anusha Patel, Elizabeth Jelezniakov, Abdul M. Mohammed, Elisa Franco, and Rebecca Schulman. "Characterizing the length-dependence of DNA nanotube end-to-end joining rates." Molecular Systems Design & Engineering 5, no. 2 (2020): 544-558.

2.1 Abstract

We model the evolution of length distribution in a DNA nanotube population where two distinct subpopulations, grown from different types of DNA origami seeds, join to form hybrid nanotubes. The goal of the model is to obtain an estimate for the joining rate of the subpopulations. The model takes into account nucleation, and joining, polymerization and depolymerization processes in the nanotube population. The continuous length distribution is segmented, and the behavior of nanotubes in each length bin is modeled using ordinary differential equations and equivalent chemical reactions.

2.2 Introduction

Two species of nanotubes (species A and species B) were built that are both seeded at one end, and mixed together. As a result, joining can only occur via a reaction between a member of species A and a member of species B. The resulting structure can't join with anything else because it has a seed on both ends.

To be able to distinguish each of these types of structures, seed A is labeled in red, nanotubes that were grown from seed A are in dark green, seed B is in blue and nanotubes grown from it are light green. The scheme of the experiment conducted is given in Fig. 2-1.

The hypothesis to be tested in this study is that: 'Do complementary nanotube subpopulations join as a function of nanotube length? Short nanotubes should join earlier as they have greater mobility'. To test this hypothesis, we counted the number and measured the length of nanotubes of all species of each of the pre-joined population and the joined population for a series of time points (t = 0hr, 5hr, 10hr, 25hr, 50hr) to identify whether joining rates depend on length or not.

We formulate a mathematical model for these seeded nanotubes that describes how the joining of the tubes is a function of the length varies over time in a population of nanotubes. This model is coarse-grained in the sense that the nanotube population is segmented by length in a number of bins, and we use ordinary differential equations to describe how the population of each bin varies over time. The processes that we have taken into account are joining, nucleation, polymerization and depolymerization.

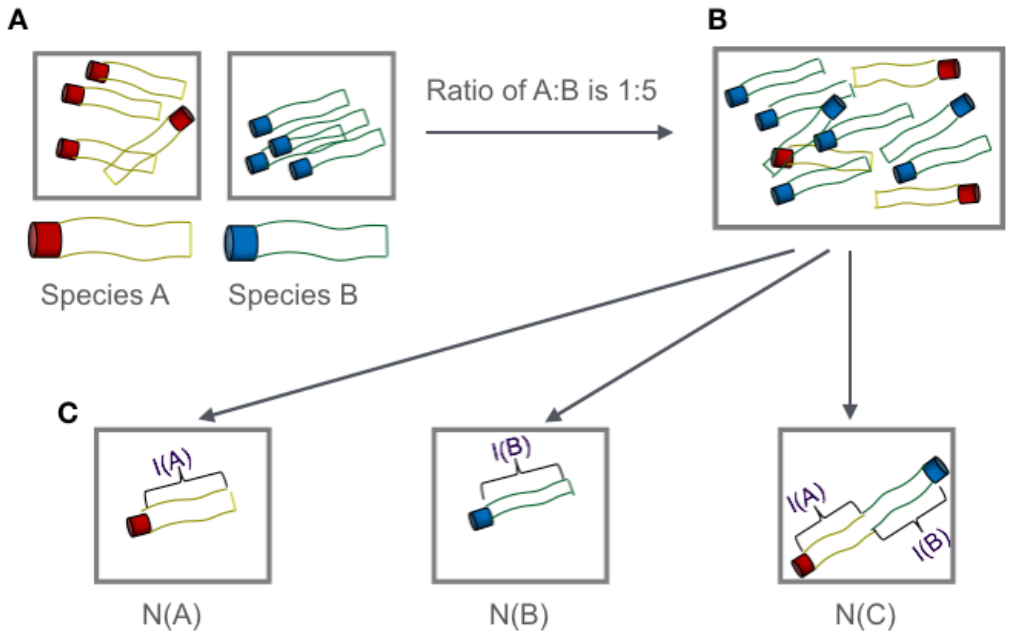

Figure 2-1 Overview of DNA nanotube growth and end-to-end joining. (A) 2 nanotube species A and B are allowed to nucleate from 2 distinct DNA origami seeds depicted in red and blue. They are grown at 20ºC for 15 hours. (B) The 2 species are mixed after 15 hours in the molar ratio of Species A : Species B = 1 : 5. (C) Types of nanotube species that can be observed post mixing. N(A) = number of species A, l(A) = nanotube contour length of tube made by species A

2.3 Model derivation

Binning based on length

We consider a solution including assembled nanotubes and unpolymerized tiles. Our sample includes tubes having any length $l \in [0, l_{max}]$, where l_{max} is the maximum observed length. To build a model that is computationally tractable, we segment the population of molecular species present in the system. We assume the sample includes tiles, whose concentration is indicated as T; nucleated assemblies of tiles, or nuclei, whose concentration is L_0; nanotubes, which are binned by length, so that variable L_n indicates the concentration of nanotubes in bin n.

The bin width, which we indicate as l_b, can be chosen depending on the acceptable level of coarseness (and complexity) of the model, because it determines the number of species.

We can bin the tubes of Species A and B based on their length in eight intervals like following:

$$Species A(L^A) = \overbrace{\underbrace{L_1^A}_{\text{A-type tube of length } 1\mu\text{m}} + L_2^A + L_3^A + L_4^A + L_5^A + L_6^A + L_7^A + L_8^A}^{\text{binning based on length}}$$

$$Species B(L^B) = \overbrace{\underbrace{L_1^B}_{\text{B-type tube of length } 1\mu\text{m}} + L_2^B + L_3^B + L_4^B + L_5^B + L_6^B + L_7^B + L_8^B}^{\text{binning based on length}}$$

Since the maximum length of and of these species does not exceed 8μm.

For example, if l_b = 1 μm, variable L_1 is the concentration of tubes of length between 0 nm to 0.5 μm. If l_{max} = 50μm, the number of variables in the model is n_{max} = [l_{max}/l_b] = 50. Segmentation introduces implicitly the assumption that a tube can switch from bin n to bin $n \pm 1$ only if it acquires or loses a number n_b of tiles, which are the tiles forming a tube segment of length l_b.

As an example, let us take again l_b = 1 μm; let us assume that the nanotube circumference is on average 7 tiles, each ≈ 14 nm wide; then we find n_b = 500 (This is the calculation: 1000/14=71.42, 71.42*7 = 500 tiles in the bin).

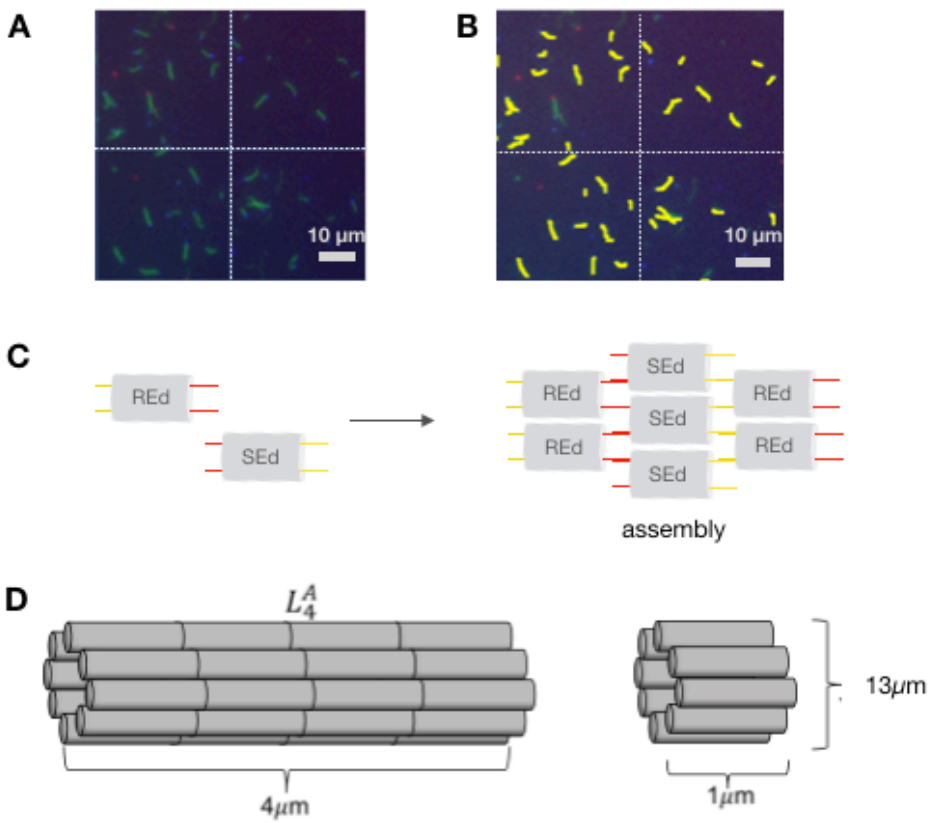

Figure 2-2: Fluorescence microscopy images for length estimation and binning. (A) Fluorescence microscopic image of sample with 3 distinct nanotube species, originating from red and blue seeds and the ones that join. Image is divided into quadrants for ease of length estimation. (B) Contour lengths of detected tubes is drawn with yellow color on top of the tubes. (C) DNA nanotubes design contain two tiles, REd and SEd, that can assemble into a lattice with diagonal stripes, adapted from[3] (D)Sample tube length (left) and one individual chunk(right). Scale bar is 10 μm.

2.4 Modeled process

Nucleation: We use seeds to nucleate nanotubes. Because the free tile concentration is low (18 nM), spontaneous nucleation of nanoubes is negligible.[1] Seeds are used to control the DAE-E tile DNA nanotube assembly as it is our understanding that they greatly accelerate nanotube nucleation and growth because they serve as nanotube nucleation templates. Tile assembly occurs on the seed, which can be assumed as tubes with length 0 (L_0). When modeling spontaneous nuclation, a critical number of tiles must bind simultaneously to form

nuclei, from which further polymerization of a nanotube can be initiated. Here, we assume that nucleation depends on the concentration of tiles (we assume tile concentation to be *T*) and nuclei L_0, and proceeds with rate $k_{nucl}T^{nnucl}$, where n_{nucl} is the critical nucleation size.

It is unclear if cooperativity (n_{nucl} >1) of binding is required to model nucleation from seeds.

The equivalent phenomenological reaction describing nucleation is:

$$L_0^A + n_{nucl}T \xrightarrow{k_{nucl}} L_1^A$$
$$where, L_0^A = k_{nucl\,A}L_0^A + k_d.L_1^A$$

Polymerization and depolymerization Nuclei and nanotubes grow as tiles bind to accessible sites. The polymerization rate depends on the concentration of tiles as well as the availability of binding sites: for tubes of length n, polymerization occurs at rate k_pTL_n. Tiles can also dissociate from tubes at a rate that depends exclusively on the concentration of tubes: for tubes of length n, the depolymerization rate is k_dL_n; for nuclei, we consider a different depolymerization rate $k_{d0}L_0$. Equivalent phenomenological reactions describing polymerization and depolymerization are:

$$n_bT + L_n \xrightarrow{k_p} L_{n+1} \qquad\qquad L_{n+1} \xrightarrow{k_d} L_n + n_bT$$

Joining of A-type and B-type nanotubes Nucleated A-type and B-type nanotubes diffusing in solution bind to form a C-type nanotubes, as described in Fig. 2-1. A simplified chemical equation describing this phenomenon is:

$$A + B \xrightarrow{k_{join}} C$$

Within our coarse grained model, the formation of C-type tubes is captured by the following reactions:

$$\begin{array}{lll} L_1^A + L_1^B \xrightarrow{k_{1,1}} L_{1,1}^C & L_2^A + L_1^B \xrightarrow{k_{2,1}} L_{1,1}^C & L_8^A + L_1^B \xrightarrow{k_{8,1}} L_{1,1}^C \\ L_1^A + L_2^B \xrightarrow{k_{1,2}} L_{1,2}^C & L_2^A + L_2^B \xrightarrow{k_{2,2}} L_{1,2}^C & L_8^A + L_2^B \xrightarrow{k_{8,2}} L_{1,2}^C \\ \vdots & \vdots \quad \cdots & \vdots \\ L_1^A + L_8^B \xrightarrow{k_{1,8}} L_{1,8}^C & L_2^A + L_8^B \xrightarrow{k_{2,8}} L_{1,8}^C & L_8^A + L_8^B \xrightarrow{k_{8,8}} L_{1,8}^C \end{array}$$

Our goal is to determine if the joining rate of the nanotubes is length dependent. To test this hypothesis, we choose a candidate expression for the joining rate that depends on the length of the nanotubes, on their diameter *d*, and on the concentration of nanotubes in the corresponding length bins. For example, if we consider length bins *n* and *m*, we postulate that the joining rate of nanotubes in these bins is $k_{join}(n,m)L_nL_m$. An estimate for $k_{join}(n,m)$ is given below. This expression derived by Hariadi et. al.[2] assumes that DNA nanotubes are rigid rods, and that their end-joining is a diffusion controlled reaction:

$$k_{join}(m,n) = \frac{\alpha}{l_b}\left[\frac{1}{m}\ln\left(\frac{ml_b}{d}\right) + \frac{1}{n}\ln\left(\frac{nl_b}{d}\right)\right]$$

where $\alpha = (\kappa 12 k_B \mathrm{T}\, d)/\eta$. Here η is the dynamic viscosity of the liquid, k_B is the Boltzmann constant, T is the absolute temperature, d is the nanotube diameter, and κ is a factor accounting for the fraction of productive nanotube collisions. Note that each joining reaction can occur by joining of only one end of each nanotube since they are seeded at the other end and so every reaction should be accounted for only once.

Ordinary differential Equations (ODE's)

We get the following ODE's for this model (here dL_x^Y/dt indicates the time derivative of the concentration of tile L_x^Y).

Although two tile types were utilized in experiments, we model the tile population with a single species. We think is an acceptable simplification because both tile types are incorporated stoichiometrically in growing nanotubes, and their total concentration in solution is the same.

$$\frac{dT}{dt} = -k_{nucl}T^{n_{nucl}}L_0^A - k_{nucl}T^{n_{nucl}}L_0^B + \\ + \sum_{i=1}^{8}(-k_pTL_i^A + k_dL_i^A - k_pTL_i^B + k_dL_i^B)$$

For the Nuclei:

$$\frac{dL_0^A}{dt} = -k_{nucl}T^{n_{nucl}}L_0^A + k_dL_1^A$$
$$\frac{dL_0^B}{dt} = -k_{nucl}T^{n_{nucl}}L_0^B + k_dL_1^B$$

We have 8 equations describing the concentration of A-type nanotubes in each bin:

$$\frac{dL_1^A}{dt} = k_pTL_0^A - k_dL_1^A - \Sigma k_{i,j}L_i^AL_j^B,$$
$$\frac{dL_i^A}{dt} = k_pTL_{i-1}^A - k_dL_i^A - \Sigma k_{i,j}L_i^AL_j^B$$

where, $i \in [2,8]$ and $j \in [1,8]$

Similarly we have 8 equations describing the concentration of B-type nanotubes in each bin:

$$\frac{dL_1^B}{dt} = k_p T L_0^B - k_d L_1^B - \Sigma k_{i,j} L_i^A L_j^B,$$
$$\frac{dL_j^B}{dt} = k_{p_j} T L_{j-1}^B - k_d L_j^B - \Sigma k_{i,j} L_i^A L_j^B$$

where, $i \in [1,8]$ and $j \in [2,8]$

We have 64 equations describing the concentration of C-type nanotubes in each bin

$$\frac{dL_{1,1}^C}{dt} = k_{1,1} L_1^A L_1^B$$
$$\vdots$$
$$\frac{dL_{m,n}^C}{dt} = k_{m,n} L_m^A L_n^B$$
$$\vdots$$
$$\frac{dL_{8,8}^C}{dt} = k_{8,8} L_8^A L_8^B$$

where, $m,n \in [1,8]$

2.9 Experimental data

Length data are shown in 3, where the fraction of population of species C is plotted versus the lengths of their A and B components. The species grow symmetrically, that is majority of the population have approximately equal lengths of the consisting A part

and the B part. We can also conclude by these plots that the species present at 5 hours continue to be present at later imaging time points and longer species C tubes are getting added to the population.

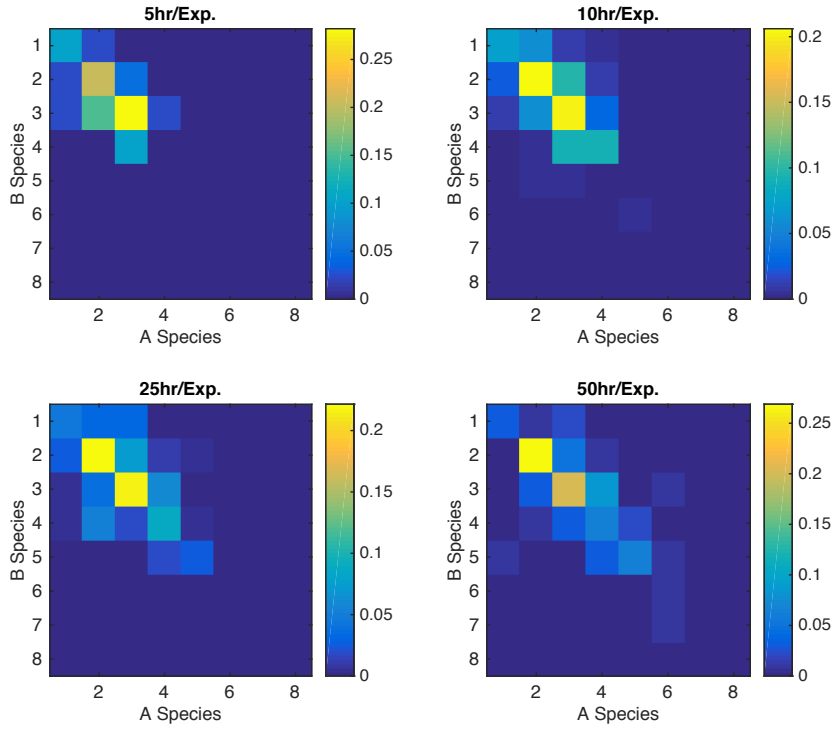

Figure 2-3: Composition of C-type nanotubes based on experimental data. X and Y axis represent the lengths of A part and B part respectively. Note: the sidebars represent different scales.

2.8 Data Fitting

To minimize the objective function, several fitting runs were conducted. This is a non-convex process, thus the fitting run converges at a local minima which depends on the chosen initial conditions of the parameter values. Here we report the best fitting results.

We consider different scenarios as far as assumptions made on the model parameters. For simulation we have assumed the Tile concentration to be 1μM.[4]

Length-dependent joining rate: Distinct nucleation rates for A and B-type nanotubes

In this simulation, we assumed distinct nucleation rates for Species A and B and the Kjoin was calculated using Bernie's formula. The parameters are stated in Table1.

Table 2-1: **Fitting parameters and results.** This table lists the parameters of Model that were fitted, including lower bound (L.B.) and upper bounds (U.B.) used in the fitting procedure.

Parameter	Units	L.B.	U.B.	Sim1	Definition
k_p	$M^{-1}s^{-1}$	10^{-5}	10^{1}	1.071×10^{-4}	Polymerization rate
k_d	s^{-1}	10^{-8}	10^{4}	1.000×10^{-6}	Depolymerization rate
α	$\mu m\ M^{-1}s^{-1}$	10^{-10}	10^{5}	6.607×10^{-3}	End-joining parameter
k_{nucl}	$M^{1-n_{nucl}}s^{-1}$	10^{-10}	10^{4}	1.023×10^{-10}	Nucleation - species A
k_{nucl}	$M^{1-n_{nucl}}s^{-1}$	10^{-10}	10^{4}	3.388×10^{-7}	Nucleation - species B

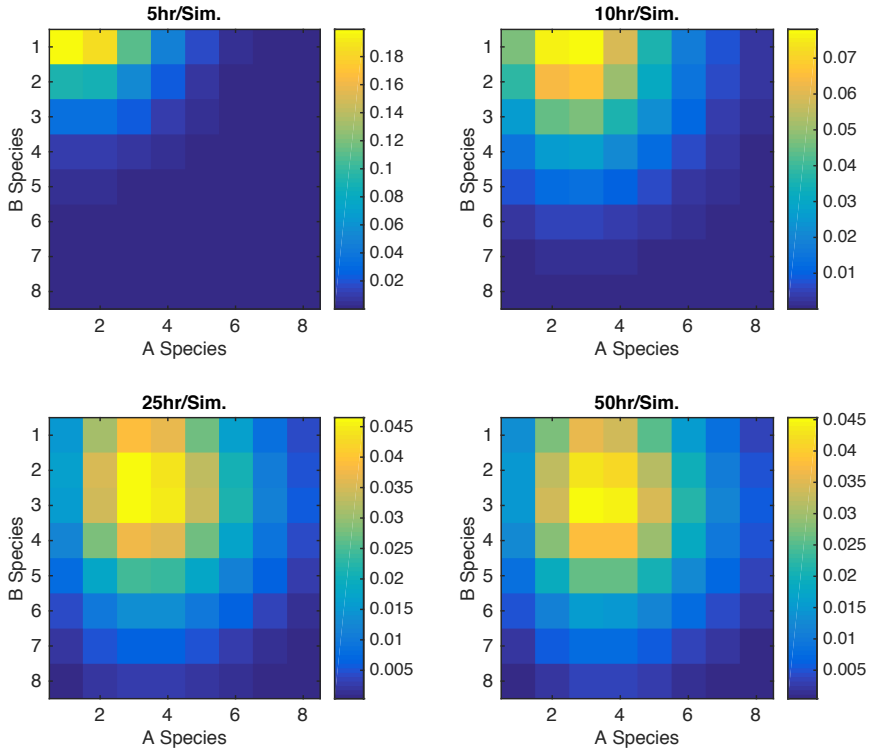

Figure 2-4: Simulated fraction of Species C at different times for length dependent joining and distinct nucleation rates. X and Y axis represent the lengths of A part and B part respectively. Note: the sidebars represent different scales

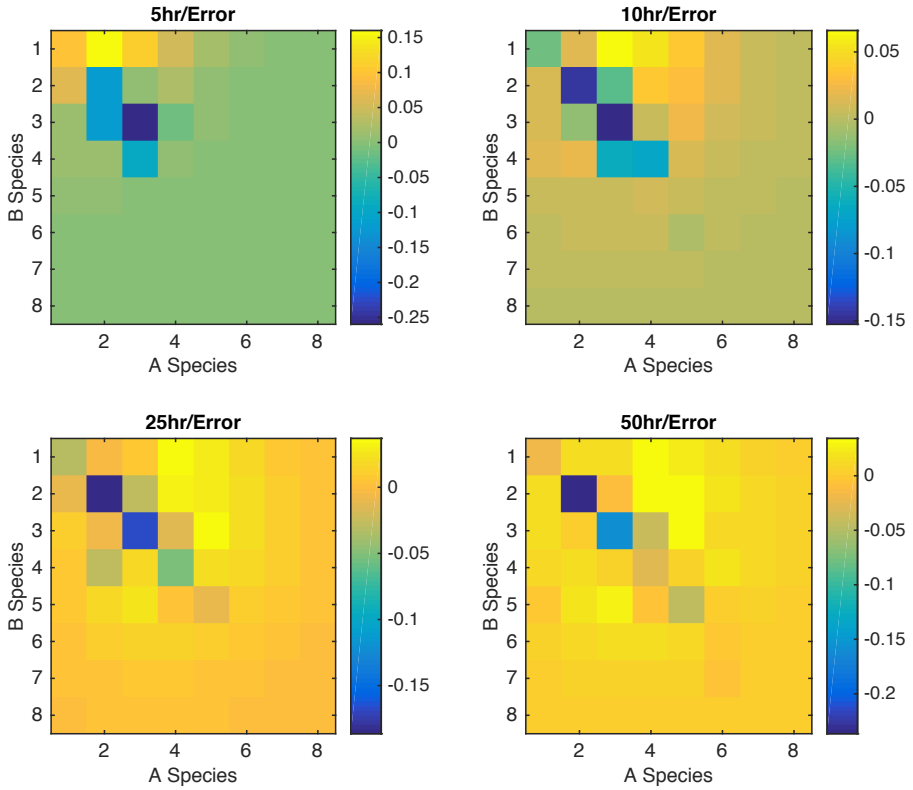

Figure 2-5: Error in between experimental data and fitted model for fraction of Species C at different times for length dependent joining and distinct nucleation rates: X and Y axises represent the lengths of A part and B part respectively. Note: the sidebars represent different scales.

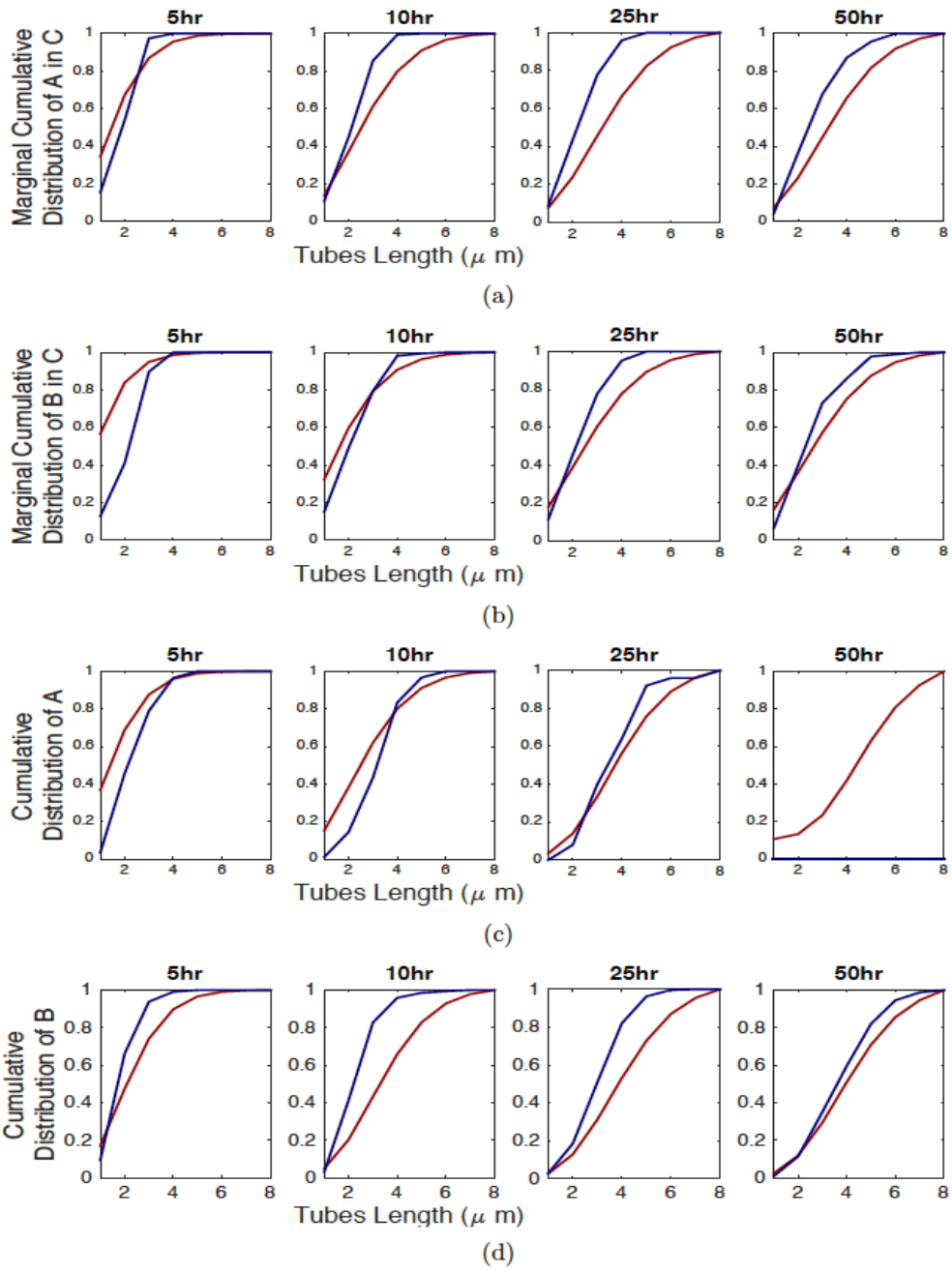

Figure 2-6: Comparing experimental results with simulated predictions for length dependent joining and distinct nucleation rates. (a) A comparison of experimental and simulation results between marginal cumulative distribution of A part in Species C, (b)Experimental and simulated marginal cumulative distributions of B part in Species C,(c)Experimental and simulated marginal cumulative distributions of Species A (all A-type nanotubes are depleted at 50 hours, (d)Experimental and simulated marginal cumulative distributions of Species B.

Length-dependent joining rate: Identical nucleation rates for A and B-type nanotubes

In this simulation, we assumed equal nucleation rates for Species A and B and the Kjoin was calculated using Bernie's formula. The parameters are stated in Table2.

Table 2-2 **Fitting parameters and results.** This table lists the parameters of Model that were fitted in Simulation 2, including lower bound (L.B.) and upper bounds (U.B.) used in the fitting procedure.

Parameter	Units	L.B.	U.B.	Sim2	Definition
k_p	$M^{-1}s^{-1}$	10^{-5}	10^{1}	1.412×10^{-3}	Tube polymerization rate
k_d	s^{-1}	10^{-8}	10^{4}	1.000×10^{-6}	Tube depolymerization rate
α	$\mu m\ M^{-1}s^{-1}$	10^{-10}	10^{5}	1.584×10^{-5}	End-joining parameter
k_{nucl}	$M^{1-n_{nucl}}s^{-1}$	10^{-10}	10^{4}	1.122×10^{-7}	Nucleation rate of species A
k_{nucl}	$M^{1-n_{nucl}}s^{-1}$	10^{-10}	10^{4}	1.122×10^{-7}	Nucleation rate of species B

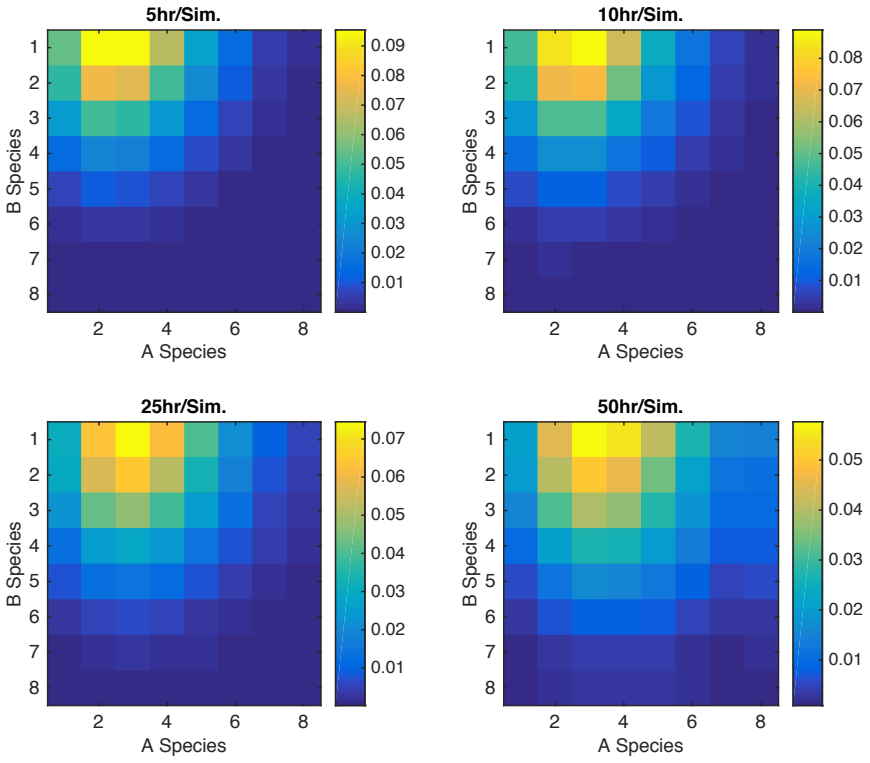

Figure 2-7: Simulated fraction of Species C at different times for length dependent joining and identical nucleation rates. X and Y axis represent the lengths of A part and B part respectively. Note: the sidebars represent different scales.

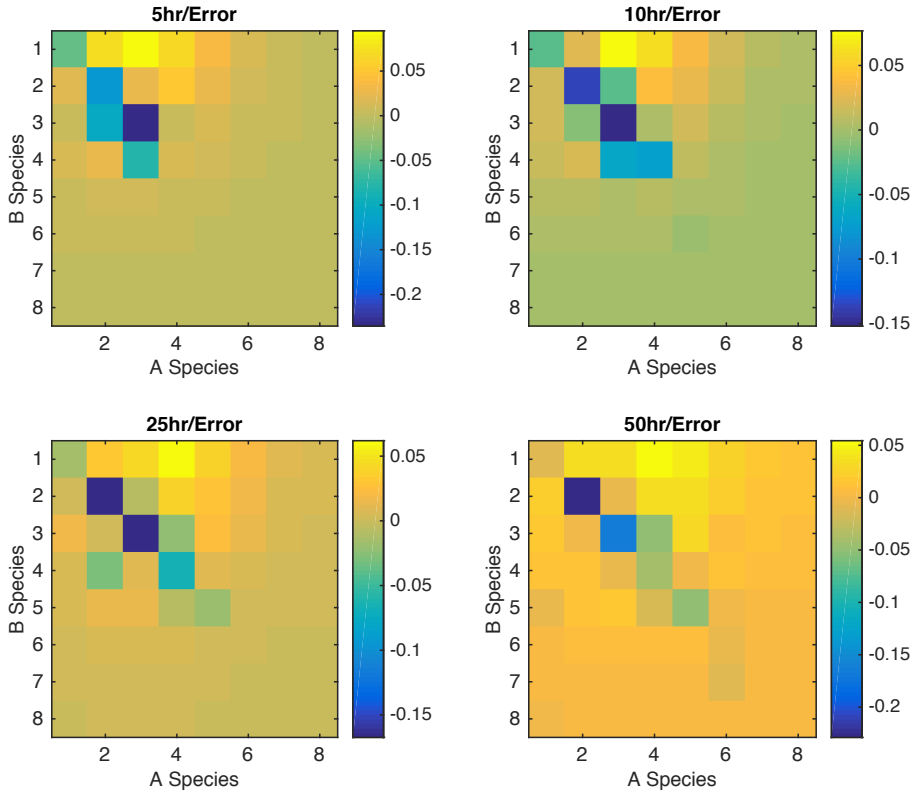

Figure 2-8: Error in between experimental data and fitted model for fraction of Species C at different times for length dependent joining and identical nucleation rates. X and Y axises represent the lengths of A part and B part respectively. Note: the sidebars represent different scales.

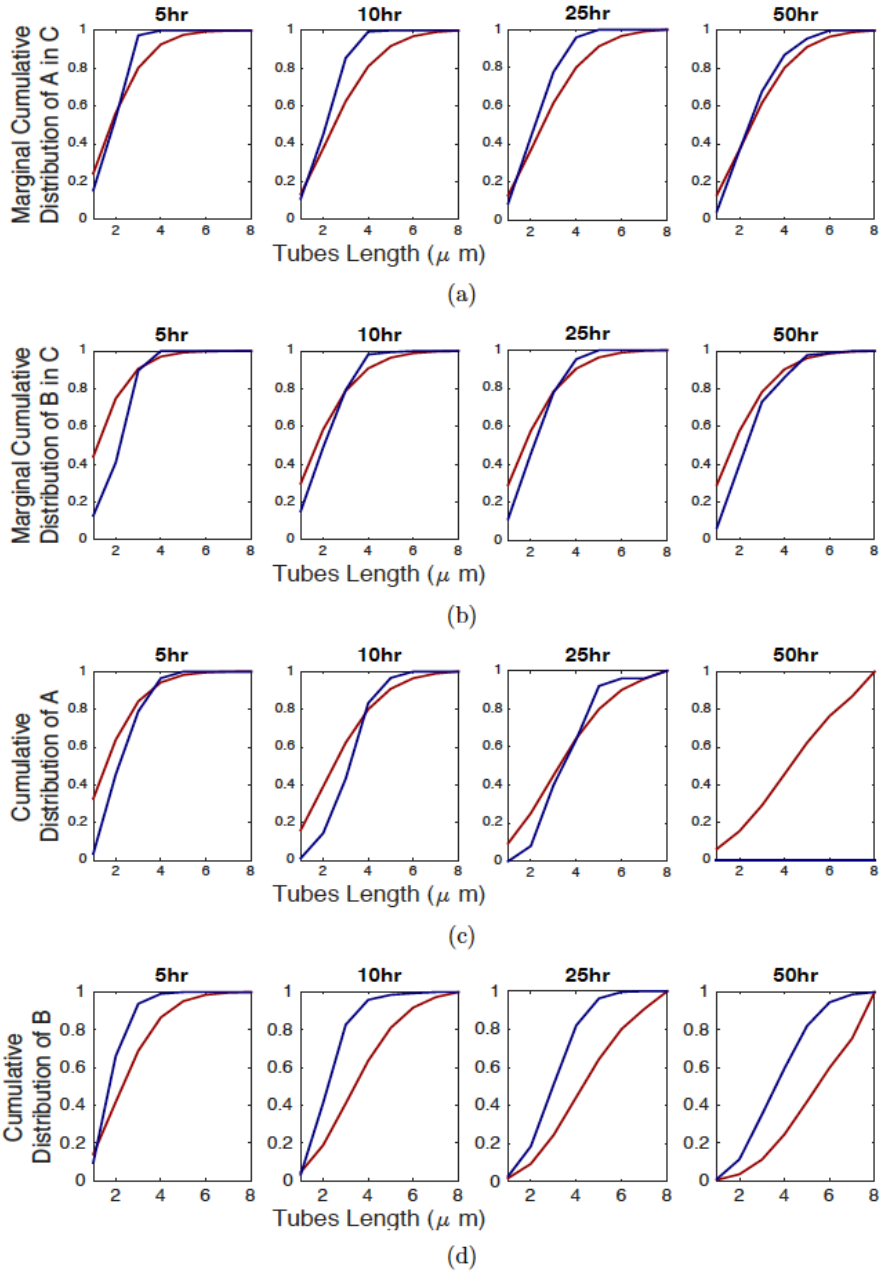

Figure 2-9: Comparing experimental results with simulated predictions for length dependent joining and identical nucleation rates. (a) A comparison of experimental and simulation results between marginal cumulative distribution of A part in Species C, (b)Experimental and simulated marginal cumulative distributions of B part in Species C,(c)Experimental and simulated marginal cumulative distributions of Species A (all A-type nanotubes are depleted at 50 hours, (d)Experimental and simulated marginal cumulative distributions of Species B.

Length-independent joining rate: Distinct nucleation rates for A and B-type nanotubes

In this simulation, we assumed equal nucleation rates for Species A and B and the Kjoin was also assumed to be constant. The parameters are stated in Table3.

Table 2-3 **Fitting parameters and results.** This table lists the parameters of Model that were fitted in Simulation 3, including lower bound (L.B.) and upper bounds (U.B.) used in the fitting procedure.

Parameter	Units	L.B.	U.B.	Sim3	Definition
k_p	$M^{-1}s^{-1}$	10^{-5}	10^{1}	1.258×10^{-4}	Tube polymerization rate
k_d	s^{-1}	10^{-8}	10^{4}	1.318×10^{-5}	Tube depolymerization rate
α	$\mu m\ M^{-1}s^{-1}$	10^{-10}	10^{5}	1.698×10^{-8}	End-joining parameter
k_{nucl}	$M^{1-n_{nucl}}s^{-1}$	10^{-10}	10^{4}	4.466×10^{-9}	Nucleation rate of species A
k_{nucl}	$M^{1-n_{nucl}}s^{-1}$	10^{-10}	10^{4}	4.466×10^{-9}	Nucleation rate of species B

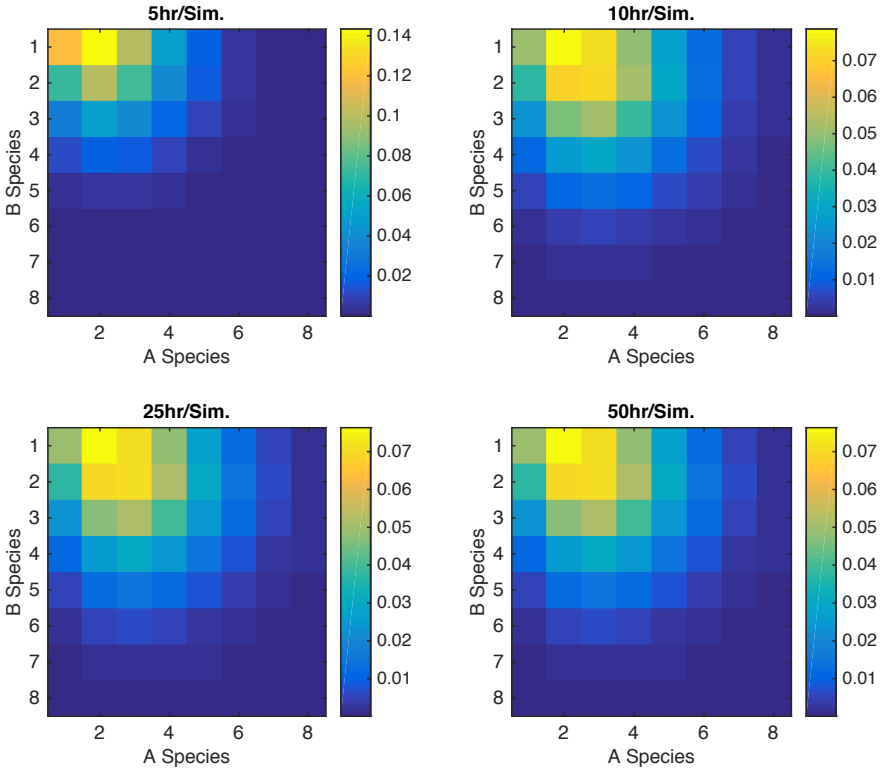

Figure 2-10: Simulated fraction of Species C at different times for length independent joining and distinct nucleation rates. X and Y axis represent the lengths of A part and B part respectively. Note: the sidebars represent different scales.

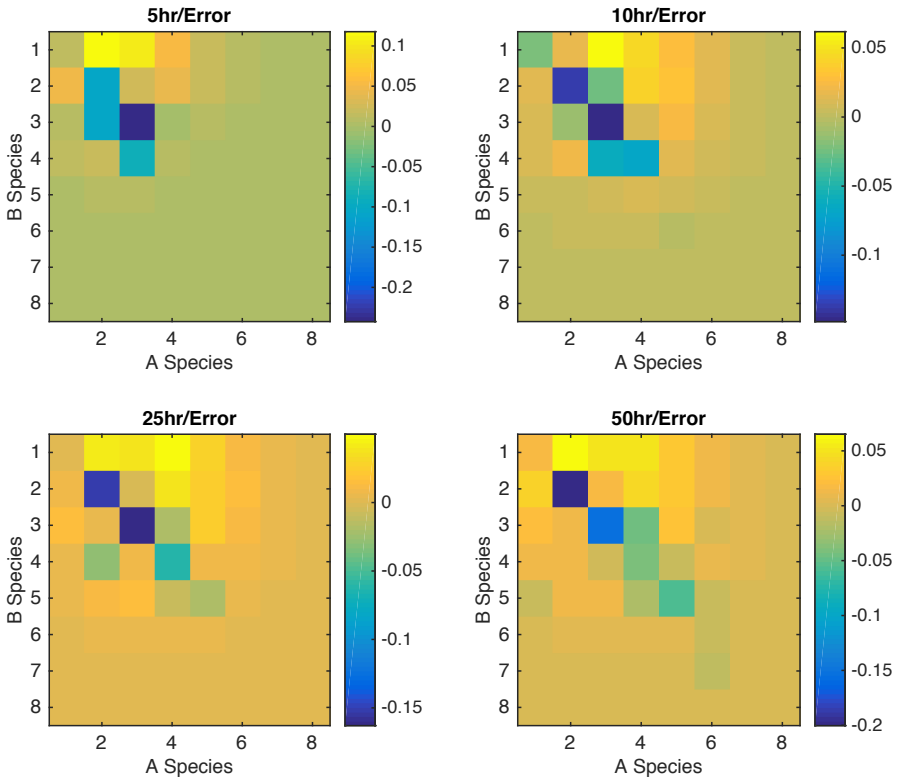

Figure 2-11: Error in between experimental data and fitted model for fraction of Species C at different times for length independent joining and distinct nucleation rates. X and Y axis represent the lengths of A part and B part respectively. Note: the sidebars represent different scales.

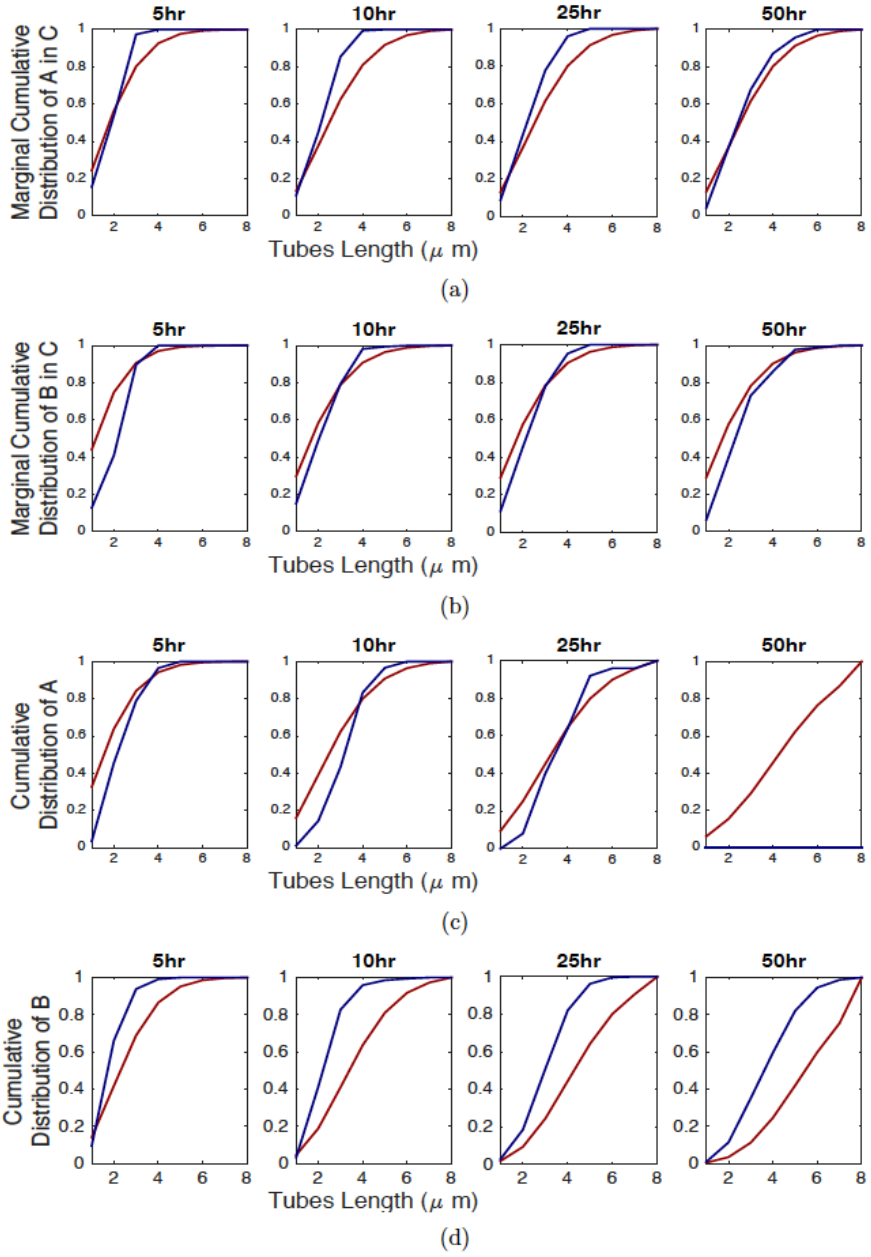

Figure 2-12: Comparing experimental results with simulated predictions for length independent joining and distinct nucleation rates. (a) A comparison of experimental and simulation results between marginal cumulative distribution of A part in Species C, (b)Experimental and simulated marginal cumulative distributions of B part in Species C,(c)Experimental and simulated marginal cumulative distributions of Species A (all A-type nanotubes are depleted at 50 hours, (d)Experimental and simulated marginal cumulative distributions of Species B.

Length-independent joining rate: Identical nucleation rates for A and B-type nanotubes

In this simulation, we assumed un-equal nucleation rates for Species A and B but the Kjoin was assumed to be constant. The parameters are stated in Table 2.4.

Table 2-4: **Fitting parameters and results.** This table lists the parameters of Model that were fitted in Simulation 4, including lower bound (L.B.) and upper bounds (U.B.) used in the fitting procedure.

Parameter	Units	L.B.	U.B.	Sim4	Definition
k_p	$M^{-1}s^{-1}$	10^{-5}	10^{1}	1.230×10^{-4}	Tube polymerization rate
k_d	s^{-1}	10^{-8}	10^{4}	1.288×10^{-5}	Tube depolymerization rate
α	$\mu m\ M^{-1}s^{-1}$	10^{-10}	10^{5}	6.761×10^{-8}	End-joining parameter
k_{nucl}	$M^{1-n_{nucl}}s^{-1}$	10^{-10}	10^{4}	3.890×10^{-9}	Nucleation rate of species A
k_{nucl}	$M^{1-n_{nucl}}s^{-1}$	10^{-10}	10^{4}	1.000×10^{-1}	Nucleation rate of species B

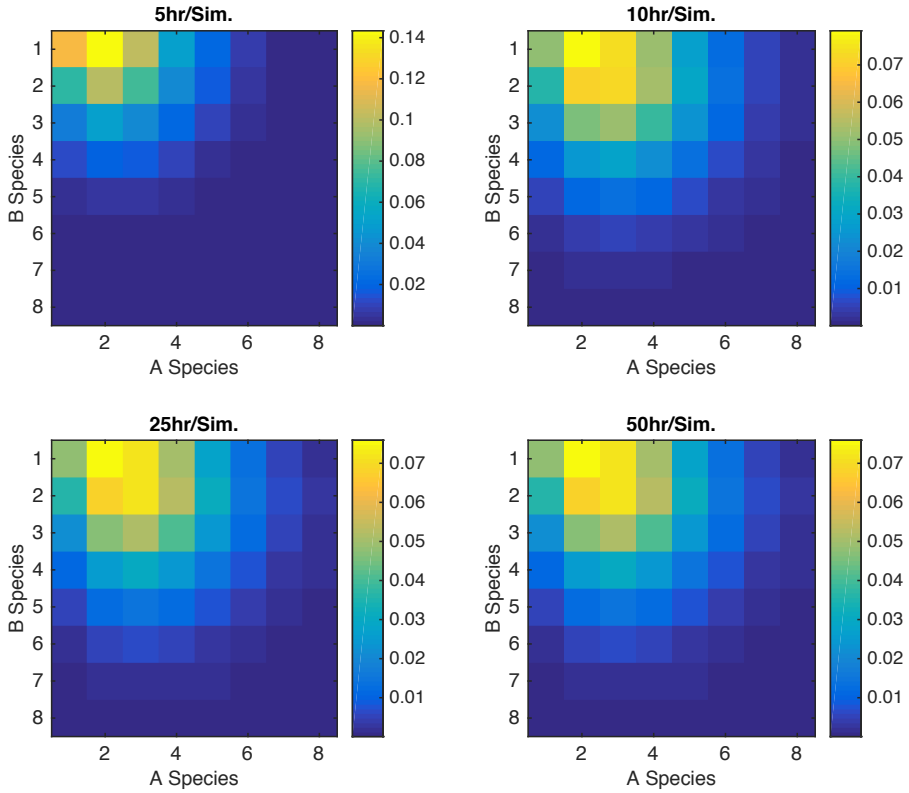

Figure 2-13: Simulated fraction of Species C at different times for length independent joining and identical nucleation rates. X and Y axises represent the lengths of A part and B part respectively. Note: the sidebars represent different scales.

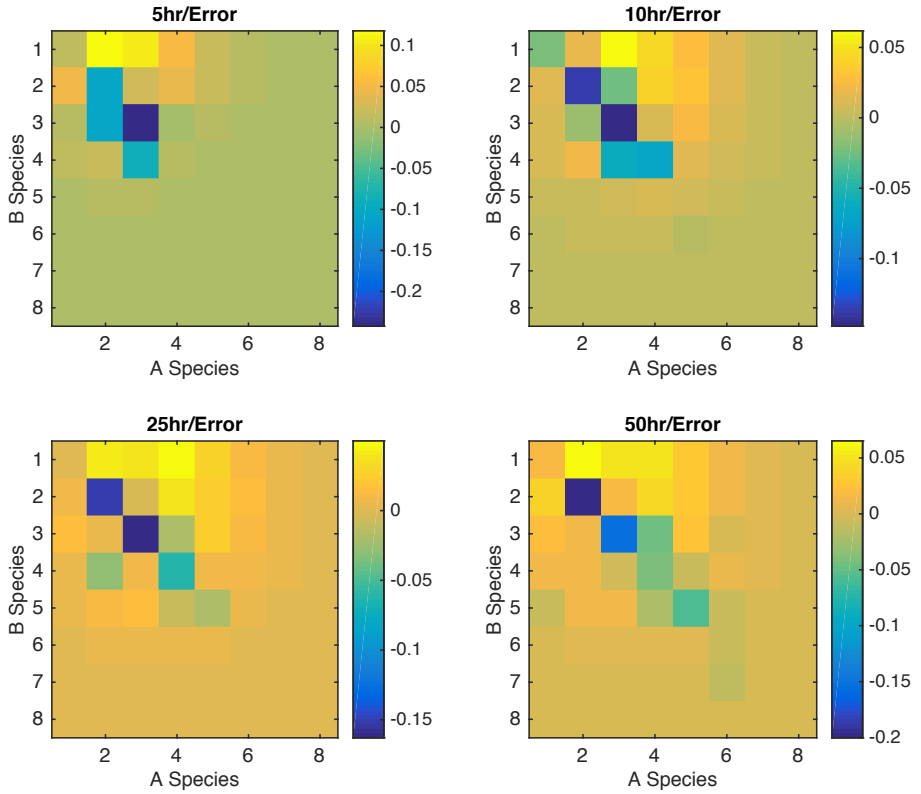

Figure 2-14: Error in between experimental data and fitted model for fraction of Species C at different times for length independent joining and identical nucleation rates. X and Y axises represent the lengths of A part and B part respectively. Note: the sidebars represent different scales.

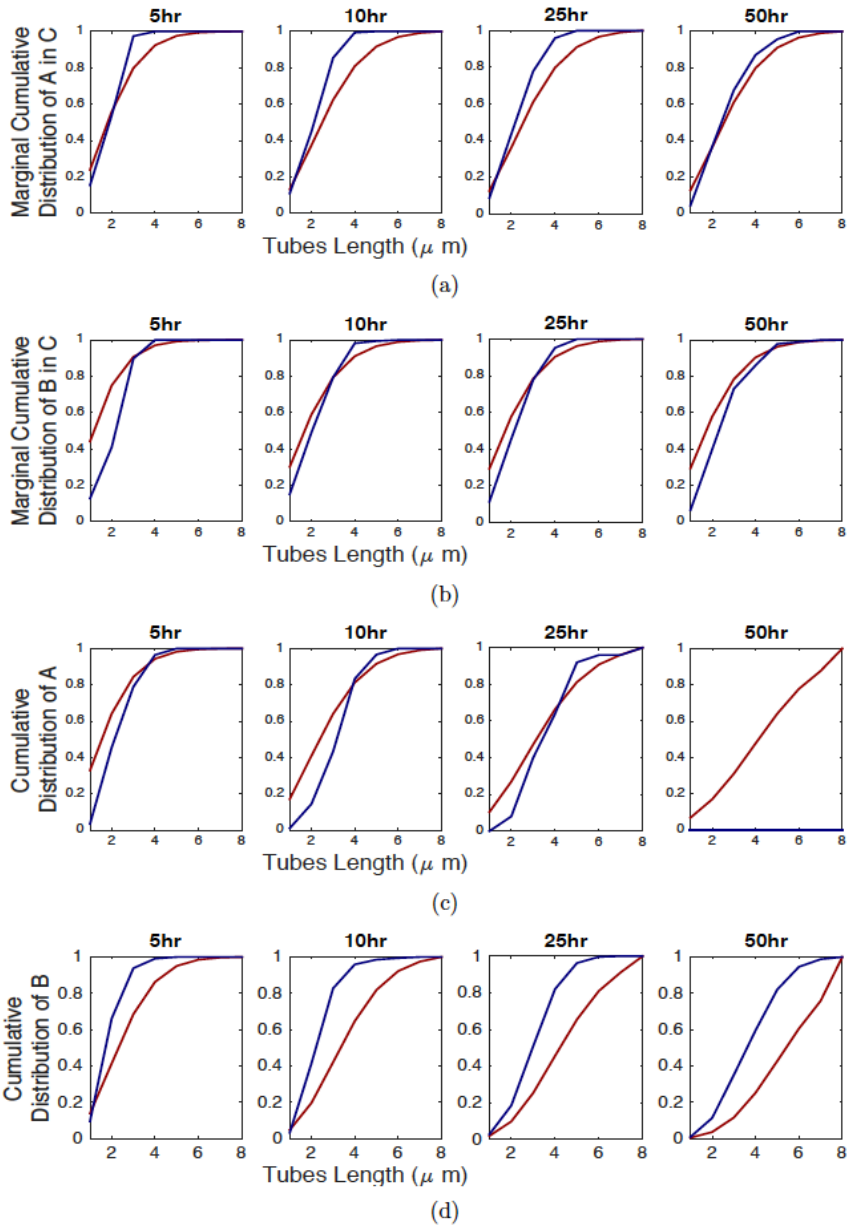

Figure 2-15: Comparing experimental results with simulated predictions for length independent joining and identical nucleation rates. (a) A comparison of experimental and simulation results between marginal cumulative distribution of A part in Species C, (b)Experimental and simulated marginal cumulative distributions of B part in Species C,(c)Experimental and simulated marginal cumulative distributions of Species A (all A-type nanotubes are depleted at 50 hours, (d)Experimental and simulated marginal cumulative distributions of Species B.

2.9 Methods

Nanotube joining experiments

DNA nanotube and seed assembly mixtures. We grew seeded DNA nanotubes following the protocol outlined by Mohammed.[1] Tile, adapter, and seed strand sequences used in this study are listed in Supplementary Information (section 2.12). DNA tile, adapter, and staple strands were synthesized by Integrated DNA Technologies, Inc. Adapter and tile strands were PAGE purified. “A” seeds were labelled using 50% atto488 fluorescent dye and 50% atto647 fluorescent dye allowing fluorescence imaging of the seed. To distinguish “B” seeds from “A” seeds, “B” seeds were labelled using 100% atto488 fluorescent dye. DNA nanotubes nucleated from “A” seeds were labelled with cy3 dye and nanotubes nucleated from “B” seeds were labelled with atto647. All samples were prepared in TAE buffer (40 mM tris-acetate, 1 mM EDTA) to which 12.5 mM magnesium acetate was added. In the initial A solution, the strands for each tile were present at 55 nM except for the strands presenting sticky ends, which were present at 110 nM to minimize the concentration of malformed tiles. In the initial B solution, the strands for each tile were present at 175 nM (sticky end strands at 350 nM.)

Nanotube annealing. Samples were annealed using an Eppendorf Mastercycler in a two-pot reaction. In one pot, DNA tiles were annealed from 90°C to 20°C at 1°C per min. In a second pot, DNA origami seeds were annealed using the protocol described by Agrawal et al. After annealing, the seeds were purified using centrifugal filtration to remove excess staples and adapters not incorporated into seeds purified seeds were then added to the annealed tiles at a concentration of approximately 6 pM and incubated at 20 °C for 15 hours. “A” solution and “B” solution samples were prepared separately during this process. Note that because the concentration of DNA origami seeds is the same in both the A and B solutions (6 pM), the

concentration of seeded nanotubes is approximately the same in both solutions, despite both solutions having differing concentrations of DNA tiles. The higher concentration of atto647 labelled B tiles vs. cy3 labelled A tiles (175 nM vs. 55 nM) is necessary because the critical concentrations needed for seeded nucleation are different for each tile type. After separately incubating the A and B solutions for 15 hours, the solutions were combined in a 1:5 A:B ratio and incubation was continued at 20 °C. We measured nanotube joining rates at 20 °C.

Fluorescence microscopy. After combining the A and B solutions, fluorescence microscopy images were taken at 0.5 h, 2.5 h, and 4.5 h post mixing. 6 μL of the combined A/B solution was transferred to an 18 mm by 18 mm glass coverslip for fluorescence imaging. The samples were imaged on an inverted microscope (Olympus IX71) using a 60×/1.45 NA oil immersion objective using an Olympus cy3 filter cube set (Z532BP). Images were captured on a cooled CCD camera (iXon3, Andor).

Nanotube image processing. Fluorescence microscopy images of nanotubes were processed using ImageJ. Nanotube lengths were calculated by drawing a line next to the nanotube and calculating the length of the line.

2.10 Conclusion

DNA nanotubes provide an ideal model system for the measurement of polymer end-to-end joining rates. However, it is unclear how well our results translate to joining processes that do not occur because of Watson–Crick hybridization. In this study, we experimentally characterized the length-dependence of the end-to-end joining rate of DNA nanotubes by measuring the lengths of nanotubes before and after joining at different times during the joining process. We tested the ability of the Hariadi model[2] for end-to-end joining rate to reproduce the

experimental length data using an ODE model of nanotube joining. We tested it in conditions where joining is dependent or independent of lengths of two species with distinct nucleation rates and same nucleation rates. The length-independent joining that we observe in this study disagrees with prior results on microtubules,[5] amyloid fibrils,[6] and actin filaments,[7] all of which obey the length-dependent model prescribed by Hill. Our length-independent joining rates suggest that translational and rotational diffusion of DNA nanotubes is not the rate-limiting step in end-to-end joining.

Better understanding of what controls these rates will be critical for the kinetic control of DNA self-assembly. We need to determine what factors affect and do not affect the rates of DNA nanostructure binding. There is evidence that multi-valency (the existence of multiple single-stranded binding sites that can hybridize on each of the reactions),[8] temperature[9] and salt composition[10] affect the rates of reaction. However, one potential advantage of the similarity of DNA nanostructure hybridization rates across such a wide range of reactant size scales is that we can reasonably assume a single rate of interaction between many different DNA nanostructures. In combination with the ability to predict the free-energy of association,[10] this fact should allow us to design relatively accurate models of the kinetics of DNA self-assembly processes without the need to measure the thermodynamics and kinetics of association for each potential component or intermediate.

2.11 References

1 Mohammed, A.M., Schulman, R.: Directing self-assembly of dna nanotubes using programmable seeds. Nano letters **13**(9) (2013) 4006–4013

2 Hariadi, R.F., Winfree, E., Yurke, B.: Determining hydrodynamic forces in bursting bubbles using dna nanotube mechanics. Proceedings of the National Academy of Sciences **112**(45) (2015) E6086–E6095

3 Rothemund, P.W., Ekani-Nkodo, A., Papadakis, N., Kumar, A., Fygenson, D.K., Winfree, E.: Design and characterization of programmable dna nanotubes. Journal of the American Chemical Society **126**(50) (2004) 16344–16352

4 Mardanlou, V., Green, L.N., Subramanian, H.K., Hariadi, R.F., Kim, J., Franco, E.: A coarse-grained model of dna nanotube population growth. In: International Conference on DNA-Based Computers, Springer (2016) 135–147

5 M. Bachand, N. F. Bouxsein, S. Cheng, S. J. von Hoyningen-Huene, M. J. Stevens and G. D. Bachand, Directed self-assembly of 1D microtubule nano-arrays, RSC Adv., 2014, 4(97), 54641–54649

6 J. D. Harper, S. S. Wong, C. M. Lieber and P. T. Lansbury, , Jr., Assembly of A beta amyloid protofibrils: an in vitro model for a possible early event in Alzheimer's disease, Biochemistry, 1999, 38(28), 8972–8980

7 A. Teubner and A. Wegner, The rate of annealing of actin tropomyosin filaments depends strongly on the length of the filaments, Biochim. Biophys. Acta, Protein Struct. Mol. Enzymol., 1996, 1297(2), 214–218

8 J. Nangreave, H. Yan and Y. Liu, Studies of thermal stability of multivalent DNA hybridization in a nanostructured system, Biophys. J., 2009, 97(2), 563–571

9 L. E. Morrison and L. M. Stols, Sensitive fluorescence-based thermodynamic and kinetic measurements of DNA hybridization in solution, Biochemistry, 1993, 32(12), 3095–3104

10 J. SantaLucia Jr. and D. Hicks, The thermodynamics of DNA structural motifs, Annu. Rev. Biophys. Biomol. Struct., 2004, 33, 415–440

2.12 Supplementary Information

DNA nanotube and seed design sequences

REd tile sequences:

RE-4bp-1: CGTATTGGACATTTCCGTAGACCGACTGGACATCTTCG

RE-4bp-2EE01: TGGTCCTTCACACCAATACGGCAT

RE-4bp-3Cy3:/Cy3/TCTACGGAAATGTGGCAGAATCAATCATAAGACACCAGTCGG

RE-4bp-4:CAGACGAAGATGTGGTAGTGGAATGC

RE-4bp-5:TCCACTACCTGTCTTATGATTGATTCTGCCTGTGAAGG

SEd tile sequences:

SE-4bp-1: CTCAGTGGACAGCCGTTCTGGAGCGTTGGACGAAACTC

SE-4bp-2DIAG:TCTGGTAGAGCACCACTGAGAGGT

SE-4bp-3Cy3: /Cy3/CCAGAACGGCTGTGGCTAAACAGTAACCGAAGCACCAACGCT

SE-4bp-4DIAG:ACCAGAGTTTCGTGGTCATCGTACCT

SE-4bp-5:ACGATGACCTGCTTCGGTTACTGTTTAGCCTGCTCTAC

Here /Cy3/ denotes a covalently attached Cy3 fluorophore.

Seed staple sequences:

T_5R12F_CYC_HP:
GGAATTACCACCACCCGTGAGGCGTTTTCGCCTCACTTTCATTTTCCGTAACAC

T_5R12E_CYC_HP:
CTCAGAGCGAGGCATAGGCTCCGCTTTTGCGGAGCCTTGTAAGAGCACAGGTAG

T_3R12F_CYC_HP:
CATAACCCACCGCCACCTGGCTCGTTTTCGAGCCAGTTCCTCAGAAACAACGCC

T_3R12E_CYC_HP:
CCCTCAGATCGTTTACCGCTTGCGTTTTCGCAAGCGTTCAGACGACTTAATAAA

T_1R12F_CYC_HP:
CCAAAATATACTCAGGTGCGGTCGTTTTCGACCGCATTAGGTTTAGATAGTTAG

T_1R12E_CYC_HP:
TATCACCGGCGAGAGGCTGCGTCGTTTTCGACGCAGTTCTTTTGCAATCCTGAA

T1R12F_CYC_HP:
TCTTACCATATAAGTACCGAGGCGTTTTCGCCTCGGTTTAGCCCGGAATAGGTG

T1R12E_CYC_HP:
AGGGTTGAACGCTAACGCCAGGACTTTTGTCCTGGCTTGAGCGTCTGAACACCC

T3R12F_CYC_HP:
CCTAATTTACCAGGCGTCGGAGCGTTTTCGCTCCGATTGATAAGTGGGGGTCAG

T3R12E_CYC_HP:
TGCTCAGTGCCAGTTAGGTGGTCGTTTTCGACCACCTTCAAAATAAACAGGGAA

T5R12F_CYC_HP:
ATTATTTAGAAGGATTGCCATCGCTTTTGCGATGGCTTAGGATTAGAAACAGTT

T5R12E_CYC_HP:
CCTCAAGATCCCAATCCGTGGAGCTTTTGCTCCACGTTCAAATAAGATAGCAGC

T_5R2F_HP:
TGAGTTTCAAAGGAACGTCCACCGTTTTCGGTGGACTTAACTAAAGATCTCCAA

T_5R4F_HP:
AAAAAAGGCTTTTGCGGTGGTCCGTTTTCGGACCACTTGGATCGTCGGGTAGCA

T_5R6F_HP:
ACGGCTACAAGTACAACTCGGCACTTTTGTGCCGAGTTCGGAGATTCGCGACCT

T_5R8F_HP:
GCTCCATGACGTAACACGGATCGCTTTTGCGATCCGTTAAGCTGCTACACCAGA

T_5R10F_HP:
ACGAGTAGATCAGTTGCACCGCTGTTTTCAGCGGTGTTAGATTTAGCGCCAAAA

T_5R2E_HP:
GAGAATAGGTCACCAGCGGAACCGTTTTCGGTTCCGTTTACAAACTCCGCCACC

T_5R4E_HP:
AAAGGCCGCTCCAAAACCGTGGCGTTTTCGCCACGGTTGGAGCCTTAGCGGAGT

T_5R6E_HP:
GCGAAACAAGAGGCTTGTGCTGCGTTTTCGCAGCACTTTGAGGACTAGGGAGTT

T_5R8E_HP:
CCAAATCATTACTTAGACGCTGGCTTTTGCCAGCGTTTCCGGAACGTACCAAGC

T_5R10E_HP:
AAAGATTCTAAATTGGCGACGGACTTTTGTCCGTCGTTGCTTGAGATTCATTAC

T_3R2F_HP:
TGTAGCATAACTTTCAGGCATCCGTTTTCGGATGCCTTACAGTTTCTAATTGTA

T_3R4F_HP:
TCGGTTTAGGTCGCTGGCTGACGCTTTTGCGTCAGCTTAGGCTTGCAAAGACTT

T_3R6F_HP:
TTTCATGATGACCCCCACCAGCCGTTTTCGGCTGGTTTAGCGATTAAGGCGCAG

T_3R8F_HP:
ACGGTCAATGACAAGACGGAGGCGTTTTCGCCTCCGTTACCGGATATGGTTTAA

T_3R10F_HP:
TTTCAACTACGGAACACTCGCTGCTTTTGCAGCGAGTTACATTATTAACACTAT

T_3R2E_HP:
TGCTAAACTCCACAGAGCCAGTGCTTTTGCACTGGCTTCAGCCCTCTACCGCCA

T_3R4E_HP:
ATATATTCTCAGCTTGCCGTCCGCTTTTGCGGACGGTTCTTTCGAGTGGGATTT

T_3R6E_HP:
CTCATCTTGGAAGTTTCGGATGGCTTTTGCCATCCGTTCCATTAAACATAACCG

T_3R8E_HP:
AGTAATCTTCATAAGGTCTGGTCGTTTTCGACCAGATTGAACCGAACTAAAACA

T_3R10E_HP:
ACGAACTATTAATCATGGCACCTGTTTTCAGGTGCCTTTGTGAATTTCATCAAG

T_1R2F_HP:
CGTAACGAAAATGAATCCTGCCTGTTTTCAGGCAGGTTTTTCTGTAGTGAATTT

T_1R4F_HP:
CTTAAACAACAACCATCGGTGCCGTTTTCGGCACCGTTCGCCCACGCGGGTAAA

T_1R6F_HP:
ATACGTAAGAGGCAAACTCGGTCGTTTTCGACCGAGTTAGAATACACTGACCAA

T_1R8F_HP:
CTTTGAAAATAGGCTGCCGAGGACTTTTGTCCTCGGTTGCTGACCTACCTTATG

T_1R10F_HP:
CGATTTTAGGAAGAAACGGCAGGCTTTTGCCTGCCGTTAATCTACGGATAAAAA

T_1R2E_HP:
ACGTTAGTTCTAAAGTCGCTTGGCTTTTGCCAAGCGTTTTTGTCGTGATACAGG

T_1R4E_HP:
CAATGACAGCTTGATATGGCGAGCTTTTGCTCGCCATTCCGATAGTCTCCCTCA

T_1R6E_HP:
AAACGAAATGCCACTACCACCTCGTTTTCGAGGTGGTTCGAAGGCAGCCAGCAA

T_1R8E_HP:
CCAGGCGCGAGGACAGCTCTGGACTTTTGTCCAGAGTTATGAACGGGTAGAAAA

T_1R10E_HP:
GGACGTTGAGAACTGGCGAGGCACTTTTGTGCCTCGTTCTCATTATGCGCTAAT

T1R2F_HP:
AGTGTACTATACATGGCTCCTGCGTTTTCGCAGGAGTTCTTTTGATCTTTCCAG

T1R4F_HP:
GAGCCGCCCCACCACCGTCAGGCGTTTTCGCCTGACTTGGAACCGCTGCGCCGA

T1R6F_HP:
AATCACCACCATTTGGCGTCCTGCTTTTGCAGGACGTTGAATTAGACCAACCTA

T1R8F_HP:
TACATACACAGTATGTCGGACCTGTTTTCAGGTCCGTTTAGCAAACTGTACAGA

T1R10F_HP:
ATCAGAGAGTCAGAGGCGAGGTCGTTTTCGACCTCGTTGTAATTGAACCAGTCA

T1R2E_HP:
TAAGCGTCGGTAATAACAGGAGCGTTTTCGCTCCTGTTGTTTTAACCCGTCGAG

T1R4E_HP:
AACCAGAGACCCTCAGGCAGTCGCTTTTGCGACTGCTTAACCGCCACGTTCCAG

T1R6E_HP:
GACTTGAGGTAGCACCGTCTGGCGTTTTCGCCAGACTTATTACCATATCACCGG

T1R8E_HP:
TTATTACGTAAAGGTGTGGCTGCGTTTTCGCAGCCATTGCAACATACCGTCACC

T1R10E_HP:
TGAACAAAGATAACCCAGTGCCTGTTTTCAGGCACTTTACAAGAATAAGACTCC

T3R2F_HP:
TGCCTTGACAGTCTCTGTCGGTGCTTTTGCACCGACTTGAATTTACCCCTCAGA

T3R4F_HP:
GCCACCACTCTTTTCACGGTCGGCTTTTGCCGACCGTTTAATCAAATAGCAAGG

T3R6F_HP:
CCGGAAACTAAAGGTGGACCTGGCTTTTGCCAGGTCTTAATTATCATAAAAGAA

T3R8F_HP:
ACGCAAAGAAGAACTGTCGGCTCGTTTTCGAGCCGATTGCATGATTTGAGTTAA

T3R10F_HP:
GCCCAATAGACGGGAGCACAGGCGTTTTCGCCTGTGTTAATTAACTTTCCAGAG

T3R2E_HP:
GGAAAGCGGTAACAGTGTGGCAGCTTTTGCTGCCACTTGCCCGTATCGGGGTTT

T3R4E_HP:
GTTTGCCACCTCAGAGACCAGGCGTTTTCGCCTGGTTTCCGCCACCGCCAGAAT

T3R6E_HP:
TTATTCATGTCACCAAGCTCGCTGTTTTCAGCGAGCTTTGAAACCATTATTAGC

T3R8E_HP:
ATACCCAAACACCACGCCTACCGCTTTTGCGGTAGGTTGAATAAGTGACGGAAA

T3R10E_HP:
GCGCATTAATAAGAGCCTGGACGCTTTTGCGTCCAGTTAAGAAACAATAACGGA

T5R2F_HP:
AATGCCCCATAAATCCGCTCGGACTTTTGTCCGAGCTTTCATTAAAAGAACCAC

T5R4F_HP:
CACCAGAGTTCGGTCAGCCGAGCGTTTTCGCTCGGCTTTAGCCCCCTCGATAGC

T5R6F_HP:
AGCACCGTAGGGAAGGTCGGAGGCTTTTGCCTCCGATTTAAATATTTTATTTTG

T5R8F_HP:
TCACAATCCCGAGGAACTGGTGGCTTTTGCCACCAGTTACGCAATAATGAAATA

T5R10F_HP:
GCAATAGCAGAGAATACCGCAGGCTTTTGCCTGCGGTTACATAAAAACAGCCAT

T5R2E_HP:
ACAAACAACTGCCTATCACGACGCTTTTGCGTCGTGTTTTCGGAACCTGAGACT

T5R4E_HP:
TCGGCATTCCGCCGCCGTCGCTGCTTTTGCAGCGACTTAGCATTGATGATATTC

T5R6E_HP:
ATTGAGGGAATCAGTACGGAGCACTTTTGTGCTCCGTTGCGACAGACGTTTTCA

T5R8E_HP:
GAAGGAAAAATAGAAAGCCTAGCGTTTTCGCTAGGCTTATTCATATTTCAACCG

T5R10E_HP:
CTTTACAGTATCTTACCGCTCGTGTTTTCACGAGCGTTCGAAGCCCAGTTACCA

A-seed adapter sequences

A-4bp-1REd_1: CAGCCAAGACGCAGGTAGCGAGACAGAGCTGAAAGTATTAAGAGG

A-4bp-1_2REd_3: TCGCTACCTGCGTTCGTCGGATGGTGAGGTCCACGCTCTGTC

A-4bp-1_2REd_5:CTATTATTCTGAAACAGTGGACCTCACCATCCGACGACACGAGCA

A-4bp-2REd_2: TGGTTGCTCGTGCTTGGCTGGCAT

A-4bp-3SEd_1: CACGGAGTCGAAGCGTAGGACGGTAGCCAGTCAGACGATTGGCCT

A-4bp-3_4SEd_3: GTCCTACGCTTCGGACCTTGGTGATGCTGGACTGTGGCTACC

A-4bp-4SEd_5: CAGGAGGTTGAGGCAGCAGTCCAGCATCACCAAGGTCGCTCGGCA

A-4bp-3_4SEd_2: TCTGTGCCGAGCACTCCGTGAGGT

A-4bp-5REd_1: CAGAGCCACGGCATGGTCTTGCGTTGGAGGCGTCAGACTGTAGCG

A-4bp-5_6REd_3: CAAGACCATGCCGACCTCATCCTCGCTTTCGGTGCTCCAACG

A-4bp-6REd_5: ATCAAGTTTGCCTTTACACCGAAAGCGAGGATGAGGTGCGGACGA

A-4bp-5_6REd_2: TGGTTGCTCGTGCTTGGCTGGCAT

A-4bp-7SEd_1: CACGGAGTCTACGGCAGTGACCGATCTCCAGACAAAAGGGCGACA

A-4bp-7_8SEd_3: GTCACTGCCGTAGCTCACGAGGCACAACCACAGCGGAGATCG

A-4bp-8SEd_5: GGTTTACCAGCGCCAAGCTGTGGTTGTGCCTCGTGAGGCTCGGCA

A-4bp-7_8SEd_2: TCTGTGCCGAGCACTCCGTGAGGT

A-4bp-9REd_1: CAACCGTCGTTCCACAGGACTCGCACTTCGCAGATAGCCGAACAA

A-4bp-9_10REd_3: AGTCCTGTGGAACACCACGAGACGCCATCGAGCGGAAGTGCG

A-4bp-10SRd_5: TTTTTAAGAAAAGTAACGCTCGATGGCGTCTCGTGGTAAGCCTGA

A-4bp-9_10SRd_2: TGGTTGCTCGTGCTTGGCTGGCAT

A-4bp-11SEd_1: CACGGAGTCAAGGCTACGAGTCAGACAGGAACGTCAAAAATGAAA

A-4bp-11_12SEd_3: ACTCGTAGCCTTGGACCGCACTCACCACTGCTCGCCTGTCTG

A-4bp-12SEd_5: AAACGATTTTTTGTTTCGAGCAGTGGTGAGTGCGGTCGCTCGGCA

A-4bp-11_12SEd_2: TCTGTGCCGAGCACTCCGTGAGGT

B-seed adapter sequences

B-4bp-1REd_1:
AGGGATAGCAAGCCCACAACGTGAGGACACTTGGAGGCTGCACTCG

B-4bp-1_2REd_3: TGTCCTCACGTTGCTGGATGCCGATCCTACGACACCTCCAAG

B-4bp-2REd_5: TCGCTGACTTGTCGTAGGATCGGCATCCAGATAGGAACCCATGTAC

B-4bp-1_2REd_4: CAGACGAGTGCAGAGTCAGCGAATGC

B-4bp-3SEd_1: GAATTGCGAATAATAAGTGACCTTGCTGTACCGTCGAGATGGAGTC

B-4bp-3_4SEd_3: ACAGCAAGGTCACCGCAGTTGGCACTAGGCGACATCGACGGT

B-4bp-4SEd_5: ACCACAACCTGTCGCCTAGTGCCAACTGCGTTTTTTCACGTTGAAA

B-4bp-3_4SEd_4: ACCAGACTCCATCGGTTGTGGTACCT

B-4bp-5REd_1:
ACCCTCAGCAGCGAAACGAGTACGGCAACACGGTGAGAGCCTACGG

B-4bp-5_6REd_3: GTTGCCGTACTCGACTGGTCACGAACGTCTCCAACTCACCGT

B-4bp-6REd_5:
TGCTCTGCCTTGGAGACGTTCGTGACCAGTGACAGCATCGGAACGA

B-4bp-5_6REd_4: CAGACCGTAGGCTGGCAGAGCAATGC

B-4bp-7SEd_1:
TGTATCATCGCCTGATCAACGGTACGAGATGCGAAGCACAGAGTGC

B-4bp-7_8SEd_3: TCTCGTACCGTTGCCAGTAGACCTAGCCGACGTGGCTTCGCA

B-4bp-8SEd_5: AGTCACGCTCACGTCGGCTAGGTCTACTGGAAATTGTGTCGAAATC

B-4bp-7_8SEd_4: ACCAGCACTCTGTAGCGTGACTACCT

B-4bp-9REd_1: CATTCAGTGAATAAGGACGCTATGCCTATCGCTCTAGGACCTCTGG

B-4bp-9_10REd_3: ATAGGCATAGCGTTGCTCCAGTCTGCTGCTCAGGCTAGAGCG

B-4bp-10REd_5:
TCCACGACTCCTGAGCAGCAGACTGGAGCACTTGCCCTGACGAGAA

B-4bp-9_10REd_4: CAGACCAGAGGTCAGTCGTGGAATGC

B-4bp-11SEd_1:
GAATACCACATTCAACACCGATGAGGATCACGGCACTCGACACTGC

B-4bp-11_12SEd_3: GATCCTCATCGGTCAAGCGAAGGTGCGAGCCTGTAGTGCCGT

B-4bp-12SEd_5:
AGCGGACTGACAGGCTCGCACCTTCGCTTGTAATGCAGATACATAA

B-4bp-11_12SEd_4: ACCAGCAGTGTCGCAGTCCGCTACCT

Dye-labelling strand sequences

Labeling_strand_ATTO647N_seed /5ATTO647NN/AAGCGTAGTCGGATCTC

Labeling_strand_ATTO488_cap /5ATTO488N/AAGCGTAGTCGGATCTC

Dye-labelling strand attachment sequences

Unused_m13mp18_01
AAATTCTTACCAGTATAAAGCCAACTTTTGAGATCCGACTACGC

Unused_m13mp18_02
GCCTGTTTAGTATCATATGCGTTATTTTTGAGATCCGACTACGC

Unused_m13mp18_03
ACACCGGAATCATAATTACTAGAAATTTTGAGATCCGACTACGC

Unused_m13mp18_04
GATAAATAAGGCGTTAAATAAGAATTTTTGAGATCCGACTACGC

Unused_m13mp18_05
TTTAATGGTTTGAAATACCGACCGTTTTTGAGATCCGACTACGC

Unused_m13mp18_06
TTAGTTAATTTCATCTTCTGACCTATTTTGAGATCCGACTACGC

Unused_m13mp18_07
ACGCGAGAAAACTTTTTCAAATATATTTTGAGATCCGACTACGC

Unused_m13mp18_08
GATGCAAATCCAATCGCAAGACAAATTTTGAGATCCGACTACGC

Unused_m13mp18_09
TGGGTTATATAACTATATGTAAATGTTTTGAGATCCGACTACGC

Unused_m13mp18_10
ACTACCTTTTTAACCTCCGGCTTAGTTTTGAGATCCGACTACGC

Unused_m13mp18_11
AATTTATCAAAATCATAGGTCTGAGTTTTGAGATCCGACTACGC

Unused_m13mp18_12
TTAAGACGCTGAGAAGAGTCAATAGTTTTGAGATCCGACTACGC

Unused_m13mp18_13
TCCTTGAAAACATAGCGATAGCTTATTTTGAGATCCGACTACGC

Unused_m13mp18_14
TCGCTATTAATTAATTTTCCCTTAGTTTTGAGATCCGACTACGC

Unused_m13mp18_15
AGTGAATAACCTTGCTTCTGTAAATTTTTGAGATCCGACTACGC

Unused_m13mp18_16
GAAACAGTACATAAATCAATATATGTTTTGAGATCCGACTACGC

Unused_m13mp18_17
ATTTCATTTGAATTACCTTTTTTAATTTTGAGATCCGACTACGC

Unused_m13mp18_18
AGAAAACAAAATTAATTACATTTAATTTTGAGATCCGACTACGC

Unused_m13mp18_19
CAAAAGAAGATGATGAAACAAACATTTTTGAGATCCGACTACGC

Unused_m13mp18_20
GCGAATTATTCATTTCAATTACCTGTTTTGAGATCCGACTACGC

Unused_m13mp18_21
AATACCAAGTTACAAAATCGCGCAGTTTTGAGATCCGACTACGC

Unused_m13mp18_22
CAATAACGGATTCGCCTGATTGCTTTTTTGAGATCCGACTACGC

Unused_m13mp18_23
TAACAGTACCTTTTACATCGGGAGATTTTGAGATCCGACTACGC

Unused_m13mp18_24
CAGGTTTAACGTCAGATGAATATACTTTTGAGATCCGACTACGC

Unused_m13mp18_25
CAGAAATAAAGAAATTGCGTAGATTTTTTGAGATCCGACTACGC

Unused_m13mp18_26
CCATATCAAAATTATTTGCACGTAATTTTGAGATCCGACTACGC

Unused_m13mp18_27
TCTGAATAATGGAAGGGTTAGAACCTTTTGAGATCCGACTACGC

Unused_m13mp18_28
TATAATCCTGATTGTTTGGATTATATTTTGAGATCCGACTACGC

Unused_m13mp18_29
GATTATCAGATGATGGCAATTCATCTTTTGAGATCCGACTACGC

Unused_m13mp18_30
AAGGAGCGGAATTATCATCATATTCTTTTGAGATCCGACTACGC

Unused_m13mp18_31
CATTTTGCGGAACAAAGAAACCACCTTTTGAGATCCGACTACGC

Unused_m13mp18_32
TAATTTTAAAAGTTTGAGTAACATTTTTTGAGATCCGACTACGC

Unused_m13mp18_33
GTATTAAATCCTTTGCCCGAACGTTTTTTGAGATCCGACTACGC

Unused_m13mp18_34
TAGACTTTACAAACAATTCGACAACTTTTGAGATCCGACTACGC

Unused_m13mp18_35
ATAATACATTTGAGGATTTAGAAGTTTTTGAGATCCGACTACGC

Unused_m13mp18_36
CAACTAATAGATTAGAGCCGTCAATTTTTGAGATCCGACTACGC

Unused_m13mp18_37
TATCTAAAATATCTTTAGGAGCACTTTTTGAGATCCGACTACGC

Unused_m13mp18_38
ACTGATAGCCCTAAAACATCGCCATTTTTGAGATCCGACTACGC

Unused_m13mp18_39
GAATGGCTATTAGTCTTTAATGCGCTTTTGAGATCCGACTACGC

Unused_m13mp18_40
AGAATACGTGGCACAGACAATATTTTTTTGAGATCCGACTACGC

Unused_m13mp18_41
ATAGAACCCTTCTGACCTGAAAGCGTTTTGAGATCCGACTACGC

Unused_m13mp18_42
ATAAAAGGGACATTCTGGCCAACAGTTTTGAGATCCGACTACGC

Unused_m13mp18_43
GCAGATTCACCAGTCACACGACCAGTTTTGAGATCCGACTACGC

Unused_m13mp18_44
ATCGTCTGAAATGGATTATTTACATTTTTGAGATCCGACTACGC

Unused_m13mp18_45
ATGGAAATACCTACATTTTGACGCTTTTTGAGATCCGACTACGC

Unused_m13mp18_46
CCAGCCATTGCAACAGGAAAAACGCTTTTGAGATCCGACTACGC

Unused_m13mp18_47
CTGGTAATATCCAGAACAATATTACTTTTGAGATCCGACTACGC

Unused_m13mp18_48
GTAGAAGAACTCAAACTATCGGCCTTTTTGAGATCCGACTACGC

Unused_m13mp18_49
TGATTAGTAATAACATCACTTGCCTTTTTGAGATCCGACTACGC

Unused_m13mp18_50
AAATTAACCGTTGTAGCAATACTTCTTTTGAGATCCGACTACGC

Unused_m13mp18_51
CCGAGTAAAAGAGTCTGTCCATCACTTTTGAGATCCGACTACGC

Unused_m13mp18_52
GAAGTGTTTTTATAATCAGTGAGGCTTTTGAGATCCGACTACGC

Unused_m13mp18_53
GACAGGAACGGTACGCCAGAATCCTTTTTGAGATCCGACTACGC

Unused_m13mp18_54
AACAGGAGGCCGATTAAAGGGATTTTTTTGAGATCCGACTACGC

Unused_m13mp18_55
TCCTCGTTAGAATCAGAGCGGGAGCTTTTGAGATCCGACTACGC

Unused_m13mp18_56
GCTTTGACGAGCACGTATAACGTGCTTTTGAGATCCGACTACGC

Unused_m13mp18_57
CGCCGCTACAGGGCGCGTACTATGGTTTTGAGATCCGACTACGC

Unused_m13mp18_58
TAACCACCACACCCGCCGCGCTTAATTTTGAGATCCGACTACGC

Unused_m13mp18_59
TGGCAAGTGTAGCGGTCACGCTGCGTTTTGAGATCCGACTACGC

Unused_m13mp18_60
AAGCGAAAGGAGCGGGCGCTAGGGCTTTTGAGATCCGACTACGC

Unused_m13mp18_61
CGAACGTGGCGAGAAAGGAAGGGAATTTTGAGATCCGACTACGC

Unused_m13mp18_62
GATTTAGAGCTTGACGGGGAAAGCCTTTTGAGATCCGACTACGC

Unused_m13mp18_63
TAAATCGGAACCCTAAAGGGAGCCCTTTTGAGATCCGACTACGC

Unused_m13mp18_64
TTTTGGGGTCGAGGTGCCGTAAAGCTTTTGAGATCCGACTACGC

Unused_m13mp18_65
TACGTGAACCATCACCCAAATCAAGTTTTGAGATCCGACTACGC

Unused_m13mp18_66
AAACCGTCTATCAGGGCGATGGCCCTTTTGAGATCCGACTACGC

Unused_m13mp18_67
ACGTGGACTCCAACGTCAAAGGGCGTTTTGAGATCCGACTACGC

Unused_m13mp18_68
TTTGGAACAAGAGTCCACTATTAAATTTTGAGATCCGACTACGC

Unused_m13mp18_69
CCGAGATAGGGTTGAGTGTTGTTCCTTTTGAGATCCGACTACGC

Unused_m13mp18_70
AAATCCCTTATAAATCAAAAGAATATTTTGAGATCCGACTACGC

Unused_m13mp18_71
TGTTTGATGGTGGTTCCGAAATCGGTTTTGAGATCCGACTACGC

Unused_m13mp18_72
CTGGTTTGCCCCAGCAGGCGAAAATTTTTGAGATCCGACTACGC

Unused_m13mp18_73
TGAGAGAGTTGCAGCAAGCGGTCCATTTTGAGATCCGACTACGC

Unused_m13mp18_74
AGCTGATTGCCCTTCACCGCCTGGCTTTTGAGATCCGACTACGC

Unused_m13mp18_75
TTTCTTTTCACCAGTGAGACGGGCATTTTGAGATCCGACTACGC

Unused_m13mp18_76
GTTTGCGTATTGGGCGCCAGGGTGGTTTTGAGATCCGACTACGC

Unused_m13mp18_77
GAATCGGCCAACGCGCGGGGAGAGGTTTTGAGATCCGACTACGC

Unused_m13mp18_78
GAAACCTGTCGTGCCAGCTGCATTATTTTGAGATCCGACTACGC

Unused_m13mp18_79
TGCGCTCACTGCCCGCTTTCCAGTCTTTTGAGATCCGACTACGC

Unused_m13mp18_80
GAGTGAGCTAACTCACATTAATTGCTTTTGAGATCCGACTACGC

Unused_m13mp18_81
TAAAGTGTAAAGCCTGGGGTGCCTATTTTGAGATCCGACTACGC

Unused_m13mp18_82
TTCCACACAACATACGAGCCGGAAGTTTTGAGATCCGACTACGC

Unused_m13mp18_83
CTGTGTGAAATTGTTATCCGCTCACTTTTGAGATCCGACTACGC

Unused_m13mp18_84
ATTCGTAATCATGGTCATAGCTGTTTTTTGAGATCCGACTACGC

Unused_m13mp18_85
TAGAGGATCCCCGGGTACCGAGCTCTTTTGAGATCCGACTACGC

Unused_m13mp18_86
CAAGCTTGCATGCCTGCAGGTCGACTTTTGAGATCCGACTACGC

Unused_m13mp18_87
ACGACGTTGTAAAACGACGGCCAGTTTTTGAGATCCGACTACGC

Unused_m13mp18_88
TTGGGTAACGCCAGGGTTTTCCCAGTTTTGAGATCCGACTACGC

Unused_m13mp18_89
AGGGGGATGTGCTGCAAGGCGATTATTTTGAGATCCGACTACGC

Unused_m13mp18_90
CTCTTCGCTATTACGCCAGCTGGCGTTTTGAGATCCGACTACGC

Unused_m13mp18_91
CTGTTGGGAAGGGCGATCGGTGCGGTTTTGAGATCCGACTACGC

Unused_m13mp18_92
GCGCCATTCGCCATTCAGGCTGCGCTTTTGAGATCCGACTACGC

Unused_m13mp18_93
CGCTTCTGGTGCCGGAAACCAGGCATTTTGAGATCCGACTACGC

Unused_m13mp18_94
ATCGCACTCCAGCCAGCTTTCCGGCTTTTGAGATCCGACTACGC

Unused_m13mp18_95
GACGACGACAGTATCGGCCTCAGGATTTTGAGATCCGACTACGC

Unused_m13mp18_96
GTAACCGTGCATCTGCCAGTTTGAGTTTTGAGATCCGACTACGC

Unused_m13mp18_97
GGTCACGTTGGTGTAGATGGGCGCATTTTGAGATCCGACTACGC

Unused_m13mp18_98
AAACGGCGGATTGACCGTAATGGGATTTTGAGATCCGACTACGC

Unused_m13mp18_99
ACAACCCGTCGGATTCTCCGTGGGATTTTGAGATCCGACTACGC

Unused_m13mp18_100
TTCATCAACATTAAATGTGAGCGAGTTTTGAGATCCGACTACGC

3. Dynamic Self-assembly of Compartmentalized DNA Nanostructures

Adapted with permission from S. Agarwal, M. Klocke, P. Pungchai and E. Franco, "Dynamic self-assembly of compartmentalized DNA nanotubes." Nature communications 12, no. 1 (2021): 1-13.

3.1 Abstract

Bottom-up synthetic biology aims to engineer artificial cells capable of life-like behaviors by using a minimal set of molecular components. An important challenge toward this goal is the development of programmable biomaterials that can provide active spatial organization in cell-like compartments. Here, we demonstrate the dynamic self-assembly of nucleic acid (NA) nanotubes inside cell-sized droplets. We develop methods to encapsulate and assemble different types of DNA nanotubes from programmable DNA monomers, and demonstrate temporal control of assembly via designed pathways of RNA production and degradation. We examine the dynamic response of encapsulated nanotube assembly and disassembly with the support of statistical analysis of droplet images. Our study provides a toolkit of methods and components to build increasingly complex and functional NA materials to mimic life-like functions in synthetic cells.

3.2 Introduction

Synthesis of dynamic, programmable molecular scaffolds is an important challenge towards the development of living materials and artificial cells.[1,2] In biological cells, the cytoskeleton plays an active role in transporting components, determining the cell's mechanical properties, and coordinating division and motility. While the cytoskeleton is primarily composed of filaments (including actin and microtubules), its operation is orchestrated by a large number of organizing proteins and interactions with the cell membrane.[3] The development of scaffolding systems that are inspired by the cytoskeleton's architecture promises to endow synthetic cells and materials with the capacity to adapt, partition, and move.[4-6] These scaffolding systems should be easy to customize, and exploit components already established in cell-free synthetic biology.

The most direct approach to build minimal scaffolds inside artificial cells is that of isolating relevant cellular biomolecules and reconstituting them in cell-sized compartments.[5,6] Native cytoskeletal filaments have been encapsulated in a variety of droplets or vesicles; however, achieving dynamic behaviors beyond assembly in confinement is challenging due to both restrictive environmental conditions and laborious purification and reconstitution protocols.[7-11] Encapsulated full cytoplasmic extracts are able to generate assembly, disassembly and contraction of actomyosin networks.[8,12,13] The inclusion of motor proteins (as well as ATP production and oxygen scavenging) is key to achieve contraction and directed motion.[14] These advances point to exciting opportunities toward harnessing native cytoskeletal systems in synthetic cells. However, the numerous components of the cytoskeleton co-evolved with high levels of cross-talk,

and these interactions are often not measurable. This makes it difficult to identify the minimal number of components as well as the expression levels needed to achieve a target behavior.[5]

To circumvent the complexity of reconstituting the cytoskeleton, synthetic hydrogels and polymers have been developed as scaffolds for artificial protocells.[4,15] These scaffolded compartments have been engineered to have a multi-layer architecture and to respond to specific chemical inputs as well as to temperature and light.[16,17] However, as they are primarily developed for applications like drug delivery and cosmetics, these scaffolds are not optimized to interact with out-of-equilibrium chemical reactions, nor with active molecular processes and genetic parts that require cytoplasmic conditions.

Nucleic Acid (NA) nanotechnology has demonstrated a multitude of scaffolds and dynamic circuits, built by programming a finite number of DNA or RNA molecules.[18,19] NA molecules are rationally designed to match prescribed structural or temporal patterns by assigning complementary domains that bind according to Watson-Crick-Franklin base-pairing rules. The sequences in each domain are typically optimized through computer algorithms, which make it possible to generate a variety of structurally or functionally identical components with distinct sequences.[20] While there are many approaches to building NA structures, methods based on assembly of tiles have produced a variety of synthetic filaments structurally comparable to actin filaments and microtubules.[21-24] DNA or RNA tiles interact via engineered single-stranded sticky-end domains and form micrometer-sized nanotubes with prescribed tiling patterns.[21-24] These nanotubes can in turn be seeded, capped, and spatially organized by DNA structures folded with the

origami approach, to build cytoskeletal-like networks.[25-27] In parallel, NA nanotechnology has also developed methods to build molecular circuits with programmable logic and dynamic behaviors operating in vitro and in vivo.[28-30] By exploiting enzymatic production and degradation of RNA, these circuits can recapitulate biological gene networks and respond to a variety of organic and inorganic signals sensed by NA aptamers.[31-33] As NA structural elements, circuits, and sensors share the same base-pairing rules to encode their interactions, all these devices can be modularly interconnected. In particular, DNA nanotubes were modified to respond to the release of NA molecules from NA circuits and sensors: dynamic assembly and disassembly of the nanotubes was controlled in a predictable way by pulse generating circuits, oscillators, and chemical signals such as pH.[34-36] These examples indicate that NA structures, circuits, and sensors may be collectively used to build modular mimics of dynamic cytoskeletal filaments inside artificial cells.

The operation of NA devices in cell-sized compartments has been demonstrated with a particular focus on reaction networks. Out of equilibrium NA circuits that comprise enzymes have been encapsulated in water-in-oil droplets to characterize the circuit bifurcation diagram as well as the robustness of its dynamics to partitioning noise.[37-39] Synthetic transcriptional networks operating in cell-free extracts were also engineered to generate patterns in communicating droplets.[40] Enzyme-free DNA circuits were encapsulated in proteinosomes and used for spatially organized protocell computation.[41] DNA nanostructures have been successfully engineered to serve as synthetic membrane receptors, scaffolding membrane elements, and multi-cell organizers.[42-45] However, little attention has been dedicated to encapsulation and growth of DNA scaffolds inside

droplets and vesicles. Two dimensional DNA motifs have been encapsulated inside droplets to increase mechanical stability of vesicles or sense pH. Rapid folding of another 2-d DNA origami was confirmed by subsequent extraction, however, studies of DNA scaffold assembly and operation inside compartments are still lacking.[46-48] More importantly, the encapsulation of a multi-component NA system comprising circuits and scaffolds has not been explored.

In this work, we demonstrate the encapsulation of a modular NA toolkit to build a minimal dynamic scaffolding system for synthetic cells. This toolkit includes DNA nanotubes as a self-assembling scaffold and transcriptional processes to control nanotube assembly and disassembly. We develop a variety of assays for encapsulating DNA nanotubes in cell-sized, water-in-oil droplets, highlighting that multiple nanotube species can be assembled and can coexist. We employ two distinct nanotube designs to control the start of assembly, and characterize the kinetics of polymerization inside compartments using quantitative statistical analysis. By implementing a DNA-RNA hybrid nanotube design, we demonstrate enzyme-mediated control of assembly and disassembly that yields transient presence of nanotubes inside compartments. The density of assembled nanotubes, as well as their lifetime in the droplets, are tunable properties of this system. The methods and components characterized here are a first step toward the bottom-up development of NA cytoskeletal mimics for synthetic minimal cells. Because of the modularity of NA components, this toolkit could be enriched with NA sensors to encode responses to external stimuli, and more complex dynamic networks for autonomous behaviors. Further, the encapsulation of NA structures and condensates promoting the formation of higher-order nanotube architectures would make it possible to

systematically specify the overall internal organization and the mechanical properties of protocells.

3.3 Results

DNA nanotubes self-assemble from pre-formed monomers at constant temperature.

NA nanotechnology offers many options to build filamentous structures through different assembly pathways.[22,24,49] Because our goal is to build an artificial scaffolding system with the capacity to assemble and disassemble in the absence of thermal treatment, we selected a class of DNA nanotubes that polymerize at constant temperature from pre-annealed tiles or monomers.[50] Our tiles consist of five strands that form two parallel heteroduplexes held together at two points where strands cross over (double-crossover, or DX) from one duplex to the other, and are known as DAE-E tiles (Fig. 3-1a).[51] As DX tile variants differ by the orientation of DNA strands and by the crossover distances, the “DAE-E” acronym describes precisely the tile structure, indicating the number of crossovers (double), the orientation of the strands through the crossover (antiparallel), the number of half-turns between intramolecular crossovers (even), and the number of half-turns between intermolecular crossovers (even).

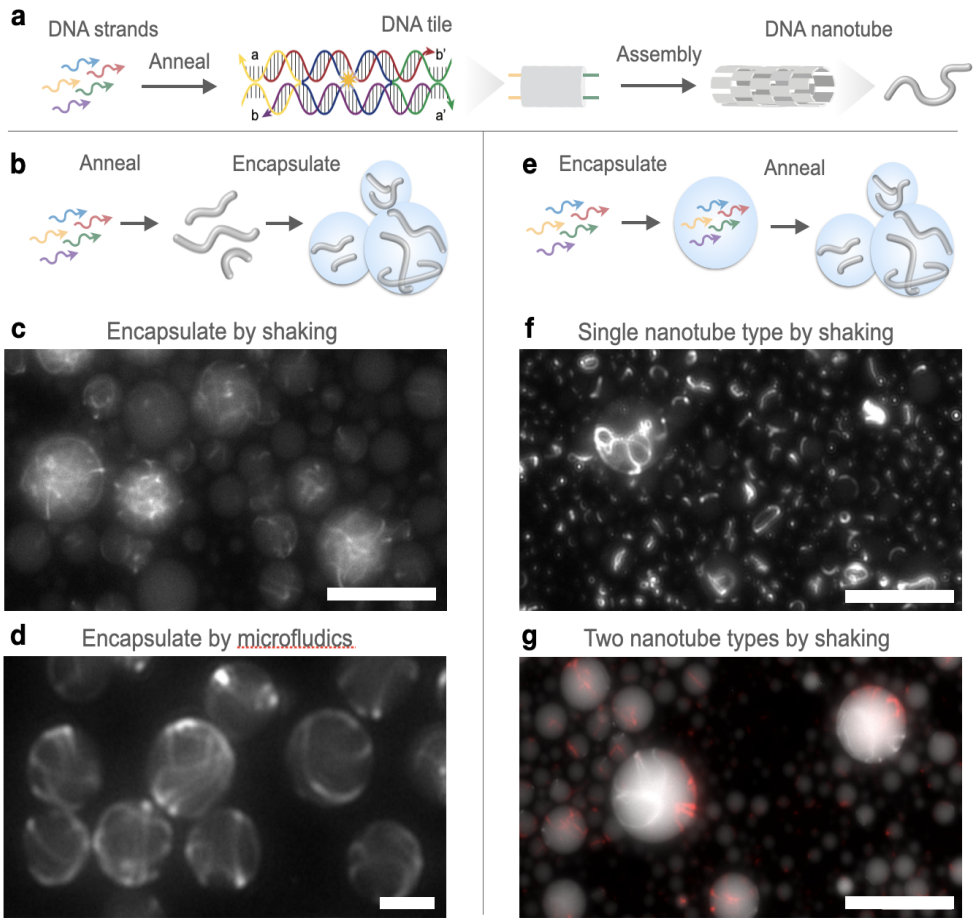

Figure 3-1: Schematic of DNA tiles and nanotubes and different methods for encapsulating and assembling DNA nanotubes in water-in-oil droplets. (a) DNA tiles composed of 5 unique ssDNA oligomers (shown in blue, red, yellow, green and purple strands) that self-assemble into DNA nanotubes. Assembly occurs via hybridization of single-stranded complementary domains known as sticky-ends (marked as a, complementary to a', and b complementary b'). These tiles self-assemble into nanotubes due to an intrinsic curvature at the binding site between two tiles. Tiles are labeled with a fluorescent molecule, indicated here by the yellow star, for easy observation of DNA nanotubes under fluorescence microscopy. (b) DNA nanotubes can be pre-annealed from constituent oligomers in vitro before encapsulation in water-in-oil droplets. Representative fluorescence microscopy images of pre-annealed DNA nanotubes inside droplets using two different encapsulation protocols. (c) Nanotubes encapsulated via the shaken protocol at room temperature. Tile concentration is 500 nM. (d) Nanotubes encapsulated via the microfluidic protocol at room temperature. Tile concentration is 350 nM. (e) Constituent oligomers can be encapsulated inside the droplets and later annealed to form nanotubes. Multiple species of nanotubes can be simultaneously annealed in the droplets if the required strands are present in the initial encapsulated solution. (f) Representative fluorescence microscopy image of a single nanotube species annealed inside droplets (250 nM tile concentration) and then imaged at room temperature. (g) Example fluorescence image of two distinct species of DNA nanotubes annealed inside droplets (250 nM each tile), labelled with Cy3 dye (white) and Atto647N dye (red) respectively and then imaged at room temperature. Scale bars: 30 μm.

Two strands (yellow and green in Fig. 3-1a, on opposite sides of the tile) include sticky-end domains that allow tiles to recognize complementary domains present on other such tiles to self-assemble into a nanotube. By designing the sequences of bases in the sticky-end domains we can program tile interactions and tile assembly in a modular manner. An important advantage of this class of DNA tiles is that pre-annealed tiles bind to each other, forming nanotubes in a range of constant temperatures dependent on the melting temperatures of the sticky-ends (typically between 25-40 °C).[50] Tile nucleation and polymerization, and thus the yield of nanotubes, are also influenced by other conditions like tile concentration, level of positive cations, and presence of certain enzymes, but such conditions have been abundantly studied in the literature making DX tiles an ideal platform to develop synthetic scaffolds. Nanotube growth is typically monitored via epifluorescence microscopy, by labeling one of the tile strands with a fluorescent dye.[22,50] Here, we take advantage of several well-characterized DAE-E tile variants to explore and develop methods to encapsulate DNA nanotubes with distinct assembly pathways.

Encapsulation of DNA nanotubes in micrometer sized droplets.

Water-in-oil droplets are a simple approach to generate isolated compartments with high-throughput and with size that ranges from a few microns to tens of microns in diameter, which is comparable to a wide range of cell types. We selected a droplet system, consisting of a fluorinated oil and biocompatible-surfactant mixture, and an

aqueous medium containing nanotube components and buffer.[52] The surfactant stabilizes the aqueous droplets within the oil/surfactant medium, prevents coalescence and transfer of materials from droplet to droplet, minimizes adsorption of DNA to the surface, and confers resilience to temperature fluctuations.[37,53] In this way, each droplet is an isolated environment that remains stable and can be stored for days at room temperature. While these water-in-oil droplets do not fully mimic the cellular environment, which can freely exchange resources with the surrounding aqueous media, they make it possible to monitor assembly of DNA nanotubes in confined, cell-size compartments for extended periods of time.

In our first series of experiments, we encapsulated nanotubes that assemble from a single fluorescently tagged tile (a single set of five unique strands).[22,35] This class of tiles folds and then self-assembles into nanotubes during the annealing process, unless the sample is stored at a temperature above the sticky-end melting temperature. First, we explored the encapsulation of nanotubes that were pre-annealed (Fig. 3-1b,c,d) using two techniques: a “shaken” protocol and a microfluidic protocol (Supplementary Information).

The shaken droplet protocol is rapid, requires little expertise and employs only a bench vortexer to emulsify the oil and liquid phase and generate surfactant-stabilized water-in-oil droplets (Fig. 3-1c). These droplets present a wide range of diameters, and their size may only be controlled via filtration. Droplet samples were transferred to Ibidi imaging chambers for observation as described in supplementary Information.

While we successfully encapsulated pre-annealed nanotubes with the shaken protocol, we qualitatively observed major variability in the number of nanotubes per

droplet, which could be the result of partitioning noise.[37] In sparsely populated droplets, nanotubes do not exhibit unpredicted morphologies or disordered joining. In densely populated droplets, nanotubes appear tightly entangled. It is probable that shear forces during the encapsulation process cause nanotubes to fragment, or promote formation of defects and aggregation in the assemblies. Nanotubes appear to be about as long as the diameter of their confining droplet, or much shorter, although precise measurements of nanotube length are not possible, as is discussed later in the manuscript.

The adoption of a microfluidic chip allows for formation of controlled/discrete sizes of droplets and for reduction of partitioning noise and damage to the nanotubes during encapsulation (Fig. 3-1d). Nanotubes encapsulated via microfluidics were much more uniformly distributed throughout the droplets than those encapsulated with the shaken protocol. Additionally, nanotubes appear to be longer than the diameter of the droplets confining them, causing them to wrap around the interior surface of the droplets, rather than form a tangled mesh in the center of the droplets as seen for nanotubes encapsulated with the shaken protocol. These results suggest that encapsulation of annealed nanotubes using microfluidics is less destructive than using the shaken method, yet this approach is significantly more laborious than the shaken protocol and requires at least 15 minutes to encapsulate samples. To monitor early nanotube assembly reactions in droplets, we employed the shaken droplet protocol for the remainder of experiments within the paper.

To continue using the rapid shaken protocol while avoiding damaging pre-annealed nanotubes during the process, we developed methods to encapsulate constituent strands inside droplets and subsequently anneal the nanotubes. This is

feasible because these droplets remain stable at high temperatures. We first encapsulated, and then annealed the 5 unique strands of a single tile (Fig. 3-1f), observing assembly of nanotubes that were qualitatively comparable in length and morphology to pre-annealed nanotubes encapsulated via microfluidics. Because structurally identical DNA tiles can be designed to include orthogonal (non-interacting) sequences, it is possible to build distinct tile populations that assemble into distinct nanotubes in the same environment. Thus in our next experiments, we encapsulated the constituent strands of two-tile species, labeled with different fluorophores. Droplets with the encapsulated tile variants were then annealed, and we observed assembly of nanotube populations presenting different colors (Fig. 3-1g).

Although achievable, annealing nanotubes inside droplets introduced some difficulties. First, we observed evaporation of a portion of droplets; evaporation can be mitigated by covering samples with a protective layer of hexadecane or water, which however makes it difficult to extract nanotube-containing droplets. Further, constituent strands for some nanotube designs labeled with alternative fluorescent dyes aggregate towards the surface of droplets without assembling into nanotubes after annealing, likely due to interactions between the droplet surface and tiles labeled with hydrophobic dyes.

In addition, it is desirable to develop synthetic scaffolds with the capacity to assemble and disassemble at a constant temperature, like cytoskeletal filaments. For these reasons, we sought to work with alternative tile designs that allow for assembly within droplets without annealing, and we developed methods to aggregate information about assembly in sets of droplets.

Isothermal growth of an encapsulated two-tile nanotube design.

The potential usefulness of artificial biomolecular scaffolds goes beyond introducing a spatial organization within compartments. Like cellular scaffolds, which adapt to stimuli by assembling and disassembling dynamically, a synthetic scaffold could provide temporal control of compartment properties. To achieve this potential, it is important to identify methods enabling assembly at specific times and to assess the kinetics of assembly within the compartment.

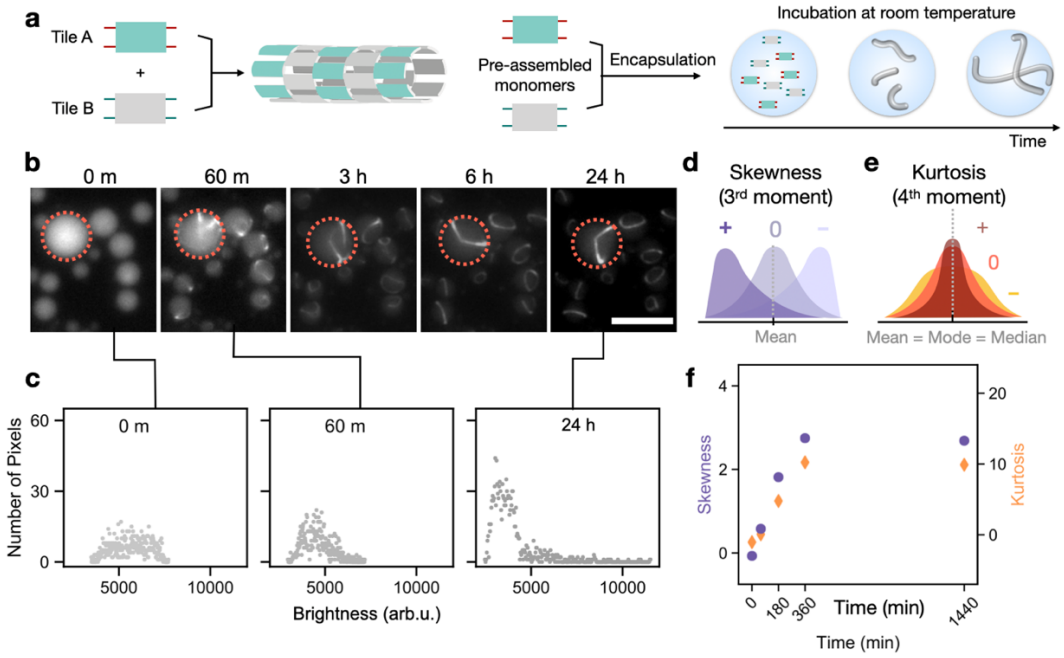

Figure 3-2: Statistical analysis of droplet fluorescence microscopy images makes it possible to track the condensation of nanotubes in a population of droplets. (a) The two-tile nanotube design requires both tile A and B (shown in green and grey), each with sticky-ends complementary to those of the other tile, for nucleation and polymerization of nanotubes. The tiles are annealed in vitro separately and mixed immediately before encapsulation. (b) Temporal sequence of representative fluorescence microscopy images of droplets encapsulating the two-tile nanotubes at room temperature (each tile at 100 nM). (c) We examine the distribution of pixel brightness across a single droplet over time. As nanotubes assemble, a change in the shape of the distribution also occurs. Each plot shows the histogram of pixel brightness within the droplet of interest at the associated time. Data for this illustrative figure were extracted by hand using ImageJ. (d) Skewness is a measure of the asymmetry of the distribution of a random variable about its mean. As nanotubes polymerize, the skewness of the distribution of pixel brightness in a given droplet shifts from zero to a positive value, indicating that the distribution shifts from being relatively symmetric to having a tail on the right side. (e) Kurtosis is a measure of the "tailedness" of the distribution of a random variable. All three of these distributions have mean of 0, standard deviation of 1, and skewness of 0, and all are plotted on the same horizontal and vertical scale. (f) The skewness and kurtosis values (represented as purple dots and orange diamonds respectively) increase as nanotubes start growing and becoming more apparent over time inside the droplet. This graph represents a single droplet only. Source data for this figure is provided as a source data file. Scale bar: 20 μm.

To begin to address these challenges, we sought to encapsulate a nanotube design that requires the simultaneous presence of two distinct, interacting tiles (Fig. 3-2a).[22,54] The sticky-ends are designed so that complementary sequences to sticky-ends of Tile A are present on Tile B, thus self-assembly can proceed only if both species are present. Tiles A and B can be separately pre-annealed and stored as monomers. Once A and B tiles are mixed and rapidly encapsulated with the shaken protocol (which takes only a couple of minutes from the time of mixing the two tiles), nanotube assembly can be monitored from the early stages of assembly (Fig. 3-2b). Fluorescence microscopy images do not reveal discernable structures immediately after encapsulation. But within 1 hour of incubation at room temperature, we see tubular structures inside the droplets. We also observe that as time progresses, the nanotubes appear to elongate and join. Encapsulated assemblies are stable for over 72 hours at room temperature (SI Fig. S3.39). In some cases, nanotubes form rings, a behavior also observed in droplet-encapsulated actin filaments and microtubules.[7,55] It is likely that the rings observed in droplets are actually formed by nanotube bundles. They appear to be larger and less curved than loose rings formed by non-encapsulated DNA nanotubes, whose measured persistence length is 4-5 μm.[22,56] Bundling and localization of nanotubes near the droplet surface were confirmed using confocal microscopy (SI Fig. S3.11). Bundling may be due to spurious interactions between assembled tiles or between the hydrophobic dyes and the surface, or to confinement effects, as nanotube bundles appear to be longer than the diameter of the droplets. While aggregation of non-encapsulated nanotubes has been observed, it is unclear whether ordered bundles can form in the absence of confinement. We note that addition of DNase to the aqueous phase during encapsulation fully

suppresses nanotube growth, while addition of DNase to the oil phase has no effect on nanotube growth because this type of emulsion does not support protein exchange (Supplementary Figure S3.43).

Tracking nanotube assembly through statistical properties of droplet images.

While qualitative observations of assembly can be directly made from visual inspection of epifluorescence microscopy images, we sought a less subjective method to track assembly (Fig. 3-2b). Non-encapsulated nanotubes are typically imaged on glass slides, and statistics about their number and length can be collected with automated image processing.[35] However, this is impractical, if not impossible, inside water-in-oil droplets due to nanotubes intersecting, bundling, and moving within the droplets during confocal microscopy. One could measure the total length of visible segments evident in the microscopy images to get a sense of the polymerization of encapsulated nanotubes at a particular time. This is time consuming, as common methods of separating objects of interest from backgrounds fail to effectively separate nanotubes from background fluorescence in the droplet. In addition, it is still not an accurate reflection of nanotube length, as the total length of visible contours decreases beyond 180 min which disagrees with previous reports on nanotube polymerization kinetics (Supplementary Information Fig S3.42).[35,36] An alternative route is the examination of statistical measures of droplet epifluorescence microscopy images: the shape of the distribution of pixel intensities within a single droplet clearly evolves over time as nanotubes are qualitatively observed to grow (Fig. 3-2c). Before nanotubes have polymerized, tiles and corresponding bound fluorescent molecules will be evenly dispersed over the entire volume of a droplet. This

uniform spread of tiles, and thus fluorescent signal, will redistribute as tiles are recruited during nanotube polymerization, resulting in distinct bright and dark pixels where there are and are not nanotubes within the droplet, respectively. It is worth noting that the epifluorescence microscopy images we are using to observe nanotube polymerization are a two-dimensional projection of fluorescent signals from within the three-dimensional droplet, with planes above and below the focal plane contributing unfocused signal to the overall image. Thus, one way to assign a quantitative measurement to assembly of nanotubes in individual droplets, is to examine the shape of the distribution of pixel brightness.

Skewness and kurtosis, also respectively known as third and fourth standardized moments, are measures that describe the shape of a distribution. Skewness describes the distribution of any variable about its mean, while kurtosis describes the “tailedness” of a distribution (Fig. 3-2de).[57-59] Because these are statistical measures describe the shape of a distribution, they are agnostic to differing exposure times provided that no pixels of the camera used during imaging are saturated, and all pixel brightness values for an image fall within the dynamic range of the camera (Supplementary Information Fig. S3.17). Skewness and kurtosis have been previously used to quantify the temporal evolution of actin polymerization and of phase separation of liquid crystals.[60,61]

As nanotubes assemble, the distribution of intensities within a droplet shifts from being symmetric about the mean brightness value to a bulk of the pixels becoming darker while a small number remains bright. This is reflected in the skewness value progressing from near zero at the start of the experiment, before nanotubes have polymerized, to increasing in positive magnitude as nanotubes polymerize. For unpolymerized

nanotubes, we expect a negative or near zero kurtosis value, reflecting the heavily tailed distribution of pixel values, which increases to a positive value as nanotubes have polymerized and the distribution shifts to a high peak with weak tails. Indeed, as nanotubes assemble we observe a progressive increase in the skewness and kurtosis values for the distribution of pixel intensities within a single droplet, with a greater relative change in the skewness (Fig. 3-2f).

Skewness and kurtosis are influenced not only by assembly of nanotubes, indicated by a condensation in the total fluorescent signal but also by the number of free fluorescently-labeled tiles creating a background signal. This is visible by comparing the images and pixel brightness plots in Fig. 3-2b at 60 minutes and 3+ hours. At both timepoints, nanotubes are visibly polymerized in the droplet, but the amount of free tiles contributing to background noise are different, which is reflected in the shape of the pixel brightness profiles. For this reason, skewness and kurtosis are not a direct measurement of the presence of nanotubes, rather they provide a qualitative picture of condensation through quantitative measurements of statistical properties of droplet images. Skewness and kurtosis measured at a given time point appear to be independent of droplet size, thus we opted for not binning droplets by radius in our analysis.

To track and compare nanotube growth in populations of droplets, we collected skewness and kurtosis measurements for a subpopulation of droplets within the field-of-view. We report the mean and standard deviation of skewness and kurtosis for several assays. A larger standard deviation may be taken as an indication of unequal encapsulation of reagents during the shaken droplet protocol. To automate image processing, we also developed a droplet detection code using Python to find droplets

and extract their pixel intensities (Supplementary Information).[62] A random sample of droplets at each time-point is measured and individual droplets are not tracked through the duration of each experiment. The number of droplets considered for each experiment is shown in the supplementary information, with further discussion on the detection and data extraction process. Unless otherwise noted, data are gathered using the automated droplet detection code.

Varying concentration of nanotube components and introduction of crowding agents affect morphology and assembly kinetics.

In live cells, the assembly and disassembly of cytoskeletal filaments is driven by the concentration of activated protein monomers. Similarly, the concentration of tiles encapsulated in our droplets should influence nanotube assembly. We illustrate this idea with a computational tile assembly model reported in Supplementary Information. The model, based on deterministic ordinary differential equations (ODEs), shows that the higher the tile concentration, the faster nanotube nucleation and elongation reach completion.[63] Expecting to observe similar results in droplet experiments, we encapsulated different concentrations of the two-tile system (Fig. 3-2a) and continuously monitored nanotube assembly. To prepare the monomers Tile A and Tile B, stoichiometric quantities of the respective 5 constituent strands were mixed together in TAE buffer containing 12.5 mM Mg^{2+} and annealed (1 °C/min) from 95 °C to room temperature. Pre-annealed Tile A and Tile B were introduced in the aqueous phase simultaneously before encapsulation. Incubation and subsequent measurements were performed immediately after mixing at room temperature.

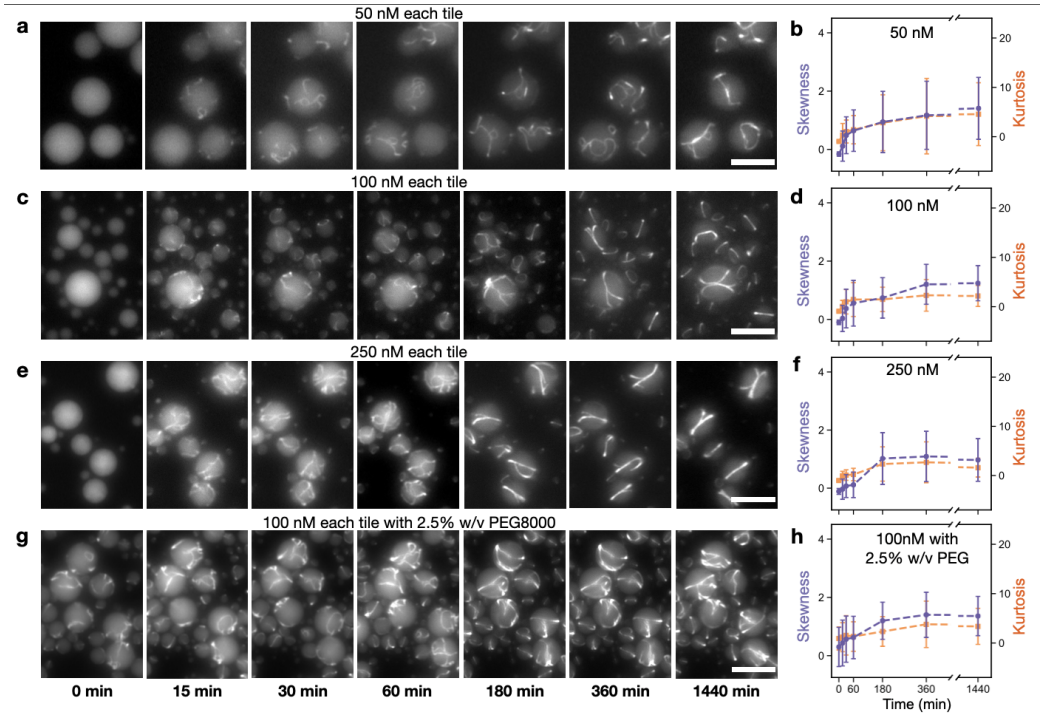

Figure 3-3: Isothermal assembly of encapsulated two-tile DNA nanotubes at room temperature. Tiles were pre-annealed and mixed immediately before encapsulation. (a, c, e) Representative temporal sequence of fluorescence microscopy images of two-tile nanotubes encapsulated at 50, 100, and 250 nM concentration for each tile. (b, d, f) Plots of the mean skewness (purple) and kurtosis (orange). (g) Representative images of two-tile nanotubes encapsulated at 100 nM each tile, with 2.5% w/v PEG. (h) Plot of the mean skewness (purple) and kurtosis (orange) over time for isothermal assembly of tiles encapsulated with PEG. Data is presented as mean values +/- standard deviation. Data extracted using droplet detection code. Source data for this figure can be provided on reasonable request. Scale bars: 20 μm.

We monitored encapsulated two-tile nanotubes at 50, 100, and 250 nM each tile for over 24 hours (Fig. 3-3a-f). (For comparison, example images of non-encapsulated nanotubes are in SI Fig. S3.38.) Qualitatively, small nanotubes were discernible within an hour for all the samples. At 15 and 30 minutes nanotubes appear to be more numerous and longer in the 250 nM tile sample. At 24 hours, nanotubes in all samples appear to have elongated, joined, and formed circular bundles that are qualitatively comparable, although they appear significantly thicker and less curved in the 250 nM sample.

Additional images of droplets after 24h incubation are in SI Fig. S3.10, which includes example images of encapsulated nanotubes produced at 25 nM tile concentration. In this case, nanotube bundling and alignment is not observed as most droplets appear to include only one or two short nanotubes (see also SI Fig. S3.12).

To gather and compare information about assembly as it occurs in a collection of droplets, we compared skewness and kurtosis of droplet fluorescence microscopy images taken over time, using the image processing protocol described earlier, and Supplementary Information (Fig. 3-3bdf). A first observation is that the "steady state" value of kurtosis and skewness is roughly the same in each of these 3 samples, and thus does not appear significantly affected by the tile concentration. In contrast, the skewness and kurtosis value before the 1 hour mark are dependent on concentration, with both skewness and kurtosis increasing more slowly at higher tile concentration. This highlights that skewness and kurtosis are not a measure of the concentration of nanotubes in encapsulation. They, instead, are a measure of the fluorophores (or tiles since each has one fluorophore) incorporated in a structure versus those which are unincorporated. As assembly of nanotubes begins, the ratio of incorporated to unincorporated tiles starts increasing, thus resulting in a rise in skewness and kurtosis. The rate of increase of skewness and kurtosis within 1 hour is fastest in the 50 nM sample since the total number of unincorporated tiles itself is low. As there are more unincorporated tiles in the 250 nM sample, the rate of increase of skewness and kurtosis is much slower. For higher tile concentrations, more free tiles contribute to a brighter overall signal for individual droplets (SI Fig. S3.41).

Next, we examined the effects of macromolecular crowding on encapsulated nanotube assembly. Macromolecular crowding inside living cells influences diffusion thereby changing intracellular reaction rates, and is a major driving force in phase separation. Thus, we included a common crowding agent, polyethylene glycol 8000 (PEG), in our droplets. In a sample containing, 2.5% PEG, assemblies were visible immediately after encapsulation (Fig. 3-3g). In this case (Fig. 3-3h), the starting value and rate of increase of skewness and kurtosis in the first 30 minutes are higher than that of the sample without PEG (Fig. 3-3d), suggesting that the crowding agent assists assembly (Fig. 3-3h). Additional experiments show that increased concentration of PEG results in an increase in both skewness and kurtosis (SI Fig. S3.16). However, with concentrations as high as 10% w/v PEG, we observe rapid formation of aggregates rather than programed assemblies (SI Fig. S3.16c). We hypothesize that at 10% w/v PEG kinetically favored formation of aggregates instead of the intended thermodynamically favored nanotube structures.

Overall, these experiments support the expectation that assembly of encapsulated nanotubes is influenced by tile concentration. In agreement with computational predictions, our droplet images confirm that at higher tile concentration more nanotubes form because nucleation rates are faster (SI Fig. S3.44). Yet, based on the droplet brightness and the skewness and kurtosis plots, a substantial fraction of non-assembled tiles appears to persist at all concentrations tested on a timescale of hours, in contrast with model predictions, presumably due to unmodeled depolymerization and joining reactions.[64]

Activating nanotube assembly inside droplets via RNA triggers.

To expand the toolkit of NA scaffolds that can be formed inside droplets, we adopted a DNA tile whose assembly into nanotubes is triggered by RNA molecules (Fig. 3-4a).[36] In general, assembly of nanotubes cannot occur if one or both of the sticky-end strands is missing from the tile monomer. By excluding one sticky-end strand from the tile annealing mix, it is possible to form inactive tiles that are activatable by the addition of the missing strand, which can be either DNA or RNA. Agarwal et. al previously demonstrated assembly of DNA-RNA hybrid nanotubes within minutes of adding the activating RNA "trigger" strand to pre-annealed inactive DNA tiles at room temperature.[36] RNA can be transcribed as needed from small amounts of templates, a process that can be temporally controlled through transcriptional gene circuits. While it is difficult to produce large assemblies exclusively with RNA, nanostructures made of both DNA and RNA offer a promising route toward transcriptionally-controlled assemblies.[65]

To begin characterizing assembly of DNA-RNA hybrid nanotubes, we added varying concentrations of gel-purified trigger RNA to inactive tiles and subsequently encapsulated the sample. For both 1:1 gel-purified RNA to inactive tile (1x, Fig. 3-4b) and 4:1 (4x, Fig. 3-4c) samples, assemblies are visible within 15 minutes. Focusing on the droplets during fluorescence microscopy is non-trivial before nanotubes assemble. When assemblies are present, the skewness and kurtosis values across the sample of droplets measured varies greatly. Fluorescence microscopy images suggest that the

assemblies with 4x RNA are disordered aggregates, rather than filaments. We hypothesize that the high concentration of trigger RNA relative to inactive tiles results in undesired hybridization between multiple RNA strands and a single inactive tile, which disrupts the assembly of (defect-less) hybrid nanotubes. These results highlight the limitations of characterizing assembly via skewness and kurtosis, as these measures do not distinguish between predictably assembled nanotubes and disordered aggregates.

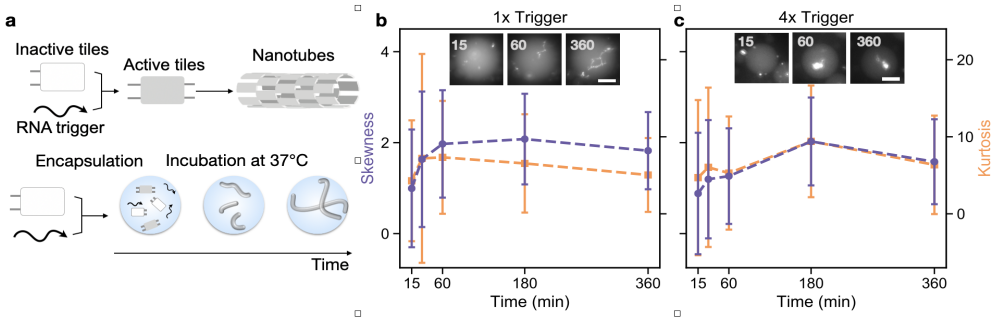

Figure 3-4: Isothermal assembly of hybrid DNA-RNA nanotubes inside compartments at 37°C. (a) Inactive DNA tile, lacking sticky-ends necessary for self-assembly on one side of the tile, is activated by the addition of RNA molecules and triggers self-assembly into nanotubes. Inactive tiles and trigger RNA are mixed immediately before encapsulation and incubated at 37°C. (b-c) Representative fluorescence microscopy images of droplets encapsulated with 500 nM inactive tiles, and 1x and 4x RNA trigger (insets) with plots of mean skewness (purple) and kurtosis (orange). Data is presented as mean values +/- standard deviation. Data extracted using droplet detection code as described in Supplementary information. Scale bars: 20 μm.

Transcriptional control of nanotube assembly inside droplets.

In living cells, all molecular components are continuously produced and degraded, including those participating in complex cytoskeletal dynamics. To embed a similar architecture in our system, we use a well-characterized *in vitro* strategy to produce RNA molecules from linear DNA templates or synthetic genes using bacteriophage T7 RNA

polymerase (RNAP) inside droplets.[37] The RNA trigger described in the previous section was transcribed inside droplets in the presence of inactive tiles to operate as an activator that promotes growth of encapsulated nanotubes (Fig. 3-5a-c).[36]

First, we investigated how the concentration of template producing trigger RNA affects the temporal evolution of nanotube assembly inside droplets given a fixed concentration of inactive tiles and transcription conditions (buffer mix, NTPs, and RNAP). Simulations using a deterministic ODE model using realistic parameters that capture transcription, RNA-mediated tile activation, and tile assembly (Supplementary information) illustrate that both the kinetics and the fraction of assembled tiles become faster with increasing synthetic gene concentration (Fig. 3-5b). Taking into account loss of activity of RNAP, these simulations also suggest that the equilibrium fraction of assembled tiles can be controlled.

Fig. 3-5d-g show the corresponding experimental results with representative droplet images and skewness/kurtosis plots of DNA-RNA hybrid nanotubes obtained by *in situ* RNA production inside droplets. No assembly occurs in the absence of the synthetic gene, as shown in SI Fig. S3.13. The steady-state values of skewness and kurtosis are reached more rapidly in experiments with higher concentration of genes, presumably due to faster RNA production and tile activation. While this appears to agree with the picture illustrated by the model, several considerations are in order.

First, unlike the two-tile or gel-extracted RNA trigger experiments, nanotubes were not visible via co-transcription without the addition of 2.5% PEG 8000 (SI Fig. S3.14). Through further assays with varied concentrations of PEG added to the encapsulated co-

transcription mix, we determined that a small amount of PEG facilitates visualization of nanotubes during co-transcription of the RNA trigger within droplets. While PEG does not promote aggregation of non-assembling tiles (SI Fig. S3.15), increased amounts of PEG seems to interfere with the tile assembly process and results in aggregation (SI Fig. S3.16). PEG is likely facilitating polymerization, promoting nanotube localization near the droplet surface, as well as enhancing the rate of RNA transcription.[66]

For all conditions, there are a number of droplets smaller than 5 μm in radius in which no nanotubes polymerize. This is likely a result of random partitioning of components across the population of droplets, whose effects are more prominent in smaller volumes: the droplets without any polymerized nanotubes may not encapsulate sufficient amounts of nanotube or transcription components (synthetic gene and RNAP) to trigger assembly. For 7.5 nM template, small nanotubes are visible in droplets larger than 15 μm in diameter by 30 minutes. For droplets of all diameters at this template concentration, nanotubes are visible within 60 minutes and continue to grow through 360 minutes. Before nanotubes have polymerized, skewness and kurtosis are near 0 with small variation across sampled droplets. As nanotubes polymerize, the average skewness and kurtosis values increase, as well as their standard deviation. Notably, nanotubes form in droplets at a lower concentration of template than previously reported in bulk solution by Agarwal et al. Although this is likely the result of the presence of the crowding agent PEG, confinement may contribute to lowering the minimum threshold of active tiles for nucleation and assembly of nanotubes, thus reducing the required transcription rate. At high gene concentration (50 and 100 nM), bright spots indicative of nanotube assembly are visible immediately after encapsulation. In smaller droplets (3-7

μm radius), a single nanotube often forms within the first 15 minutes but does not appear to elongate further. In larger droplets (>8 μm radius), branching nanotubes and aggregates are visible within 15 minutes, suggesting that overproduction of RNA promotes formation of incorrect assemblies, as individual tiles may bind to two RNA trigger strands. Consistently higher values of average skewness and kurtosis from the beginning of the experiment confirm that assembly or aggregation occur rapidly after inactive tiles are mixed with transcription components.

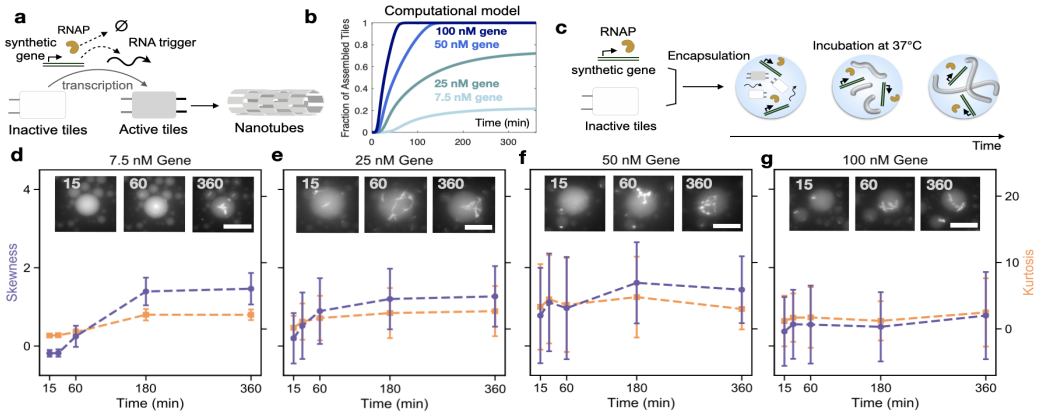

Figure 3-5: Co-transcriptional isothermal assembly of encapsulated hybrid DNA-RNA nanotubes with in-situ trigger transcription at 37°C. (a) Inactive tiles are activated by an RNA trigger transcribed using a synthetic gene and subsequently assemble into nanotubes. (b) A computational model illustrates that by increasing the concentration of synthetic gene template, we can speed up the assembly kinetics and increase the equilibrium fraction of assembled tiles. Increasing amounts of gene template are represented with darker shades of blue. (c) Inactive tiles at 500 nM concentration were encapsulated with transcription mix, 2.5% w/v PEG, and 2.5% v/v RNAP and incubated at 37°C. (d-g) Representative fluorescence microscopy images of droplet samples in which we titrated the amount of synthetic gene transcribing RNA trigger (insets) with plots of mean skewness (purple) and kurtosis (orange) for sampled droplets. The rate of increase of skewness and kurtosis correlates with the concentration of DNA template producing the trigger RNA strand. Data is presented as mean values +/- standard deviation. Images were processed using the droplet detection code as described in Supplementary information. Scale bars: 20 μm.

Transient nanotubes formation inside droplets arising from simultaneous RNA transcription and degradation.

Next, we sought to introduce nanotube disassembly using RNase H, an enzyme that hydrolyzes RNA in DNA-RNA complexes (Fig. 3-6a). RNase H has been widely used to control degradation in a variety of artificial *in vitro* transcriptional circuits as well as within nanotube systems.[35] We previously showed that RNase H can deactivate free (unpolymerized) tiles by degrading the portion of RNA trigger bound to DNA promoting nanotube disassembly.[35,36] When both RNAP and RNase H are present with inactive tiles and transcription reagents in non-encapsulated solutions, a transient pulse of nanotube assembly was observed.[36] This pulse may be attributed to a progressive loss of activity of RNAP relative to the initial transcription “burst”, and to accumulation of incomplete RNase H degradation products.[67-69] Fig. 3-6b illustrates the predictions of our unfitted computational model capturing transcription (including loss of RNAP activity), tile activation and assembly, as well as RNase H degradation: the model qualitatively predicts a pulse in fraction of assembled tiles, and the height and duration of this pulse depend on the amount of RNase H present. Thus, we expect to see this encapsulated system to yield transient nanotube assembly, with dynamics that can be tuned by changing the amount of RNase H.

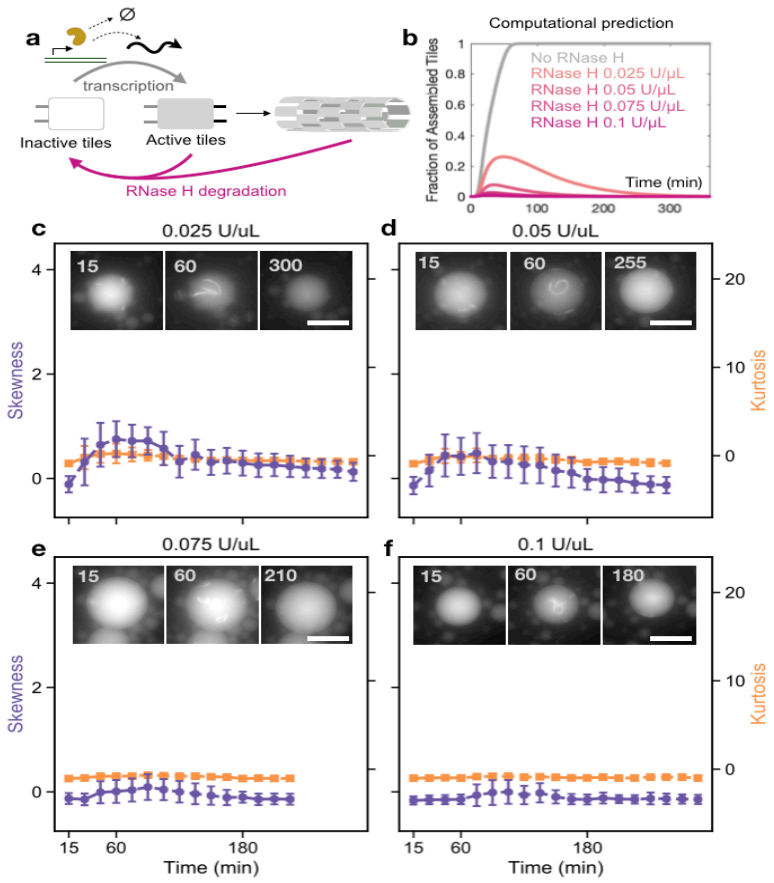

Figure 3-6: Enzyme-mediated control of assembly and disassembly of encapsulated hybrid DNA-RNA tubes at 37°C. (a) Schematic of the reactions occurring in a sample that includes inactive tiles, DNA template transcribing the RNA trigger (promoting growth of nanotubes), and RNase H (promoting degradation of nanotubes). (b) Computational prediction showing that loss of activity of RNAP against unchanged RNase H activity yields a temporal pulse in the fraction of assembled tiles, whose peak and duration depend on the amount of RNase H. Increasing amounts of RNase H are represented with darker shades of pink. (c-f) Representative fluorescence microscopy images of the RNase H titration experiments (insets) with plots of mean skewness (purple) and kurtosis (orange) for sampled droplets. Inactive tiles at 500 nM concentration were encapsulated with 100 nM gene template, 2.5% w/v PEG, 2.5% v/v RNAP, and 0.025 U/μL-0.1 U/μL RNase H. These experimental results show that, when RNA trigger transcription and degradation components are simultaneously present, a pulse of nanotube polymerization is observed. Eventually RNase H causes disassembly of the nanotubes at a speed that depends on the RNase H concentration, presumably due to a decrease of RNAP activity. Skewness and kurtosis are plotted in shades of purple and orange respectively. Data is presented as mean values +/- standard deviation. Data extracted using droplet detection code as described in Supplementary information. Scale bars: 20 μm.

We observed transient nanotube formation in droplets for different concentrations of RNase H, while the inactive tile concentration was kept at 500 nM, template at 100 nM,

and 2.5% v/v of T7 RNAP (Fig. 3-6c-f and Supplementary Movie 4). In the absence of RNase H, droplets with synthetic gene at 50 and 100 nM showed nanotube aggregation likely due to overproduction of RNA trigger (Fig. 3-5f-g). In the presence of RNase H such aggregation was not visible. The skewness and kurtosis plots exhibit a transient pulse and a small standard deviation when compared to experiments that do not include both transcription and degradation, presumably due to most tiles remaining unassembled throughout the experiment. At lower amounts of RNase H, 0.025 U/μL and 0.05 U/μL, nanotubes are visible until about 3 hours after encapsulation (Fig. 3-6cd). At higher amounts of RNase H, assembly is delayed and fewer nanotubes are visible, confirming that it is possible to tune the temporal response of assembly and the nanotube density inside the compartments (Fig. 3-6ef). At 0.05 U/μL RNase H and higher, many nanotubes appear to curl into loops in most droplets. It is unclear what is causing this morphology, but it could be a result of both crowding and degradation of RNA. As the density and dynamics of nanotubes inside droplets depends on transcription and degradation rates, both characteristics may be controlled by changing either the relative concentration of enzymes or synthetic gene for RNA production.

These experiments indicate that more complex genetic programs relying on RNA production and degradation may be encapsulated to control nanotube assembly.[35] A notable challenge toward sustained transcription and degradation dynamics is the accumulation of abortive and elongated transcripts, which can cause side reactions and crosstalk.[70] These undesired transcripts may bind to inactive tiles producing “waste” complexes that can no longer be activated by the correct RNA trigger.[36] Additional RNases may be included to reduce the influence of “waste” products in the system.[71]

3.4 Methods

DNA oligonucleotides and enzymes: Oligonucleotides were purchased from IDT DNA. T7 RNAP was purchased from Lucigen®, and RNase H was purchased from Promega™. Transcription reagents were purchased from Lucigen® and New England Biolabs. Oligonucleotide sequences and modifications, as well as further details on the preparation of DNA nanotubes and transcription reactions, are available in the Supplementary Information (Section 3.7).

Generation of microemulsion droplets: Two alternative methods for the generation of the microdroplets were employed. The first method, or 'shaken method', consisted in simply vortexing a emulsion of oil-surfactant mixture and aqueous buffer solution that contained the reagents. By adjusting mixing time and vortexing speed appropriately, we generated populations of droplets with a broad size distribution, with radii ranging from ~1 μm to >20 μm. 100 μl of droplet emulsion was generated by mixing 20 μl reaction mix with 80 μl of oil-surfactant mix (FC-40 Fluorinert™ oil (86508-42-1, Sigma-Aldrich) that contained 2% (w/v) perfluoropolyether-polyethylene glycol (PFPE-PEG) block-copolymer fluorosurfactant with Krytox-FSH via an amide group (Ran Biotechnologies)) in DNA LoBind tubes (Eppendorf) using a vortex mixer for 60 seconds. The second method consisted in using microfluidic chips to generate emulsions. This allowed us to produce large numbers of droplets with a much narrower size distribution (Fig 1d) but it was technically challenging to produce very small droplets with diameters smaller than 20 μm. For these reasons, we adopted the shaken method for all experiments reported in this paper, except for those reported in Fig. 3-1d.

Fluorescence time lapse experiments: Droplet samples were imaged using an inverted microscope (Nikon Eclipse TI-E) with Nikon Plan Fluor 20X/0.5 NA objectives. Droplets were placed in Ibidi chamber slides (µ-Slide VI $^{0.4}$, hydrophobic coating) with the inputs to the channels sealed with vacuum grease (Dow Corning®) and VWR micro slides to prevent evaporation throughout experiments. Droplets encapsulating transcription reactions were incubated in the Ibidi chambers on a ThermoPlate (Nikon Inc, Tokai Hit) set to 37°C during imaging.

Confocal fluorescence microscopy: Droplet samples were imaged in an Ibidi chamber slide (µ-Slide VI $^{0.1}$, hydrophobic coating) on a Leica TCS SP8-STED confocal microscope with 63x/1.20 NA water-immersion objective

Image analysis and data processing: Droplets were monitored for up to 24 h and images were processed using an in-house PYTHON scripts to identify droplets and extract pixel brightness values from fluorescence images. The code is available through a Github repository, but is also available upon request from the authors. To measure the skewness and kurtosis for the distribution of pixel brightness values extracted for each droplet, first a list of unique pixel brightness values was calculated for each droplet based on the number of pixels in each bin and the bin width of the histogram for each droplet. Then skewness and kurtosis are calculated for the unique pixel brightness values list using the skew and kurtosis functions in the Python Pandas library. The average skewness and kurtosis values, along with the standard deviation for each measurement, was calculated for all droplets measured at each time point of each experiment. Standard deviation was chosen over the variance or other measurements as it represents the spread of the values across the measure samples. Further details for the same are available in the SI.

3.5 Conclusion

We demonstrated the construction of artificial dynamic scaffolding systems for minimal cell mimics through the assembly of NA tubular nanostructures inside water-in-oil droplets. When compared to cytoskeletal scaffolds in biological cells, NA nanotubes offer similar structural features with a minimal number of components required for assembly and regulation.[22,35] We established that nanotube assemblies can be obtained with four different tile (monomer) designs, a toolkit that can be easily expanded. Monomers can be annealed inside droplets or pre-annealed and subsequently encapsulated. We showed that distinct, non-interacting tile types can be encapsulated and assembled simultaneously, making it possible to build distinct scaffolds. Conversely, we verified that encapsulated tiles and NA strands designed to interact generate the desired products, which is consistent with the outcome of non-encapsulated reactions. Finally, nanotube assembly was modularly integrated with RNA transcription and degradation processes, whose competition enabled the dynamic, autonomous control of self-assembly inside droplets.[36] It is remarkable that the encapsulation methods described here make it possible to operate NA structures and circuits with marginal deviation from their non-encapsulated behavior.

We have characterized different methods for scaffold encapsulation, focusing on an emulsion method that generates stable droplets with a broad range of sizes and compositional diversity. These droplets are ideal for long-term observation of nanotube assembly, however they appear inadequate to explore the capacity of nanotubes to induce compartment deformation. Control of compartment deformation has been

demonstrated using cytoskeletal polymers, by tuning compartment rigidity and size, and the stiffness of the polymers, in agreement with computational predictions.[72-74] Similar shape control could be achieved with DNA filament systems, where stiffness may be changed by tuning nanotube design or by forming nanotube networks.[75] Nanotubes may be encapsulated in liposomal and phase separated (membrane less) synthetic cells that have been used to compartmentalize various proteins and synthetic circuits.[11,76-79] However, preliminary investigations revealed many challenges in obtaining high yield encapsulation of DNA structures in cell-sized vesicles. These challenges include the selection of lipids that generate stable vesicles with minimal surface interaction with DNA nanostructures, and of methods which produce a high yield of vesicles with controllable size while avoiding damage to the nanostructures.[40,80,81] A promising route is given by microfluidic approaches that make it possible to build cell-sized vesicles with control over their membrane and internal composition.[82,83]

To track the growth of NA scaffolds in time, we complemented qualitative observations with a quantitative method that tracks statistical properties of droplet epifluorescence microscopy images. We showed that skewness and kurtosis (third and fourth moment) of intensity histograms provide high-throughput information about the extent of monomer condensation. While this statistical analysis alone does not allow for distinguishing correct and incorrect assemblies, it makes it possible to compare tile condensation in a large population of droplets under different concentrations of monomers, crowding agents, synthetic genes, as well as enzymes. We found significant diversity of condensation extent across droplets, with smaller droplets presenting the highest variability, which is likely the result of several phenomena including partitioning

noise, assembly errors, and surface interactions that may promote uneven bundling of nanotubes. Such variability increases when assembly is triggered by RNA molecules that may generate more incorrect assemblies and undesired aggregates. However, the simultaneous presence of enzymes producing and degrading RNA appears to reduce variability, as quantified by our statistical measures, a counterintuitive result given that additional interacting species are expected to amplify the effects of partitioning noise.[37] It is likely that a lower standard deviation of both skewness and kurtosis is simply due to the fact that most tiles remain unpolymerized in the presence of RNase H.

Our study points to the potential application of NA nanostructures as a rich toolkit for generating complex scaffolding components in artificial cells. Our demonstration could be immediately expanded to include multiple filamentous scaffolds to spatially organize distinct organic or inorganic ligands, and each scaffold may be individually controlled by distinct synthetic genes or circuits.[84] As chemically modified nanotubes can be made resilient to cytoplasmic conditions, they could be controlled through a multitude of circuit parts involving transcription-translation.[85,86] While we focused on assembly of one class of filamentous structures from tiles, similar tile variants can be used to build fibers and two dimensional assemblies, and RNA variants may be produced co-transcriptionally.[24,87] While our work falls short of seeking to mimic active cytoskeletal behaviors, these nanotubes may be used as tracks for molecular motors that could perform work and transfer cargo within compartments.[22,88,89] Further, NA nanotubes could be organized in higher-order structures using other types of assemblies such as DNA origami.[90] Finally, because NA scaffold assembly can be regulated by complex synthetic gene networks and strand displacement reactions within

compartments, the coordination of multi-compartment behavior through diffusing molecules could open up exciting opportunities to build artificial tissues with programmable development and patterning.[40,91]

3.6 References

1 Nguyen, P. Q., Courchesne, N. M. D., Duraj-Thatte, A., Praveschotinunt, P. & Joshi, N. S. Engineered living materials: prospects and challenges for using biological systems to direct the assembly of smart materials. *Advanced Materials* 30, 1704847 (2018).

2 Göpfrich, K., Platzman, I. & Spatz, J. P. Mastering complexity: towards bottom-up construction of multifunctional eukaryotic synthetic cells. *Trends in biotechnology* 36, 938-951 (2018).

3 Vignaud, T., Blanchoin, L. & Théry, M. Directed cytoskeleton self-organization. *Trends in cell biology* 22, 671-682 (2012).

4 Marguet, M., Bonduelle, C. & Lecommandoux, S. Multicompartmentalized polymeric systems: towards biomimetic cellular structure and function. *Chemical Society Reviews* 42, 512-529 (2013).

5 Bashirzadeh, Y. & Liu, A. P. Encapsulation of the cytoskeleton: towards mimicking the mechanics of a cell. *Soft Matter* 15, 8425-8436 (2019).

6 Hürtgen, D., Vogel, S. K. & Schwille, P. Cytoskeletal and Actin-Based Polymerization Motors and Their Role in Minimal Cell Design. *Advanced Biosystems* 3, 1800311 (2019).

7 Miyazaki, M., Chiba, M., Eguchi, H., Ohki, T. & Ishiwata, S. i. Cell-sized spherical confinement induces the spontaneous formation of contractile actomyosin rings in vitro. *Nature cell biology* 17, 480-489 (2015).

8 Ierushalmi, N. *et al.* Centering and symmetry breaking in confined contracting actomyosin networks. *Elife* 9, e55368 (2020).

9 Sato, Y., Hiratsuka, Y., Kawamata, I., Murata, S. & Nomura, S.-i. M. Micrometer-sized molecular robot changes its shape in response to signal molecules. *Sci. Robot* 2 (2017).

10 Dürre, K. *et al.* Capping protein-controlled actin polymerization shapes lipid membranes. *Nature communications* 9, 1-11 (2018).

11 Fanalista, F. *et al.* Shape and size control of artificial cells for bottom-up biology. *ACS nano* 13, 5439-5450 (2019).

12 Shah, E. A. & Keren, K. Symmetry breaking in reconstituted actin cortices. *Elife* 3, e01433 (2014).

13 Malik-Garbi, M. *et al.* Scaling behaviour in steady-state contracting actomyosin networks. *Nature physics* 15, 509-516 (2019).

14 Vogel, S. K. *et al.* Symmetry breaking and emergence of directional flows in minimal actomyosin cortices. *Cells* 9, 1432 (2020).

15 Estirado, E. M., Mason, A. F., García, M. A. n. A. n., van Hest, J. C. & Brunsveld, L. Supramolecular Nanoscaffolds within Cytomimetic Protocells as Signal Localization Hubs. *Journal of the American Chemical Society* 142, 9106 (2020).

16 Schoonen, L. & van Hest, J. C. Compartmentalization approaches in soft matter science: from nanoreactor development to organelle mimics. *Advanced Materials* 28, 1109-1128 (2016).

17 Downs, F. G. *et al.* Multi-responsive hydrogel structures from patterned droplet networks. *Nature Chemistry* 12, 363-371 (2020).

18 Seeman, N. C. & Sleiman, H. F. DNA nanotechnology. *Nature Reviews Materials* 3, 17068 (2017).

19 Simmel, F. C., Yurke, B. & Singh, H. R. Principles and applications of nucleic acid strand displacement reactions. *Chemical reviews* 119, 6326-6369 (2019).

20 Zadeh, J. N. *et al.* NUPACK: Analysis and design of nucleic acid systems. *Journal of computational chemistry* 32, 170-173 (2011).

21 Mitchell, J. C., Harris, J. R., Malo, J., Bath, J. & Turberfield, A. J. Self-assembly of chiral DNA nanotubes. *Journal of the American Chemical Society* 126, 16342-16343 (2004).

22 Rothemund, P. W. *et al.* Design and characterization of programmable DNA nanotubes. *Journal of the American Chemical Society* 126, 16344-16352 (2004).

23 Ko, S. H. *et al.* Synergistic self-assembly of RNA and DNA molecules. *Nature chemistry* 2, 1050 (2010).

24 Stewart, J. M., Geary, C. & Franco, E. Design and characterization of RNA nanotubes. *ACS nano* 13, 5214-5221 (2019).

25 Rothemund, P. W. Folding DNA to create nanoscale shapes and patterns. *Nature* 440, 297-302 (2006).

26 Agrawal, D. K. *et al.* Terminating DNA tile assembly with nanostructured caps. *ACS nano* 11, 9770-9779 (2017).

27 Mohammed, A. *et al.* Self-assembly of precisely defined DNA nanotube superstructures using DNA origami seeds. *Nanoscale* 9, 522-526 (2017).

28 Srinivas, N., Parkin, J., Seelig, G., Winfree, E. & Soloveichik, D. Enzyme-free nucleic acid dynamical systems. *Science* 358 (2017).

29 Thubagere, A. J. *et al.* Compiler-aided systematic construction of large-scale DNA strand displacement circuits using unpurified components. *Nature communications* 8, 1-12 (2017).

30 Chatterjee, G., Chen, Y.-J. & Seelig, G. Nucleic acid strand displacement with synthetic mRNA inputs in living mammalian cells. *ACS synthetic biology* 7, 2737-2741 (2018).

31 Kim, J., White, K. S. & Winfree, E. Construction of an in vitro bistable circuit from synthetic transcriptional switches. *Molecular systems biology* 2, 68 (2006).

32 Jung, C. & Ellington, A. D. Diagnostic applications of nucleic acid circuits. *Accounts of chemical research* 47, 1825-1835 (2014).

33 Schaffter, S. W. & Schulman, R. Building in vitro transcriptional regulatory networks by successively integrating multiple functional circuit modules. *Nature chemistry* 11, 829-838 (2019).

34 Green, L. N., Amodio, A., Subramanian, H. K. K., Ricci, F. & Franco, E. pH-Driven Reversible Self-Assembly of Micron-Scale DNA Scaffolds. *Nano Letters* 17, 7283-7288, doi:10.1021/acs.nanolett.7b02787 (2017).

35 Green, L. N. *et al.* Autonomous dynamic control of DNA nanostructure self-assembly. *Nature chemistry* 11, 510-520 (2019).

36 Agarwal, S. & Franco, E. Enzyme-driven assembly and disassembly of hybrid DNA–RNA nanotubes. *Journal of the American Chemical Society* 141, 7831-7841 (2019).

37 Weitz, M. *et al.* Diversity in the dynamical behaviour of a compartmentalized programmable biochemical oscillator. *Nature chemistry* 6, 295-302 (2014).

38 Genot, A. *et al.* High-resolution mapping of bifurcations in nonlinear biochemical circuits. *Nature chemistry* 8, 760 (2016).

39 Jeong, D. *et al.* Cell-free synthetic biology platform for engineering synthetic biological circuits and systems. *Methods and protocols* 2, 39 (2019).

40 Dupin, A. & Simmel, F. C. Signalling and differentiation in emulsion-based multi-compartmentalized in vitro gene circuits. *Nature chemistry* 11, 32-39 (2019).

41 Joesaar, A. *et al.* DNA-based communication in populations of synthetic protocells. *Nature nanotechnology* 14, 369-378 (2019).

42 Krishnan, S. *et al.* Molecular transport through large-diameter DNA nanopores. *Nature communications* 7, 1-7 (2016).

43 Hoerstrup, S. *et al.* Optimized growth conditions for tissue engineering of human cardiovascular structures. *The International Journal of Artificial Organs* 23, 817-823 (2000).

44 Franquelim, H. G., Khmelinskaia, A., Sobczak, J.-P., Dietz, H. & Schwille, P. Membrane sculpting by curved DNA origami scaffolds. *Nature communications* 9, 1-10 (2018).

45 Zhang, Y. *et al.* Multivalent, multiflavored droplets by design. *Proceedings of the National Academy of Sciences* 115, 9086-9091 (2018).

46 Kurokawa, C. *et al.* DNA cytoskeleton for stabilizing artificial cells. *Proceedings of the National Academy of Sciences* 114, 7228-7233 (2017).

47 Watanabe, T. *et al.* DNA origami “quick” refolding inside of a micron-sized compartment. *Molecules* 25, 8 (2020).

48 Göpfrich, K. *et al.* Dynamic actuation of DNA-assembled plasmonic nanostructures in microfluidic cell-sized compartments. *Nano letters* 20, 1571-1577 (2020).

49 Yin, P. *et al.* Programming DNA tube circumferences. *science* 321, 824-826 (2008).

50 Ekani-Nkodo, A., Kumar, A. & Fygenson, D. K. Joining and scission in the self-assembly of nanotubes from DNA tiles. *Physical review letters* 93, 268301 (2004).

51 Fu, T. J. & Seeman, N. C. DNA double-crossover molecules. *Biochemistry* 32, 3211-3220 (1993).

52 Holtze, C. *et al.* Biocompatible surfactants for water-in-fluorocarbon emulsions. *Lab on a Chip* 8, 1632-1639, doi:10.1039/B806706F (2008).

53 Weitz, M. *et al.* Communication and Computation by Bacteria Compartmentalized within Microemulsion Droplets. *Journal of the American Chemical Society* 136, 72-75, doi:10.1021/ja411132w (2014).

54 O'Neill, P., Rothemund, P. W. K., Kumar, A. & Fygenson, D. K. Sturdier DNA Nanotubes via Ligation. *Nano Letters* 6, 1379-1383, doi:10.1021/nl0603505 (2006).

55 Baumann, H. & Surrey, T. Motor-mediated cortical versus astral microtubule organization in lipid-monolayered droplets. *J Biol Chem* 289, 22524-22535, doi:10.1074/jbc.m114.582015 (2014).

56 Hariadi, R. F., Appukutty, A. J. & Sivaramakrishnan, S. Engineering Circular Gliding of Actin Filaments Along Myosin-Patterned DNA Nanotube Rings To Study Long-Term Actin–Myosin Behaviors. *ACS nano* 10, 8281-8288 (2016).

57 von Hippel, P. T. Mean, Median, and Skew: Correcting a Textbook Rule. *Journal of Statistics Education* 13, null-null, doi:10.1080/10691898.2005.11910556 (2005).

58 DeCarlo, L. T. On the meaning and use of kurtosis. *Psychological Methods* 2, 292-307, doi:https://doi.org/10.1037/1082-989X.2.3.292 (1997).

59 Fisher, R. A. Statistical methods for research workers. *Springer*, 66-70, doi:https://doi.org/10.1007/978-1-4612-4380-9_6 (1992).

60 Higaki, T., Kutsuna, N., Sano, T., Kondo, N. & Hasezawa, S. Quantification and cluster analysis of actin cytoskeletal structures in plant cells: role of actin bundling in stomatal movement during diurnal cycles in Arabidopsis guard cells. *plant journal* 61, 156-165, doi:10.1111/J.1365-313X.2009.04032.X (2010).

61 Pal, A., Gope, A. & Iannacchione, G. S. A Comparative Study of the Phase Separation of a Nematic Liquid Crystal in the Self-assembling Drying Protein Drops. *mrs advances* 4, 1309-1314, doi:10.1557/ADV.2019.209 (2019).

62 M.A. Klocke, Pungchai, P. Dynamic self-assembly of compartmentalized DNA nanotubes, dropletDetection_dynamicSelfAssemblyProject. *Zenodo*, doi:10.5281/zenodo.4763253 (2021).

63 Zhang, D. Y., Hariadi, R. F., Choi, H. M. T. & Winfree, E. Integrating DNA strand-displacement circuitry with DNA tile self-assembly. *Nature Communications* 4, 1965, doi:10.1038/ncomms2965 (2013).

64 Mardanlou, V. *et al.* A coarse-grained model captures the temporal evolution of DNA nanotube length distributions. *Natural Computing* 17, 183-199 (2018).

65 Monferrer, A., Zhang, D., Lushnikov, A. J. & Hermann, T. Versatile kit of robust nanoshapes self-assembling from RNA and DNA modules. *Nature Communications* 10, 608 (2019).

66 Chung, S. *et al.* The effect of macromolecular crowding on single-round transcription by Escherichia coli RNA polymerase. *nucleic acids research* 47, 1440-1450, doi:10.1093/NAR/GKY1277 (2019).

67 Jia, Y. & Patel, S. S. Kinetic Mechanism of Transcription Initiation by Bacteriophage T7 RNA Polymerase. *biochemistry* 36, 4223-4232, doi:10.1021/BI9630467 (1997).

68 Lima, W. F. & Crooke, S. T. Cleavage of single strand RNA adjacent to RNA-DNA duplex regions by Escherichia coli RNase H1. *Journal of Biological Chemistry* 272, 27513-27516 (1997).

69 Kim, J. & Winfree, E. Synthetic in vitro transcriptional oscillators. *Molecular systems biology* 7, 465 (2011).

70 Schaffter, S. W. *et al.* T7 RNA polymerase non-specifically transcribes and induces disassembly of DNA nanostructures. *Nucleic acids research* 46, 5332-5343 (2018).

71 Subsoontorn, P., Kim, J. & Winfree, E. Ensemble Bayesian analysis of bistability in a synthetic transcriptional switch. *acs synthetic biology* 1, 299-316, doi:10.1021/SB300018H (2012).

72 Pinot, M. *et al.* Effects of Confinement on the Self-Organization of Microtubules and Motors. *Curr. Biol.* 19, 954-960, doi:10.1016/J.CUB.2009.04.027 (2009).

73 Tsai, F.-C. & Koenderink, G. H. Shape control of lipid bilayer membranes by confined actin bundles. *soft matter* 11, 8834-8847, doi:10.1039/C5SM01583A (2015).

74 Fošnarič, M., Iglič, A., Kroll, D. M. & May, S. Monte Carlo simulations of a polymer confined within a fluid vesicle. *soft matter* 9, 3976-3984, doi:10.1039/C3SM27938C (2013).

75 Schaffter, S. W. *et al.* Reconfiguring DNA Nanotube Architectures via Selective Regulation of Terminating Structures. *acs nano*, doi:10.1021/ACSNANO.0C05340 (2020).

76 Adamala, K. P., Martin-Alarcon, D. A., Guthrie-Honea, K. R. & Boyden, E. S. Engineering genetic circuit interactions within and between synthetic minimal cells. *nature chemistry* 9, 431-439, doi:10.1038/NCHEM.2644 (2017).

77 Donau, C. *et al.* Active coacervate droplets as a model for membraneless organelles and protocells. *nature communications* 11, doi:10.1038/S41467-020-18815-9 (2020).

78 Deshpande, S. *et al.* Spatiotemporal control of coacervate formation within liposomes. *nature communications* 10, doi:10.1038/S41467-019-09855-X (2019).

79 Sato, Y., Sakamoto, T. & Takinoue, M. Sequence-based engineering of dynamic functions of micrometer-sized DNA droplets. *Science Advances* 6, eaba3471 (2020).

80 Noireaux, V. & Libchaber, A. A vesicle bioreactor as a step toward an artificial cell assembly. *Proc. Natl. Acad. Sci. U. S. A.* 101, 17669-17674, doi:10.1073/PNAS.0408236101 (2004).

81 Saha, R., Verbanic, S. & Chen, I. A. Lipid vesicles chaperone an encapsulated RNA aptamer. *nature communications* 9, 2313-2313, doi:10.1038/S41467-018-04783-8 (2018).

82 Matosevic, S. & Paegel, B. M. Layer-by-layer cell membrane assembly. *nature chemistry* 5, 958-963, doi:10.1038/NCHEM.1765 (2013).

83 Weiss, M. *et al.* Sequential bottom-up assembly of mechanically stabilized synthetic cells by microfluidics. *nature materials* 17, 89-96, doi:10.1038/NMAT5005 (2018).

84 Liu, X. *et al.* Biomimetic DNA Nanotubes: Nanoscale Channel Design and Applications. *angewandte chemie* 58, 8996-9011, doi:10.1002/ANIE.201807779 (2019).

85 Klocke, M. A., Garamella, J., Subramanian, H. K., Noireaux, V. & Franco, E. Engineering DNA nanotubes for resilience in an E. coli TXTL system. *Synthetic Biology* 3, ysy001 (2018).

86 Laohakunakorn, N. *et al.* Bottom-Up Construction of Complex Biomolecular Systems With Cell-Free Synthetic Biology. *frontiers in bioengineering and biotechnology* 8, doi:10.3389/FBIOE.2020.00213 (2020).

87 Delebecque, C. J., Lindner, A. B., Silver, P. A. & Aldaye, F. A. Organization of Intracellular Reactions with Rationally Designed RNA Assemblies. *science* 333, 470-474, doi:10.1126/SCIENCE.1206938 (2011).

88 Hariadi, R. F., Yurke, B. & Winfree, E. Toward De Novo Recapitulation of Cytoskeleton Dynamics with DNA Nanotubes. *biophysical journal* 98, doi:10.1016/J.BPJ.2009.12.3014 (2010).

89 Thubagere, A. J. *et al.* A cargo-sorting DNA robot. *science* 357, doi:10.1126/SCIENCE.AAN6558 (2017).

90 Jorgenson, T. D., Mohammed, A. M., Agrawal, D. K. & Schulman, R. Self-Assembly of Hierarchical DNA Nanotube Architectures with Well-Defined Geometries. *acs nano* 11, 1927-1936, doi:10.1021/ACSNANO.6B08008 (2017).

91 Gruner, P. *et al.* Controlling molecular transport in minimal emulsions. *nature communications* 7, 10392-10392, doi:10.1038/NCOMMS10392 (2016).

3.7 Supplementary Information

PAGE purified DNA sequences were ordered from IDT DNA (Coralville, IA, USA). Sequences of strands composing the tiles are taken from Rothemund et al., 2004[1] and Agarwal & Franco, 2019[2].

In addition to reporting DNA sequences, this section also includes schematics representing each tile type. Red circles on the blue strand represent the location Cy3 or ATTO647N fluorophores as stated in the strand sequence.

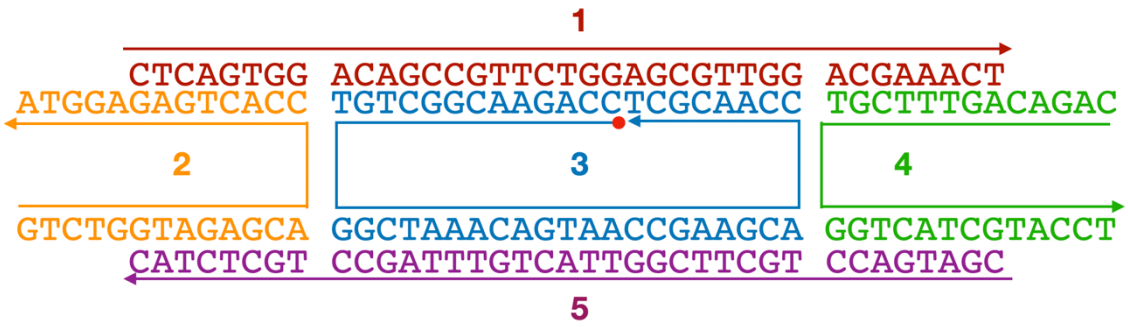

Figure S3.1: Tile designed for assembly of single-tile nanotubes, design variant 1.

Strand position	Name	Sequence
1	5bSE1	5’- CTC AGT GGA CAG CCG TTC TGG AGC GTT GGA CGA AAC T
2	5bSE2	5’- GTC TGG TAG AGC ACC ACT GAG AGG TA
2T	5bSE2 T	5’-G TCT GGT AGA GCA CCA CTG AGA GGT A
3	5bSE3	5’- cy3-CCA GAA CGG CTG TGG CTA AAC AGT AAC CGA AGC ACC AAC GCT
4	5bSE4	5’- CAG ACA GTT TCG TGG TCA TCG TAC CT
5	5bSE5	5’- CGA TGA CCT GCT TCG GTT ACT GTT TAG CCT GCT CTA C

Table S3.1: DNA sequences for single-tile nanotubes. Nomenclature of the sequences in the table reflects labeling of strands in the lab and the original name of the strands in the paper by Rothemund et al., 2004[1]. The ‘5bSE2 T’ strand was used during encapsulation of nanotubes by microfluidics (Fig 1d, SI section S4.8) and includes a short single stranded toehold that does not affect the assembly pathway.

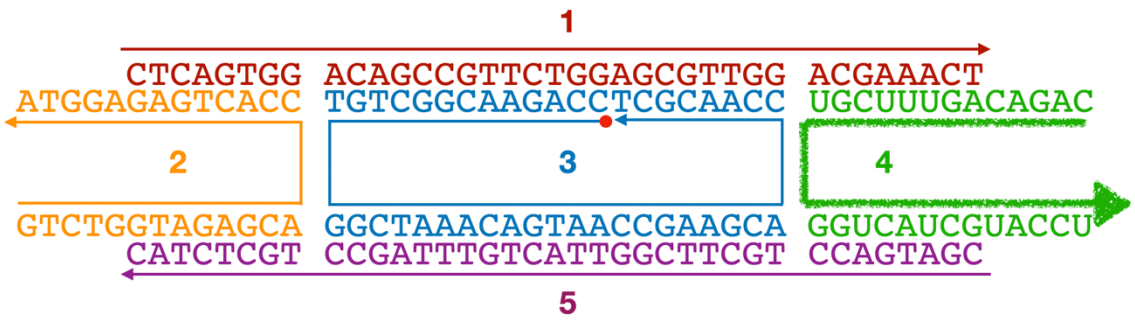

Figure S3.2: DNA-RNA hybrid tile. Strand 4 is an RNA molecule.

Strand position	**Name**	**Sequence**
1	5bSE1	5'- CTC AGT GGA CAG CCG TTC TGG AGC GTT GGA CGA AAC T
2	5bSE2	5'- GTC TGG TAG AGC ACC ACT GAG AGG TA
3	5bSE3	5'- cy3-CCA GAA CGG CTG TGG CTA AAC AGT AAC CGA AGC ACC AAC GCT
4	**RNA-5bSE4**	**5'- CAG ACA GUU UCG UGG UCA UCG UAC CU**
5	5bSE5	5'- CGA TGA CCT GCT TCG GTT ACT GTT TAG CCT GCT CTA C

Table S3.2: DNA sequences for the DNA-RNA hybrid nanotubes. Bold indicates RNA strand.

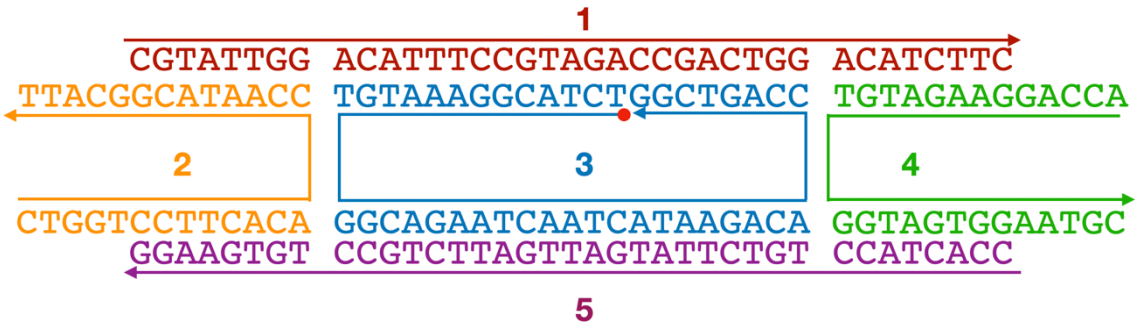

Figure S3.3: Tile designed for single-tile nanotube assembly, design variant 2.

Strand position	Name	Sequence
1	5bRE1	5'- CGT ATT GGA CAT TTC CGT AGA CCG ACT GGA CAT CTT C
2	5bRE2	5'- CTG GTC CTT CAC ACC AAT ACG GCA TT
3	5bRE3	5'- atto647N-TCT ACG GAA ATG TGG CAG AAT CAA TCA TAA GAC ACC AGT CGG
4	5bRE4	5'- ACC AGG AAG ATG TGG TAG TGG AAT GC
5	5bRE5	5'- CCA CTA CCT GTC TTA TGA TTG ATT CTG CCT GTG AAG G

Table S3.3: DNA sequences for single tile system, design variant 2. Nomenclature of the sequences in the table reflects labeling of strands in the lab and the original name of this tile variant in the paper by Rothemund et al., 2004[3].

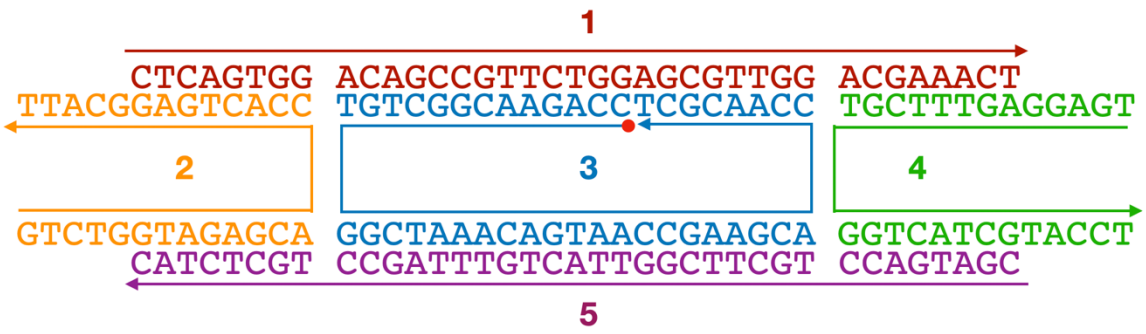

Figure S3.4: Tile A - Tiles designed for two-tile nanotube assembly.

Strand position	**Name**	**Sequence**
1	5bSEp 1	5'- CTC AGT GGA CAG CCG TTC TGG AGC GTT GGA CGA AAC T
2	5bSEp 2	5'- GTC TGG TAG AGC ACC ACT GAG GCA TT
3	5bSEp 3	5'- cy3-CCA GAA CGG CTG TGG CTA AAC AGT AAC CGA AGC ACC AAC GCT
4	5bSEp 4	5'- TGA GGA GTT TCG TGG TCA TCG TAC CT
5	5bSEp 5	5'- CGA TGA CCT GCT TCG GTT ACT GTT TAG CCT GCT CTA C

Table S3.4: DNA sequences of Tile A for nanotube assembly from two tiles. The strand nomenclature reflects the one adopted by Rothemund et al., 2004[1] to describe the two-tile nanotubes in which tiles form a perpendicular, alternated "ring" pattern.

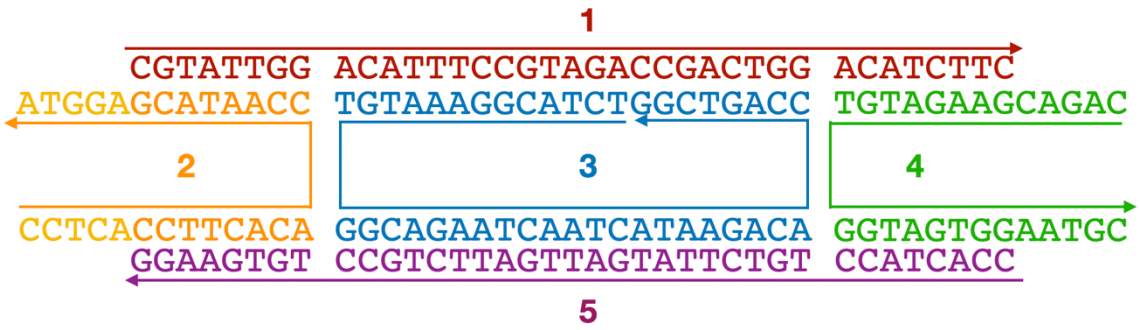

Figure S3.5: Tile B - Tiles designed for two-tile nanotube assembly.

Strand position	**Name**	**Sequence**
1	5bREp 1	5'- CGT ATT GGA CAT TTC CGT AGA CCG ACT GGA CAT CTT C
2	5bREp 2	5'- CCT CAC CTT CAC ACC AAT ACG AGG TA
3	5bREp 3	5'- TCT ACG GAA ATG TGG CAG AAT CAA TCA TAA GAC ACC AGT CGG
4	5bREp 4	5'- CAG ACG AAG ATG TGG TAG TGG AAT GC
5	5bREp 5	5'- CCA CTA CCT GTC TTA TGA TTG ATT CTG CCT GTG AAG G

Table S3.5: DNA sequences of Tile B for nanotube assembly from two tiles. The strand nomenclature reflects the one adopted by Rothemund et al., 2004[1] to describe the two-tile nanotubes in which tiles form a perpendicular, alternated "ring" pattern.

Synthetic genes for production of RNA strands

Templates (genelets) include 4 base "sealing" domains in genes at the 5' end of non-template strand, to prevent breathing at the promoter site. Each RNA strand was designed to start with 'G' on the 3' end, to ensure good transcription yield[2,4].

NonTemplate	5'- GCG CTA ATA CGA CTC ACT ATA GCA GAC AGT TTC GTG GTC ATC GTA CCT
Template	5'- AGG TAC GAT GAC CAC GAA ACT GTC TGC TAT AGT GAG TCG TAT TAG CGC

Table S3.6: DNA sequences of the synthetic gene designed to produce RNA trigger (5BSE4).

Reagents

Oligonucleotides: Lyophilized, PAGE-purified DNA oligonucleotides were purchased from Integrated DNA Technologies (Coralville, IA). All strands were resuspended in nuclease free water (Thermo Fisher Cat. no. AM9932), quantitated by UV absorbance at 260 nm using a Thermo Scientific Nanodrop 2000c Spectrophotometer, and stored at -20°C. RNA strands were transcribed, and gel-extracted in house according to the protocol in SI Section S4.12.

Enzymes: T7 RNA Polymerase was purchased from Lucigen® as part of the AmpliScribe™ T7-Flash™ Transcription Kit (Cat. No. ASF3507). RNase H was purchased from Promega™ (Ref. No. M4281, 2.1 units/μL as reported by the manufacturer). Prior to use, RNase H was diluted down to 0.25X concentration in a solution containing 1 mM DTT, 50 mM KCL and

50%v/v glycerol. Enzymes were stored at -20°C. DNase I was purchased from Lucigen® as part of the AmpliScribe™ T7-Flash™ Transcription Kit (Cat. No. ASF3507).

Buffers, dyes, and other reagents: Transcription buffer was taken from the Lucigen® AmpliScribe™ T7-Flash™ Transcription Kit (Cat. No. ASF3507). Nucleotide Triphosphates (NTPs) were purchased from New England Biolabs (NEB, Cat. No. N0450S). Tris-acetate-EDTA (TAE, Cat. no. 15558026) and Tris-borate-EDTA (TBE, Cat. no.LC6675) buffers were purchased from Thermo Scientific. SYBR™ Gold Nucleic Acid Gel Stain was purchased from Invitrogen™, Thermo Fisher Scientific (Cat. no. S11494). Polyethylene Glycol 8000 (PEG), was purchased from Thermo Fisher Scientific (Cat. no. BP233-100).

Oil and surfactant: We used Fluorinert™ FC-40, an immiscible fluorocarbon oil, for our water-in-oil droplets. Fluorinert™ FC-40 was purchased from Sigma-Aldrich™ (CAS Number 86508-42-1 MDL number MFCD00131095). We used RAN Biotech's non-ionic surfactant for droplet encapsulation (cat#: 008-FluoroSurfactant-); which is a linear poly(ethylene glycol), MW ca. 600, coupled on each end to Krytox-FSH via an amide group.

The oil-surfactant mix includes FC-40 fluorinated oil and 2% w/v perfluoropolyether-polyethylene glycol (PFPE-PEG) block-copolymer fluorosurfactant with Krytox-FSH via an amide group (Ran Biotechnologies).

Additional Methods

Single-tile DNA nanotube preparation: anneal prior to encapsulate

After annealing, DNA nanotubes were diluted to target concentration for encapsulation in 1x TAE buffer with 12.5 mM $MgCL_2$. For encapsulation with the shaken protocol, 20 µL of 5b SEs nanotubes at 500 nM dilution were pipetted into oil-surfactant mixture

and vortexed for 60 seconds following the shaken droplet protocol in section S4.7 (see experiment in Fig. 1c). For encapsulation with the microfluidic chip, nanotubes were diluted to 350 nM in 1x TAE buffer with 12.5 mM $MgCL_2$ before encapsulation using the microfluidic protocol described in section S4.8 (see experiment in Fig. 1d).

Single-tile DNA nanotube preparation: encapsulate prior to anneal

All the strands for tile variants 1 and 2 that form single-tile nanotubes were mixed for a target 250 nM tile concentration (each tile), by adding 250 nM (target concentration) of each DNA strand 1, 2, 3-Cy3/3-Atto647N, 4 and 5 to 1x TAE buffer with 12.5 mM $MgCL_2$ and nanopure water inside DNA Lo-bind tubes. After vortexing briefly, and encapsulation following the shaken droplet protocol described in section S4.7, the solution was annealed using an Eppendorf Mastercycler Gradient thermal cycler by heating to 90°C, and cooling to 25°C, over a 6-hour period. Tile variant 1 was encapsulated alone (see Fig. 1f), or simultaneously encapsulated with variant 2 (see Fig. 1g)

Two-tile DNA nanotube preparation

Tile A and tile B were annealed separately at a target 2 μM concentration by adding 2 μM (target concentration) of DNA strands 1, 2, 3-Cy3, 4 and 5 for each tile to 1x TAE buffer with 12.5 mM $MgCL_2$ and nanopure water inside two different DNA Lo-bind tubes. After vortexing briefly, each sample was annealed using an Eppendorf Mastercycler Gradient thermal cycler by heating to 90°C, and cooling to 25°C, over a 6-hour period.

For encapsulation, tile A and tile B were mixed into the same DNA Lo-bind tube at target concentrations and encapsulated via the shaken droplet protocol in section S4.7.

DNA inactive tile preparation

Inactive tile solution was prepared to target 1μM tile concentration by adding 1 μM (target concentration) of DNA strands 1, 2, 3-Cy3/3-Atto647N, and 5 to 1x TXN buffer (RNA Pol Reaction Buffer from Lucigen®) and nanopure water inside DNA Lo-bind tubes. After vortexing for 60 seconds, the solution was annealed using an Eppendorf Mastercycler Gradient thermal cycler by heating to 90°C, and cooling to 25°C, over a 6-hour period.

Activation of tile assembly by adding strand S4

Annealed inactive tiles were incubated in the Mastercycler at 37°C prior to adding the missing strand 4. RNA strand 4 was added (target strand concentration to match the tile concentration) prior to encapsulating. After encapsulation, droplets were incubated at 37°C and monitored via fluorescence microscopy.

Activation of tile assembly by co-transcription of the trigger strand

Annealed inactive tiles were incubated at 37°C prior to addition of the transcription mix and synthetic gene. The transcription mix includes RNAP (2.5% v/v RNAP (AmpliScribe™ T7-Flash™ Transcription Kit, Cat. No. ASF3507)) and 1x transcription buffer (AmpliScribe™ T7-Flash™ Transcription Kit, Cat. No. ASF3507), 4 mM each nucleoside triphosphates (NTPs) 2.5% w/v PEG 8000 and 10 mM $MgCL_2$. Unless otherwise noted, we used 100 nM annealed synthetic template for transcribing missing RNA strand 4 for an inactive tile concentration of 0.5 μM. Inactive tiles, transcription mix, and synthetic gene were mixed, rapidly encapsulated, and droplets were incubated 37°C as described in section S4.7. Droplets were imaged using a fluorescence microscope for several hours as described in section S4.9.

Shaken method for water-in-oil droplet formation

The procedure described here is for the formation of 100 μl droplet emulsion. We pipette 80 μl oil-surfactant mix into a microtube. We then add to it 20 μl of the oligonucleotide containing aqueous phase. Emulsion droplets are formed by vortexing for 60s on a benchtop

vortexer. Successful emulsification is indicated by a milky appearance of the sample (the aqueous phase will be dispersed throughout the oil phase at this point). We note that the average droplet size is affected by both time and vortexing speed, thus consistency of this step is essential for repeatable results. Pipetting the sample for imaging directly after emulsification yields too dense a sample of droplets which will result in stacked, multilayers of droplets within the imaging. If droplet overlap is excessive, data from individual droplets cannot be gathered and processed. In addition, overlap inhibits code-based droplet detection (Section S4.13). In that case image processing/droplet identification must be done manually. To get a monolayer of droplets, the emulsion should be allowed to set for 30-60 seconds before pipetting 50-70 µl of the emulsion from below the dense droplet layer at the top of the sample into the well of an Ibidi chamber slide (µ-Slide VI $^{0.4}$ - hydrophobic coating). To prevent contamination and evaporation of the sample, we seal the well by covering the top edge of each input with vacuum grease (Dow Corning®) and cover with a glass coverslip. The assembly process begins as soon as the encapsulation step is completed so imaging via fluorescence microscopy is started directly after the sample is loaded into the imaging chamber as described in section S4.9.

For confocal microscopy, the sample is mixed and allowed to set for at least 2 hours prior to imaging. Nanotube motion during confocal imaging will result in poorly focused and blurry images.

Microfluidic method for water-in-oil droplet formation

Microfluidic droplets were produced using the Dolomite 3D flow focusing 100 µm chip (hydrophobic coating, #3200434) and associated connectors (Linear Connector 4-way # 3000024 x2, Chip Interface H #3000155). Before preparing the droplet samples, the syringe pumps and microfluidic devices were assembled and the microscope was brought into focus on the junction of the chip sitting in the Chip Interface H. Next, 3 input, 1 output, and 4 extra pieces

of tubing (IDEX Health and Science, FEP 1/16x.020x100ft #1548XL) were cut; input and output tubing were cut long enough to reach from syringe pumps to the microscope stage, while the 4 extra pieces of tubing were only 1 inch long each. Tubing was threaded through the linear connectors: 3 inputs and 1 extra piece for one connector, and 1 output and three extra pieces for the other connector. The tips of the tubing should either even or slightly drawn into the gasket of the linear connector. Extra 1inch pieces of tubing are present only to hold the shape of the gasket for a good seal with the chip. Nanotube samples were prepared using single tile nanotube variant 1 with strands 5bSE1, 5bSE2 T, 5bSE3, 5bSE4 and 5bSE5 as described in section S4.1. 200 µL 350 nM 5-base Toehold nanotubes was loaded into a syringe (BD 1 mL Syringe Luer-Lok™ Tip with 25g x ⅝ BD PrecisionGlide™ Needle secured with Parafilm), and two syringes were loaded with 300 µL of oil-surfactant mixture each. After threading input tubings with the appropriate syringe needles, tubing was primed by pumping at a rate of 0.2 mL/min via syringe pumps (SyringePump.com #NE-4000, #NE-300). When fluid was visible at the linear connectors, priming was stopped, and the microfluidic chip was loaded into the Chip Interface H and linear connectors attached. Droplets were made by flowing the aqueous sample at 2,000 µL/h and oil phase at 3,000 µL/h, after first flowing the aqueous sample phase only. Droplets were collected in a DNA Lo-bind tube before being loaded into an Ibidi imaging chamber (µ-Slide VI $^{0.4}$, hydrophobic coating) for imaging via fluorescence microscopy.

Epifluorescence microscopy

All fluorescent samples inside droplets were imaged using an inverted microscope (Nikon Eclipse TI-E) with Nikon Plan Fluor 20X/0.5 NA objective. All unencapsulated samples were imaged using a 60X/1.4 NA oil immersion objective.

Control experiments of non-encapsulated nanotubes were imaged at 50 nM tile concentration in corresponding experimental buffer conditions (either 1x TAE and 12.5 mM

$MgCL_2$, or 1x transcription buffer); samples were placed on a Fisherbrand microscope glass slide (12-545E No. 1, thickness=0.13 to 0.17 mm; size: 50 x 22 mm) and gently covered with VWR Micro Slides (Plain, Selected, Pre-cleaned, 25 x 75 mm, 1.0 mm thick) or Fisherbrand™ Cover Glasses (cat. No. 12-545F).

Droplet-encapsulated nanotubes were imaged in an Ibidi chamber (µ-Slide VI $^{0.4}$, µ-Slide VI $^{0.1}$, hydrophobic coating) with the inputs to the channels sealed with vacuum grease (Dow Corning®) and VWR micro slide or Fisherbrand™ Cover Glasses (cat. No. 12-545F) to prevent evaporation. Droplets encapsulating transcription reactions were incubated in the Ibidi chambers on a ThermoPlate (Nikon Inc, Tokai Hit) set to 37°C during imaging.

Encapsulated nanotubes labeled with Cy3 fluorescent molecules were imaged using the Cy3 filter. Nanotubes, labeled with ATTO 647 N on strand S3, were imaged using the Cy5 filter (excitation and emission wavelength are comparable to ATTO 647N). The image of two different species of single-tile nanotubes in Figure 1g is a superposition of images acquired with the filters for Cy3 and Cy5 dyes individually.

Exposure times for non-encapsulated samples was 90 ms. For encapsulated samples, exposure varied in different experiments, depending on tile concentration and fluorophore used. Exposure times for all two-tile experiments were 3 seconds for all time points. Exposure times for 1x RNA trigger experiment was 1 second for all timepoints except at 24 hours, which had an exposure of 3 seconds. The 4x RNA trigger experiment had an exposure time of 128 ms for all timepoints, as the aggregates formed by crowding of RNA trigger were much brighter than assembled nanotubes. Exposure times for gene titration experiment series were 2-3 seconds. Exposure times for RNase H titration experiments were 2-3 seconds. In SI section S5.8 we report control experiments that demonstrate how exposure time does not affect skewness and kurtosis measurements.

Confocal fluorescence microscopy

Confocal laser scanning microscopy was performed at the Advance Light Microscopy/Spectroscopy Laboratory and the Leica Microsystems Center of Excellence at the California NanoSystems Institute at UCLA. Nanotube samples were imaged on a Leica TCS SP8-STED confocal microscope with 63x/1.20 NA water-immersion objective. Images for Cy3 and Atto 647 N labeled samples were obtained with the white light laser and detector set to the maximum excitation/emission wavelengths for Cy3 and Alexa 647, respectively. Droplets were collected in a DNA Lo-bind tube before being loaded into an Ibidi imaging chamber (μ-Slide VI $^{0.1}$, hydrophobic coating) for imaging. Images were line averaged during acquisition, with the number of line-averages noted in the caption of each image, and the z-step size was system optimized to get the maximum number of steps for each z-stack possible.

Polyacrylamide gel electrophoresis (PAGE)

Denaturing PAGE: Gel pre-mix was prepared (for a final volume of 100 mL) by adding 42 g of urea to 25 ml of nanopure water, the mixture was then heated until the urea completely dissolved. This mixture was allowed to cool to room temperature, then acrylamide/bis-acrylamide 19:1, 40% solution was added. The pre-mix was added in appropriate ratios with TBE and nanopure water, ammonium persulfate (APS), and Tetramethylethylenediamine (TEMED) to cast the desired polyacrylamide percentage. Gels were cast in 10X10 cm, 1 mm thick disposable mini gel cassettes (ThermoScientific, Cat. No. NC2010) and allowed to polymerize for at least 2 hours before electrophoresis. Gels were run at room temperature at 100 V in 1X TBE unless otherwise noted. Gels were stained in SYBR Gold Nucleic Acid Gel Stain for 20-30 minutes and then imaged using the Biorad ChemiDocTM MP system. We

purchased the 10bp DNA ladder used in denaturing gels from Invitrogen™ (Cat. No. 10821-015).

Non-Denaturing PAGE: Acrylamide/bis-acrylamide 19:1, 40% solution, TAE, Magnesium Chloride 12.5 mM (final concentration), APS, and TEMED were added together at appropriate concentrations for the desired polyacrylamide percentage, then cast in 10X10 cm, 1 mm thick disposable mini gel cassettes (Thermo Scientific, Cat. No. NC2010) and allowed to polymerize for at least 2 hours before electrophoresis. Gels were run at 4°C at 150 V in 1X TBE buffer. After electrophoresis gels were stained in SYBR Gold Nucleic Acid Gel Stain for 20 minutes then imaged using the Biorad ChemiDocTM MP system.

RNA extraction

RNA was transcribed using the AmpliScribe-T7-Flash Transcription Kit (Lucigen®). The following components were mixed at room temperature: RNase-free water, 1-1.5mg template, AmpliScribe T7-Flash 1X Reaction Buffer (Cat. No. ASF3507, Lucigen®), 9 mM NTPs, 40 U/mL RiboGuard RNase Inhibitor (Cat. No. RG90925, Lucigen®), and 2mL of AmpliScribe T7-Flash Enzyme Solution (Cat. No. ASF3507, Lucigen®). This mix was then incubated at 37°C for 4 hours.

After transcription, the samples were loaded on a PAGE gel and run at 100V; the gel was then stained in 80 mL 1X TBE and 1mL SYBR Gold Nucleic Acid Gel Stain (Thermo Scientific, Cat. No. S-11494) for 20-30 minutes. The stained gel was placed on a TLC silica gel 60 W F254S aluminum sheet (EMD Millipore, Cat. No. 1055590001) covered in plastic wrap. The gel was then illuminated with UV light and the desired RNA band was excised, crushed and eluted using 200mL of 0.3 M sodium acetate at pH 5.3. The elution reaction was done in 0.5 mL DNA Lobind tubes (Eppendorf, Cat. No. 022431005), incubated at 42°C for ~20 hours. After incubation, the sodium acetate was removed and placed into 1.7 mL RNase/DNase free tubes.

The old Lobind tubes were further rinsed with 100mL of 0.3 M sodium acetate pH 5.3, which was added to the new tubes. Then 1 mL of freezer cold 100% ETOH and 1mL of glycogen was added into each tube and the sample was incubated at -20°C for 20 hours.

Next, the samples were spun at 13500 rpm at 4°C for 15 minutes. The white precipitate pellet (RNA) at the bottom of the tube was located and the supernatant was carefully pipetted out of the tubes to avoid removal of the pellet. Then, 500mL of 70% freezer cold ETOH was added to the tubes and spun at 13500 rpm at 4°C for 5 minutes. The supernatant was carefully decanted again with a pipette. This washing procedure was repeated a third time. After the last wash, as much supernatant was removed as possible, then the tubes were opened and placed in the vacuum concentrator and allowed to spin at room temperature for 15 minutes. The samples were then re-suspended in 10-15mL of Invitrogen™ nuclease free water (ThermoFisher Scientific, Cat. No. AM9932).

Droplet detection and pixel brightness value extraction via Python

Extracting pixel brightness values (PBV) data from fluorescence microscopy images by hand is both time consuming and prone to human error. By employing a few basic Python packages, we wrote a script which extracts PBV data from fluorescence microscopy images for hundreds of droplets in minutes. The foundation of the Digital Image Processing (DIP) script we wrote for detecting droplets in epifluorescence microscopy images is built upon the scikit-image image processing library.[5] We implemented the Circular Hough Transform (CHT) algorithm tailored to detect circles across a wide range of radii and remove a majority of artifacts from the returned values.

The droplet detection script is available at Github[6]:

https://github.com/klockemel/dropletDetection_dynamicSelfAssemblyProject.

Before applying the CHT, it is helpful to pre-process the images to improve detection of droplets especially in samples presenting large droplets or aggregation of fluorescently labeled tiles. Prior to running the droplet detection script, all 16-bit .nd2 images are duplicated. Duplicates are brightness-adjusted using the “Auto” setting in the Brightness/Contrast tool of ImageJ and saved as 8-bit tiff files. Brightness-adjusted images are only used for droplet detection, while PBV are extracted from the raw images with full bit depth (Fig S5). Brightness-adjusting the images in which droplets are detected enables a future thresholding step to more accurately separate droplets from the background of the image than would be separated otherwise, even in the presence of bright spots in the image.

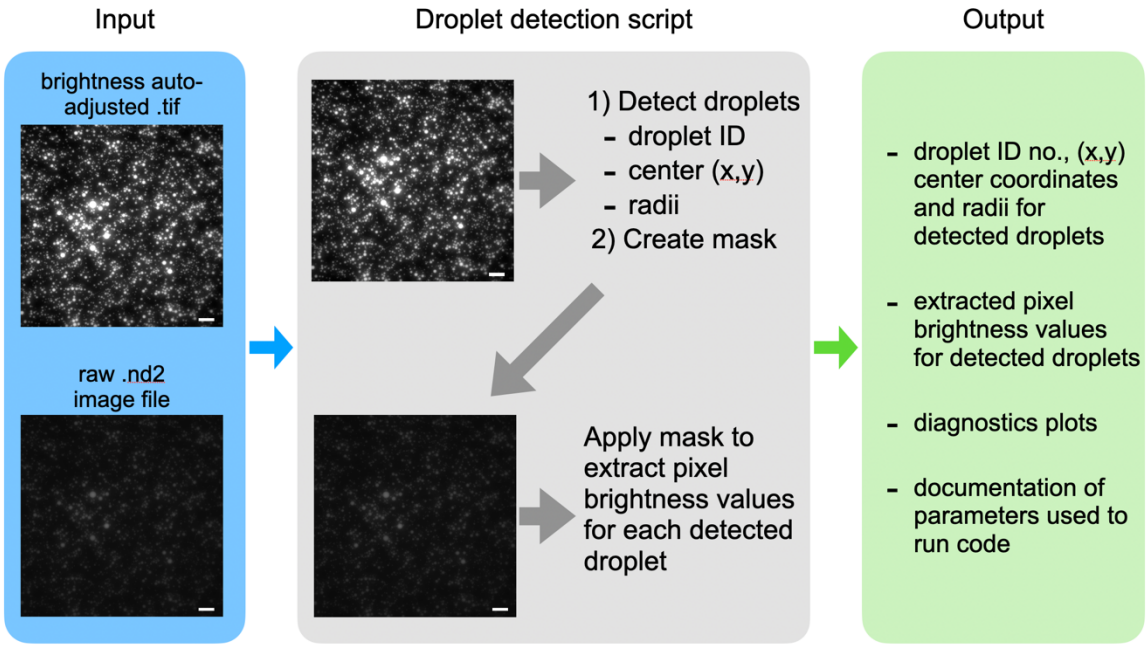

Figure S3.6: Diagram summarizing the process of the automated droplet detection and data extraction script. First, droplets are detected using the circular Hough transform (CHT) algorithm from the scikit-image package on a brightness-adjusted image. The radii, (x, y) center coordinates, and Hough intensity for each detected circle are filtered to remove circles with low Hough intensities and circles which are overlapping. A mask is created using the detected circles to extract pixel brightness values (PBV) from the raw image file. Diagnostics plots, a reference image with detected droplets labeled, and the information for extracted PBV and circle parameters are the final output. These example images are from the 7.5 nM template co-transcriptional activation of DNA-RNA nanotubes at 0 minutes after encapsulation (Main text Section “Transcriptional control of nanotube assembly inside droplets”). Scalebars are 50 μm.

The droplet detection script requires both the raw and brightness-adjusted images, as well as a few parameters to run. The minimum and maximum radii to search for must be provided in pixels, in addition to the step size. The step size determines which discrete radius values to search for, within the range of the minimum and maximum radii. For a step size of one, all radii between the min and max will be considered, while for a step size of 2, every other value will be skipped, and so on. Droplets made via the shaken protocol described in SI Section S4.7 are heterogeneous in size, and we commonly searched with a minimum of 10 and maximum of 50-70 pixels. As searching over such a large range of radii becomes computationally demanding, radii are broken into subsets of ten for detection with the results from each group compiled for further processing following detection. The final parameter is a limit on the number of droplets allowed in each subset of radii sizes. Varying these parameters determines the computational time, detection accuracy, and number of droplets returned from sample images. (For example, without a numeric limit to the number of droplets which can be found, the script may return hundreds of artifacts, or false detections, and take upwards of 30 minutes to complete processing an image.)

To detect droplets, the following CHT algorithm is applied over each subset of radii. First a Canny edge detector is applied (skimage.feature.canny). The Canny edge detector function first removes noise from the image via Gaussian smoothing. Gradients in pixel brightness across the image are found using horizontal and vertical Sobel operators, or kernels. Edges are located when pixels lie normal to horizontal, vertical or diagonal gradients with large magnitudes, and weighted according to the magnitude of the neighboring gradient. Edge weights are compared locally and thinned to 1 pixel in width before being thresholded. Pixels connected to edges, with an edge weight value above a smaller threshold are also labeled as edges. The function returns a Boolean image array in which the edges are labeled as True. The CHT transform function (skimage.transform.hough_circle) is then applied to the Boolean edge

array. The CHT function in scikit-image returns an array for each radius with the Hough intensities for detected circles. The Hough circle peaks function (skimage.transform.hough_circle_peaks) then reads the Hough circle arrays and returns peak Hough intensity values in the “accums” variable, and the associated (x, y) coordinates and radii for detected droplets.

After detecting circles with the above algorithm, artifacts and overlapping circles are filtered out. First, center (x, y) coordinates and radii for circles with low accums values are dropped. Overlapping circles, often circles sharing the same center coordinates but with different radii, are dropped if the distance between the centers is less than the sum of their radii. The circle with the lower accums value is dropped in this case. Finally, if the number of remaining circles is greater than the user defined limit, the circles with the lowest accums values are dropped until the limit is reached. The results for each subset are compiled to create a list of detected droplets across the range of the minimum and maximum radii parameters. After compiling circles from all radii subsets, overlapping circles and circles with low accums values are once more filtered out.

The center coordinates and radii of the remaining droplets are used to generate a mask labeled with droplet ID, which is then applied to the raw image to extract PBV. A reference image is created in which detected droplets are drawn in red on the brightness-adjusted fluorescence image with their ID numbers. ID numbers are printed in a new color every 100 droplets to help improve legibility for images in which many droplets are detected. The output of the droplet detection script are the reference image with labeled droplets, supplementary diagnostics plots shown in the previous figures, and three comma-separated value (csv) files: 1) the user defined parameters used

in the run, 2) droplet ID number, radii, and center coordinates, and 3) the PBV in the form of a 256-bin list-form histogram with appropriate droplet IDs.

Before PBV data is further processed, reference images are visually inspected, and any remaining artifacts are removed from the final data using their ID numbers. In some cases, detected circles are merely artifacts (as an example, see number 170 in Fig S6b). Other circles which need to be removed from data may have radii off by more than a few pixels (number 197), inaccurate centers (number 175), or are cut-off by the edge of the image.

To quantify our observations of nanotube polymerization and depolymerization we measure the skewness and kurtosis, also respectively known as third and fourth standardized moments, which describe the shape of a distribution. Skewness describes the distribution of any variable about its mean, while kurtosis describes the “tailedness” of a distribution. More specifically, skewness describes where the bulk of a distribution lies relative to its mean, with a negative skew value indicating that the bulk of a distribution is above the mean, a zero skewness value indicates a normal distribution, and a positive skew value indicates the bulk of the distribution is below the mean.[7] Kurtosis is a statistical measure that defines how the tails of a distribution differ from the tails of a normal distribution.[8] We use Fisher’s definition to calculate kurtosis (also termed as excess kurtosis), where 3 is subtracted from the result so that kurtosis of the normal distribution is zero.[9] A distribution with heavy tails on either side (ex. Laplace distribution), indicating large outliers, has a positive kurtosis. A distribution with thin tails (ex. Uniform distribution) has a negative kurtosis, indicating fewer outliers in a distribution.

To measure the skewness and kurtosis for the distribution of pixel brightness values extracted for each droplet, first a list of unique pixel brightness values was calculated for each droplet based on the number of pixels in each bin and the bin width of the histogram for each droplet. Then skewness and kurtosis are calculated for the unique pixel brightness values list

using the skew and kurtosis functions in the Python Pandas library (pandas.DataFrame.skew and pandas.DataFrame.kurtosis respectively). The average skewness and kurtosis values, along with the standard deviation, were calculated for all droplets measured at each time point of each experiment. Standard deviation was chosen over the variance or other measurements as it represents the spread of the values across the measure samples.

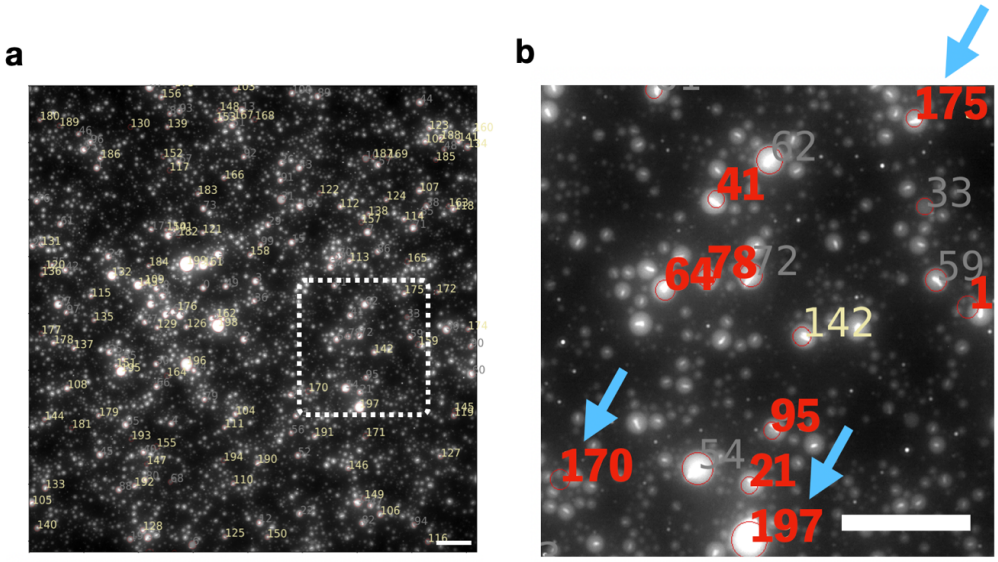

Figure S3.7: Representative reference images for detected droplets. This is representative image are from experiments in which we used 7.5 nM template for co-transcription of RNA to activate DNA-RNA nanotubes; image is taken at 360 minutes after encapsulation (Main text Section “Transcriptional control of nanotube assembly inside droplets”). (a) The full image with all labeled detected droplets labeled and marked by red circles. (b) An inset of the image marked by the dotted line. Artifacts which are removed before further processing are labeled in bold, red numbers (red font superimposed for illustrative purposes). Blue arrows indicate examples of droplets that were removed (for different reasons) before data analysis. Not only are artifacts removed (170), but also droplets for which the radius is off by more than a few pixels (197), droplets with inaccurately detected center coordinates (175), or a combination of both. Scalebars are 50 μm.

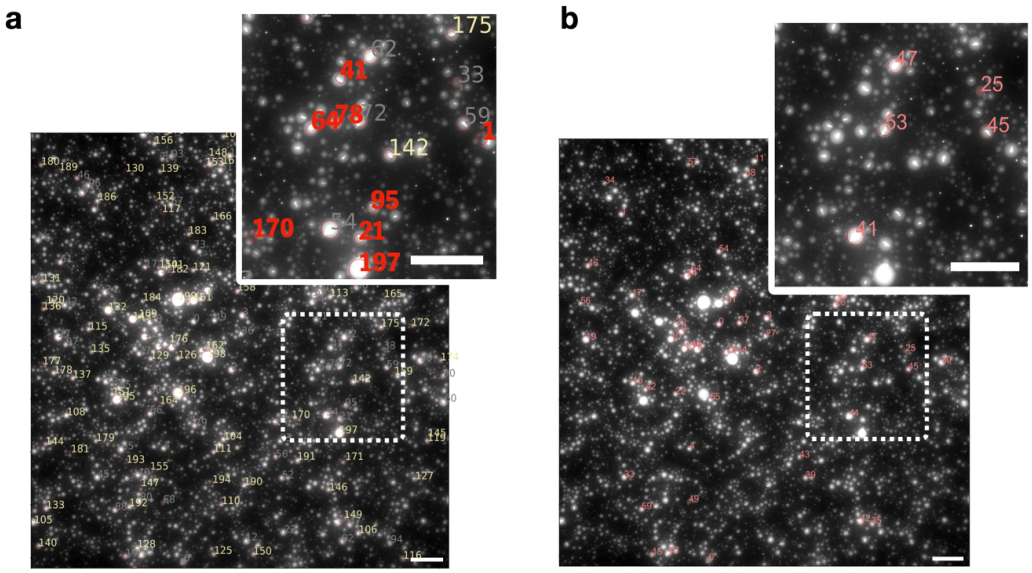

Figure S3.8: Representative images of detected droplets before (a) and after (b) removing artifacts and incorrectly detected droplets. Detected circles which are removed are indicated by bold, red numbers in inset. Insets are magnified views of the areas indicated by the dotted lines. The images are from the 7.5 nM template co-transcription of DNA-RNA nanotubes at 360 minutes after encapsulation (Main text Section “Transcriptional control of nanotube assembly inside droplets”). Scalebars are 50 μm.

Additional data and analysis

Positioning of droplets inside Ibidi chamber (µ-Slide VI $^{0.4}$)

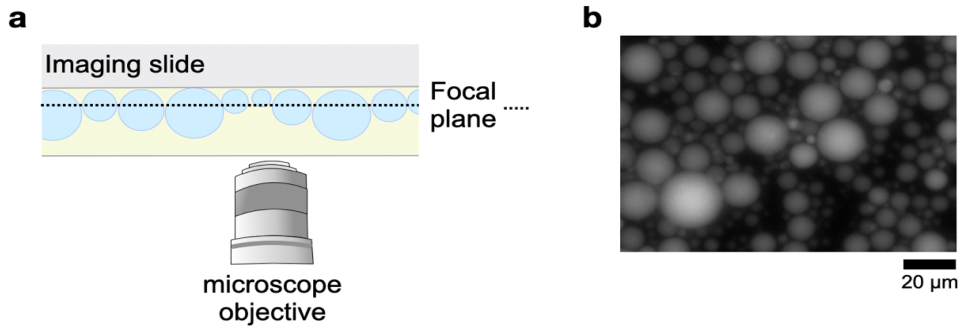

Figure S3.9: Imaging water-in-oil droplets of different sizes. (a) Cartoon schematic of the cross section of an imaging chamber during observation. As the water droplets (blue) float to the top of the oil phase (yellow), and droplets are not all the same size, the ideal focal plane for imaging each droplet is different. Ideally, we would image near the center of a droplet. (b) Representative fluorescence microscopy image of shaken droplets, immediately after encapsulation. Because the sample is made up of droplets of different sizes, not all droplets can be in focus in a single image. For our experiments, we made the effort to both find a field of view and an optimal focal plane for droplets 6-15 µm in diameter.

Morphology of mature two-tile nanotubes after 24 hours of incubation

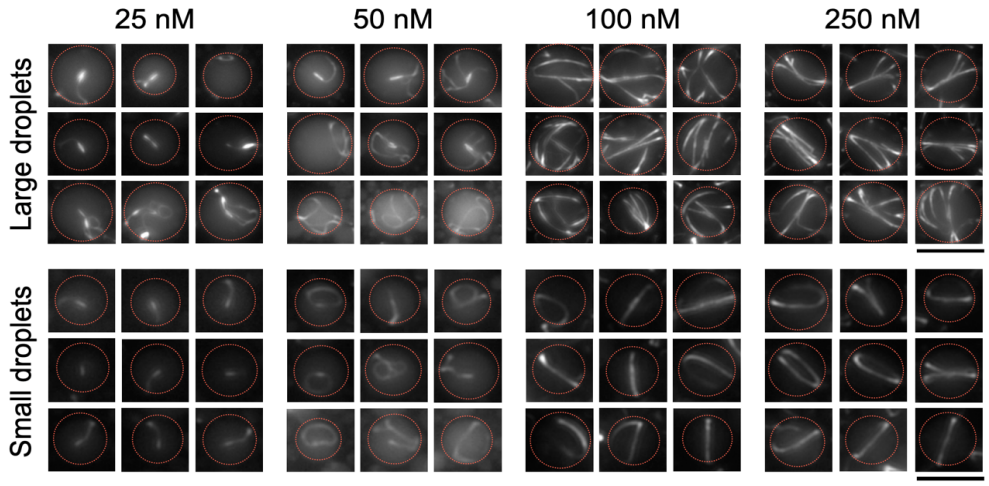

Figure S3.10: Concentration affects morphology of mature two-tile nanotubes. For very dilute concentrations of 25 and 50 nM, mature nanotubes at 24 h following encapsulation appear more flexible with some small networked or bundled regions. Nanotubes also appear to be distributed throughout the droplet, while ends of some nanotubes localize near the inner surface of the droplets. For higher concentrations, 100 and 250 nM each tile, bundling of nanotubes around the inner circumference of the droplets is clear in droplets 20 μm in diameter and larger, while smaller droplets appear to contain on long nanotube wrapping around the inner surface of the droplet. Confocal microscopy for the 100 nM two-tile sample at 24 h confirms that nanotubes are bundled and wrap around the inner surface of the droplets (figure S11). Scale bars: 25 μm (top) and 15 μm (bottom).

Confocal Microscopy images

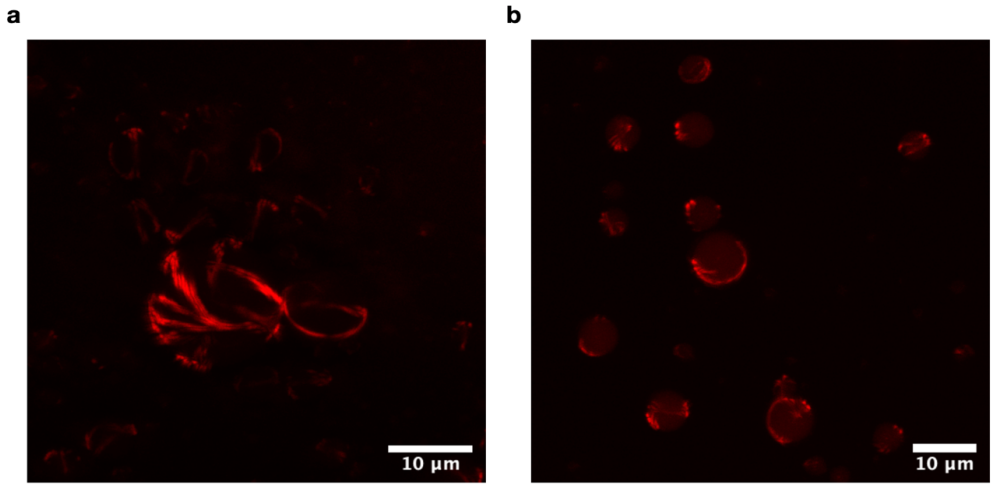

Figure S3.11: Representative confocal microscopy images of two-tile nanotubes. Here we encapsulated each tile at 100 nM. We are imaging nanotubes at 24 h in water-in-oil droplets without (a) and with 2.5% w/v PEG (b). These results suggest that a majority of the mature nanotubes in this sample are at the surface of the droplets and nanotubes appear to be forming bundle-like structures, as seen in (a). Image (a) is a 6-line average projection, image (b) is a 16-line average projection. See also Supplementary Video 2.

Two-tile nanotube system at 25 nM concentration

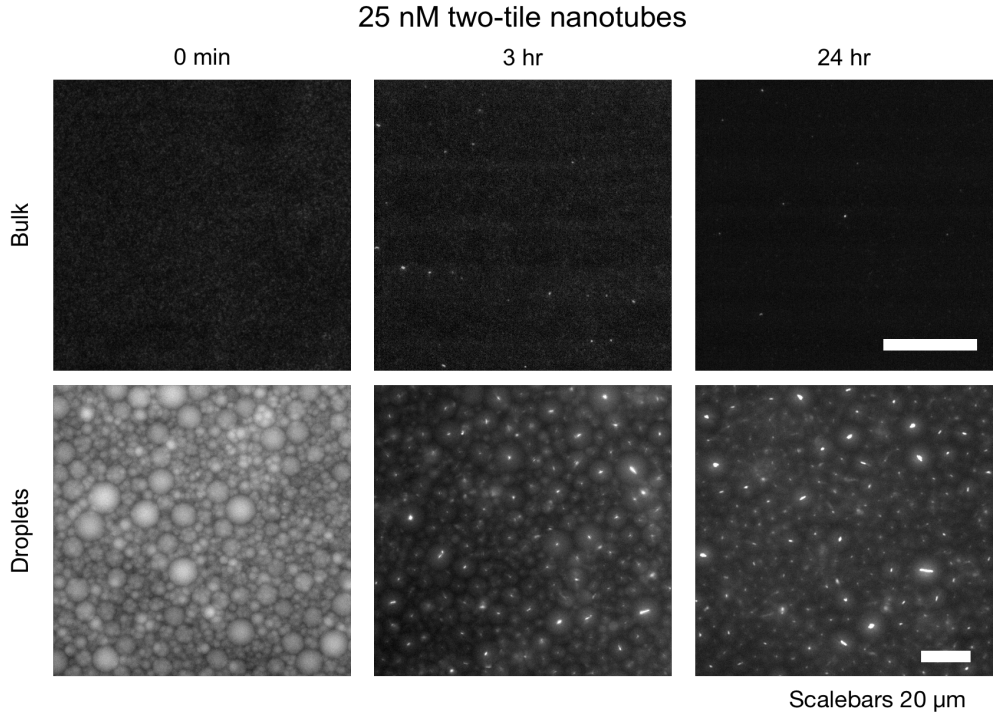

Figure S3.12: Representative fluorescence microscopy images of 25 nM two-tile nanotubes in non-encapsulated, bulk sample (top) and encapsulated in water-in-oil droplets (bottom). Here we observe that the nanotubes form inside encapsulated system even if the concentration is too low for a non-encapsulated, bulk setting.

DNA-RNA hybrid tiles without gene template

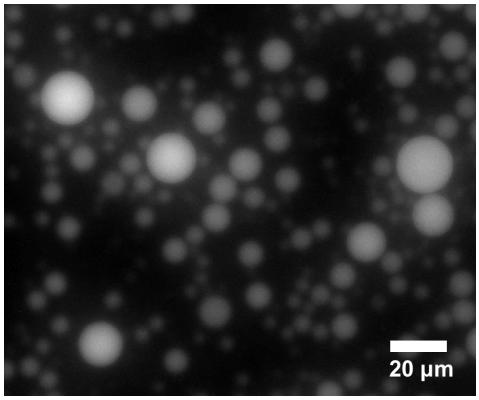

Figure S3.13: Representative fluorescence microscopy image of DNA-RNA hybrid tiles without the gene template required for production of RNA trigger in droplets. In the absence of the gene template, no assemblies are visible. Inactive tile concentration was 500 nM. Image captured 10 hours after encapsulation.

Co-transcriptional assembly without crowding agent

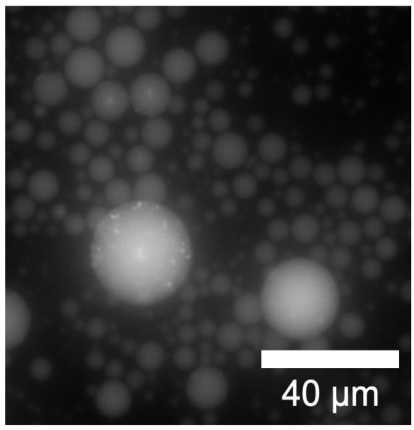

Figure S3.14: Representative fluorescence microscopy image of DNA-RNA hybrid nanotubes with co-transcription of RNA trigger in droplets without PEG. In the absence of PEG, only few small assemblies are visible. Inactive tile concentration was 500 nM, and template concentration was 100 nM. Image captured 4 hours after encapsulation.

Effects of crowding agent on two-tile nanotube system

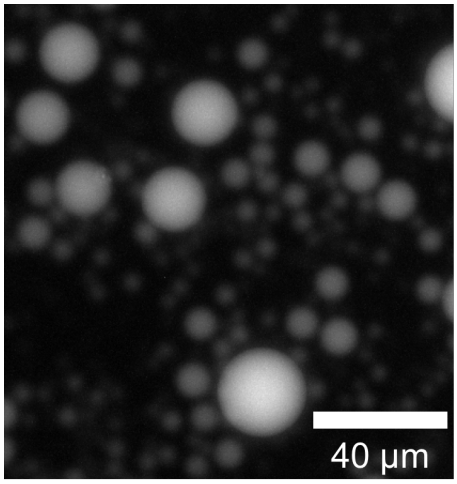

Figure S3.15: Crowding agents do not cause aggregating of individual tiles in droplets. Representative fluorescence microscopy image of tile A of the two-tile system encapsulated in shaken water-in-oil droplets with 2.5% w/v PEG 180 minutes after encapsulation. As there is only one of the two tiles in the droplets, no nanotube polymerization occurs.

Influence of PEG on transcriptionally activated nanotubes

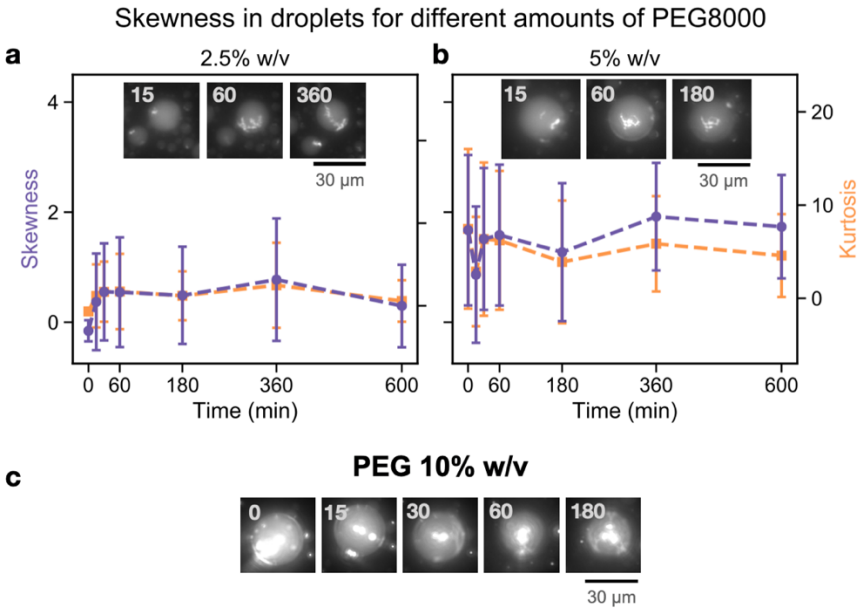

Figure S3.16: Representative fluorescence microscopy images (insets) showing the influence of PEG on transcriptionally activated nanotubes. We show mean skewness and kurtosis measurements at varying amounts of PEG in droplets (2.5% w/v in (a) and 5% w/v in (b)). Inactive tile concentration was 500 nM, and template/gene concentration was 100 nM. (c) Droplets could not be detected for 10% w/v PEG assay. Data is presented as mean values +/- standard deviation. The number of droplets sampled and a histogram data of radii for sampled droplets in SI section S5.9 and S5.10. Scale bars: 30 µm.

Influence of exposure time on skewness and kurtosis

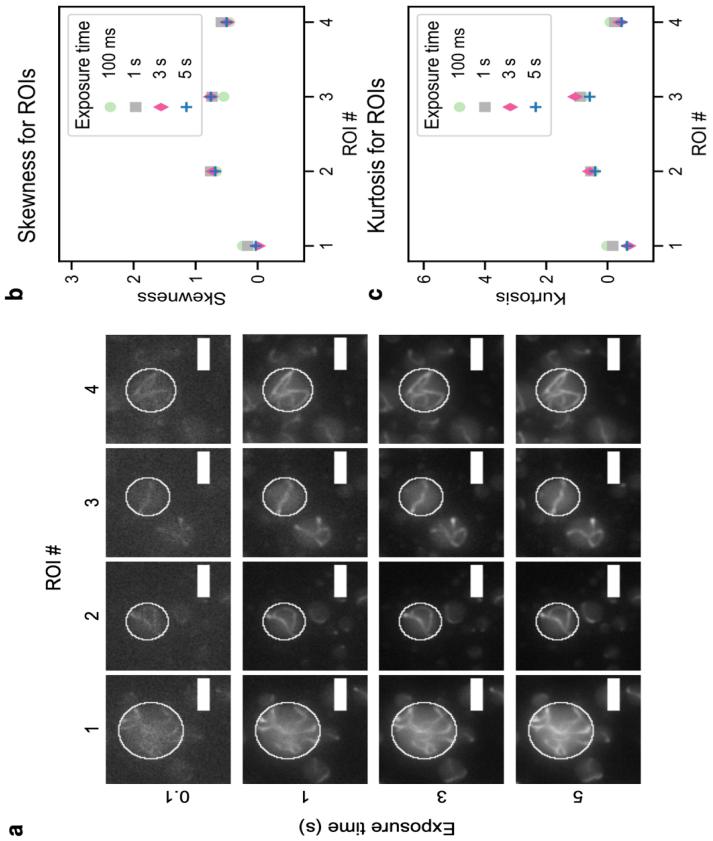

Figure S3.17: Skewness and kurtosis are not significantly influenced by exposure time. In this control experiment, we show computed skewness and kurtosis for different exposure times over four different droplets from a repeated assay of the 100 nM two-tile nanotubes incubated at room temperature. The images processed are from 3 h into the experiment. (a) Fluorescence microscopy images of the droplets, or Regions Of Interest (ROIs), used for the control measurements. Four droplets were chosen in which the nanotubes did not appear to move between the different images. Four exposure times were chosen that represented a range of exposure times used for assays in this work – 100 ms, 1, 3, 5 s. Pixel brightness values were extracted for each droplet, or ROI, from images captured with each exposure time, and skewness (b) and kurtosis (c) values were calculated from there. Skewness and kurtosis values are close across all exposure times. For ROI number 1 and 3, there is a slight difference in skewness and kurtosis, but close inspection of the nanotubes within those droplets suggest there may have been some shifting within the droplet between images captured with exposure times that varied. As no skewness and kurtosis for exposure times were consistently different for all droplets measured, we conclude that data captured with different exposure times is comparable provided the image is not over- or under-exposed. As shown in figure S18, the 100 ms exposure is slightly under-exposed, but skewness and kurtosis values do not appear drastically affected. Data for this figure were extracted by hand using ImageJ. Scale bars 10 μm.

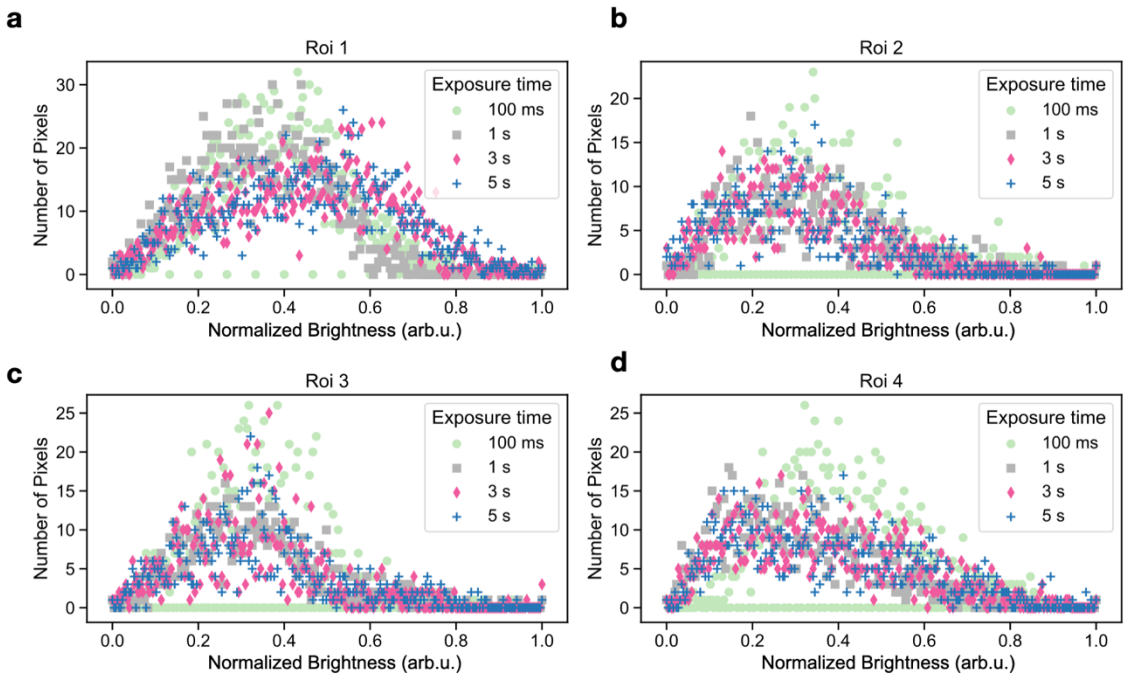

Figure S3.18: Normalized brightness of the pixels detected in each ROI with different exposure time: (a-d) Normalized distributions of pixel brightness values for the same four droplets, or ROIs, at each of the four exposure times discussed in figure S12. (Normalization formula: $I\ normalized = \frac{(I - I\ minimum)}{(I\ maximum - I\ minimum)}$). From these distributions, we can see that the 100 ms exposure is slightly under-exposed, as there are a number of the 256 bins of pixel brightness values which are empty. There is a difference in the shape of the distributions for ROI 1, which is reflected in the slight disagreement of the skewness and kurtosis values between the 100 ms and 1 s exposures, and the 3 s and 5 s exposures. We also see a difference in distribution shape between the 100 ms exposure and the 1, 3 and 5 s exposures for ROI 3. In this study we do not observe a consistent relation between exposure time and the shape of the pixel brightness histogram across all four droplets. Hence, it is likely slightly disagreeing measurements are due to some small shift in the nanotube position inside the droplets, and comparing the skewness and kurtosis values for images captured with different exposure times is valid provided no droplets are under- or over-exposed.

Number of droplets detected in each experimental study

Here we provide the number of droplets selected for computing the skewness and kurtosis in each experiment. The number of droplets vary at each time point in an experimental study because of reasons as described in the droplet detection method (S4.13). As our experiments did not include labeled oligomers or dyes as fluorescence references, and droplets were identified with an edge-based detection algorithm, detection becomes less accurate for samples in which most of the tiles have been recruited to nanotubes. For this reason, as the free tiles in droplets decrease, the number of droplets detected and processed also decreases. Thus, as time progresses, the number of droplets detected by the method reduce. Inclusion of a secondary inert dye, not involved in the nanotube polymerization process would address this limitation and provide consistency in droplet detection and processing for all stages of the experiment. As skewness and kurtosis are affected by the distribution of pixel brightness values, out-of-focus images would have different skewness and kurtosis values than in-focus images of the same subject. For experiments in which the 0 min image is out-of-focus, we processed the data from 15 minutes, the next time-point, onwards.

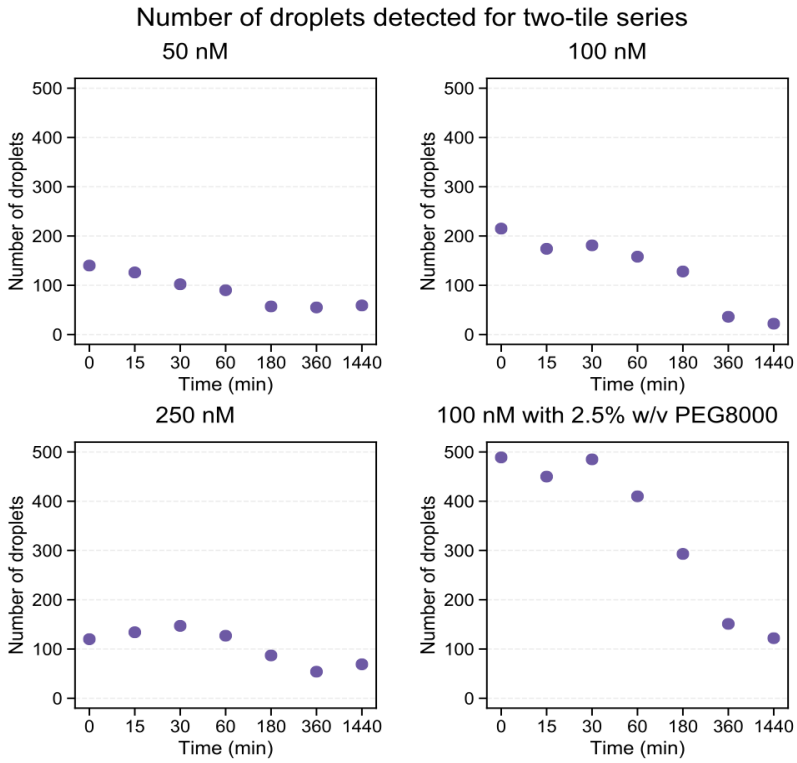

Figure S3.19: Number of droplets detected using the custom developed script for two-tile experiments in Figure 3-3 of the main text.

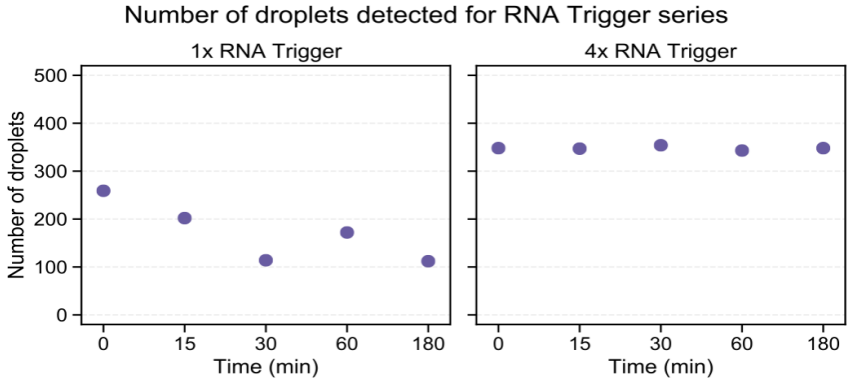

Figure S3.20: Number of droplets detected using the custom developed script for the DNA-RNA hybrid nanotubes with gel-extracted RNA trigger experiments (Figure 3-4).

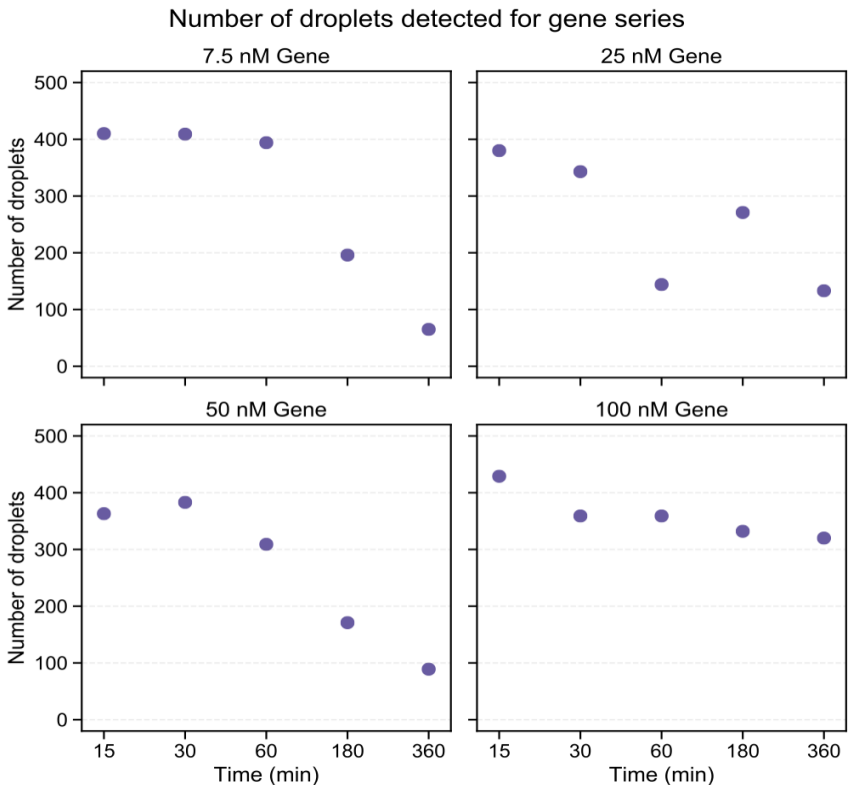

Figure S3.21: Number of droplets detected using the custom developed script for the DNA-RNA hybrid nanotubes with varying concentrations of template, or gene, experiments (Figure 3.5).

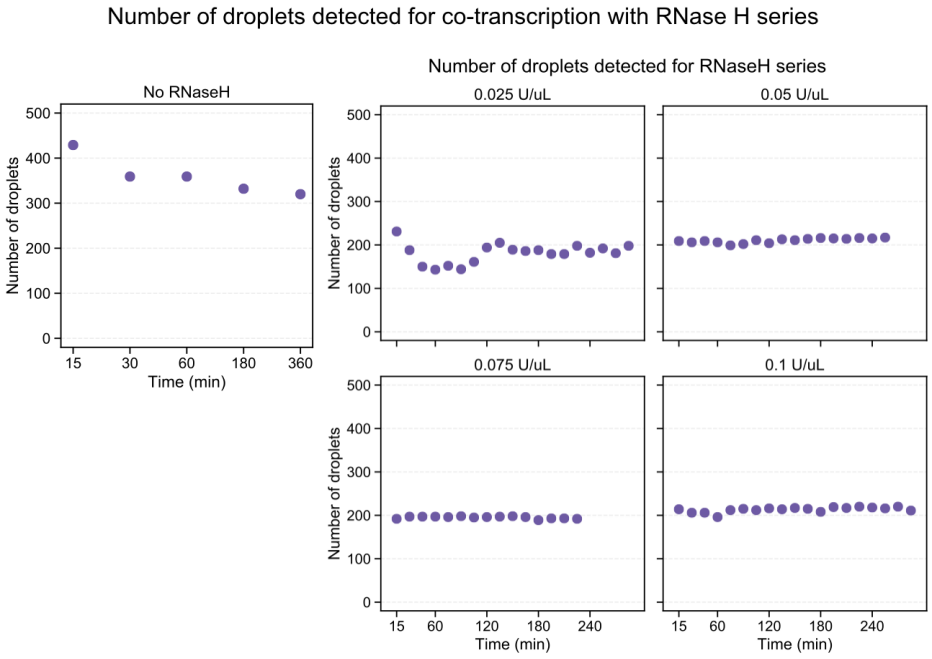

Figure S3.22: Number of droplets detected using the custom developed script for the DNA-RNA hybrid nanotubes with varying concentrations RNase H experiments (Figure 3-6). “No RNase H” data is the same as “100 nM Gene” from figure S3.21.

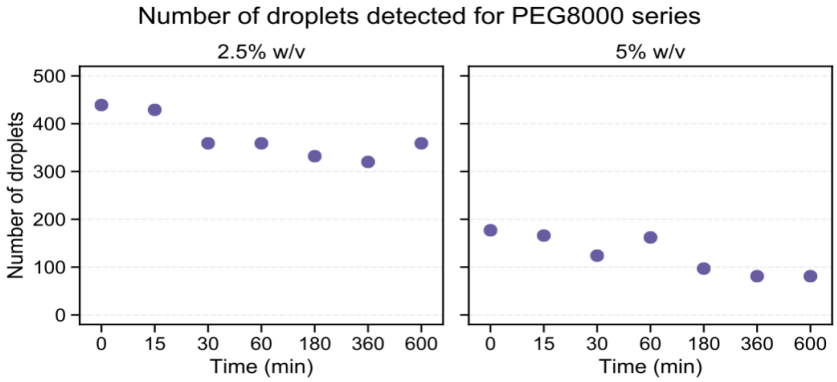

Figure S3.23: Number of droplets detected using the custom developed script for the DNA-RNA hybrid nanotubes with varying concentrations of PEG experiments (Figure S3.16). Droplets were not tracked for the duration of the experiment.

Radii of the detected droplets in each experimental study

Here we provide the histograms of the radii of droplets selected for computing the skewness and kurtosis in each experiment. The droplet radii vary in each experimental study because the shaken protocol for water-in-oil droplet method (S4.7) produces a wide range of droplet sizes. Differences in detected droplet sizes can also occur in the droplet detection step (S4.13).

Another reason for omitted detection of droplets can be if they are overlapping inside the imaging chamber. Images collected of such droplets have fluorescent signal from multiple droplets on top of each other in the z-plane. Thus, individual droplets become indistinguishable in that area and have to be discarded in order to get the most accurate skewness and kurtosis value. We did not encapsulate a reference dye or fluorescently labeled oligomer to aid in the detection of droplets.

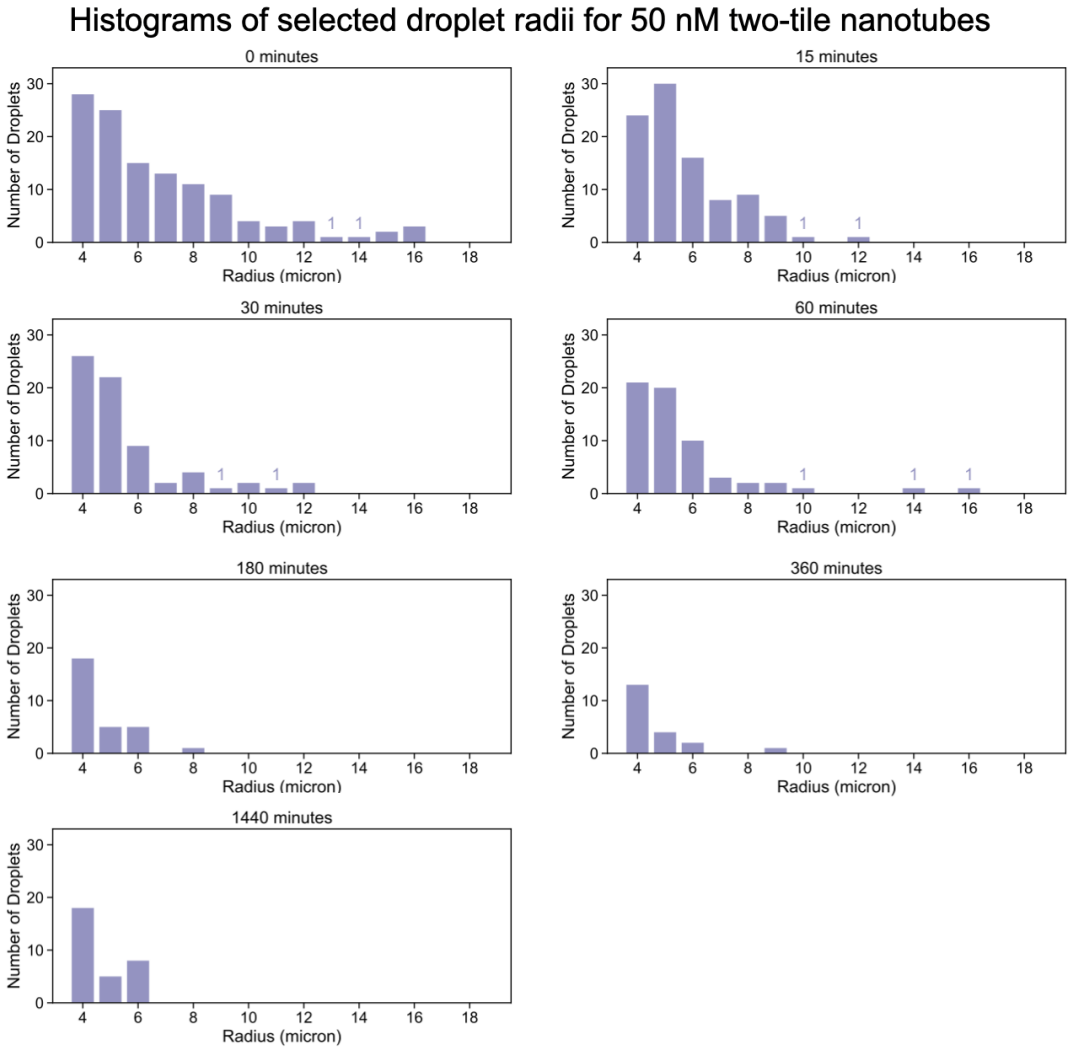

Figure S3.24: Histograms of the radii of measured droplets for the 50 nM two-tile nanotubes in water-in-oil droplets experiment (Figure 3-3). Droplets were detected with the custom developed script.

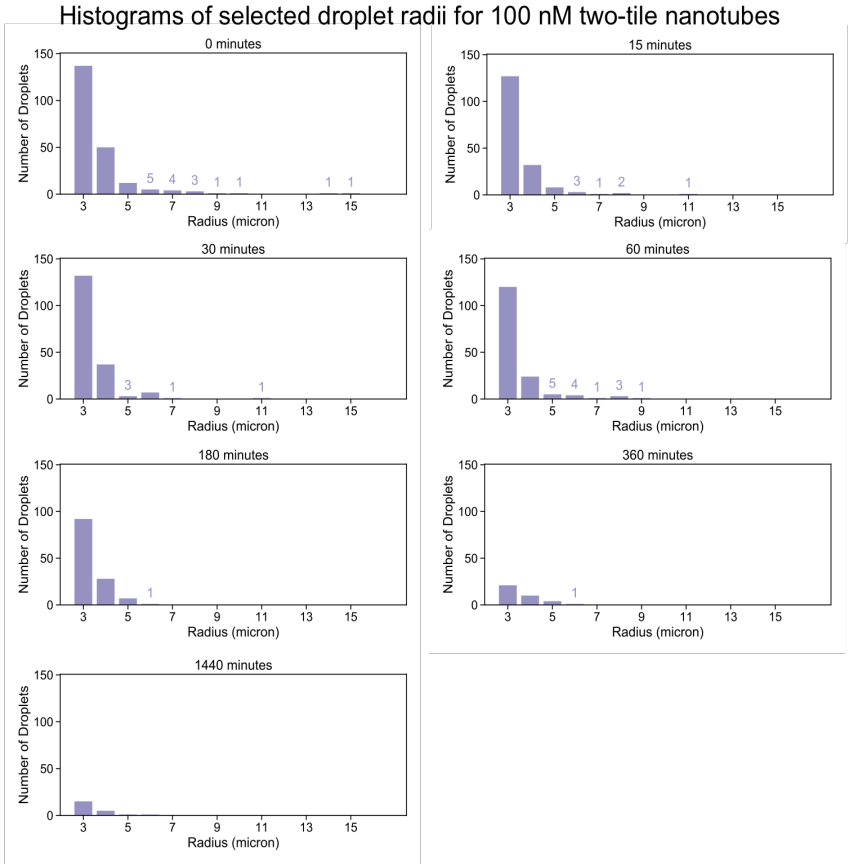

Figure S3.25: Histograms of the radii of measured droplets for the 100 nM two-tile nanotubes in water-in-oil droplets experiment (Figure 3-3). Droplets were detected with the custom developed script.

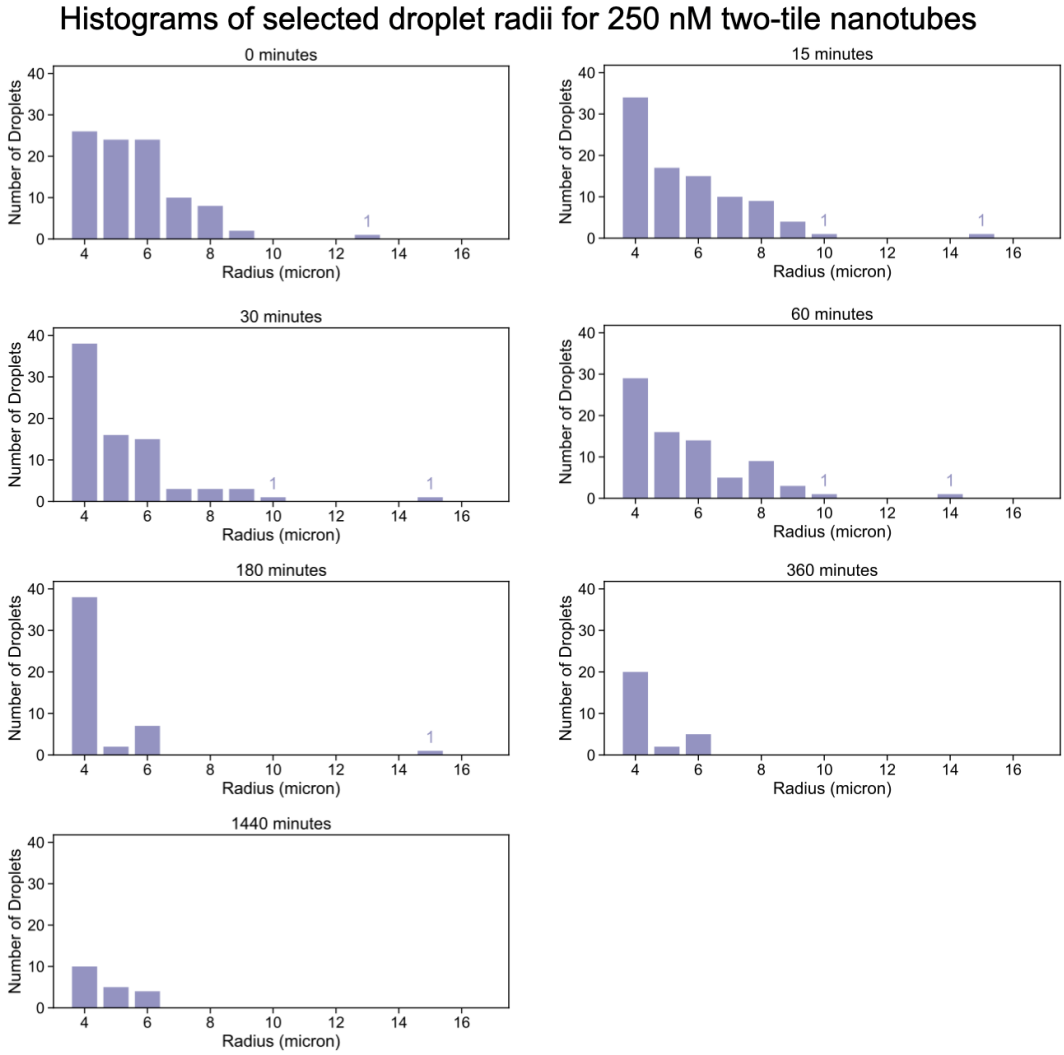

Figure S3.26: Histograms of the radii of measured droplets for the 250 nM two-tile nanotubes in water-in-oil droplets experiment (Figure 3-3). Droplets were detected with the custom developed script.

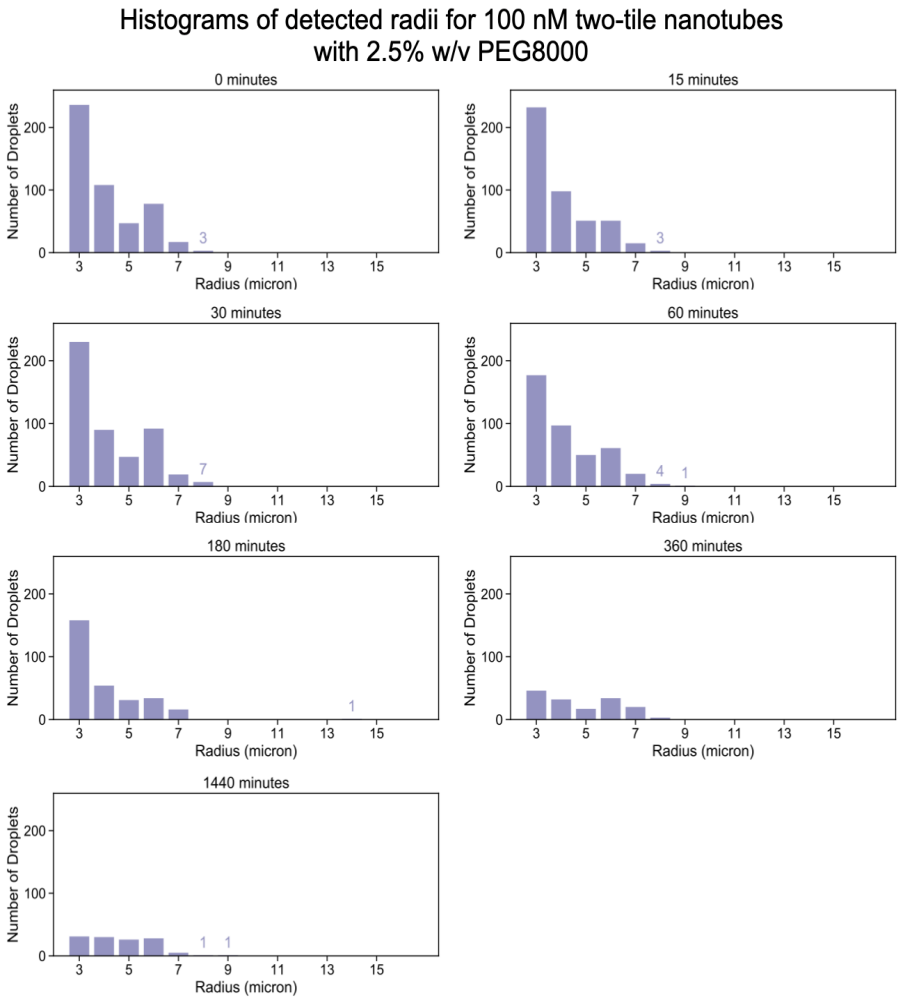

Figure S3.27: Histograms of the radii of detected droplets for the 100 nM two-tile nanotubes with 2.5% w/v PEG in water-in-oil droplets experiment (Figure 3-3). Droplets were detected with the custom developed script.

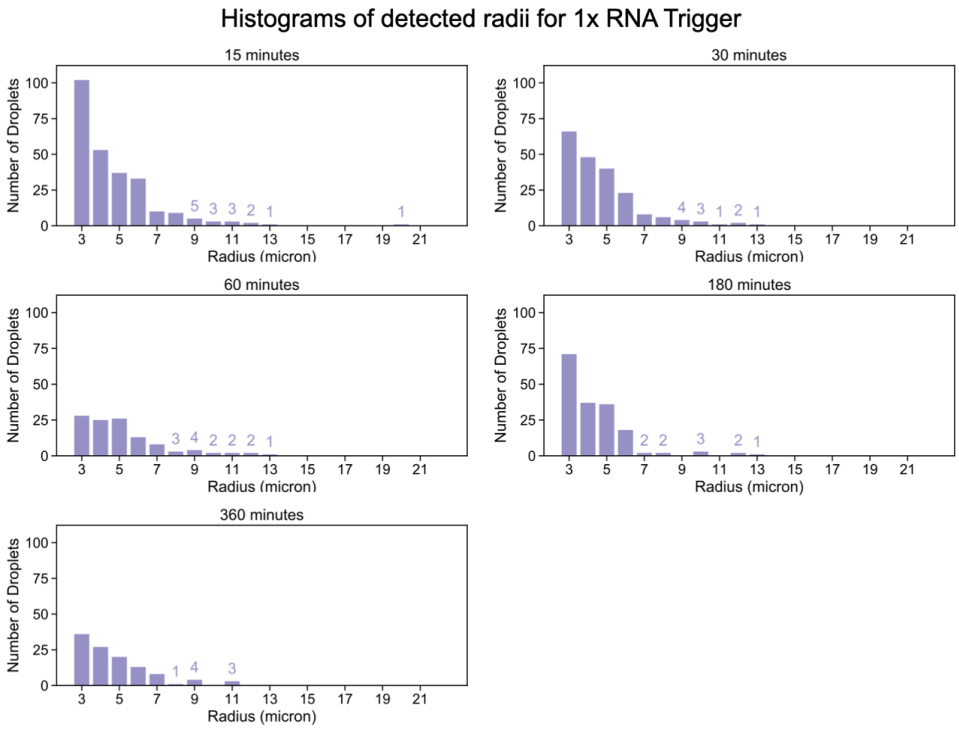

Figure S3.28: Histograms of the radii of detected droplets for the DNA-RNA hybrid nanotubes with 1x gel-extracted RNA trigger in water-in-oil droplets experiment (Figure 3-4). Droplets were detected with the custom developed script.

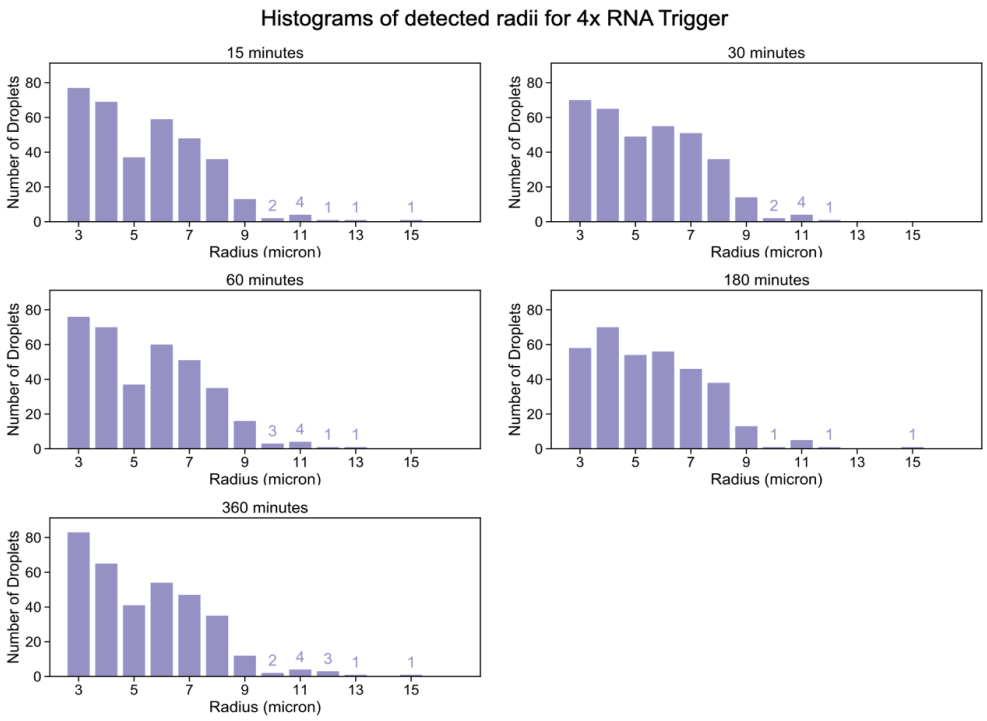

Figure S3.29: Histograms of the radii of detected droplets for the DNA-RNA hybrid nanotubes with 4x gel-extracted RNA trigger in water-in-oil droplets experiment (Figure 3-4). Droplets were detected with the custom developed script.

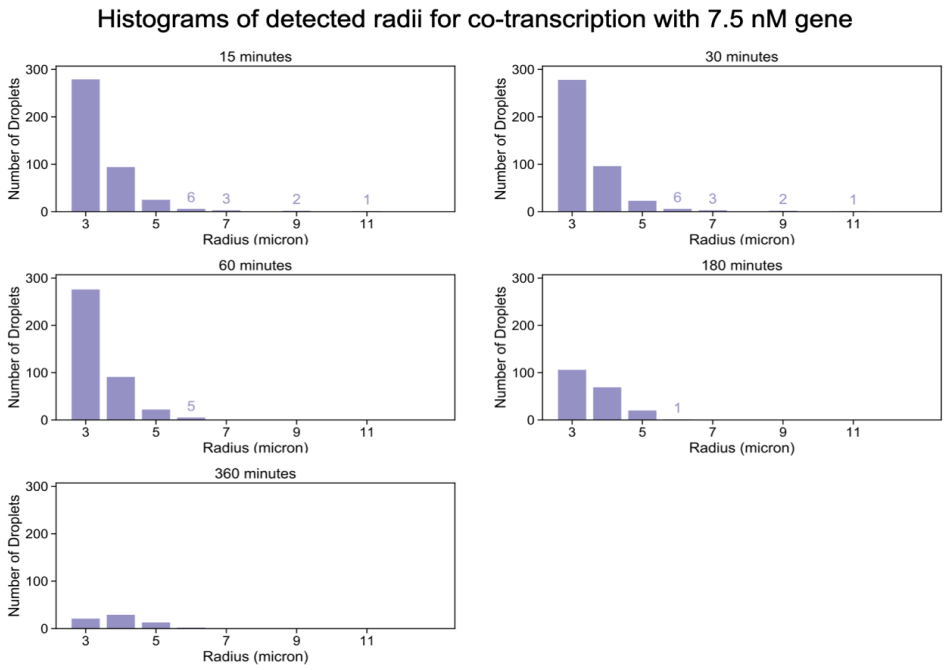

Figure S3.30: Histograms of the radii of detected droplets for the DNA-RNA hybrid nanotubes with co-transcription of RNA trigger from 7.5 nM template/gene in water-in-oil droplets experiment (Figure 3-5). Droplets were detected with the custom developed script.

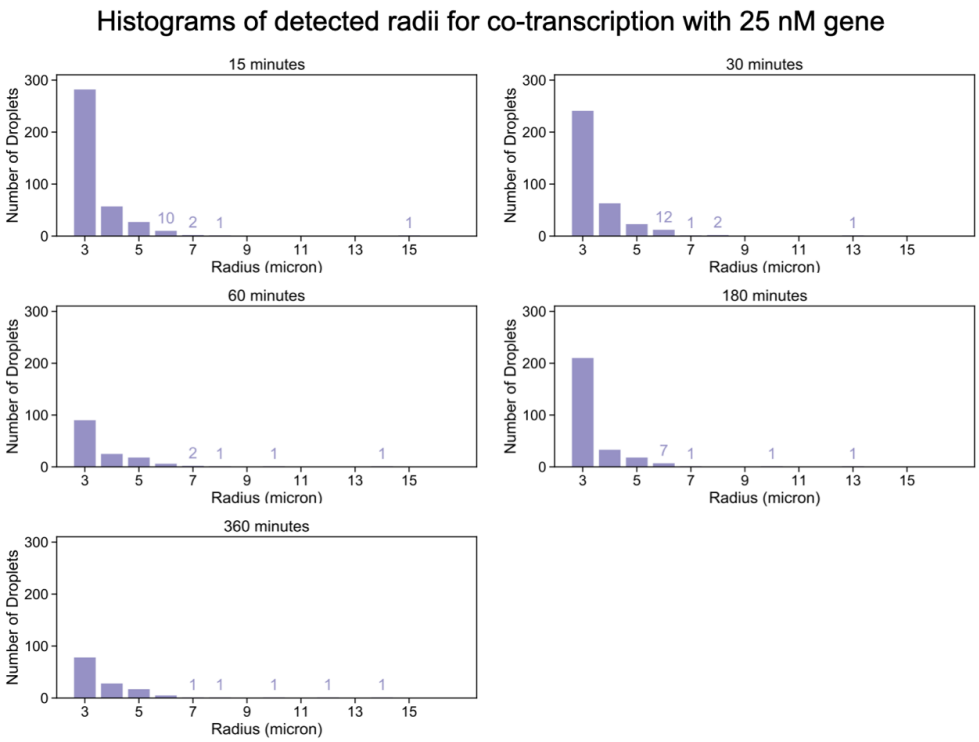

Figure S3.31: Histograms of the radii of detected droplets for the DNA-RNA hybrid nanotubes with co-transcription of RNA trigger from 25 nM template/gene in water-in-oil droplets experiment (Figure 3-5). Droplets were detected with the custom developed script.

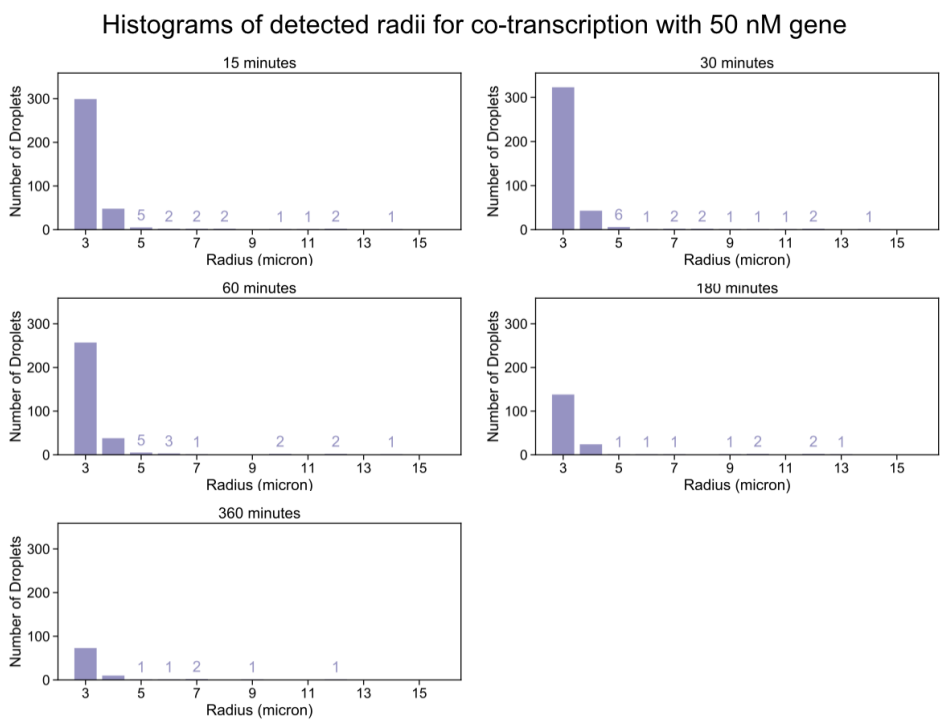

Figure S3.32: Histograms of the radii of detected droplets for the DNA-RNA hybrid nanotubes with co-transcription of RNA trigger from 50 nM template/gene in water-in-oil droplets experiment (Figure 3-5). Droplets were detected with the custom developed script.

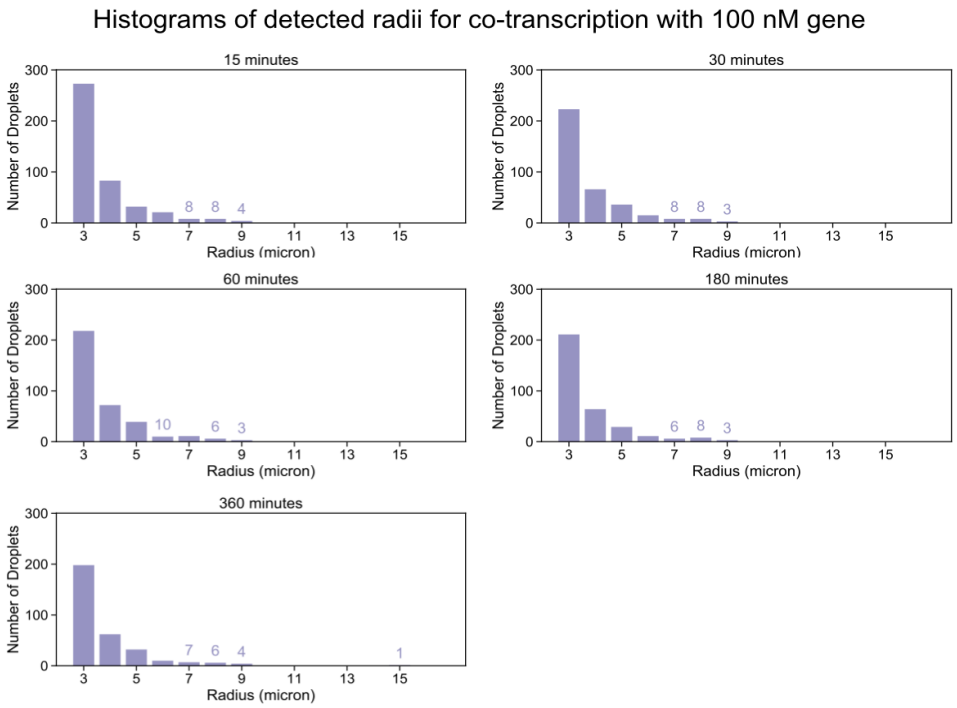

Figure S3.33: Histograms of the radii of detected droplets for the DNA-RNA hybrid nanotubes with co-transcription of RNA trigger from 100 nM template/gene in water-in-oil droplets experiment (Figure 3-5). Droplets were detected with the custom developed script.

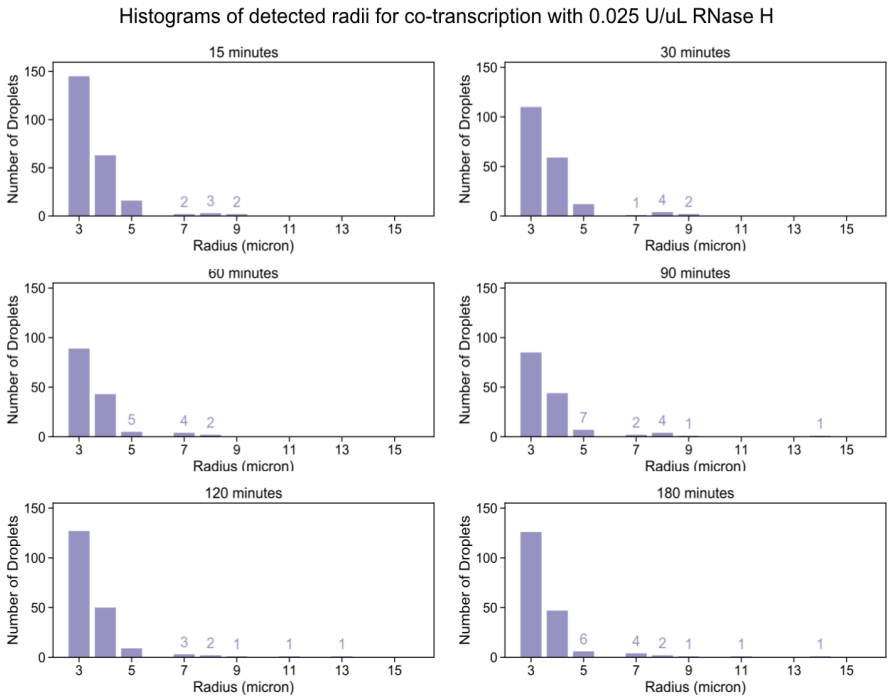

Figure S3.34: Histograms of the radii of detected droplets for the DNA-RNA hybrid nanotubes with co-transcription of RNA trigger from 100 nM template/gene and 0.025 U/μL RNase H in water-in-oil droplets experiment (Figure 3-6). Droplets were detected with the custom developed script.

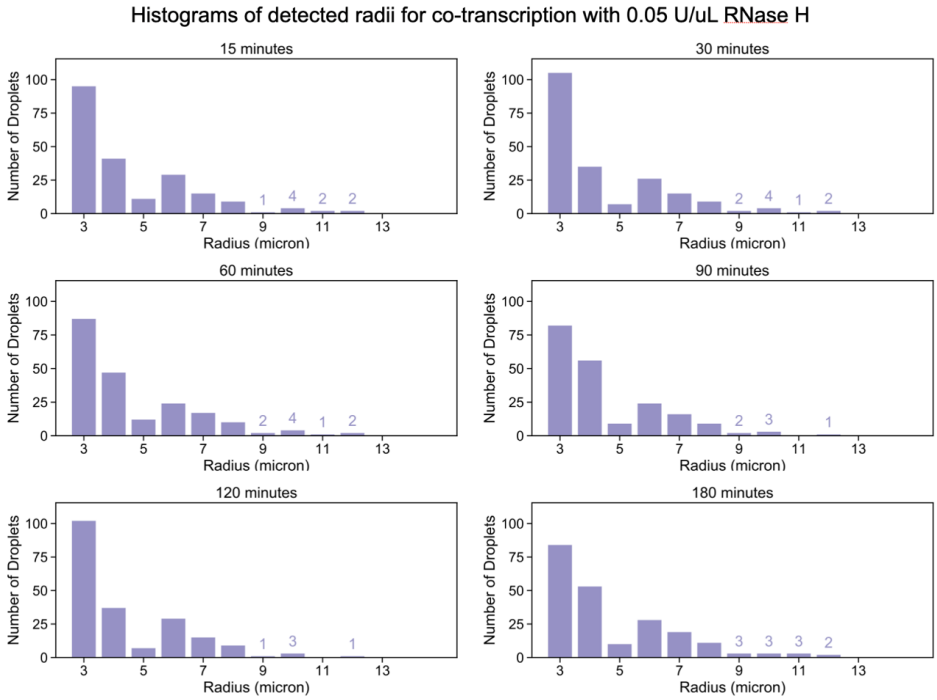

Figure S3.35: Histograms of the radii of detected droplets for the DNA-RNA hybrid nanotubes with co-transcription of RNA trigger from 100 nM template/gene and 0.05 U/μL RNase H in water-in-oil droplets experiment (Figure 3-6). Droplets were detected with the custom developed script.

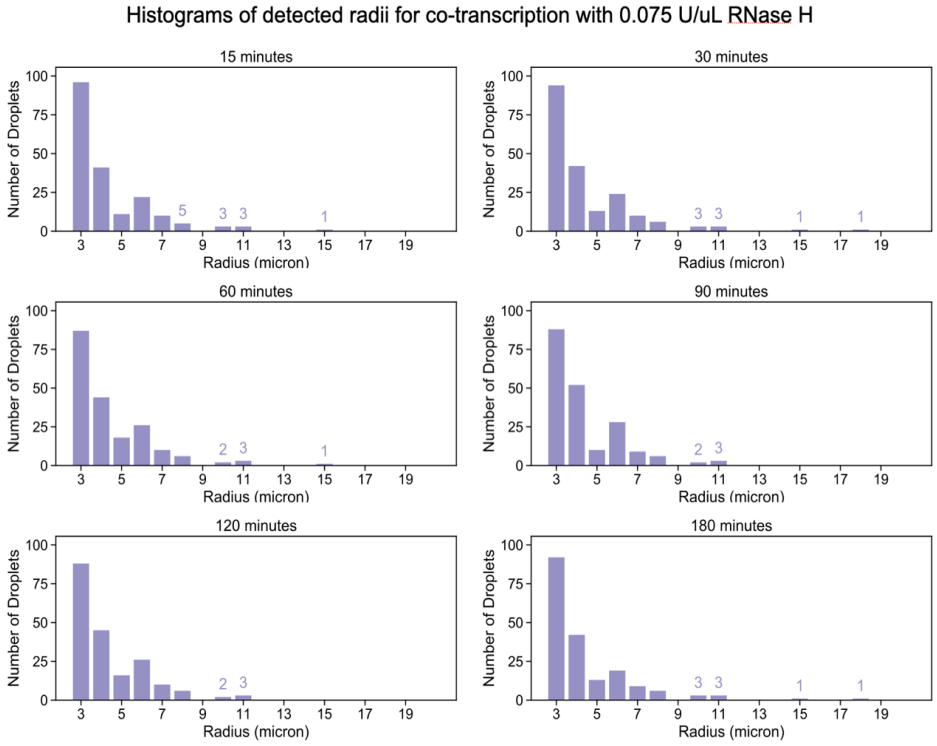

Figure S3.36: Histograms of the radii of detected droplets for the DNA-RNA hybrid nanotubes with co-transcription of RNA trigger from 100 nM template/gene and 0.075 U/μL RNase H in water-in-oil droplets experiment (Figure 3-6). Droplets were detected with the custom developed script.

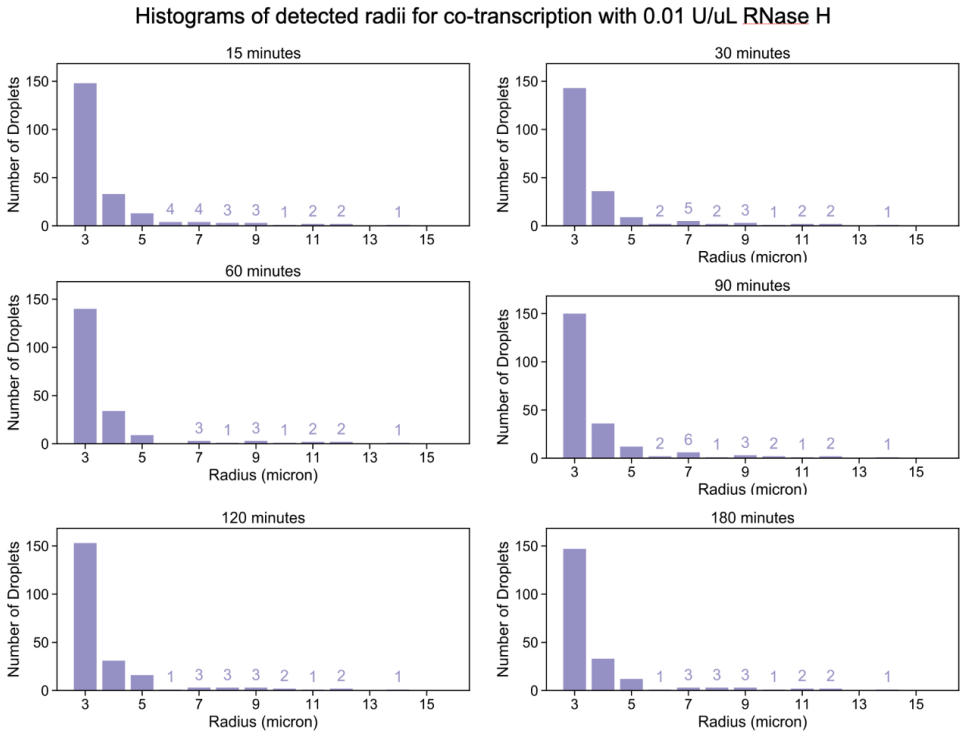

Figure S3.37: Histograms of the radii of detected droplets for the DNA-RNA hybrid nanotubes with co-transcription of RNA trigger from 100 nM template/gene and 0.1 U/μL RNase H in water-in-oil droplets experiment (Figure 3-6). Droplets were detected with the custom developed script.

Two-tile nanotubes in bulk

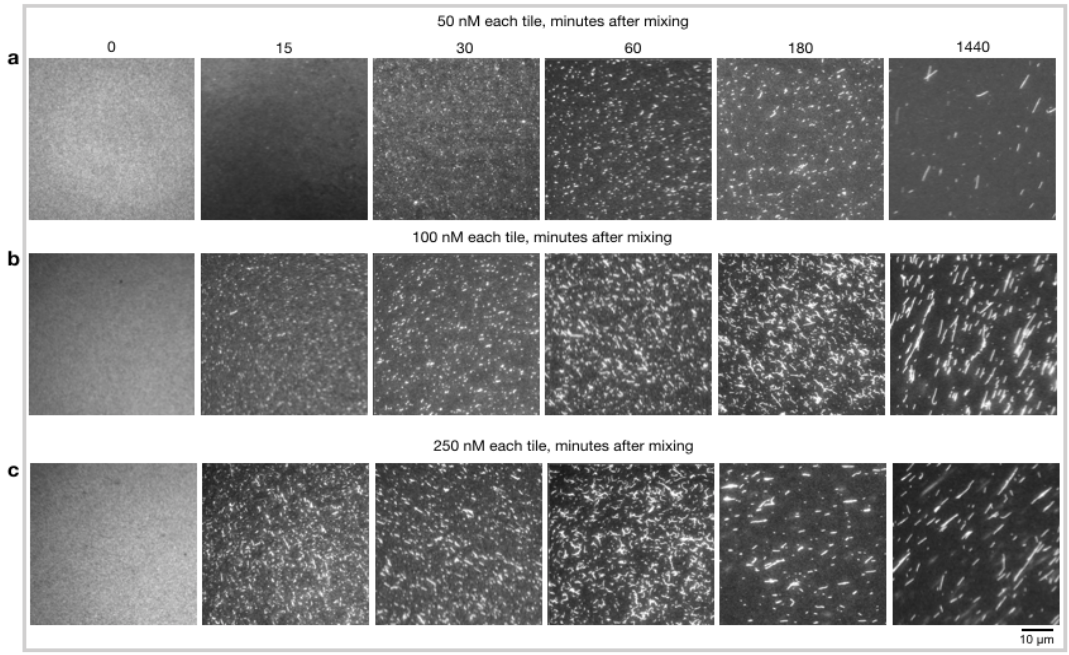

Figure S3.38: Isothermal assembly of non-encapsulated two-tile DNA nanotubes at room temperature. Tiles were pre-annealed and mixed immediately before the start of the imaging experiment. (a, b, c) Representative temporal sequence of fluorescence microscopy images of two-tile nanotubes mixtures at 50, 100, and 250 nM concentration for each tile respectively. Fluorescence microscopy images were collected after diluting each sample to 50 nM each tile at the time of slide preparation. Scale bar: 10 µm.

Two-tile nanotubes in droplets for extended observations

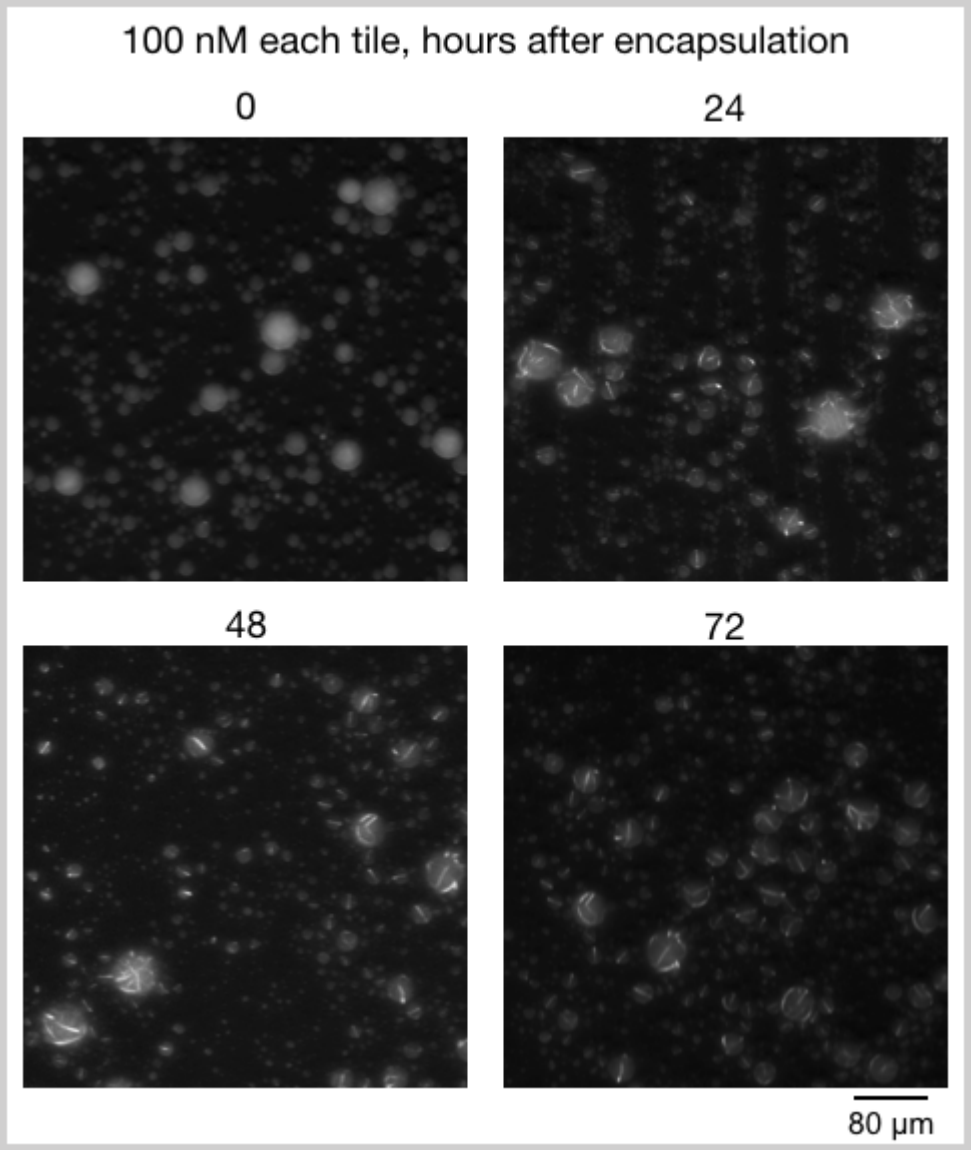

Figure S3.39: Encapsulated nanotube polymerization through 72 hours after encapsulation. Fluorescence images depict two-tile nanotube design with 100 nM each tile with 1x TAE buffer and 12.5 mM $MgCl_2$. Beyond 24h, we do not observe any discernible change in the nanotube morphology. Scale bar: 80 µm.

Autofluorescence of water-in-oil droplets without fluorescently labeled strands

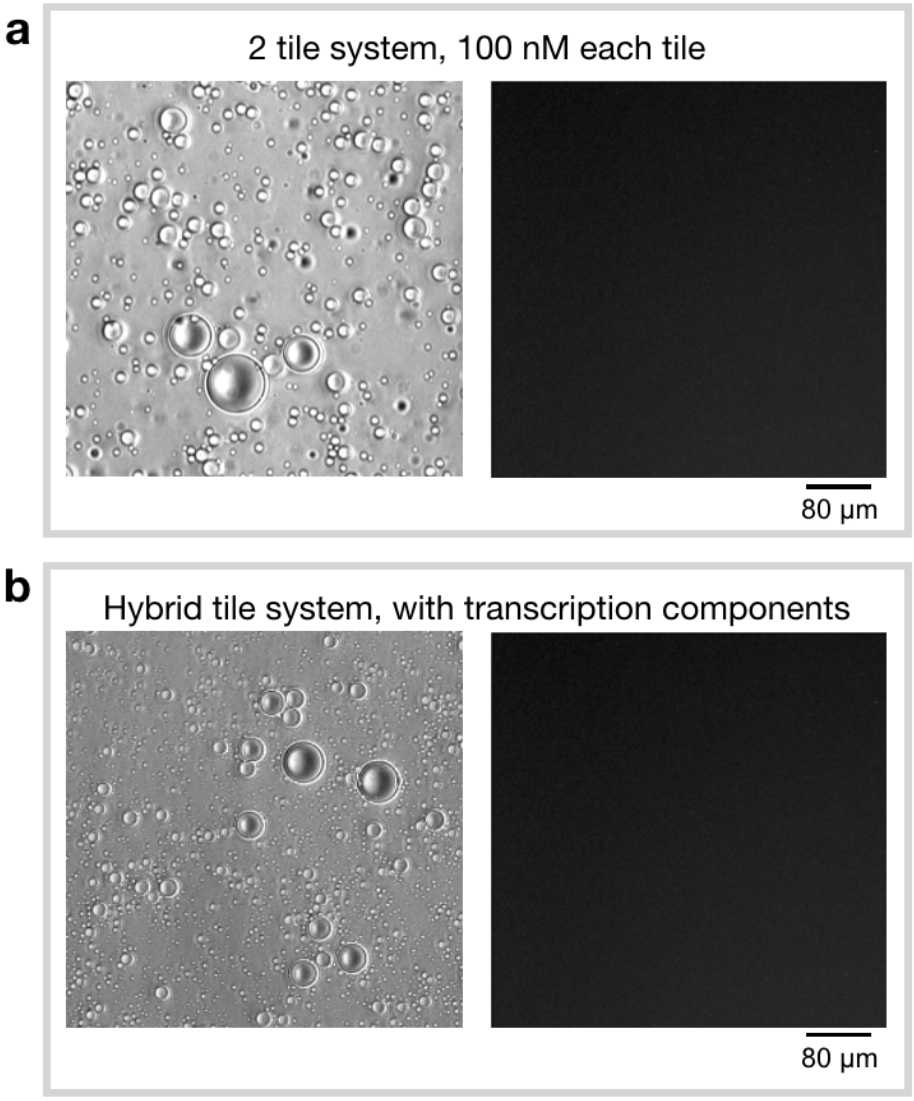

Figure S3.40: Background fluorescence of two nanotube designs without attached fluorescent dye encapsulated in water-in-oil droplets. We imaged nanotubes without an attached fluorescent dye in water-in-oil droplets to check for autofluorescence of either the droplets or surrounding oil medium. (a) Brightfield and Cy3 filter images of water-in-oil droplets containing the two-tile design, 100 nM each strand without an attached fluorescently labeled dye with 1x TAE buffer and 12.5 mM $MgCl_2$. (b) Brightfield and Cy3 filter images of water-in-oil droplets containing the hybrid design, 500 nM each strand without an attached fluorescent dye with 4 mM NTPs, 10 mM $MgCl_2$, 100 nM gene template, 2.5% w/v PEG, 2.5% v/v RNAP in 1X TXN buffer. These experiments confirm that neither the droplets themselves nor the oil/surfactant medium are fluorescent. Scale bar: 80 µm.

Increased background fluorescence for increasing tile concentration in two-tile design experiments

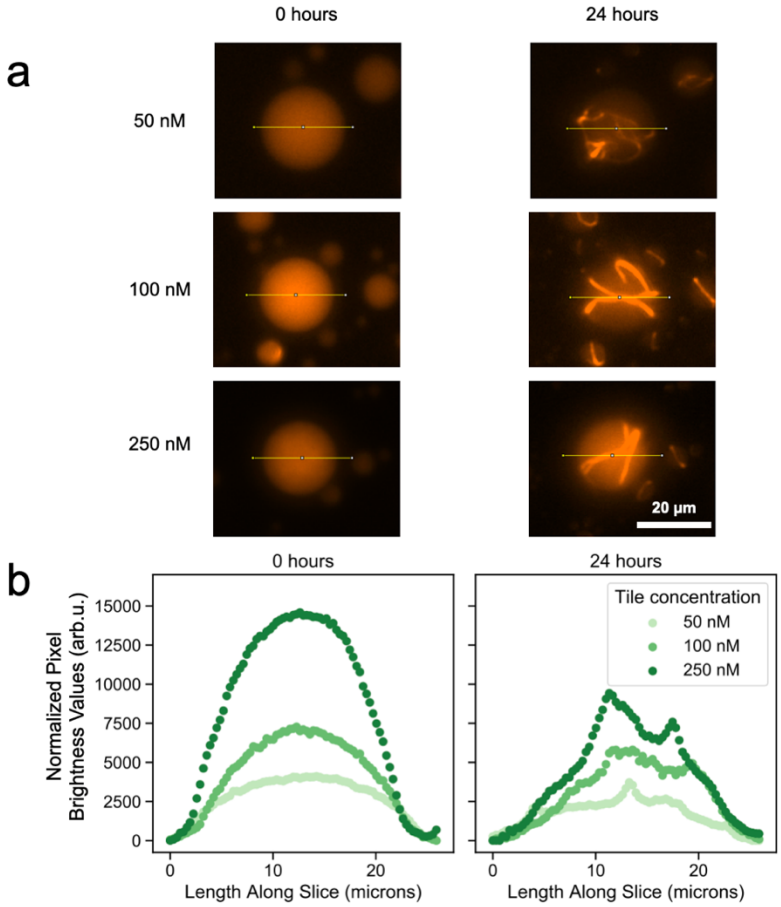

Figure S3.41: Comparison of the normalized pixel brightness values for different concentrations of two-tile nanotubes along a linear cross-section of a single droplet. a) Representative fluorescence microscopy images of a single droplet for each concentration of two-tile nanotubes reported in the main text at 0 and 24 hours. The yellow line indicates the linear segment for which normalized pixel brightness values are plotted in (b). The linear segment is the same length for all measurements. b) Normalized pixel brightness values along the length of the slice in (a) for 50, 100, 250 nM two-tile nanotubes at 0 and 24 hours. Pixel brightness values are normalized for each concentration and time point by subtracting the minimum brightness for that profile from each value such that the minimum brightness value for each profile is 0 arb.units. Scale bar: 20 μm.

Length measurement of nanotubes using two-dimensional contour projection

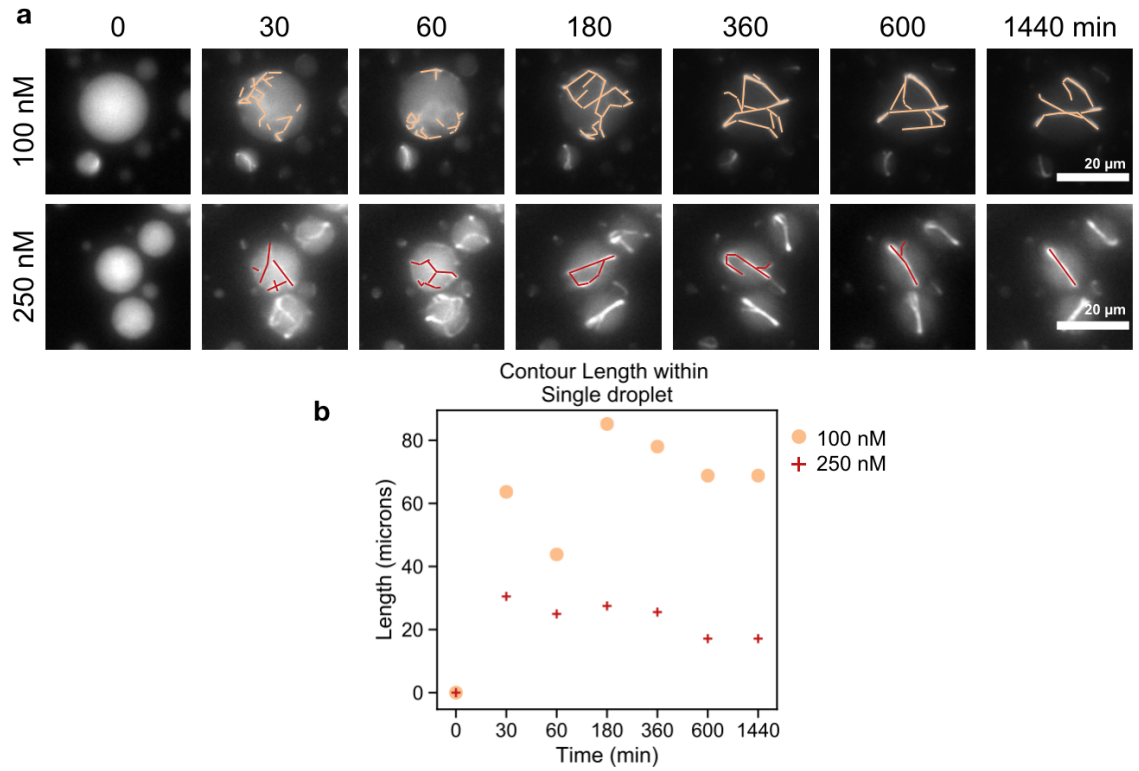

Figure S3.42: Measuring the projected contour length of nanotubes at each time point for 100 and 250 nM two-tile nanotubes within a single droplet. Epifluorescence microscopy images are a two-dimensional projection of signals coming from the focal plane, as well as planes above and below the focal plane. As a two-dimensional projection it is non-trivial, if not impossible, to determine the actual depth, angle, and length of observed nanotubes. Additionally, the number nanotubes which may be overlapping or intersecting are not distinguishable. For these droplets, we only measured each observable contour once, although the brightness and decreased curvature to the structures at 360 minutes onwards indicate there may be more than one nanotube along some contours. For these reasons, we believe contour measurement length to be misleading and non-comparable to previously reported nanotubes length measurements in bulk.[2,11] a) Representative microscopy images of the droplets for which contours are measured. Images with measured contours marked in orange (100 nM) and red (250nM) lines. Contours are measured by hand in Fiji using linear segments as indicated in (a). b) The sum of length of measured contours over time within each droplet. The length for the 100 nM sample is indicated by the light orange circles, while the 250 nM is indicated by the dark red crosses. In disagreement with both the model reported in this paper, and previous reports on nanotube assembly,[2,10] the total contour length decreases rather than reaches steady-state at some maximum total length, further confirming that contour length is not an accurate method for quantifying nanotube assembly inside droplets. Scale bar: 20 μm.

Effect of DNase I on two-tile DNA nanotubes

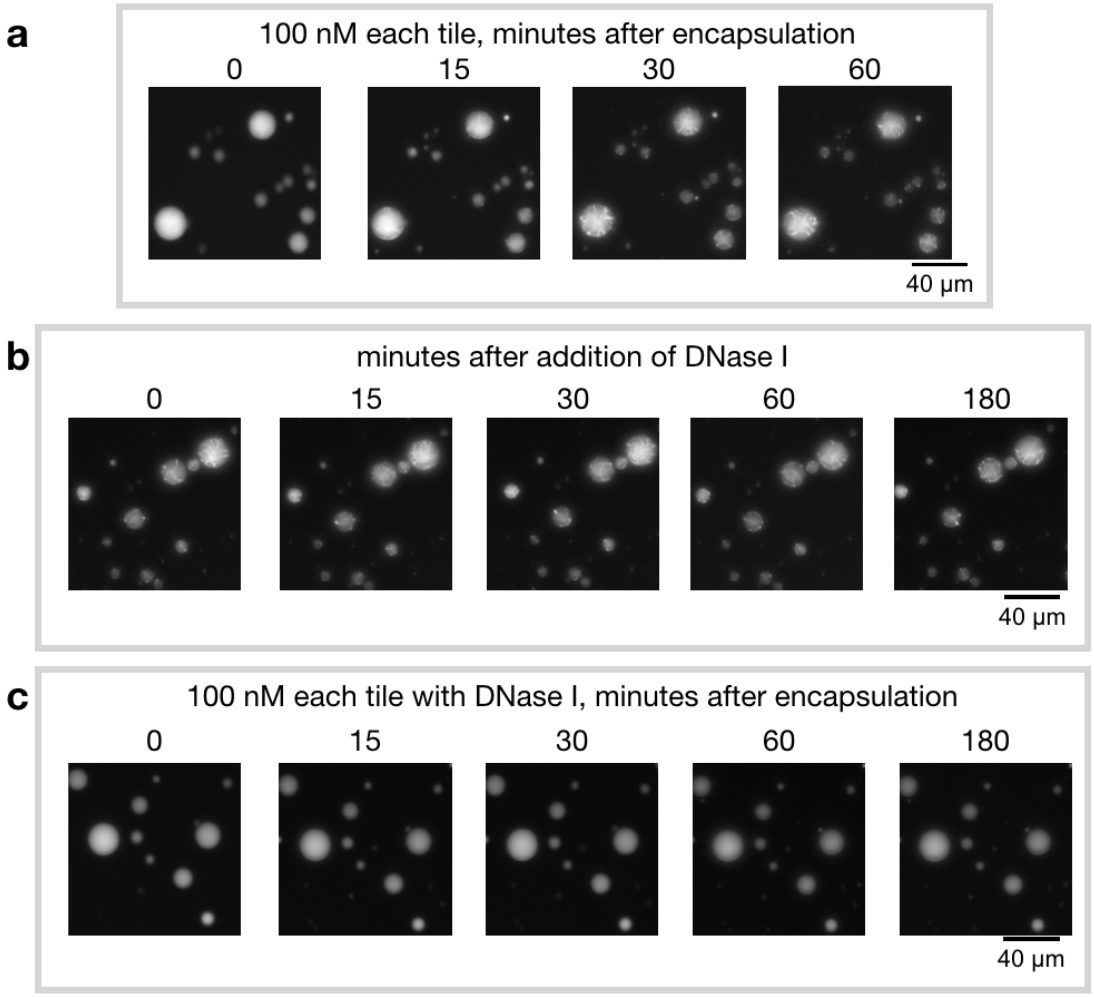

Figure S3.43: Encapsulation of DNase I in water-in-oil droplets. DNase I can inhibit growth of nanotubes by degrading the monomer tile made of DNA oligomers but DNase I cannot penetrate through water-in-oil droplets if added to the oil phase (a) Encapsulated DNA nanotubes were grown (two-tile nanotube design with 100 nM each tile with 1x TAE buffer and 12.5 mM MgCl2) for 60 minutes. (b) 5μl of 1U/μl of DNase 1 to the oil phase to see if DNase can penetrate through the droplet but no change was observed in the morphology of nanotubes inside the droplets. (c) Control experiment where DNase was encapsulated with the tile mixture inside the droplets (two-tile nanotube design with 100 nM each tile with 1x TAE buffer and 12.5 mM MgCl2 and 5μl of 1U/μl of DNase 1). DNase 1 successfully prevents any nanotube formation. Scale bar: 40 μm.

Computational modeling

We built a series of deterministic models to illustrate the temporal dynamics of the following processes:

1) tile assembly

2) tile activation using a single stranded activator, also called trigger, and

3) tile activation/deactivation using transcription of RNA trigger and degradation (mediated by RNase H) of DNA-RNA hybrid complexes.

The models described here are derived based on models of tile assembly developed in (Zhang et al. 2013)[11], and from models of transcriptional circuits developed in (Kim et al., 2006, Weitz et al. 2014)[12,13]. Both classes of models are deterministic ordinary differential equations (ODEs), that rely on the assumption that molecular species are at high concentration and stochastic effects can be neglected. Our encapsulated experiments satisfy this assumption, as all DNA species are present at concentration above 50 nM. For experiments including RNase H, partitioning noise may affect the system operation as RNase H is likely present only at few nanomolar concentration, but we focus on droplets with a diameter above 6 μm, which means more than 100 copies of the enzyme are present in each droplet. Deterministic ODEs are still suited to capture this scenario.

The models we developed were not fitted to our data. The purpose of our modeling efforts is to illustrate our understanding of experimental behaviors observed in our experiments, not to recapitulate such behaviors quantitatively. To solve the ODEs via numerical integration, we adopted parameters provided in the literature. These parameters were identified in the cited

literature by fitting the models to data collected from experiments comparable to the ones described here, but not encapsulated in droplets.

Tile assembly models

Our goal is to model the fraction of tiles that are assembled into growing nanotubes. A simple ODE model that captures tile assembly into nanotubes was proposed and fitted to data by (Zhang et al. 2013)[11].

The model by Zhang et al. includes two reactions:

Nucleation

$$n \cdot \ Tile \xrightarrow{k_{nuc}} Nanotube$$

Elongation

$$Nanotube + Tile \xrightarrow{k_{elong}} Nanotube$$

Using the law of mass action, these reactions were mapped to two ODEs describing the temporal evolution of free tiles and nanotubes:

$$\frac{d\,[Tile]}{dt} = \ -nk_{nuc}[Tile]^n - k_{elong}[Tile][Nanotube] \qquad (1)$$

$$\frac{d\,[Nanotube]}{dt} = \ nk_{nuc}[Tile]^n$$

Assuming the total tile concentration T^{tot} remains constant, the fraction of assembled tiles can be derived by subtracting the concentration of free tiles from T^{tot}. The model parameters, nucleation stoichiometry (n), nucleation rate parameter (k_{nuc}) and elongation rate parameter (k_{elong}), were fitted and validated experimentally in Zhang et al. This model does not include depolymerization, which in practice reduces growth rate; also this model does not include

nanotube joining (Ekani Nkodo et al. 2004, Mardanlou et al. 2018)[13,14]. Thus, it likely overestimates assembly rates and nanotube number.

We adapted the Zhang model to a scenario in which two separate tile species interact to nucleate and then polymerize, however the kinetic parameters of the reactions are identical (for simplicity) for each species. Nucleation and elongation can only occur if both tile species are present. Adopting for consistency the same notation as in the Zhang models, we have:

Nucleation: we assume that only half the number of tiles of each species are needed to achieve the nucleation stoichiometry n

$$\frac{n}{2} \cdot Tile\ A + \frac{n}{2} \cdot Tile\ B \xrightarrow{k_{nuc}} Nanotube$$

Elongation: Because we use a two-tile design in which tiles form a perpendicular ring pattern, we model nanotubes elongation using the same reaction assumed by Zhang for the single-tile design. However, we also assume on average half the nanotube population is growing a Tile A edge and the other half is growing a Tile B edge; this assumption is reflected in the ODE model (2) that follows.

$$Nanotube + Tile\ A \xrightarrow{k_{elong}} Nanotube$$

$$Nanotube + Tile\ B \xrightarrow{k_{elong}} Nanotube$$

Using the law of mass action, we derive the following ODEs:

$$\frac{d\,[Tile\ A]}{dt} = \frac{-n}{2} k_{nuc}[Tile\ A]^{\frac{n}{2}}[Tile\ B]^{\frac{n}{2}} - \frac{1}{2} k_{elong}[Tile\ A][Nanotube]$$

$$\frac{d\,[Tile\ B]}{dt} = \frac{-n}{2} k_{nuc}[Tile\ A]^{\frac{n}{2}}[Tile\ B]^{\frac{n}{2}} - \frac{1}{2} k_{elong}[Tile\ B][Nanotube]$$

$$\frac{d\,[Nanotube]}{dt} = k_{nuc}[Tile\ A]^{\frac{n}{2}}[Tile\ B]^{\frac{n}{2}}$$

Adopting the parameters in Table S3.6, these ODEs were integrated numerically using MATLAB with a custom script implementing the Euler method with a step size of 0.1 s.

We assumed the total concentration of each tile to be 50 nM, 100 nM or 250 nM (for consistency with the experiments in Figure 3 of the main text). The computed fraction of assembled tiles and the estimated number of nanotubes in a droplet of 3μm radius are shown in Fig. S3.38. This plots illustrates that the higher the tile concentration, the faster tiles are incorporated into nanotubes, and the faster nanotubes nucleate, reaching higher numbers.

In our experiments monitoring assembly of nanotubes in droplets (Figure 3 of the main text) nanotubes appear to nucleate at higher tile concentration in agreement with the predictions of this simple model. However the droplet brightness suggests that a large number of tiles may remain unpolymerized beyond 2-3 hours, suggesting that depolymerization may be a non-negligible reaction. Unlike the predicted fraction of assembled tiles, skewness appears to increase faster at lower concentrations, likely due to the high fluorescence background at high tile concentrations.

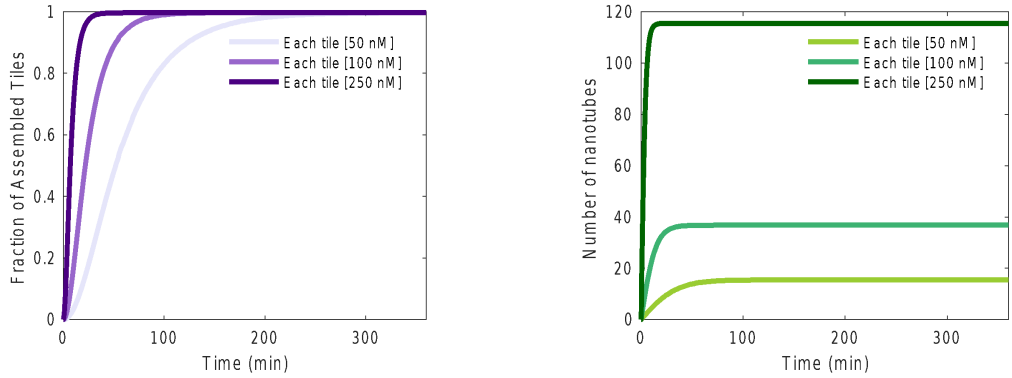

Figure S3.44: Predicted fraction of assembled tiles and number of nanotubes in a droplet of 3μm radius using the developed model. Simulation parameters are listed in Table S3.6.

Model capturing transcription of RNA and RNA-mediated tile activation and assembly

We now derive a simple model for activation of tiles through an RNA molecule that is transcribed by a synthetic gene.

First, activation of tiles can be modeled with the macroscopic chemical reaction:

$$RNA_{Trigger} + Inactive\ Tile \xrightarrow{k_{TAI}} Active\ Tile$$

Next, we assume the system includes a constant amount of synthetic gene, or template, that produces RNA trigger, which we denote $T_{RNA.}$ RNA polymerase binds to the template and produces RNA trigger according to the following steps:

$$RNAP + T_{RNA} \underset{k-}{\overset{k+}{\Leftrightarrow}} RNAP \cdot T_{RNA} \xrightarrow{K_{CAT,ON}} RNA_{Trigger} + RNAP + T_{RNA}$$

We further assume that RNAP loses activity according to a first order reaction:

$$RNAP \xrightarrow{k_{loss}} 0$$

Because in our experiments we used the Ampliscribe Flash transcription kit that recommends 4 hour incubation, we assumed k_{loss} to be 0.00019/s which corresponds to a loss of more than 50% activity in four hours of reaction.

Active tiles nucleate and contribute to nanotube elongation according to model (1). The additional ODEs for RNA production and tile activation are derived using the law of mass action:

(3)

$$\frac{d\,[T_{RNA}]}{dt} = K_{CAT,ON}\,[RNAP \cdot T_{RNA}] + k_{-}\,[RNAP \cdot T_{RNA}] - k_{+}[RNAP \cdot T_{RNA}]$$

$$\frac{d[RNA_{trigger}]}{dt} = K_{CAT,ON}\,[RNAP \cdot T_{RNA}] - k_{TAI}[RNA_{Trigger}][Inactive\ Tile]$$

$$\frac{d\,[Inactive\ Tile]}{dt} = -k_{TAI}[RNA_{Trigger}][Inactive\ Tile]$$

$$\frac{d\,[Active\ Tile]}{dt} = k_{TAI}[RNA_{Trigger}][Inactive\ Tile]$$

$$\frac{d\,[RNAP \cdot T_{RNA}]}{dt} = -K_{CAT,ON}\,[RNAP \cdot T_{RNA}] - k_{-}[RNAP \cdot T_{RNA}] + k_{+}[RNAP][T_{RNA}]$$

$$\frac{d\,[RNAP]}{dt} = K_{CAT,ON}\,[RNAP \cdot T_{RNA}] + k_{-}[RNAP \cdot T_{RNA}] - k_{+}[RNAP][T_{RNA}] - k_{loss}[RNAP]$$

These equations were numerically integrated with custom MATLAB scripts, using the parameters in Table S3.6.

The manufacturer did not provide information about the estimated concentration RNAP batch we used in our experiments. To estimate the RNAP amount based on the volume we used in the encapsulated reactions (2.5% v/v of the transcription and tile mix), we reasoned that the transcription kits we used were optimized for rapid yield, like kits adopted in previous research on transcriptional circuits (Weitz et al. 2014)[13]. Thus, we assumed that the stock concentration of our enzyme should be in the range of 3-4μM (Weitz et al. 2014)[13]. Remaining consistent with the 218 nM concentration of RNAP estimated in (Weitz et al. 2014)[13] for experiments that used a 10% (v/v) RNAP, we assumed the RNAP concentration to be 54 nM.

Figure S3.45 shows the fraction of assembled tiles computed using model (3). This simulation illustrates that tile assembly proceeds more rapidly when a higher template concentration is used. At low template concentrations, assembly proceeds more slowly and settles to a low equilibrium level due to the assumption that RNAP loses activity and becomes inactive after a period of time.

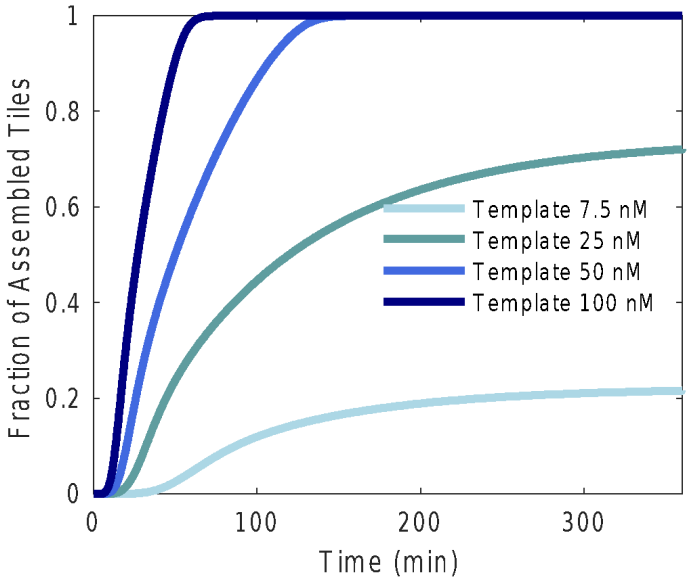

Figure S3.45: Illustrative simulation obtained using the developed model for the temporal evolution of the fraction of assembled tiles from synthetic gene template. Using equation in (3) the concentration of the synthetic gene template is varied between 7.5 and 100 nM. This plot is also reported in Figure 5 of the main text. Simulation parameters are listed in Table S3.6.

Model capturing transcription and degradation of RNA and RNA-mediated tile activation and assembly

We model the effects of RNase H by assuming that active tiles, assembled tiles, and nucleated nanotubes are degraded and revert to inactive tiles, with a net consumption of RNA.

These processes are modeled through the following reactions:

$$RNase\ H + Active\ Tile \underset{k-,H}{\overset{k+,H}{\Longleftrightarrow}} RNase\ H \cdot Active\ Tile \xrightarrow{K_{CAT,H}} Inactive\ Tile + RNase\ H$$

$$RNase\ H + Nanotube \underset{k-,H}{\overset{k+,H}{\Longleftrightarrow}} RNase\ H \cdot Nanotube \xrightarrow{K_{CAT,H}} Inactive\ Tile + RNase\ H$$

$$RNase\ H + Assembled\ Tile \underset{k-,H}{\overset{k+,H}{\Longleftrightarrow}} RNase\ H \cdot Nanotube \xrightarrow{K_{CAT,H}} Inactive\ Tile + RNase\ H$$

Using conservation of mass for the tiles, the concentration of the Assembled Tile species can be found as:

$$Assembled\ Tile = [Inactive\ Tile]_0 - [Inactive\ Tile] - [Active\ Tile] - [RNase\ H \cdot Active\ Tile] - [Nucleus] - [RNase\ H \cdot Nucleus] - [RNase\ H \cdot Assembled\ Tile]$$

Using the law of mass action, we can then find the following 11 ODEs:

4)

$$\frac{d\,[T_{RNA}]}{dt} = K_{CAT,ON}\ [RNAP \cdot T_{RNA}] + k_{-}\ [RNAP \cdot T_{RNA}] - k_{+}[RNAP \cdot T_{RNA}]$$

$$\frac{d[RNA_{trigger}]}{dt} = K_{CAT,ON}\ [RNAP \cdot T_{RNA}] - k_{AI}[RNA_{Trigger}][Inactive\ Tile]$$

$$\frac{d\,[Inactive\ Tile]}{dt} = -k_{AI}\left[RNA_{Trigger}\right][Inactive\ Tile] + K_{CAT,H}\ [RNase\ H \cdot Active\ Tile] + K_{CAT,H}\ [RNase\ H \cdot Nanotube] + K_{CAT,H}\ [RNase\ H \cdot Assembled\ Tile]$$

$$\frac{d\,[Active\ Tile]}{dt} = k_{AI}\left[RNA_{Trigger}\right][Inactive\ Tile] + k_{-,H}\,[RNase\ H \cdot Active\ Tile] - nk_{nuc}[Active\ Tile]^n - k_{+,H}\ [RNase\ H][Active\ Tile] - k_{elong}[Nanotube][Active\ Tile]$$

$$\frac{d\,[Nanotube]}{dt} = nk_{nuc}[Active\ Tile]^n - k_{+,H}\,[RNase\ H][Active\ Tile] + k_{-,H}\,[RNase\ H \cdot Nanotube]$$

$$\frac{d\,[RNase\ H \cdot Active\ Tile]}{dt} = k_{+,H}[RNase\ H][Active\ Tile] - k_{-H}[RNase\ H \cdot Active\ Tile] - K_{CAT,H}\,[RNase\ H \cdot Active\ Tile]$$

$$\frac{d\,[RNase\ H \cdot Nanotube]}{dt} = k_{+,H}[RNase\ H][Nanotube] - k_{-H}[RNase\ H \cdot Nanotube] - K_{CAT,H}\,[RNase\ H \cdot Nanotube]$$

$$\frac{d\,[RNase\ H \cdot Assembled\ Tile]}{dt} = k_{+,H}[RNase\ H][Assembled\ Tile] - k_{-H}[Assembled\ Tile] - K_{CAT,H}\,[Assembled\ Tile]$$

$$\frac{d[RNase\ H]}{dt} = K_{CAT,H}\,[RNase\ H \cdot Assembled\ Tile] + K_{CAT,H}[RNase\ H \cdot Nanotube] + K_{CAT,H}[RNase\ H \cdot Active\ Tile] + k_{-,H}[RNase\ H \cdot Assembled\ Tile] + k_{-,H}[RNase\ H \cdot Nanotube] + k_{-,H}[RNase\ H \cdot Active\ Tile] - k_{+,H}[RNase\ H][Assembled\ Tile] - k_{+,H}[RNase\ H][Nanotube] - k_{+,H}[RNase\ H][Active\ Tile]$$

$$\frac{d\,[RNAP \cdot T_{RNA}]}{dt} = -K_{CAT,ON}\,[RNAP \cdot T_{RNA}] - k_{-}[RNAP \cdot T_{RNA}] + k_{+}[RNAP][T_{RNA}]$$

$$\frac{d\,[RNAP]}{dt} = K_{CAT,ON}\,[RNAP \cdot T_{RNA}] + k_{-}[RNAP \cdot T_{RNA}] - k_{+}[RNAP][T_{RNA}] - k_{loss}[RNAP]$$

Model (4) was integrated numerically using custom MATLAB scripts, and using the parameters in Table S3.6. For consistency we assumed 54 nM RNAP concentration, the same value used to generate Fig. S3.39. Because we were not able to obtain from the manufacturer the estimated stock concentration of RNase H, we estimated a plausible RNase concentration using the estimates for a similar product reported in (Weitz et al, 2014)[12]. Our reasoning relies on the assumption that for practical purposes the RNase H activity/units is comparable between Promega RNase H (this project) and Ambion RNase H (Weitz et al.), although their definition is not the same. For the Weitz paper, based on their estimate of stock concentration, RNase H volume added to the aqueous phase, and vendors' units per microliter of the stock, we estimated that 0.015 units/μl correspond to 1 nM RNase H concentration. Thus, for these simulations, we estimate that a 0.025 units/μl RNase H amount corresponds to a concentration of 1.6 nM, 0.05 units/μl correspond to 3.2 nM and so on.

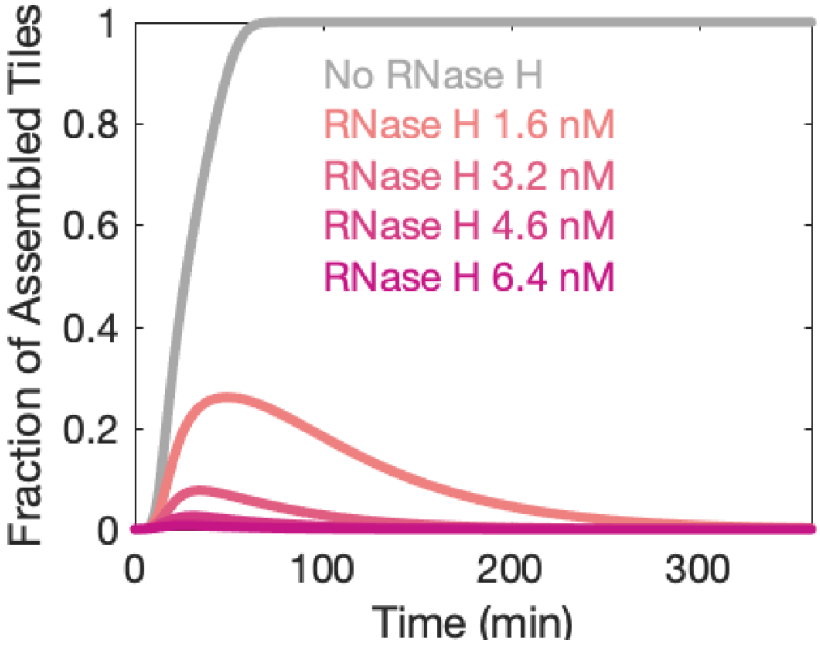

Fig. S3.46: Illustrative simulation showing the transient pulse predicted by the simulated fraction of assembled tiles, as the concentration of RNase H is varied. This plot is also reported in Fig. 6 of the main text.

Parameter	Value and units	Reference	Range (literature)
k_A	6.96 x 10^4/M/s	Kim et al., 2006[12], Zhang et al, 2013[11]	10^4-10^7
$k_{-, H}$	0.125 /M/s	Weitz et al., 2014[13]	0.01
$k_{+, H}$	7.13 x 10^5/M/s	Weitz et al., 2014[13]	10^5- 10^7
$K_{CAT, H}$	0.552 /s	Weitz et al., 2014[13]	0.01 - 1
n	2.5	Zhang et al. 2014[16]	N/A
k_{nuc}	2.0 x 10^5 /M/s	Zhang et al. 2013[11]	N/A
k_{elong}	3.4 x 10^6 /M/s	Zhang et al. 2013[11]	N/A
k_+	1.9 x 10^5 /M/s	Weitz et al., 2014[13]	N/A
k_-	0.0446 /M/s	Weitz et al., 2014[13]	N/A
$K_{CAT, ON}$	0.0186 /M/s	Weitz et al., 2014[13]	N/A
k_{loss}	0.00019/s		

Table S3.6: Parameters used in computational simulations.[6]

References for the supplement

1 Rothemund, P. W. *et al.* Design and characterization of programmable DNA nanotubes. *Journal of the American Chemical Society* **126**, 16344-16352 (2004).

2 Agarwal, S. & Franco, E. Enzyme-driven assembly and disassembly of hybrid DNA–RNA nanotubes. *Journal of the American Chemical Society* **141**, 7831-7841 (2019).

3 Rothemund, P. W. K. *et al.* Design and Characterization of Programmable DNA Nanotubes. *Journal of the American Chemical Society* **126**, 16344-16352, doi:10.1021/ja044319l (2004).

4 Milligan, J. F., Groebe, D. R., Witherell, G. W. & Uhlenbeck, O. C. Oligoribonucleotide synthesis using T7 RNA polymerase and synthetic DNA templates. *Nucleic acids research* **15**, 8783-8798 (1987).

5 Van der Walt, S. *et al.* scikit-image: image processing in Python. *PeerJ* **2**, e453 (2014).

6 M.A. Klocke, P. Pungchai. Dynamic self-assembly of compartmentalized DNA nanotubes, dropletDetection_dynamicSelfAssemblyProject. *Zenodo*, doi:10.5281/zenodo.4763253 (2021).

7 von Hippel, P. T. Mean, Median, and Skew: Correcting a Textbook Rule. *Journal of Statistics Education* **13**, null-null, doi:10.1080/10691898.2005.11910556 (2005).

8 DeCarlo, L. T. On the meaning and use of kurtosis. *Psychological Methods* **2**, 292-307, doi:https://doi.org/10.1037/1082-989X.2.3.292 (1997).

9 Fisher, R. A. Statistical methods for research workers. *Springer*, 66-70, doi:https://doi.org/10.1007/978-1-4612-4380-9_6 (1992).

10 Green, L. N. *et al.* Autonomous dynamic control of DNA nanostructure self-assembly. *Nature chemistry* **11**, 510-520 (2019).

11 Zhang, D. Y., Hariadi, R. F., Choi, H. M. T. & Winfree, E. Integrating DNA strand-displacement circuitry with DNA tile self-assembly. *Nature Communications* **4**, 1965, doi:10.1038/ncomms2965 (2013).

12 Kim, J., White, K. S. & Winfree, E. Construction of an in vitro bistable circuit from synthetic transcriptional switches. *Molecular systems biology* **2**, 68 (2006).

13 Weitz, M. *et al.* Diversity in the dynamical behaviour of a compartmentalized programmable biochemical oscillator. *Nature chemistry* **6**, 295-302 (2014).

14 Ekani-Nkodo, A., Kumar, A. & Fygenson, D. K. Joining and scission in the self-assembly of nanotubes from DNA tiles. *Physical review letters* **93**, 268301 (2004).

15 Mardanlou, V. *et al.* A coarse-grained model captures the temporal evolution of DNA nanotube length distributions. *Natural Computing* **17**, 183-199 (2018).

16 Zhang, F., Nangreave, J., Liu, Y. & Yan, H. Structural DNA Nanotechnology: State of the Art and Future Perspective. *Journal of the American Chemical Society* **136**, 11198-11211, doi:10.1021/ja505101a (2014).

4 Conclusion and Future Work

4.1 Conclusion

This work contributes to the ever growing scientific literature which attempts to understand how to build, control and improve nucleotide assemblies and program their interaction with their environment. Overall this thesis attempts to develop nucleotide filaments as the foundation for a synthetic cytoskeletal system.

Chapter 1 specifically focusses on the development of DNA monomers which respond to specific RNA trigger molecules in order to get activated, similar to trigger activation of some cytoskeletal filaments inside biological cells.[1] In this system RNA serves as a fuel that enables the assembly of nanoscale tiles into micrometer sized nanotubes. More importantly, we demonstrated that the kinetics assembly and disassembly of our DNA-RNA nanotubes can be controlled isothermally by managing the enzymatic production and degradation of RNA activating the tiles; this can be done by using molecular circuits whose outputs are RNA molecules with programmable concentration kinetics. An important feature of this system is its ability to operate isothermally at 37ºC, which makes it potentially useful for biological applications.[1]

Chapter 2 contributes towards testing the ability of theoretical models to describe end-to-end joining rates in DNA nanotube systems.[2] We experimentally characterized the length-dependence of the end-to-end joining rate of DNA nanotubes by measuring the lengths of nanotubes before and after joining at different times during the joining process. We tested the ability of the Hariadi model[3] for end-to-end joining rate to reproduce the experimental length data using an ODE model of nanotube joining.

Chapter 3 provides insights in the reconstitution of DNA or DNA-RNA hybrid assemblies in cell sized compartments.[4] This includes DNA nanotubes as a self-assembling scaffold and transcriptional processes to control nanotube assembly and disassembly. We develop a variety of assays for encapsulating DNA nanotubes in cell-sized, water-in-oil droplets, highlighting that multiple nanotube species can be assembled and can coexist. We employ two distinct nanotube designs to control the start of assembly, and characterize the kinetics of polymerization inside compartments using quantitative statistical analysis. By implementing a DNA-RNA hybrid nanotube design, we demonstrate enzyme-mediated control of assembly and disassembly that yields transient presence of nanotubes inside compartments. The density of assembled nanotubes, as well as their lifetime in the droplets, are tunable properties of this system. The methods and components characterized here are a first step toward the bottom-up development of NA cytoskeletal mimics for synthetic minimal cells.[4]

4.2 Future Work

Engineering nanomaterials has been one of the key challenges of the past few decades. Although we have been using nanoscale materials for hundreds of years without realizing it, for example stained glasses in medieval churches have been made using nanoscale gold or silver particles, modern science have been attempting to find different ways to deliberately make nanomaterials to utilize their enhanced properties such as lighter weight, higher strength or greater chemical reactivity.[5] Recent advances in the top-down manufacturing, especially by the semiconductor industry has given us a variety of complex nanopatterns, but they still are costly and difficult to generate.[6] As an alternative, DNA nanotechnology has emerged as a reliable method to rationally design and build nanomaterials through bottom up self-assembly.[6] There

are some feasible directions that we can envision as a result of the work presented in this thesis.

From the results of Chapter 1, we could expand the hybrid DNA-RNA nanotube system to perform multiple rounds of operation reliably which is a desirable feature of synthetic molecular machines. These nanotubes could also be functionalized with protein binding domains or small RNA molecules with therapeutic properties (siRNA, microRNA or antisense RNA)[7,8]. Hybrid DNA-RNA nanotubes are thus a good candidate to be used together with synthetic biochemical networks in natural and artificial cells, and have potential to serve as a model system in engineering nano-machines operating out of equilibrium.

The results in Chapters 2 provide a direction for further development and testing of the theory behind multicomponent self-assembly of finite sized structures. It will be useful to build a model that has the ability to capture nanotube population dynamics, in a number of different reaction conditions. Future research would focus on modelling nanotube length distributions where tiles are activated or deactivated over time by DNA or RNA species released by upstream dynamic circuits.[1] A detailed numerical sensitivity analysis will be useful to clarify the influence of individual processes (nucleation, polymerization/depolymerization, fragmentation and joining) on the kinetics and steady states of the length distributions, in particular considering different concentration regimes and alternative reaction mechanisms.[9, 10]

The results in Chapters 3 points to the potential application of NA nanostructures as a rich toolkit for generating complex scaffolding components in artificial cells. Our demonstration could be immediately expanded to include multiple filamentous scaffolds to spatially organize distinct organic or inorganic ligands, and each scaffold may be individually controlled by distinct synthetic genes or circuits.[11] Further, NA nanotubes could be organized in higher-order

structures using other types of assemblies such as DNA origami.[12] Finally, because NA scaffold assembly can be regulated by complex synthetic gene networks and strand displacement reactions within compartments, the coordination of multi-compartment behavior through diffusing molecules could open up exciting opportunities to build artificial tissues with programmable development and patterning.[13,14]

4.3 References

1 S. Agarwal and E. Franco, "Enzyme-Driven Assembly and Disassembly of Hybrid DNA–RNA Nanotubes." Journal of the American Chemical Society 141, no. 19 (2019): 7831-7841.

2 Pacella, M. S., Mardanlou V., Agarwal S., Patel A. , Jelezniakov E., Abdul M. Mohammed, E. Franco, and R. Schulman. "Characterizing the length-dependence of DNA nanotube end-to-end joining rates." Molecular Systems Design & Engineering 5, no. 2 (2020): 544-558.

3 Hariadi, R.F., Winfree, E., Yurke, B.: Determining hydrodynamic forces in bursting bubbles using dna nanotube mechanics. Proceedings of the National Academy of Sciences 112(45) (2015) E6086–E6095

4 S. Agarwal, M. Klocke, P. Pungchai and E. Franco, "Dynamic self-assembly of compartmentalized DNA nanotubes." Nature communications 12, no. 1 (2021): 1-13.

5 Bhushan, B., & Baumann. (2007). Springer handbook of nanotechnology (Vol. 2). B. Bhushan (Ed.). Berlin: Springer.

6 Seeman, N. C., & Sleiman, H. F. (2017). DNA nanotechnology. Nature Reviews Materials, 3(1), 1-23

7 Stewart, J. M. et al. Programmable RNA microstructures for coordinated delivery of siRNAs. Nanoscale 8, 17542-17550 (2016).

8 Sharma, A. et al. Nanogel—an advanced drug delivery tool: Current and future. Artificial cells, nanomedicine, and biotechnology 44, 165-177 (2016).

9 Markvoort AJ, Eikelder HMt, Hilbers PA, de Greef TF (2016) Fragmentation and coagulation in supramolecular (Co) polymerization kinetics. ACS Cent Sci 2(4):232–241

10 Mardanlou, V., Green, L.N., Subramanian, H.K., Hariadi, R.F., Kim, J., Franco, E.: A coarse-grained model of dna nanotube population growth. In: International Conference on DNA-Based Computers, Springer (2016) 135–147

11 Liu, X. et al. Biomimetic DNA nanotubes: nanoscale channel design and applications. Angew. Chem. 58, 8996–9011 (2019).

12 Jorgenson, T. D., Mohammed, A. M., Agrawal, D. K. & Schulman, R. Self-assembly of hierarchical DNA nanotube architectures with well-defined geometries. ACS Nano 11, 1927–1936 (2017).

13 Dupin, A. & Simmel, F. C. Signalling and differentiation in emulsion-based multi-compartmentalized in vitro gene circuits. Nature Chemistry 11, 32–39 (2019).

14 Gruner, P. et al. Controlling molecular transport in minimal emulsions. Nature Communications. 7, 10392–10392 (2016).